Atmospheric Pressure Plasmas for More Sustainable Chemical Processes and Environmental Applications

PhD Thesis

Paula de Navascués Garvín

UNIVERSIDAD DE SEVILLA

CSIC
Consejo Superior de Investigaciones Científicas

Sevilla 2022
Instituto de Ciencia de Materiales de Sevilla

Atmospheric Pressure Plasmas for More Sustainable Chemical Processes and Environmental Applications

PhD Thesis

Paula de Navascués Garvín

Departamento de Física Atómica, Molecular y Nuclear

Instituto de Ciencia de Materiales de Sevilla (CSIC-US)

Universidad de Sevilla

Sevilla, 2022

Atmospheric Pressure Plasmas for More Sustainable Chemical Processes and Environmental Applications

A dissertation submitted for the degree of Doctor (Ph.D.) in Physics by the University of Seville

Memoria presentada para optar al grado de Doctora en Física por la Universidad de Sevilla

Seville, March 2022

Paula de Navascués Garvín

Directed by:

Dr. Ana Mª Gómez Ramírez
Profesora Titular
Departamento de Física Atómica, Molecular y Nuclear
Universidad de Sevilla (US)

Prof. Agustín Rodríguez González-Elipe
Profesor de Investigación
Instituto de Ciencia de Materiales de Sevilla
Consejo Superior de Investigaciones Científicas (CSIC)

Mentor:

Dr. Ana Mª Gómez Ramírez
Profesora Titular
Departamento de Física Atómica, Molecular y Nuclear
Universidad de Sevilla (US)

“Si yo encontrara la estrella
que me guiara,
yo la metería mu dentro de mi pecho
y la venerara.
Si encontrara la estrella
que en el camino me alumbrara.”

Estrella – Enrique Morente

Resumen

La tecnología de plasmas no térmicos permite llevar a cabo a presión atmosférica y temperatura ambiente reacciones químicas que, mediante métodos químicos convencionales, requieren altas presiones y temperaturas. Esto es posible gracias a la elevada energía de los electrones, así como a la presencia de otras especies excitadas en el plasma, que permiten la activación de reacciones químicas mientras el gas permanece a temperatura ambiente. Los reactores de plasma no térmico son de pequeño tamaño, pueden operar de manera distribuida y se caracterizan por un funcionamiento fácil y seguro. Además, el tiempo necesario para alcanzar el estado estacionario de operación es despreciable frente a las técnicas catalíticas convencionales y pueden ser alimentados de forma intermitente con energía procedente de fuentes renovables. De esta manera, con vistas a una industria química verde (entendida como de bajo consumo energético y sin emisiones de carbono), de diseño y funcionamiento circular y operación descentralizada, los reactores de plasma no térmico se sitúan como candidatos óptimos en la búsqueda de soluciones de impacto tecnológico.

Esta Tesis Doctoral desarrolla un estudio experimental, a escala laboratorio, de distintos procesos químicos de interés utilizando reactores de plasma operados a presión atmosférica. El trabajo de investigación se ha desarrollado en los laboratorios del grupo de investigación de Nanotecnología en Superficies y Plasma perteneciente al Instituto de Ciencia de Materiales de Sevilla (centro mixto del Consejo Superior de Investigaciones Científicas y la Universidad de Sevilla). Los procesos químicos estudiados han sido la síntesis y la descomposición de amoniaco, así como la eliminación de la molécula de CO_2 y su revalorización, usando para esto último mezclas con metano.

Las fuentes de plasma no térmico utilizadas en esta Tesis Doctoral se conocen como reactores de lecho empaquetado (en inglés, *packed-bed reactors*). Su funcionamiento se basa en las denominadas “Descarga de Barrera Dieléctrica”, que consisten en el encendido de un plasma en la región comprendida entre dos electrodos entre los que se sitúa, al menos, una barrera de material aislante. El mantenimiento en el tiempo de estas descargas permite el tratamiento de gases que se difunden a lo largo del reactor, en el espacio libre situado entre los dos

electrodos, produciéndose las reacciones químicas de interés. En configuración *packed-bed*, todo el espacio comprendido entre los electrodos se rellena con *pellets* de material aislante, formándose el plasma en el volumen libre entre los *pellets*. De esta forma, las especies del plasma pueden interaccionar con el material de barrera, dando lugar a posibles sinergias. Por este motivo, este trabajo de investigación se enmarca en los campos conocidos como Química del Plasma y Plasma Catálisis.

Esta tesis doctoral se ha estructurado en tres grandes bloques. Un primer bloque, que abarcaría los Capítulos 1, 2, y 3, contiene una introducción a la temática propuesta, así como una descripción de los objetivos planteados y la metodología empleada para alcanzar dichos objetivos. El segundo bloque engloba la discusión de los resultados y se ha organizado a su vez en tres partes. En primer lugar, en el Capítulo 4 se analiza el comportamiento eléctrico de los reactores de lecho empaquetado en función del material (ferroeléctrico o dieléctrico) que se incorpora entre los electrodos. A este material se le conoce como moderador de la descarga. Una conclusión de este capítulo es la conveniencia de trabajar con materiales ferroeléctricos, de alta permitividad dieléctrica, en lugar de con dieléctricos convencionales. Concretamente, la cerámica PZT (Zirconato Tinatato de Plomo) se ha seleccionado como material moderador de cara a conseguir un mayor rendimiento y eficiencia energética en las reacciones de amoniaco y CO_2 estudiadas en los capítulos siguientes.

La segunda parte de la discusión de resultados, contenida en los Capítulos 5, 6 y 7, desarrolla un estudio sobre reacciones de amoniaco. En el Capítulo 5 se presenta un análisis de los mecanismos de reacción para la síntesis y la descomposición de amoniaco. Con este objetivo, se aplica una metodología de marcado isotópico que, aunque comúnmente aplicada en procesos catalíticos convencionales, no ha sido usada hasta la fecha con generalidad en estudios de Plasma Catálisis. Esta metodología permite poner de manifiesto determinados mecanismos de reacción, lo que posibilita la identificación de procesos intermedios que no contribuyen a mejorar la eficiencia energética de las reacciones de interés. Así mismo, ha permitido demostrar la contribución de la superficie del moderador de la descarga, PZT en nuestro caso, en la reacción de síntesis de amoniaco. En los Capítulos 6 y 7 se estudian las reacciones de síntesis y descomposición de amoniaco incorporando un catalizador de rutenio al lecho empaquetado de PZT, con vistas a analizar cómo afecta al rendimiento y a la eficiencia energética de ambos procesos. Un estudio sistemático ha permitido concluir que la introducción del catalizador no es una estrategia eficiente para la síntesis de amoniaco, mientras

que sí permite mejorar en cierta medida el rendimiento para la producción de hidrógeno mediante la descomposición de amoniaco.

Seguidamente, los Capítulos 8 y 9 presentan sendos estudios sobre reacciones de CO_2. Por un lado, en el Capítulo 8 se presenta la eliminación de CO_2 mediante su conversión mayoritaria en CO y O_2. En vistas a la operación de estos reactores en condiciones reales de aplicación, se han estudiado mezclas de dicho gas con oxígeno y con aire, logrando la eliminación de CO_2 sin emitir subproductos de reacción nocivos para el medio ambiente y la salud. Por otro lado, el Capítulo 9 aborda el estudio de mezclas más complejas, concretamente de CO_2 y CH_4, para la revalorización de ambos gases de efecto invernadero. Dichas mezclas cuentan con una amplia variedad de posibles productos de reacción, como hidrocarburos de distinto tipo. Mediante el uso de la técnica de marcado isotópico (utilizando el isótopo $^{13}CO_2$) se concluye que CO_2 y CH_4 siguen caminos de reacción en el plasma mayoritariamente independientes.

Para finalizar, el último bloque de la tesis contiene las principales conclusiones obtenidas (Capítulo 10), así como una lista de los trabajos científicos publicados en relación con la tesis doctoral.

Abstract

Nonthermal plasma technology operated at atmospheric pressure is an ideal candidate to induce chemical reactions and overcome the current limitations of conventional catalytic methods carried out at high pressures and temperatures. In nonthermal plasmas, the high energy of the electrons, together with the existence of radicals and excited species, make possible the activation of different chemical processes. Nonthermal plasma reactors are small in size, can be operated in a distributed way, are easy to operate and to scale up, and do not entail significant risks. Furthermore, the induction time is negligible as compared to conventional catalytic techniques, and they can be powered by intermittent renewable energy sources. It could be said that, in terms of the promotion of the green chemical industry, nonthermal plasma technology represents a non-aggressive alternative characterized by low energy costs and reduced carbon dioxide emissions. Nonthermal plasma reactors are straightforward candidates in the search for innovative and more sustainable solutions to replace thermally induced methods.

This thesis work has been developed in the Laboratory of Nanotechnology on Surfaces and Plasma of the Materials Science Institute of Seville, which is a join research center between the Spanish National Research Council and the University of Seville. The thesis addresses an experimental study, carried out using an atmospheric-pressure plasma reactor, of various highly impact chemical processes, such as the ammonia synthesis and decomposition reactions, the splitting removal of CO_2, as well as its revaluation, using mixtures with methane in this latter case.

The nonthermal plasma reactors used in this thesis work are known as packed-bed reactors. Their operating mode is similar to that of Dielectric Barrier Discharges (DBDs), where a self-sustained plasma is generated between two electrodes separated by, at least, one dielectric barrier. The stable ignition of these discharges enables the processing of gases flowing through the free space between the reactor electrodes, thus promoting the realization of specific chemical reactions. In a packed-bed configuration, the space between electrodes is filled with pellets of dielectric materials (note that in classical DBDs the dielectric barrier(s) is/are usually situated onto the electrode(s)) and the plasma is ignited in

the voids between the pellets. Therefore, chemical reactions can occur not only at the plasma bulk but also at the barrier material surface, which can contribute to promote new reaction pathways and plasma-catalysis synergies. Accordingly, this research work focuses on the fields known as *Plasma Chemistry* and *Plasma Catalysis*.

The thesis is structured in three main sections. The first section, encompassing Chapters 1, 2, and 3, summarizes the background frame of the research, as well as a description of the objectives and the materials and methods utilized to accomplish these objectives. The second section contains the discussion of the obtained results, and it is also divided into three parts: Chapter 4, Chapters 5-7, and Chapters 8-9. Firstly, in Chapter 4, the electrical behavior of the packed-bed reactor is characterized as a function of the utilized barrier material: classical dielectrics and high dielectric constant ferroelectrics. It is demonstrated the convenience of using the latter and the importance of the material´s Curie temperature. More specifically, PZT (Lead Zirconate Titanate) has been selected as a suitable moderator material providing high reaction yields and energy efficiencies for the ammonia and CO_2 reactions studied in following Chapters. Chapters 5, 6, and 7, present a comprehensive study of ammonia reactions. Chapter 5 is focused on the study of the reaction mechanisms for ammonia synthesis and decomposition reactions. By applying a disruptive isotope labeling methodology, commonly used in conventional catalysis but scarcely used in Plasma Catalysis, it has been possible to identify reaction mechanisms and intermediate processes that do not contribute to the ammonia synthesis and, therefore, limit the efficiency of the plasma-assisted process. Furthermore, it has allowed us to experimentally demonstrate the contribution of the surface of the moderator material (PZT) to the overall process. In Chapters 6 and 7, addressing respectively the ammonia synthesis and decomposition reactions, it has been studied the incorporation of a ruthenium-based catalyst into the PZT barrier to analyze how it affects the reaction yield and energy efficiency. A systematic study concludes that the use of a metal catalyst is not an efficient strategy for optimizing the ammonia synthesis reaction, but can increase, to some extent, the reaction yield for hydrogen production through the decomposition of ammonia.

Chapters 8 and 9 present the study of CO_2 reactions. On the one hand, Chapter 8 deals with the conversion of CO_2 into CO and O_2 in the packed-bed plasma reactor moderated with PZT, achieving conversion rates and energy efficiencies higher than those obtained with other more commonly used

ferroelectric materials. To analyze the CO_2 splitting process under more realistic conditions, mixtures of CO_2 with O_2 and with dry air have been studied, obtaining high efficiencies and without formation of harmful products. On the other hand, CO_2 and CH_4 mixtures have been studied in Chapter 9, focusing on the valorization of these two greenhouse gasses. The ignition of these plasmas gives rise to a wide range of possible products, particularly in the form of multiple types of hydrocarbons. The application of the isotope labeling methodology has allowed us to conclude that CO_2 and CH_4 roughly follow independent reaction pathways and that they scarcely interact in the plasma.

Finally, the last section of the thesis work contains the general conclusions (Chapter 10) and a summary of the scientific production in relation to the work of the Ph.D candidate.

Table of Contents

Chapter 1

Introduction

1.1. General Context and Motivation of the Thesis

The current environmental situation of our planet demands the best of our societies. Humanity is facing both a rapid increase in the concentration of greenhouse gases in the atmosphere – with its multi-dimensional consequences – and a continued depletion of natural resources. The Sustainable Development Goals (SDGs), approved by the United Nations in 2015 with the intention that they can be achieved by the year 2030, attempt to fight the consequences of the fastest-growing Earth's Climate change ever happening, which is taking place because of anthropogenic factors [1]. The SDGs demand not only the development of alternative processes to sustain human lives, but also a revision about the how a large part of humanity produces and consumes. Among the 17 SDGs, there are some goals directly related to the subject of this thesis, like Goal 7 (Affordable and Clean Energy), 11 (Sustainable Cities and Communities), and 13 (Climate Action). Since the 17 objectives are tightly cross-linked, working towards the achievement of just one of them would contribute to the accomplishment of the others. Such big challenges require integral solutions.

Diverse and multidisciplinary solutions should be applied to reach zero emissions of greenhouse gases by 2050, a goal recently approved by the European Union [2]. To this end, dealing with alternative energy sources is one of the most important requirements. The replacement of fossil fuels – oil, natural gas, and coal –by renewable power sources is crucial because the burning of fossil fuels is responsible for 75% of global emissions [2]. Nevertheless, this substitution entails the change in the design of many industrial processes, in such a way that they can be powered with intermittent energy sources, generally backed by renewable electricity rather than by continuously operated combustion processes.

During the last few decades, hydrogen has emerged as a sustainable fuel, especially if it is obtained from CO_X-free compounds like water or ammonia. In particular, ammonia has been proposed as a promising hydrogen vector because of

its high hydrogen content and the availability of existing infrastructure for its storage and worldwide distribution [3]. Additionally, the enthalpy of the ammonia decomposition reaction is lower than that of the water-splitting reaction [4]. These features prove the benefits of ammonia decomposition processes for the production of hydrogen.

Although the replacement of fossil fuels by other energy sources is a crucial target, additional changes should be introduced in many other industrial activities, in particular in the chemical industry. Returning to the example of ammonia, the Haber-Bosch (H-B) process, which is widely utilized for the synthesis of this compound – mainly for the production of fertilizers –, is under serious discussion. H-B ammonia synthesis is carried out at high temperatures and pressures and is responsible for 1% - 2 % of the world energy demand and for 1.2% of CO_2 global emissions [5]. The reduction of this enormous CO_2 fingerprint has fostered the search for alternative nitrogen fixation procedures.

Achieving zero CO_2 emissions is a challenge difficult to reach in the short-term, mainly because the development and implementation of new industrial processes avoiding greenhouse gas emissions will take time. Therefore, one of the mitigation strategies proposed at short- and mid-terms is the capture and the use of these emissions before they diffuse into the atmosphere. Technologies targeting this purpose include the Carbon Capture Storage (CCS) and the Carbon Capture Utilization (CCU). These strategies are based on the *cradle-to-cradle* proposal from Braungart and McDonough [6], which defines how wastes could be utilized as raw compounds for the synthesis of new valuable products.

The previous considerations strongly support the need of new low energy cost processes suitable to be coupled with renewable power sources, able to be fed by electricity, and designed in a circular way to reuse wastes. These wastes, rather than being discarded, would be used as raw recycled compounds.

Within this context, this thesis focuses on the study and design of nonthermal plasma procedures that, powered with electricity, are conceived to carry out sustainable chemical processes, including the possibility of reusing carbon emissions. Owing to the characteristics of nonthermal plasmas, chemical processes can be performed at atmospheric pressure and ambient temperature with low energy costs and zero CO_2 emissions. These benefits justify the use of plasma technology as a strategic option for the future [7].

This thesis frames within the general topic known as Plasma Chemistry, which has many different applications. The research carried out in this thesis focuses on Gas Processing and, in part, in an emerging discipline named Plasma Catalysis, concepts that are explained in detail in the upcoming pages of this first chapter. The thesis work contemplates the study of four highly demanded processes: (1) ammonia synthesis from nitrogen and hydrogen, (2) ammonia decomposition to produce hydrogen, (3) the conversion of carbon dioxide into carbon monoxide and oxygen, and (4) the valorization of carbon dioxide and methane mixtures. We expect that the results obtained and the discussions carried out in this report will attract the interest of readers and contribute to the development of state-of-the-art solutions.

1.2. Nonthermal Plasmas Sources

1.2.1. General Concepts about Plasmas

Plasmas are partially ionized, electrically quasi-neutral gases, characterized by a collective behavior of their constituents [8]. Some authors consider plasma as *the fourth state of matter* [8,9], but other authors think that this consideration is not correct from a thermodynamic point of view and propose that plasmas are gases that can be ionized to a different degree. Because of its partially ionized state, in plasmas there are electrons, ions, and neutral particles. In addition, plasmas contain other components such as radicals, photons, or electronically and vibrationally excited species, all of them playing an important role in plasma's behavior.

Any comprehensive introduction to plasmas requires the classification of these systems. There are many different criteria to classify these physical systems. In terms of the average energy of their main components (i.e., temperature), a common approach is to classify plasmas into two major groups: thermal and nonthermal plasmas [10]. Thermal plasmas are characterized by that electrons and heavy particles present similar energies and are in thermodynamic equilibrium. Classic examples of thermal plasmas are those of fusion or star plasmas [8]. The second group, nonthermal plasmas, is characterized by higher energy of the electrons with respect to that of heavy particles, implying that they are systems far from the thermodynamic equilibrium. Nonthermal plasmas, also called "cold plasmas" or "gas discharges", have been handled and managed in the laboratory

since their discovery in the 19th century. There are also examples of nonthermal plasmas in nature, like the aurora borealis [8].

Although an equivalency between energy and temperature is only strictly correct when the particles follow a Maxwellian distribution function, in plasma technology these concepts are indistinctly used, and electron energy is commonly referred to as electron temperature (T_e). More comments on the Electron Energy Distribution Function (EEDF) in plasmas are provided in **section 1.2.3**.

The density of charged species defines the ionization degree of the plasma. The ionization degree is calculated as the ratio of the density of charged particles (ions) to the total particle concentration [11]. When this ratio is near to the unit (1), these systems are known as completely ionized plasmas. Conversely, when there are more neutral than charged particles, the plasma is considered weakly ionized. The gas discharges under study in this thesis are weakly ionized plasmas and have ionization degrees between 10^{-7} and 10^{-4} [12].

Another classification, quite important for possible applications of plasma technology, relies on the gas pressure. Gas discharges have been traditionally developed and operated at low pressures. These plasmas have had many applications in Material Science during the last few decades and have contributed to strategic advances in different key technological fields like microelectronic manufacturing [9]. However, plasmas can be also operated at atmospheric or even higher pressures [8], as in the stars, where pressures around 10^{14} Pa can be reached [8]. In the laboratory, atmospheric-pressure plasmas have many different applications, like driving chemical reactions for gas processing; the study presented in this thesis is an example of this approach. The increasing interest in these plasmas relates to various technological solutions for final applications incompatible with vacuum conditions [13]. Some examples are the treatment of living tissues for medical purposes [14,15], the treatment of seeds to improve their germination rates [16,17], or that of water for its decontamination [18,19].

In plasmas, the pressure is a very important parameter, because it controls the mean free path of the particles. At high-pressure conditions, the mean free path of the particles is small, and the plasma properties are determined by collisions between particles. However, at low-pressures, the mean free path of the particles is larger than at high pressure, and it is possible to control the trajectory of charged particles towards given locations using electromagnetic fields. It will be discussed below that collisions in plasmas determine the efficiency of the transference of

energy (and momentum) between heavy particles (ions and neutrals). Meanwhile, interactions between electrons and heavy particles are responsible for phenomena such as the breaking of bonds in molecules or the molecular ionization [11].

A common configuration to generate a plasma consists of two electrodes and a power electromagnetic source. Generally, when applying a voltage between the electrodes under well-defined operating conditions, the gas situated between the electrodes can be ignited, producing a discharge whose control is critical for applications. In this context, plasmas can be also classified as a function of the electromagnetic field applied: DC, pulsed DC, or AC; and for AC power sources: microwaves (MW), radiofrequency (RF), Hz and kHz frequencies [20].

Taking into account the aforementioned concepts, **Figure 1.1** summarizes the properties of the plasma sources utilized for the experiments of this thesis: nonthermal weakly ionized plasmas, which are operated at atmospheric pressure and ambient temperature, and that present electron temperatures (T_e) generally between 1 and 20 eV [7] and electron densities (n_e) between 10^8 and 10^{14} cm^{-3} [13]. They are ignited using AC power sources in the range of a few kHz. To operate these discharges, the applied technology is the so-called Dielectric Barrier Discharge (DBD), which will be explained in more detail in the upcoming sections.

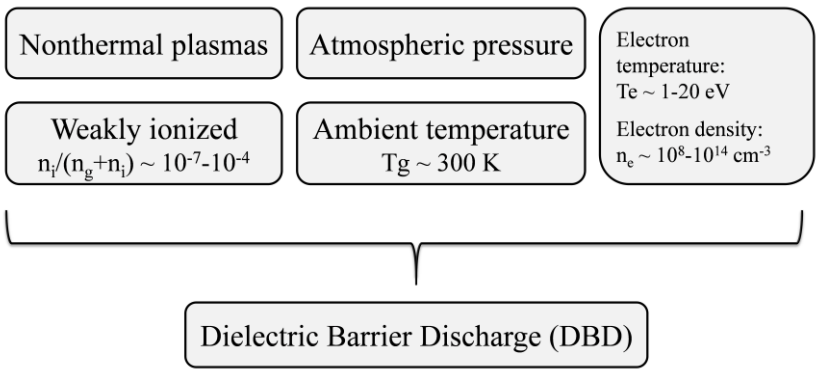

Figure 1.1. Summary of the main properties of the atmospheric plasmas utilized for the experiments of this thesis. In the scheme, n_i refers to the density of ions and n_g and T_g to the density and temperature of neutral particles, respectively.

It has been previously indicated that nonthermal plasmas are systems far from the thermodynamic equilibrium where electrons are much more energetic than ions and neutral species. The range of electron temperatures and the high

reactivity of plasma-activated species are suitable to induce different chemical reactions [11]. According to the Drexel Plasma Institute (US) reputed researcher Alexander Fridman, these properties situate plasma "as a high-tech magic wand of modern technology" [8]. As Fridman states, the success of plasma technology is due to the lack of a competitor technology with the same possibilities; in other words, to the unique performances of the plasma technology. Nowadays, there is a broad range of cold plasma applications such as surface treatment, nanomaterials processing, ozone production, or water purification, to name a few [9]. Regarding environmental applications, plasmas can be used to remove non-desired products present in the atmosphere (e.g., greenhouse gases, like carbon dioxide), as well as pollutants or pharmaceutical residues present in drinking water [21]. Regarding gas processing, atmospheric-pressure plasmas can also be used to produce valuable chemical products such as ammonia, hydrogen, hydrocarbons, or other compounds [22].

1.2.2. Breakdown Mechanisms in Nonthermal Plasmas

A very important concept is that of *plasma breakdown*, not only because it explains how plasmas are ignited and sustained, but also because it is related to the most fundamental plasma process: ionization. Although breakdown mechanisms in low-pressure plasmas are well understood and described in terms of the Townsend mechanism and Paschen's Law [8], the concepts involved cannot be applied directly to atmospheric-pressure plasmas.

To figure out the breakdown process, we may think about two parallel electrodes that are separated at a distance 'd' (known as the *gap*), with a gas located between the electrodes at a pressure 'p', and a voltage applied between them. Traditionally, the concept of plasma breakdown can be defined as the transition from a *dark discharge* to a *glow discharge* when the breakdown voltage (V_B) is applied [23]. The *dark discharge* is characterized by the first ionization coefficient of Townsend, α, which accounts for the electron-ion pairs formed in avalanches after a first electron is emitted by the cathode. On the other hand, the glow discharge is characterized by the emission of secondary electrons from the cathode due to different processes such as ion impact or photoemission. The glow discharge is related to the second ionization coefficient of Townsend, γ, which accounts for the secondary electron yield per ion formed [23]. Both α and γ coefficients are an exponential function of the applied electric field and are used to derive the

Paschen's Law [8], which establishes a relation between the breakdown voltage and the p·d value. Nevertheless, this explanation is not valid for plasmas operated at high pressures. In high-pressure plasmas, it is supposed that the breakdown occurs on a nanosecond scale, i.e., faster than the time required by electron avalanches produced by secondary emission processes [13]. There is no agreement in literature about the validity of the classical Paschen's Law in the upper and lower range of p·d, with various assessments and a wide range of values depending on the operating conditions. For example, Brugemann *et al.* proposed a limiting p·d value of 1000 Torr·cm for air plasmas [13]. Other authors like A. Fridman [8] have proposed higher values, in the order of 4000 Torr·cm. Otherwise, there is a vivid debate around the accuracy of Paschen's Law in the lower range of p·d values [24], although this point is not relevant in this thesis.

To get a proper understanding of the breakdown mechanism for plasmas operated at high pressure – like atmospheric pressure – it is necessary to introduce the concept of *streamer*. At high pressure, there is an increase in the number of collisions, producing ionization and affecting the breakdown mechanism. **Figure 1.2** illustrates this process for two electrodes separated by a *gap* 'd' and a voltage applied between them, producing an electric field E_0 in the region between the electrodes. Firstly, when the voltage is applied and the electric field is generated, the primary avalanche of electrons generates a charge distribution in the gas volume (see **Figure 1.2**, *Primary avalanche*). This space charge can locally produce an enhancement in the electric field and, consequently, give rise to avalanches of secondary electrons mainly initiated by photo-ionization. The channel formed by positive charges, electrons, and photons is called a *streamer* [13] (see **Figure 1.2**, *Streamer initiation*). Specifically, if the *streamer* propagates from the anode to the cathode it is referred to as positive or *cathode-directed streamer* [8,13]. Negative or *anode-directed* streamers are less important, since they are only formed at high over-voltages and large gaps [25]. The streamer initiation requires certain conditions, referred as the Meek criterion: the perturbation of the electric field by the space charge must be high enough to promote electron secondary avalanches [8].

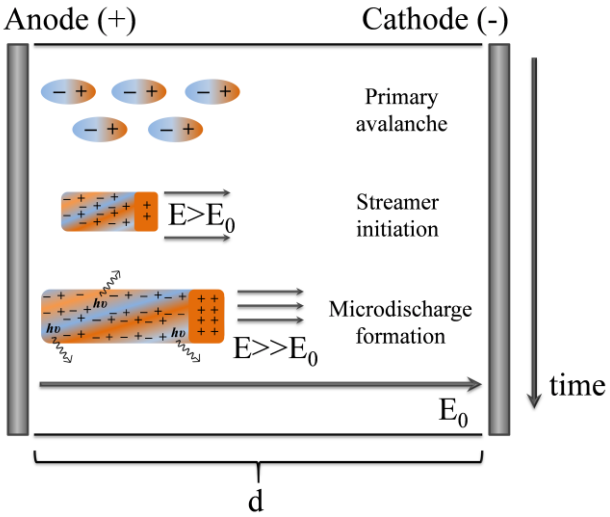

Figure 1.2. Breakdown mechanism in high-pressure plasmas based on the formation of streamers and the subsequent microdischarges after primary avalanches. These ionized channels propagate from the anode to the cathode in a nanosecond timescale.

The aforementioned considerations imply that a streamer is a weakly ionized and quasi-neutral plasma, with positive charges accumulated and oriented to the cathode [13]. Furthermore, the set of local processes that take place until the stramers cross the *gap* are named with the general term of *microdischarge* [8] (see **Figure 1.2**, *Microdischarge formation*). The microdischarges leave charges in the gas volume and at the surface of the electrodes. This charge accumulation facilitates the formation of a subsequent microdischarge when the polarity of the applied field changes (memory effect). The groups of microdischarges, that can be macroscopically observed, are usually called *filaments* [26].

According to the Meek criterion, at atmospheric pressure the discharges can be strictly filamentary – governed by the streamers formation – or more diffuse (homogenous) – dominated by electron secondary emission, i.e., without satisfying the Meek criterion. Ulrich Kogelsatz [26] and Françoise Massines [27] published different studies about these two mechanisms in the first decade of the 2000s. In many plasma sources utilized for gas processing the two discharge's behaviors can coexist.

Different factors determine the breakdown mechanism in plasmas operated at atmospheric pressure. They include the reactor configuration, the electrical parameters, or the type of gas [28,29]. Regarding the latter factor, many studies

have reported changes in the breakdown mechanisms when adding small percentages of other gases to a pure gas plasma [30,31]. For example, CO_2 discharges at atmospheric pressure are generally filamentary. However, when nitrogen is added to the mixture, the discharges become partially diffuse due to the presence in the plasma of nitrogen metastable species [32]. It has been proposed that these species produce seed electrons that induce a Townsend breakdown [33]. This issue is quite relevant for this thesis, which contains a study about real mixtures of CO_2 and air (see **Chapter 8**).

1.2.3. Elementary Reactions in Plasmas: the Role of Electrons

When a potential drop is applied between two electrodes, electrons – the lightest and most mobile particles – are fed in the plasma by the electromagnetic power source. It has been explained above that electrons sustain the plasma by ionization reactions, that is, by interaction with neutral particles to produce electron-ion pairs. However, ionization is not the only process that electrons can promote. In atmospheric-pressure plasmas, many other electron-impact promoted processes have a high probability to occur [11]. An outline of the main elementary reactions promoted by electrons is summarized in **Table 1.1**. Note that negative ions are not considered, because they are not abundant in high-pressure plasmas, except for plasmas of high electronegative gases [8]. Some of the most important elementary reactions in atmospheric-pressure plasmas involve the electronic and vibrational excitation of atoms and molecules by electron impact.

Table 1.1. Outline of main processes taking place in atmospheric plasmas promoted by electrons. Species designed with $^{(*)}$ mean that they can be electronically or vibrationally excited.

Ionization	$e^- + A_2 \rightarrow A_2^+ + 2\,e^-$
Dissociation	$e^- + A_2 \rightarrow 2A + e^-$
Dissociative Ionization	$e^- + A_2 \rightarrow A + A^+ + 2e^-$
Electron Recombination	$e^- + A_2^+ \rightarrow A_2$
Excitation	$e^- + A_2 \rightarrow A_2^* + e^-$
Synthesis	$e^- + A^{(*)} + A^{(*)} \rightarrow e^- + A_2$
Decomposition	$e^- + A_2^{(*)} \rightarrow A^{(*)} + A + e^-$

Reactions in plasmas may involve not only electrons but also other components. For example, the aforementioned excited species, radicals, and other metastable species are very reactive and may play a very important role in Plasma Catalysis.

The probability of the reactions promoted by electrons depends on electron energy. This dependence can be straightforwardly illustrated for ionization reactions, which only take place if the energy of the colliding electron is higher than the first ionization potential of the involved atom or molecule. This probability can be described in terms of a *reaction cross section*, which is a fundamental characteristic of plasma elementary processes [8]. The cross section provides a measurement of the probability of a given elementary reaction: the higher the value of the cross section the higher the probability of the process to occur[1]. Another interesting parameter regarding elementary plasma reactions is the *reaction rate coefficient*, which is usually expressed in cm^3/s and refers to the volume of species formed in a reaction per time unit [8].

Usually, numerical values of *reaction cross sections* and *rate coefficients* are determined experimentally. In general, the probability of a process 'P' depends on the number of electrons that have energy above a certain threshold. Owing to this requirement, an important concept in atmospheric-pressure plasmas is the Electron Energy Distribution Function (EEDF), $f(\varepsilon)$, which describes the probability of an electron to have an energy 'ε'. An EEDF can be defined for nonthermal plasmas, even if they are not in equilibrium conditions. For atmospheric-pressure plasmas, the EEDF strongly differs from that corresponding to an equilibrium distribution and depicts a non-maxwellian behavior. For higher values of the electric field and pressure, the EEDF approaches a Druyvesteyn distribution, with the mean and maximum values shifted to higher values than those corresponding to a maxwellian distribution [8]. EEDF can be calculated using computational methods such as the BOLSIG+ code [34], commonly accepted as a valuable tool to obtain numerical solutions of the Boltzmann equation for electrons in weakly ionized gases and uniform electric fields [35].

To properly understand the complexity of plasma-chemistry reactions, it is important to consider, besides elementary processes mediated by electrons, all

[1] A. Fridman defines the reaction cross section as an imaginary circle of area σ that is escorting one of the collision partners. When the center of the other collision partner intersects σ, then the elementary process occurs [8].

possible reactions between the different plasma components. For this purpose, research in Plasma Chemistry & Catalysis relies on experimental studies to provide consistent models of the chemical reactions taking place in plasmas [36–39]. Although this thesis has a clear experimental approach, some modeling examples will be also proposed to discuss the results obtained.

1.3. Dielectric Barrier Discharge for Gas Processing

1.3.1. Fundamentals of the Dielectric Barrier Discharge

The Dielectric Barrier Discharge (DBD) is a nonthermal plasma firstly developed by Siemens in the middle of the 19th century to produce ozone [26,40]. This early design consisted of two electrodes and at least one dielectric barrier located between them. Main DBD reactor configurations are based on either parallel-plate or cylindrical geometries (see **Figure 1.3**). To ignite the discharge, a high voltage AC signal is applied between the electrodes. Since dielectrics are insulators, their activation is not possible with DC signals: DBDs operate in AC mode at frequencies between 50 Hz and 1 MHz [11].

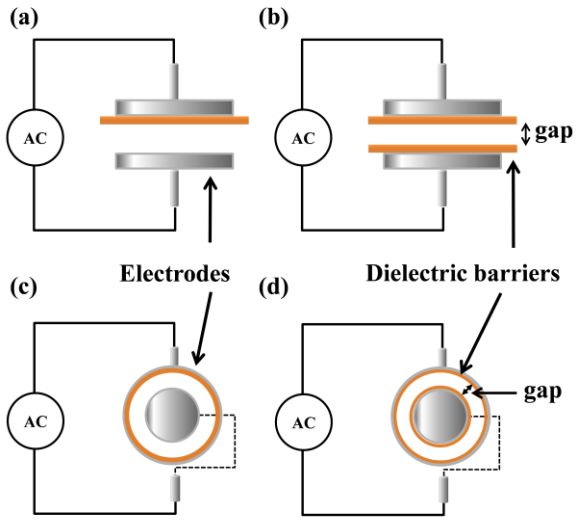

Figure 1.3. Examples of DBD configurations based on parallel-plate (a-b) and cylindrical geometries (c-d). Electrodes and dielectric barriers are indicated, as well as the gap distance defined by the free space between the electrodes.

The barrier material controls the charge transferred during the discharge. This charge is temporally accumulated on the barrier surface and, owing to this fact, the dielectrics are often referred to as *discharge moderators* [41]. The presence of dielectrics acting as current ballasts enables the generation of cold plasmas, even for large p·d products. The applied AC electric field limits the discharge duration and, due to that, these self-limited plasmas are also named *transient discharges* [13].

In DBD reactors, the distance between electrodes or gap may vary between hundreds of microns and several centimeters, depending on the application of the technology. For gas processing, the gap usually vary between millimeters and centimeters, the voltage amplitude between 1 and 10 kV, and the current amplitude between 1 and 100 mA [11].

DBD reactors enable the operation of plasmas at atmospheric pressure and room temperature. The involved discharges are characterized by a low or even null induction period to reach steady-state conditions. This makes very straightforward their integration with intermittent renewable energy sources. Moreover, DBD plasmas are safe and do not entail significant risks for humans and nature. Another feature of interest for the industry is that DBD plasma reactors can be scaled-up easily. A classic example of a large DBD discharge aims at the large-scale production of ozone [26], carried out by companies like Ozonia Ltd. for more than forty years [42]. Other examples of industrial applications of DBD are plasma TVs (now replaced by LED and Quantum Dot technologies) or the activation and decontamination of surfaces [26,43].

During the last decade, to improve the energy efficiency of chemical processes relying on this technology, some changes have been introduced in the traditional designs. This thesis focuses on the study of the Ferroelectric Barrier Discharge (FBD) in packed-bed configurations. Innovative concepts and experimental designs related to the FBDs used in this work will be explained in the upcoming subsections.

1.3.2. Ferroelectrics as Discharge Moderators

The selection of the barrier material is very important to obtain plasmas with predefined properties. The use of ferroelectrics in a FBD configuration for gas processing was firstly reported at the end of the last century (for example, in the

study of T. Opalińska and A. Szymański about ozone production published in 1996 [44]). Since then, due to the improvement in the efficiency of the plasma-driven chemical processes, the use of ferroelectrics as discharge moderators has significantly increased, particularly during the last few years.

Ferroelectric materials present a spontaneous polarization P, stemming from a preferential orientation of its dipoles, even in the absence of an applied electric field. This dipole moment appears because of a particular distribution of the constituent atoms in the crystal structure. Perovskites (ABX_3 structures) are a typical example of ferroelectrics. They depict the structure shown in **Figure 1.4,** exemplified for Lead Zirconate Titanate (PZT), the main ferroelectric material used in this thesis. Ferroelectrics are multifunctional materials since ferroelectricity encompasses other properties like piezoelectricity or pyroelectricity, which make these materials very useful for novel applications in Material Science [45]. **Figure 1.4** shows that PZT may depict two different phases: the ferroelectric phase and the paraelectric phase. The transition from the first to the second occurs when the Curie Temperature (T_C) is reached. In the paraelectric phase, the polarization of the material drops to zero, and the advantages of operating plasmas with ferroelectrics disappear.

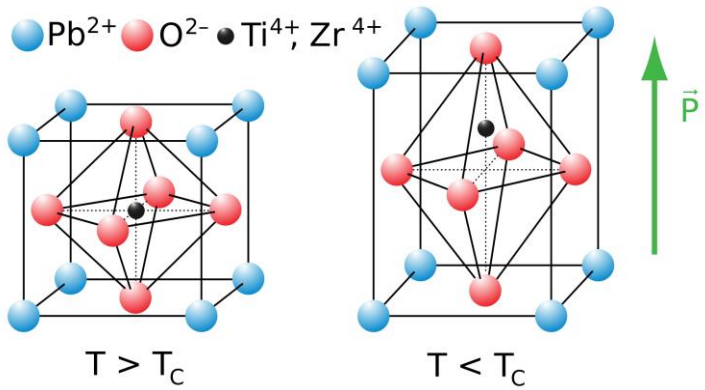

Figure 1.4. Distribution of atoms in the unit cell in PZT structures in the paraelectric phase ($T>T_c$, P=0) (left) and ferroelectric phase ($T<T_c$, P≠0) (right) (taken from [46]).

The most important characteristic of ferroelectrics for their application in DBD reactors is the high value of their relative dielectric permittivity (ε_r)[2]. Due to

[2] In this thesis the terms *relative dielectric permittivity* and *dielectric constant* are used indistinctly, although it should be remarked that the latter is the product of the former (ε_r) and the dielectric permittivity of vacuum (ε_0).

this feature, replacing a classic dielectric barrier by a ferroelectric one produces a significant increase of the charge transferred during the discharge [7,41].

Although not included in this thesis for brevity, in 2019 we reported a phenomenological comparative study of the discharge's properties in a FBD vs. a DBD parallel-plate reactor [41]. The distribution of electrodes and barriers was similar as that shown in **Figure 1.3(b)**. In this study, we showed that for similar gaps and applied voltages, the transferred charge is higher when fused silica (linear dielectric) was substituted by Lithium Niobate ($LiNbO_3$, ferroelectric material) (see **Figure 1.5**). In addition, we reported other interesting phenomena like a memory effect for the transference of charge when operating with ferroelectrics.

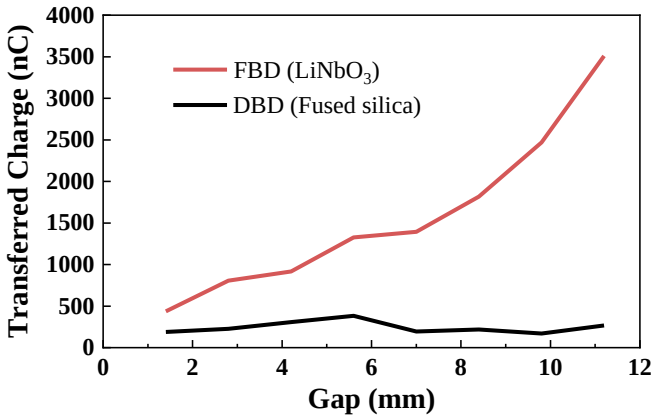

Figure 1.5. Evolution of the transferred charge vs. the inter-electrode distance (i.e., gap) in FBD and DBD parallel-plate reactors. For similar operating conditions (frequency of 1 kHz and applied voltages between 0.5 and 3 kV), the transferred charge is higher for the FBD operation. More details of this study can be found in [41].

1.3.3. Packed-bed Configurations

To further increase the energy efficiency of gas processing using atmospheric-pressure plasmas, ferroelectrics should be properly distributed between the electrodes to increase the electric field intensity without consuming too much energy. Therefore, packed-bed reactors are designed aiming at both reducing the operating voltage and increasing the transferred charge.

In a packed-bed reactor, the plate(s) that are typically placed between the electrodes are substituted with pellets of the same material up to completely fill the gap space. Under these conditions, the discharge ignites in the free volume between the pellets, i.e., reducing the distances between dielectric/ferroelectric components where the plasma is produced. According to Gauss's Law, reducing distances by introducing pellets of materials of a high dielectric constant such as ferroelectrics will decrease the voltage needed to ignite the plasma, that is, to reach the electric field intensity required to ionize the gas. Subsequently, once ignited, it is possible to work at lower voltages, thus reducing the power consumed by the reactor and increasing the energy efficiency of the plasma-driven chemical processes.

Packed-bed configurations are possible in parallel-plate and cylindrical geometries, as shown in **Figure 1.6**. Likewise, in many packed-bed reactors, at least one of the electrodes may remain covered by a dielectric layer or plate [47,48]. Al_2O_3 and SiO_2 are the most commonly utilized dielectric materials for packed-bed reactors [7,49,50], while Barium Titanate ($BaTiO_3$) is the most common ferroelectric [47,51–53].

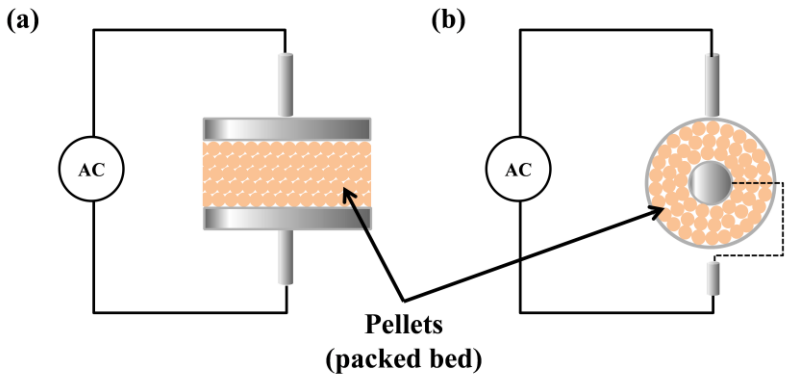

Figure 1.6. Packed-bed reactors with parallel-plate (a) and cylindrical (b) configurations.

A successful application of the packed-bed technology requires a deep understanding of discharge properties. When packed-bed reactors are operated at atmospheric pressure, they often depict a combination of two behaviors: (1) filamentary discharges between adjacent pellets and (2) homogenous discharges around the surface of the pellets (the so-called surface discharges) [29]. As explained in **section 1.2.2**, filamentary discharges involve a streamer breakdown mechanism that produces microdischarges. Meanwhile, homogenous discharges involve a Townsend breakdown mechanism, based on secondary electron

emissions. This latter type of discharges occurs around the surface of the pellets, probably because they may act as a source of seed electrons that induce the breakdown. Accordingly, W. Wang *et al.* using fluid modeling and iCCD imaging demonstrated that pellets with a high dielectric constant promote more filamentary discharges, while pellets with a low dielectric constant mainly produce surface discharges [54].

The combination of these two discharge behaviors can be observed in the picture in **Figure 1.7**. This photograph, that has been taken in our laboratory, shows a plasma of helium ignited in a packed-bed reactor filled with pellets of Barium Titanate.

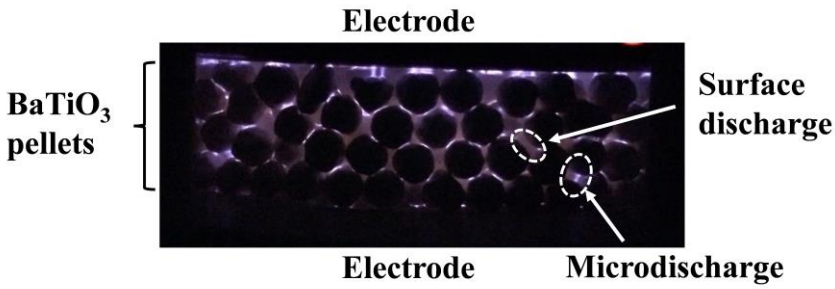

Figure 1.7. Combination of microdischarges and surface discharges in a helium plasma ignited in a packed-bed reactor. To enable the observation of the discharge the reactor walls were made of fused silica, while Barium Titanate pellets were used as discharge moderator.

The discharge behavior affects the reaction mechanisms. For example, A. Bogaerts and coworkers in the University of Antwerp (Belgium), modeling the ammonia synthesis reaction, have recently shown that different compounds are expected depending on whether the discharges have an "uniform" (homogeneous) or filamentary character [55]. Furthermore, filling the gap of a packed-bed reactor introduces an additional effect. In general, chemical reactions occurring in plasma reactors may take place both in the plasma (gas) phase and at the available surfaces, either at the reactor walls or at electrodes surfaces. The incorporation of pellets extraordinarily increases the surface area in contact with the discharges and therefore extensively promotes the occurrence of surface reactions. The control of this enhanced surface chemistry can be used to increase the energy efficiency and reaction yield of the chemical processes of interest, which brings us to the field of Plasma Catalysis where this thesis work is framed.

1.4. Plasma Catalysis

1.4.1. General Concepts About Plasma Catalysis

Through the reduction of the operating voltage, packed-bed reactors can increase the energy efficiency of the plasma-driven chemical processes. However, an increase in energy efficiency is not synonymous of an efficient control over the type of final product. A way to increase the production of a given compound or compounds of interest is precisely controlling the surface chemistry at the surface of pellets. This means that reaction s*electivity* can be improved incorporating pellets with specific catalytic properties.

Plasma Catalysis[3] designates the combination of nonthermal plasmas and heterogeneous catalysis [50]. *Catalysis* is defined as "the science and technology of influencing the rates of chemical reactions" [56]. It should be understood not only in terms of an acceleration of chemical reactions, but also as an enhancement of selectivity towards the formation of desired products. Catalysis is promoted by a material, the catalyst, that is not exhausted during the process. Specifically, *heterogeneous catalysis* is a process in which the reactants and the catalyst are not in the same phase, occurring the reactions in the interface between them [56]. In conventional catalysis, i.e., thermal catalysis, the catalytic properties of the materials are activated by heat, and the reaction processes take place at elevated temperatures. However, in plasma-catalysis the reactions will occur thanks to the synergy between the reactive species of the plasma and the properties of catalytic materials; in this case, the energy comes primarily from the plasma discharge instead of a heat source.

Kim *et al.* claimed that the first plasma-catalysis experiment was performed in the 1920s when A. B. Ray and F. O. Aderegg ignited a discharge of carbon monoxide and oxygen to produce carbon dioxide and exposed the plasma species to a silver catalyst [57]. The production rate of CO_2 obtained was higher than in equivalent experiments carried out by P. E. M. Berthelot without a catalyst [58]. This seminal experiment demonstrated the existence of clear synergies between the plasma and the catalyst. Nevertheless, the research in this field was scarcely

[3] Plasma Catalysis is usually called plasma-enhanced, plasma-assisted, or plasma-driven catalysis. In this thesis we will use the expressions Plasma Catalysis or the hyphenated version (i.e. plasma-catalysis).

developed until the 1990s, when it started to increase exponentially, and continued doing up to the present time [50].

1.4.2. Reaction Mechanisms and Energy Efficiency in Plasma Catalysis

When plasma-activated species interact with a catalytic material, surface reactions may be promoted. In particular, some reaction mechanisms borrowed from standard thermal catalysis can be used to account for the surface reactions in plasma-catalysis processes. Widely utilized reaction schemes include the Eley-Rideal (E-R), the Langmuir-Hinshelwood (L-H), and the Mars-van Krevelen (MvK) mechanisms [7]. The E-R mechanisms contemplate the interaction between a species adsorbed on the surface and another in the gas phase. In the L-H mechanisms, two adsorbed species react on the surface. In both cases, the product is formed on the surface and then desorbed to the gas phase. Meanwhile, the MvK mechanism involves the incorporation of species from the lattice of the catalyst into the reaction process, leading to the gradual exhaustion of the catalyst. **Figure 1.8** provides a scheme of each of these mechanisms. E-R and L-H mechanisms are usually mentioned in the literature for plasma-catalysis processes, whereas MvK mechanisms are considered to be less important in this area.

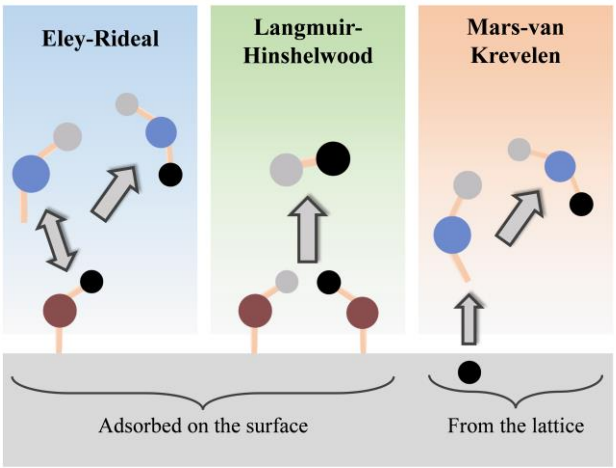

Figure 1.8. Scheme of Eley-Rideal (E-R), Langmuir-Hinshelwood (L-H), and Mars-van Krevelen (MvK) reaction mechanisms. The plasma phase is indicated with blue, green, and orange shading for the E-R, L-H, and MvK mechanisms, respectively, while the surface of the catalyst is drawn in gray color. It is indicated whether surfaces

species are adsorbed on the surface of the catalyst (E-R and L-H) or come from its lattice (MvK).

There is a certain controversy in the scientific community about the type of reaction pathways that should be interpreted as catalytic in plasma reactors. Some authors consider that plasma-catalysis encompasses all the reactions that take place at the surface [7,52,55]. Other authors have a more conservative perspective and make a clear distinction between *surface-enhanced processes* and *catalytic processes* [59]. Within this latter perspective, a surface process is designated as catalytic only when the reactive molecules are dissociated on the surface of the catalyst. This is the case, for example, of the catalytic ammonia synthesis in N_2+H_2 plasmas, when nitrogen and hydrogen reactive atomic species are formed by the dissociative adsorption of the molecules on the catalyst surface followed by their subsequent reaction [59]. However, other authors have stated that the dissociation of nitrogen and hydrogen molecules may take place in the plasma phase and the catalyst surface just contributes to their bonding association towards the formation of ammonia [60].

Proving the existence of synergy between plasma and catalysis requires unambiguous experimental evidence. A rather well-established criterion is that of an increase in the energy efficiency of the reaction when comparing values for plasma-catalysis and pure plasma processes [50]. It is also noteworthy that the formation of a given product through plasma-catalysis reactions may compete with other processes taking place in the same medium as the decomposition of the formed product molecules by electron impact [38,61]. Processes inducing the decomposition of a product before leaving the reactor are designated here as *back-reactions*. A direct consequence of the existence of *back-reactions* is a decrease in the overall energy efficiency of the desired process.

1.4.3. Reactor Designs for Plasma-catalytic Processes

Classic reactor designs in plasma-catalysis follow two approaches: the *one-stage* (also called in-plasma catalysis, see **Figure 1.9(a)**) and the *two-stage* configurations (also called post-plasma catalysis, see **Figure 1.9(b)**) [49]. In the *one-stage* configuration, the discharge is in contact with the catalyst, as it happens in packed-bed reactors. This configuration is the most widespread in literature and constitutes the working principle utilized in this thesis. The pellets that form the packed-bed can depict a catalytic behavior by themselves [52] or, alternatively,

they can incorporate catalytic particles or moieties, like Ruthenium for the synthesis of ammonia [61] or Nickel for the dry reforming of methane [62]. Meanwhile, in the *two-stage* configuration, reactions take place in two steps: a plasma zone and then a thermal catalyst section located afterwards [50], as illustrated in **Figure 1.9(b)**.

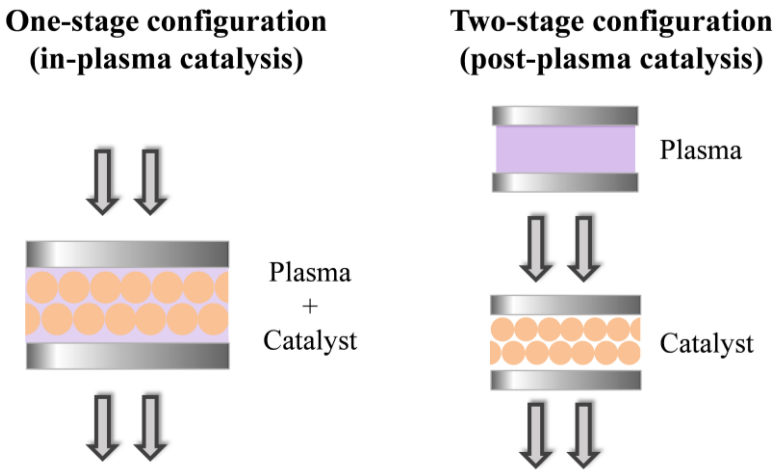

Figure 1.9. Schematic of plasma-catalysis configurations: one-stage or in-plasma catalysis (left) and two-stage or post-plasma catalysis (right).

The close interaction between plasma and catalyst in the *one-stage* configuration is a critical factor to promote the desired surface chemistry. This close contact is especially relevant because of the small mean free path of the charged species in atmospheric-pressure plasmas, generally smaller than 100 nm [50]. The timescales of collisional and transport processes also motivate the selection of this configuration. According to **Figure 1.10**, elementary plasma reactions induced by electrons occur in nanosecond scales, but chemical reactions require times in the order of microseconds [13]. The transport of the newly formed molecules and neutral species through diffusion and convection requires several seconds, as well as the transfer of heat [13], which can be indirectly promoted by the heating of the catalyst due to its direct exposure to the plasma [63].

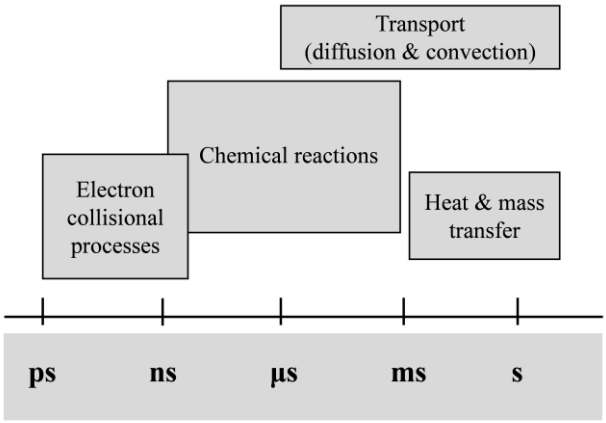

Figure 1.10. Timescales of some of the most relevant transport and collisional processes in plasma-catalysis (inspired by P. J. Brugemann *et al.* [13]).

1.4.4. Plasma & Catalyst Interactions

When plasmas and catalysts interact, there is a wide range of intermingled effects that deserve specific consideration. **Figure 1.11** gathers the main expected interactions between plasma and a catalyst, classified according to two perspectives: (1) the effects of the catalyst on plasma and (2) the effects of plasma on the catalyst.

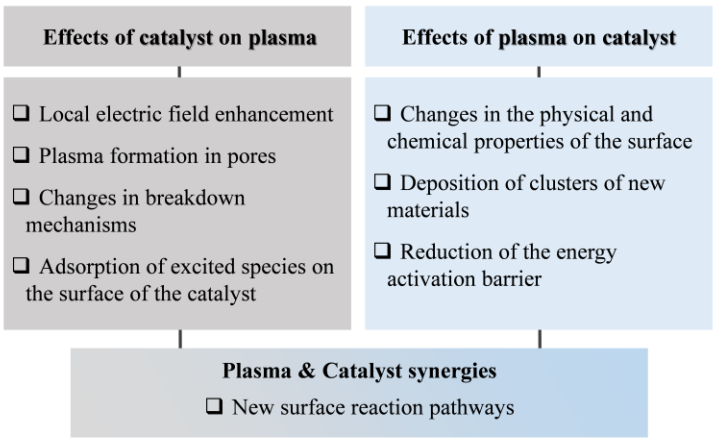

Figure 1.11. Overview of the main expected effects of the catalyst on plasma (left) and plasma on the catalyst (right). At the bottom it is indicated that, as a consequence of these effects, new surface reaction pathways can be triggered.

Regarding the effects of the catalyst on the plasma properties, a remarkable consequence is the local enhancement of the electric field (see **Figure 1.11(a)**). As discussed, the use of ferroelectrics in packed-bed reactors is a clear example of this effect due to the increase in the electric field intensity attributed to the high dielectric constant of the pellet material [7]. Similar effects can be obtained if the pellets depict an irregular topography, producing local field enhancements at the surface asperities. These two facts are relevant in this thesis work, where ferroelectric pellets characterized by a rough surface have been used to moderate the discharges.

Additionally, the catalytic pellets are often characterized by a considerable porosity. Because of this, another key question that has gained the attention of the plasma community is whether the plasma can penetrate inside the pores or not [64]. In a study by Zhang and Bogaerts [65], it is stated that the ignition of discharges inside the pores depends on their size and that the Debye length[4], usually higher than 100 nm, is the key magnitude controlling the triggering of discharges in these hollow zones.

Other effects of the catalyst on the plasma properties that are relevant for this thesis work are summarized in **Figure 1.11(a)**. These are the change in the breakdown mechanism and, therefore, the discharge behavior (homogenous or filamentary, depending on the value of the dielectric constant of the moderator material, as discussed in **section 1.3.3**) or the adsorption of excited species on the surface of the catalyst. This latter effect has resulted relevant for the study of *ammonia reactions* in upcoming **Chapters 5, 6,** and **7**.

On the other hand, plasmas can affect the physical and chemical properties of the catalyst, as indicated in **Figure 1.11(b)**. For example, depending on plasma chemistry, the discharges can change the oxidation state of the catalyst surface. Additionally, the topography of the surface can be modified by collisions with the heavy particles of the plasma. Clusters of new materials can also be formed in the plasma and be deposited onto the surface of the catalyst. A typical case is that of the deposition of carbonaceous contamination when operating plasmas of CO_2 or CH_4 [49], an issue that has been discussed for the *CO_2 reactions* studied in **Chapters 9** and **10**. Meanwhile, from a mechanistic point of view, an important

[4] The Debye length is the characteristic size of a plasma. In plasma physics it is accepted that, to have a stable discharge, it should be ignited in distances higher than the Debye length. This distance depends on different parameters like the electron density and temperature [65].

effect promoted by the plasma is the reduction of the activation energy of the catalytic processes. This effect has been widely studied for the ammonia synthesis reaction, particularly with regard to the activation of the surface chemistry through vibrationally excited states of the nitrogen molecule [66].

1.5. Ammonia: a Building Block in the Zero-carbon Energy Scenario

Ammonia is a crucial feedstock for the manufacture of fertilizers. The development of the first Haber-Bosch (H-B) industrial plant by the company BASF in 1913 in Germany inaugurated the so-called *first chemical revolution*. This artificial nitrogen fixation process was responsible for the massive production of fertilizers from the last century up to our days. Consequently, the evolution of the amount of ammonia produced in the last few decades follows the same tendency than the evolution of the global population, as illustrated in **Figure 1.12** (inspired by [67]).

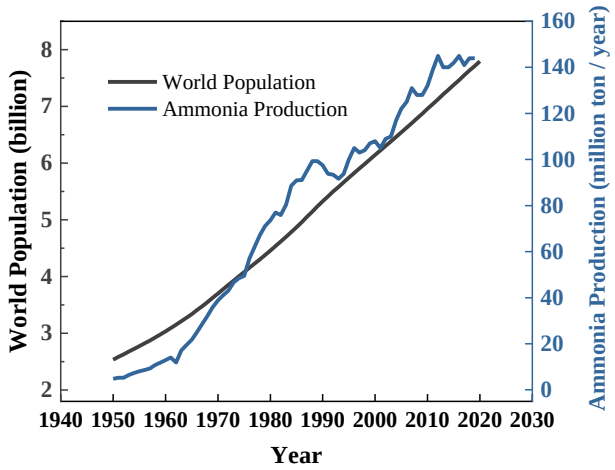

Figure 1.12. Evolution of the global amount of ammonia produced and the human population from 1950 to the present (inspired by M. Carreon [67]). Data obtained from the U.S. Geological Survey [68] and the United Nations [69].

In addition to fertilizers, ammonia has other applications: for the dye & textile industries – in fact, BASF was founded in 1865 focused on dye production – or as antimicrobial and cleaning agent [67]. Nowadays, there are prospects regarding the use of ammonia as a clean hydrogen vector. In fact, based on this

possibility, different authors have proposed that ammonia can promote a *second chemical revolution* [5].

The ammonia molecule is characterized by a high hydrogen content: one mole of ammonia contains 1.5 moles of hydrogen. Furthermore, unlike hydrocarbons, ammonia can produce hydrogen by direct decomposition without CO_2 emission. In this context, L. Torrente-Murciano states that ammonia can be considered a "portable long-term (days to months) energy storage vector," contrary to the "short-term storage (seconds to hours)" provided by batteries [5]. This possibility justifies the use of ammonia as a crucial building block in the future low-carbon energy global landscape.

Ammonia, already produced and handled at industrial level, fulfills the storage and transportation requirements for an efficient use at large scale. Additionally, its characteristic strong smell can be useful for leak identification and prevention of accidents [70]. Although ammonia is corrosive to brass and copper, this problem can be easily solved by using aluminum or stainless-steel pieces in their storage and handling systems [71].

However, to integrate the ammonia production within the new energy paradigm relying on an extensive use of renewable electricity, alternative production methods are required. The current H-B plants mainly use natural gas, oil, and coal as fuels [5], emitting more than 300 tons of CO_2 per year [72]. Moreover, even if over the last century the H-B process has been optimized, current designs are still unsuitable to face the new energetic challenges [5,73].

In particular, a critical issue is the development of small-scale electrically driven plants for ammonia production. These plants should work with renewable power sources even in geographically isolated regions. Their implementation should require low investments and their running processes should be simple and easy to control [74]. Additionally, the innovation in the use of ammonia as hydrogen vector is incomplete if there is no progress in the technologies of hydrogen production by ammonia decomposition. Consequently, the research on ammonia decomposition techniques is an active area of research, mainly focused on their implementation coupled to fuel cells [4].

The nonthermal plasma technology is a suitable candidate to carry out both the ammonia synthesis and the decomposition reactions. Specifically, the confirmed scalability and feasibility of plasma reactors based on the DBD

technology is pushing the research in this area towards the understanding of these *ammonia reactions*. However, during the last decade the plasma community has paid much attention to the study of the ammonia synthesis reaction, but very little to the study of the ammonia decomposition process. This thesis work aims at deepening our comprehension of both *ammonia reactions*, since these two processes are intimately related. To analyze these two processes, an *isotope labeling methodology* has been applied using D_2 instead of H_2, to track different reaction pathways that take place in the reactor when producing and decomposing ammonia.

The following two sections provide a summarized general overview of the approaches implemented to study the ammonia synthesis and decomposition processes. For brevity and to avoid reiterations, in the *introduction* sections of **Chapters 5** to **7** the reader can find a more specific contextualization of our work related to current results obtained by other authors.

1.5.1. Ammonia Synthesis by Nonthermal Plasmas

In parallel to other routes for ammonia production (e.g., green H-B plants, electrochemical, or photochemical), nonthermal plasma technology has emerged as a clear alternative for the ammonia synthesis process. Ammonia (NH_3) can be produced by igniting discharges of N_2 and H_2 in different plasma reactors [67]. Theoretically, its maximum energy efficiency doubles that of the classical H-B process, although the actual efficiencies determined at laboratory scale are still far from this limit [5]. The application of plasma reactors to the synthesis of ammonia is not novel. In the 19th century, different experiments studied the ammonia synthesis reaction by using plasmas. For example, in 1873 W. Donkin reported the first-known results regarding the production of ammonia with a DBD reactor [75]. A few decades later, in 1929, Brewer and Westhaver published the first systematic study on ammonia using glow discharges at low pressure [76]. However, as mentioned in **section 1.4.1**, the interest in the ammonia synthesis process launched again in the 2000s, and at present is one of the most studied topics in plasma-catalysis [77].

The ammonia synthesis reaction has been studied using different plasma sources such as DBDs, plasma jets, or radiofrequency and microwave (MW) reactors [67,77]. Although N_2 and H_2 have been traditionally used as raw materials,

there is an increasing interest in methods using water (H_2O) as the source of hydrogen atoms to produce ammonia. Different novel approaches include the combination of a plasma jet and an electrolyzer [78], the direct application of a plasma jet to water sources [79], or the ignition of discharges dosing air bubbles into water [80].

In particular, DBD technology has been the most widely used procedure to carry out the ammonia synthesis reaction, probably because the incorporation of pellets instead of dielectric plates in packed-bed reactors enables the incorporation of catalytic particles to increase the process efficiency. Ruthenium-based catalysts are the most widely studied catalysts for this purpose, followed by nickel-containing catalysts [67,77]. Different materials have been used to moderate the ammonia synthesis reaction in packed-bed reactors. Alumina (Al_2O_3), MgO and SiO_2 are the most common supports to incorporate Ru and Ni particles [67,77]. Additionally, these materials may contain Cs and K as promoters to increase the catalyst activity [81]. Other plasma sources like radiofrequency reactors may also incorporate catalytic materials (for example, the study of M. Carreon and collaborators using metal meshes as catalysts in a RF reactor [60]). Additional experimental parameters varied to study the reaction include the residence time of the gases in the discharge, the electrical operating conditions (voltage, frequency, power), or the N_2:H_2 ratio [82,83]. This latter parameter is deemed to be one of the most influential in the reaction performance and generally it is varied between 1:1 and 1:4, with the 1:3 as the most used ratio [67].

The use of ferroelectrics as moderators has further contributed to improving the process performance in packed-bed reactors. For example, in 2017, Akay and Zhang reported an interesting study where a silica-supported nickel catalyst was incorporated into a packed-bed reactor filled with $BaTiO_3$. Operating around 140ºC and at atmospheric pressure, the authors obtained reaction yields similar to those of the conventional H-B process [84]. Furthermore, in the same year, a study of our laboratory using a packed-bed reactor with Lead Zirconate Titanate (PZT) as discharge moderator and without additional catalyst showed similar reaction yields at ambient conditions of pressure and temperature [83]. These results confirm the good prospects of the use of ferroelectrics to moderate the ammonia synthesis reaction and constitute an important background of this thesis work. A more detailed description of state-of-the-art procedures for the plasma-assisted ammonia synthesis can be found in recent review publications [67,77,85].

1.5.2. Ammonia Decomposition by Nonthermal Plasmas

Unlike the ammonia synthesis reaction, the ammonia decomposition – also known as the *ammonia to hydrogen* process – has been scarcely studied using nonthermal plasmas [4]. It is also noteworthy that, the dissociation of ammonia into nitrogen and hydrogen is expected to occur when producing ammonia in plasma reactors. In fact, this has usually been interpreted as an undesirable process (a *back reaction*), because its occurrence decreases the global synthesis reaction yield of ammonia production.

However, the *second ammonia revolution* requires efficient green ammonia decomposition processes producing hydrogen to feed fuel cells, which subsequently transform the chemical energy of hydrogen molecules into electricity. With this coupled operation in mind, the US Department of Energy has proposed that the working temperature of the decomposition processes should be similar to that of Proton-exchange Membrane (PEM) fuel cells, usually in the range of 150-180 ºC [4,70]. This temperature range contrasts with recent thermocatalytic ammonia decomposition results in the literature, imposing working temperatures between 300 and 500ºC [86]. In this regard, it is remarkable a recent study by Torrente-Murciano and collaborators, working with Ru catalysts supported on carbon nanotubes and reporting results at a much lower temperature of 180 ºC [87]. In any case, within the perspective of coupling fuel cells to hydrogen-producing reactors, plasma sources operated at ambient conditions of pressure and temperature emerge at a promising technological solution for the decomposition of ammonia.

The ammonia molecule can be decomposed in plasmas following different reaction pathways. These include collisional and excitation processes in the gas phase and reactions that take place on the surface of catalysts or moderator materials. For example, in DBD reactors the decomposition of the molecule can be initiated by electron-impact processes. Moreover, the incorporation of catalytic materials in packed-bed reactors can promote the decomposition of the molecule by dehydrogenation processes on the surface of the catalyst [4].

The most remarkable results achieved in the field of plasma-catalysis regarding ammonia decomposition are those published by L. Wang *et al.* during the last decade [4]. These authors studied the ammonia decomposition at temperatures between 300 and 450 ºC in a cylindrical packed-bed reactor filled with different non-noble catalysts (Fe, Co, etc.) [88]. These initial results leave

room for improvement regarding the need to decrease the operating temperature, possibly up to ambient conditions. Additionally, although some authors have studied the ignition of diluted-ammonia flows (for example, Akiyama *et al.* reported a decomposition rate of ammonia of 50%, but in a N_2/NH_3 mixture containing only a 5% of ammonia [89]), a real application of the technology requires working with pure ammonia flows [90].

1.6. Greenhouse Gas Elimination & Revaluation as Mitigation Strategies

The European Union has established a reduction target of 55% of greenhouse gas emissions for 2030 and the goal of zero-emissions has been proposed for 2050 [2]. Confronting these challenges requires not only a reduction of emissions but also the incorporation of greenhouse gas removal procedures. These latter mitigation strategies can avoid the dilution of carbon emissions into the atmosphere and the hydrosphere [91].

Carbon dioxide (CO_2) and methane (CH_4) are the main greenhouse gases affecting the atmosphere. Specifically, the US Environmental Protection Agency published that in 2019, 80% of the total greenhouse emissions in the United States corresponded to CO_2 emissions, followed by 10% of CH_4 [92]. Upon the capture of these gases, they can be used as feedstock to produce valuable chemical compounds. For example, the CO_2 splitting reaction produces carbon monoxide, which is commonly used as a raw material in the chemical industry. In addition, methane is also a good potential feedstock because of its high hydrogen content. Moreover, the reaction of CO_2 with CH_4 can produce interesting oxygenated compounds, such as methanol or formaldehyde, which are of high interest in the chemical industry [93]. In this context, nonthermal plasmas have been proposed as feasible Carbon Capture Utilization (CCU) technologies for the revaluation of these greenhouse gases. Regarding other approaches relying on thermochemical, photochemical, or biochemical processes, nonthermal plasmas are characterized by a high versatility and straightforward scaling-up capabilities [49]. A derived advantage of plasma reactors is that they can be installed and operated close to the emission sources, thus closing the carbon cycle.

This thesis work encompasses the study of two different *CO_2 reactions*: the conversion of CO_2 into CO and O_2 by igniting different CO_2 plasmas and the

revaluation of CO_2 and CH_4 by treating mixtures of these two gases. A Carbon Capture Utilization (CCU) perspective has been applied to carry out these plasma-driven chemical processes, focusing on the production of valuable compounds minimizing energy consumption. A more detailed appraisal of the two considered *CO_2 reactions* by means of nonthermal plasmas is provided in the *introduction* section of **Chapters 8** and **9**.

1.6.1. CO_2 Conversion into CO and O_2 by Nonthermal Plasmas

The direct conversion of CO_2 into CO and O_2 using plasmas has gained increasing attention in close connection with multiple evidence about climate change. The simplicity of the so-called *CO_2 splitting* process (i.e., its direct conversion into CO and O_2) has enabled a deep understanding of this reaction [94]. Secondary reaction pathways, including carbon deposition as well as ozone formation, can take place with different probabilities depending on operating conditions [49].

There is ample literature, mainly published during the second decade of the 2000s, regarding the CO_2 splitting by means of nonthermal plasmas. As a relevant example, an up-to-date overview of the CO_2 conversion using plasmas can be found in the review article of R. Snoeckx and A. Bogaerts [49]. A general characteristic of the studied processes is that they are carried out at atmospheric pressure and ambient temperature, even under a plasma-catalysis working approximation [52]. As well as for other plasma-driven chemical processes, DBD and packed-bed reactors are the most widely used procedures for CO_2 splitting, although microwave (MW) and gliding arc (GA) reactors have been also reported to present a high energy efficiency [49]. MW and GA discharges are usually classified into a group of plasma sources known as *warm plasmas*, which operate at the boundary between thermal and nonthermal plasmas. They are characterized by a high ionization degree, rendering high electron plasma densities [8].

Depending on the electron energy distribution (i.e., the EEDF) in each type of plasma reactor, different CO_2 dissociation mechanisms can be promoted. The EEDF determines the fraction of electron energy transferred to either electronic excitation, ionization, or dissociation channels of the CO_2 molecule [49]. Snoeckx and Bogaerts studied the relative importance of these processes as a function of the

reduced electric field (E/n)[5] [95]. For example, in MW and GA reactors, characterized by E/n values below 200 Td, the main channel of CO_2 decomposition is the vibrational excitation of the molecule. Meanwhile, in DBD reactors E/n values are usually higher than 200 Td and the splitting reaction mainly occurs through electron impact [49,95].

Nevertheless, although MW and GA reactors can be operated at atmospheric pressure, their scalability is less straightforward and more complex than for DBD reactors. Therefore, the CO_2 splitting reaction has been widely studied using DBDs in classic and packed-bed configurations. A broad range of moderator materials have been used (Al_2O_3, ZrO_2, $BaTiO_3$, etc.) and many experimental parameters have been varied, such as the gas flow rate or the inter-electrode distance [49]. Furthermore, the use of ferroelectrics instead of dielectrics in packed-bed reactors [47], as well as the operation in *burst mode* (i.e., applying millisecond pulsed electrical signals) [96] are some of the strategies applied to increase the efficiency of the CO_2 splitting process using this technology.

1.6.2. CO_2 & CH_4 Valorization by Nonthermal Plasmas

The reaction of CO_2 and CH_4 may provide a wide range of products by modifying the CO_2/CH_4 ratio [49,97]. A particular case is the Dry Reforming of Methane (DRM) yielding H_2 and CO as main products. The ample set of possible reaction products account for the difficulties to systematize this process and to clearly define its efficiency [49,50].

The plasma-assisted DRM was widely studied during the first decade of the 2000s [50]. The main objective of the DRM is the formation of syngas, i.e., a mixture of CO and H_2 that can be used both as a fuel or as chemical feedstock for the Fischer-Tropsch process [98]. The reaction between CO_2 and CH_4 may also render unsaturated hydrocarbons like acetylene (C_2H_2), longer carbon chain hydrocarbons, or value-added oxygenated compounds such as methanol, formic acid, or formaldehyde [49,97].

Different plasma technologies have been essayed to carry out this reaction including spark discharges, corona discharges, or DBD reactors [49] . Each type

[5] The reduced electric field is defined as the ratio of the electric field intensity (E) to the concentration of neutral particles in the gas. E/n is given in Townsend units (Td), where 1 Td = 10^{-17} V·cm^2.

of discharge favors a certain selectivity resulting from the occurrence of particular reaction pathways. Syngas formation is the most common reaction pathway, although spark discharges are known to induce carbon deposition, while DBD reactors to produce light hydrocarbons [49]. The incorporation of catalytic materials in packed-bed reactors may promote certain chemical pathways at mild pressure and temperature conditions. An ample spectrum of catalysts has been studied, with nickel-based catalysts as the primarily utilized materials for this purpose [97].

Mixtures of CO_2+CH_4 have also been studied in DBD reactors from a fundamental perspective using different computational methods [36,99,100]. However, the complex chemistry of this type of plasmas complicates the modeling because of computational limits [49]. In this regard, different experimental methodologies can help to unravel the relative importance of chemical pathways involved, as the isotope labeling methodology used in this thesis working with $^{13}CO_2$ instead of $^{12}CO_2$, discussed in detail in **Chapter 9**.

1.7. References

[1] General Assembly United Nations, Resolution adopted by the General Assembly on 25 September 2015, New York, 2015. https://sustainabledevelopment.un.org/post2015/summit (accessed February 6, 2022).

[2] European Commission, Communication from the Commission: The European Green Deal, Brusels, 2019.

[3] G. Chehade, I. Dincer, Progress in green ammonia production as potential carbon-free fuel, Fuel. 299 (2021). https://doi.org/10.1016/j.fuel.2021.120845.

[4] Yi Y., Wang L., Guo H. (2019) Plasma-Catalytic Decomposition of Ammonia for Hydrogen Energy. In: Tu X., Whitehead J., Nozaki T. (eds) Plasma Catalysis. Springer Series on Atomic, Optical, and Plasma Physics, vol 106. Springer, Cham. https://doi.org/10.1007/978-3-030-05189-1_7.

[5] C. Smith, A.K. Hill, L. Torrente-Murciano, Current and future role of Haber-Bosch ammonia in a carbon-free energy landscape, Energy and Environmental Science. 13 (2020) 331–344. https://doi.org/10.1039/c9ee02873k.

[6] W. McDonough and B. Michael (2002), Cradle to Cradle. Remaking the Way We Make Things, North Point Press.

[7] M.L. Carreon, Plasma catalysis: A brief tutorial, Plasma Research Express. 1 (2019). https://doi.org/10.1088/2516-1067/ab5a30.

[8] A. Fridman (2008). Plasma Chemistry. Cambridge: Cambridge University Press. https://doi.org/10.1017/CBO9780511546075.

[9] K.D. Weltmann, J.F. Kolb, M. Holub, D. Uhrlandt, M. Šimek, K. (Ken) Ostrikov, S. Hamaguchi, U. Cvelbar, M. Černák, B. Locke, A. Fridman, P. Favia, K. Becker, The future for plasma science and technology, Plasma Processes and Polymers. 16 (2019). https://doi.org/10.1002/ppap.201800118.

[10] R. Hippler, P. Sigismund, M. Schmidt and K. Schoenbach (2001). Low Temperature Plasma Physics: Fundamental Aspects and Applications. Vol. 1, Wiley-Vch.

[11] J. Meichsner, M. Schmidt, R. Schneider, H.E. Wagner (2012), Nonthermal plasma chemistry and physics, CRC Press. https://doi.org/10.1201/b12956.

[12] Mizuno A., Craven M. (2019) Plasma Catalysis Systems. In: Tu X., Whitehead J., Nozaki T. (eds) Plasma Catalysis. Springer Series on Atomic, Optical, and Plasma Physics, vol 106. Springer, Cham. https://doi.org/10.1007/978-3-030-05189-1_2.

[13] P.J. Bruggeman, F. Iza, R. Brandenburg, Foundations of atmospheric pressure non-equilibrium plasmas, Plasma Sources Science and Technology. 26 (2017). https://doi.org/10.1088/1361-6595/aa97af.

[14] H. Mahdikia, F. Saadati, E. Freund, U.S. Gaipl, K. Majidzadeh-a, B. Shokri, S. Bekeschus, Gas plasma irradiation of breast cancers promotes immunogenicity, tumor reduction, and an abscopal effect in vivo, OncoImmunology, 10 (2020). https://doi.org/10.1080/2162402X.2020.1859731.

[15] E. Freund, L. Miebach, R. Clemen, M. Schmidt, A. Heidecke, T. von Woedtke, K.D. Weltmann, S. Kersting, S. Bekeschus, Large volume spark discharge and plasma jet-technology for generating plasma-oxidized saline targeting colon cancer in vitro and in vivo, Journal of Applied Physics. 129 (2021) 053301. https://doi.org/10.1063/5.0033406.

[16] H. Brust, T.M.C. Nishime, N. Wannicke, T.S.M. Mui, S. Horn, A. Quade, K.D. Weltmann, A medium-scale volume dielectric barrier discharge system for short-term treatment of cereal seeds indicates improved germination performance with long-term effects, Journal of Applied Physics. 129 (2021) 044904. https://doi.org/10.1063/5.0033369.

[17] A. Gómez-Ramírez, C. López-Santos, M. Cantos, J.L. García, R. Molina, J. Cotrino, J.P. Espinós, A.R. González-Elipe, Surface chemistry and germination improvement of Quinoa seeds subjected to plasma activation, Scientific Reports 2017 7:1. 7 (2017) 1–12. https://doi.org/10.1038/s41598-017-06164-5.

[18] M. Schneider, R. Rataj, J.F. Kolb, L. Bláha, Cylindrospermopsin is effectively degraded in water by pulsed corona-like and dielectric barrier discharges, Environmental Pollution. 266 (2020). https://doi.org/10.1016/j.envpol.2020.115423.

[19] R. Banaschik, P. Lukes, H. Jablonowski, M.U. Hammer, K.D. Weltmann, J.F. Kolb, Potential of pulsed corona discharges generated in water for the degradation of persistent pharmaceutical residues, Water Research. 84 (2015) 127–135. https://doi.org/10.1016/j.watres.2015.07.018.

[20] A. von Keudell, V. Schulz-Von Der Gathen, Foundations of low-temperature plasma physics - An introduction, Plasma Sources Science and Technology. 26 (2017). https://doi.org/10.1088/1361-6595/aa8d4c.

[21] R. Brandenburg, A. Bogaerts, W. Bongers, A. Fridman, G. Fridman, B.R. Locke, V. Miller, S. Reuter, M. Schiorlin, T. Verreycken, K. (Ken) Ostrikov, White paper on the future of plasma science in environment, for gas conversion and agriculture, Plasma Processes and Polymers. 16 (2019) 1700238. https://doi.org/10.1002/PPAP.201700238.

[22] A. Bogaerts, X. Tu, J.C. Whitehead, G. Centi, L. Lefferts, O. Guaitella, F. Azzolina-Jury, H.H. Kim, A.B. Murphy, W.F. Schneider, T. Nozaki, J.C. Hicks, A. Rousseau, F. Thevenet, A. Khacef, M. Carreon, The 2020 plasma catalysis roadmap, Journal of Physics D: Applied Physics. 53 (2020). https://doi.org/10.1088/1361-6463/ab9048.

[23] J.R. Roth (1995), Industrial Plasma Engineering. Volume 1: Principles, CRC Press, London.

[24] A.M. Loveless, A.L. Garner, Scaling laws for gas breakdown for nanoscale to microscale gaps at atmospheric pressure, Applied Physics Letters. 108 (2016) 234103. https://doi.org/10.1063/1.4953202.

[25] S. Nijdam, E. van Veldhuizen, P. Bruggeman, U. Ebert, An Introduction to Nonequilibrium Plasmas at Atmospheric Pressure, Plasma Chemistry and Catalysis in Gases and Liquids. (2012) 1–44. https://doi.org/10.1002/9783527649525.ch1.

[26] U. Kogelschatz, Dielectric-Barrier Discharges: Their History, Discharge Physics, and Industrial Applications, Plasma Chemistry and Plasma Processing 2003 23:1. 23 (2003) 1–46. https://doi.org/10.1023/A:1022470901385.

[27] F. Massines, N. Gherardi, N. Naudé, P. Ségur, Recent advances in the understanding of homogeneous dielectric barrier discharges, The European Physical Journal Applied Physics. 47 (2009) 22805. https://doi.org/10.1051/EPJAP/2009064.

[28] A. Belinger, N. Naudé, N. Gherardi, Transition from diffuse to self-organized discharge in a high frequency dielectric barrier discharge, The European Physical Journal Applied Physics. 79 (2017) 10802. https://doi.org/10.1051/EPJAP/2017160487.

[29] R. Brandenburg, Dielectric barrier discharges: progress on plasma sources and on the understanding of regimes and single filaments, Plasma Sources Science and Technology. 26 (2017) 053001. https://doi.org/10.1088/1361-6595/aa6426.

[30] R. Brandenburg, V.A. Maiorov, Y.B. Golubovskii, H.E. Wagner, J. Behnke, J.F. Behnke, Diffuse barrier discharges in nitrogen with small admixtures of oxygen: discharge mechanism and transition to the filamentary regime, Journal of Physics D: Applied Physics. 38 (2005) 2187. https://doi.org/10.1088/0022-3727/38/13/017.

[31] K. v. Kozlov, H.E. Wagner, R. Brandenburg, P. Michel, Spatio-temporally resolved spectroscopic diagnostics of the barrier discharge in air at atmospheric pressure, Journal of Physics D: Applied Physics. 34 (2001) 3164. https://doi.org/10.1088/0022-3727/34/21/309.

[32] R. Snoeckx, S. Heijkers, K. van Wesenbeeck, S. Lenaerts, A. Bogaerts, CO_2 conversion in a dielectric barrier discharge plasma: N_2 in the mix as a helping hand or problematic impurity?, Energy and Environmental Science. 9 (2016) 999–1011. https://doi.org/10.1039/c5ee03304g.

[33] H. Luo, Z. Liang, X. Wang, Z. Guan, L. Wang, Homogeneous dielectric barrier discharge in nitrogen at atmospheric pressure, Journal of Physics D: Applied Physics. 43 (2010) 155201. https://doi.org/10.1088/0022-3727/43/15/155201.

[34] BOLSIG+: Electron Boltzmann equation solver, http://www.bolsig.laplace.univ-tlse.fr/.

[35] G.J.M. Hagelaar, L.C. Pitchford, Solving the Boltzmann equation to obtain electron transport coefficients and rate coefficients for fluid models, Plasma Sources Science and Technology. 14 (2005) 722–733. https://doi.org/10.1088/0963-0252/14/4/011.

[36] C. de Bie, *Fluid Modeling of the Plasma-Assisted Conversion of Greenhouse Gases to Value-Added Chemicals in a Dielectric Barrier Discharge*, Antwerpen: Universiteit Antwerpen, 2016.

[37] S. Ponduri, M.M. Becker, S. Welzel, M.C.M. van de Sanden, D. Loffhagen, R. Engeln, Fluid modelling of CO_2 dissociation in a dielectric barrier discharge, Journal of Applied Physics. 119 (2016) 093301. https://doi.org/10.1063/1.4941530.

[38] J. Hong, S. Pancheshnyi, E. Tam, J.J. Lowke, S. Prawer, A.B. Murphy, Kinetic modelling of NH_3 production in N_2–H_2 non-equilibrium atmospheric-pressure plasma catalysis, Journal of Physics D: Applied Physics. 50 (2017) 154005. https://doi.org/10.1088/1361-6463/AA6229.

[39] L.L. Alves, A. Bogaerts, V. Guerra, M.M. Turner, Foundations of modelling of nonequilibrium low-temperature plasmas, Plasma Sources Science and Technology. 27 (2018) 023002. https://doi.org/10.1088/1361-6595/AAA86D.

[40] W. Siemens, Über die elektrostatische Induction und die Verzögerung des Stroms in Flaschendrähten, Annalen Der Physik. 178 (1857) 66–122. https://doi.org/10.1002/ANDP.18571780905.

[41] P. Navascués, A.R. González-Elipe, J. Cotrino, A. Gómez-Ramirez, Large gap atmospheric pressure barrier discharges using ferroelectric materials, Plasma Sources Science and Technology. 28 (2019). https://doi.org/10.1088/1361-6595/ab28ce.

[42] Ozonia L Ozone Generators and Ozone Systems for Municipal and Industrial Water Treatment | SUEZ, (n.d.). https://www.suezwatertechnologies.com/products/ozonia-l (accessed February 21, 2022).

[43] I. Adamovich, S.D. Baalrud, A. Bogaerts, *et al.*, The 2017 Plasma Roadmap: Low temperature plasma science and technology, Journal of Physics D: Applied Physics. 50 (2017) 323001. https://doi.org/10.1088/1361-6463/AA76F5.

[44] T. Opalińska, A. Szymański, A Barrier Discharge Reactor with Ferroelectric Electrodes I. Influence of thickness and surface area of electrodes, Contributions to Plasma Physics. 36 (1996) 63–73. https://doi.org/10.1002/CTPP.2150360104.

[45] C. Woolston, Ferroelectric materials prompt a rethink of matter, Nature. 595 (2021) S34–S35. https://doi.org/10.1038/D41586-021-01792-4.

[46] Lead zirconate titanate - Wikipedia, (n.d.). https://en.wikipedia.org/wiki/Lead_zirconate_titanate (accessed February 21, 2022).

[47] I. Michielsen, Y. Uytdenhouwen, J. Pype, B. Michielsen, J. Mertens, F. Reniers, V. Meynen, A. Bogaerts, CO_2 dissociation in a packed bed DBD reactor: First steps towards a better understanding of plasma catalysis, Chemical Engineering Journal. 326 (2017) 477–488. https://doi.org/10.1016/j.cej.2017.05.177.

[48] D. Mei, X. Zhu, Y.L. He, J.D. Yan, X. Tu, Plasma-assisted conversion of CO_2 in a dielectric barrier discharge reactor: Understanding the effect of packing materials, Plasma Sources Science and Technology. 24 (2015). https://doi.org/10.1088/0963-0252/24/1/015011.

[49] R. Snoeckx, A. Bogaerts, Plasma technology-a novel solution for CO_2 conversion?, Chemical Society Reviews. 46 (2017) 5805–5863. https://doi.org/10.1039/c6cs00066e.

[50] Whitehead J.C. (2019) Plasma Catalysis: Introduction and History. In: Tu X., Whitehead J., Nozaki T. (eds) Plasma Catalysis. Springer Series on Atomic, Optical, and Plasma Physics, vol 106. Springer, Cham. https://doi.org/10.1007/978-3-030-05189-1_1.

[51] S. Xu, J.C. Whitehead, P.A. Martin, CO_2 conversion in a non-thermal, barium titanate packed bed plasma reactor: The effect of dilution by Ar and N_2, Chemical Engineering Journal. 327 (2017) 764–773. https://doi.org/10.1016/j.cej.2017.06.090.

[52] D. Mei, X. Zhu, C. Wu, B. Ashford, P.T. Williams, X. Tu, Plasma-photocatalytic conversion of CO_2 at low temperatures: Understanding the synergistic effect of plasma-catalysis, Applied Catalysis B: Environmental. 182 (2016) 525–532. https://doi.org/10.1016/j.apcatb.2015.09.052.

[53] A. Gómez-Ramírez, V.J. Rico, J. Cotrino, A.R. González-Elipe, R.M. Lambert, Low temperature production of formaldehyde from carbon dioxide and ethane by plasma-Assisted catalysis in a ferroelectrically moderated dielectric barrier discharge reactor, ACS Catalysis. 4 (2014) 402–408. https://doi.org/10.1021/cs4008528.

[54] W. Wang, H.H. Kim, K. van Laer, A. Bogaerts, Streamer propagation in a packed bed plasma reactor for plasma catalysis applications, Chemical Engineering Journal. 334 (2018) 2467–2479. https://doi.org/10.1016/J.CEJ.2017.11.139.

[55] Y. Engelmann, K. Van'T Veer, Y. Gorbanev, E.C. Neyts, W.F. Schneider, A. Bogaerts, Plasma Catalysis for Ammonia Synthesis: A Microkinetic Modeling Study on the Contributions of Eley-Rideal Reactions, ACS Sustainable Chemistry and Engineering. 9 (2021) 13151–13163. https://doi.org/10.1021/acssuschemeng.1c02713.

[56] R. Schlögl, Heterogeneous Catalysis, Angewandte Chemie International Edition. 54 (2015) 3465–3520. https://doi.org/10.1002/ANIE.201410738.

[57] A.B. Ray, F.O. Anderegg, The Oxidation of Carbon Monoxide by Passage with Oxygen or Air Through the Silent Discharge and over Ozone Decomposing Catalysts, Journal of the American Chemical Society. 43 (2002) 967–978. https://doi.org/10.1021/JA01438A001.

[58] P.E.M. Berthelot, Recherches sur l'ozone et sur l'effuse électrique, Comptes Rendus de l'Académie Des Sciences. 88 (1879) 50–52.

[59] K.H.R. Rouwenhorst, H.-H. Kim, L. Lefferts, Vibrationally Excited Activation of N_2 in Plasma-Enhanced Catalytic Ammonia Synthesis: A Kinetic Analysis, ACS Sustainable Chemistry & Engineering. 7 (2019) 17515–17522. https://doi.org/10.1021/ACSSUSCHEMENG.9B04997.

[60] J. Shah, W. Wang, A. Bogaerts, M.L. Carreon, Ammonia Synthesis by Radio Frequency Plasma Catalysis: Revealing the Underlying Mechanisms, ACS Applied Energy Materials. 1 (2018) 4824–4839. https://doi.org/10.1021/acsaem.8b00898.

[61] K.H.R. Rouwenhorst, H.G.B. Burbach, D.W. Vogel, J. Núñez Paulí, B. Geerdink, L. Lefferts, Plasma-catalytic ammonia synthesis beyond thermal equilibrium on Ru-based catalysts in non-thermal plasma, Catalysis Science and Technology. 11 (2021) 2834–2843. https://doi.org/10.1039/d0cy02189j.

[62] Y. Zeng, X. Zhu, D. Mei, B. Ashford, X. Tu, Plasma-catalytic dry reforming of methane over γ-Al_2O_3 supported metal catalysts, Catalysis Today. 256 (2015) 80–87. https://doi.org/10.1016/J.CATTOD.2015.02.007.

[63] H.H. Kim, Y. Teramoto, A. Ogata, H. Takagi, T. Nanba, Plasma Catalysis for Environmental Treatment and Energy Applications, Plasma Chemistry and Plasma Processing 2015 36:1. 36 (2015) 45–72. https://doi.org/10.1007/S11090-015-9652-7.

[64] Y.R. Zhang, K. van Laer, E.C. Neyts, A. Bogaerts, Can plasma be formed in catalyst pores? A modeling investigation, Applied Catalysis B: Environmental. 185 (2016) 56–67. https://doi.org/10.1016/J.APCATB.2015.12.009.

[65] Q.Z. Zhang, A. Bogaerts, Propagation of a plasma streamer in catalyst pores, Plasma Sources Science and Technology. 27 (2018) 035009. https://doi.org/10.1088/1361-6595/AAB47A.

[66] P. Mehta, P. Barboun, F.A. Herrera, J. Kim, P. Rumbach, D.B. Go, J.C. Hicks, W.F. Schneider, Overcoming ammonia synthesis scaling relations with plasma-enabled catalysis, Nature Catalysis. 1 (2018) 269–275. https://doi.org/10.1038/s41929-018-0045-1.

[67] M.L. Carreon, Plasma catalytic ammonia synthesis: State of the art and future directions, Journal of Physics D: Applied Physics. 52 (2019). https://doi.org/10.1088/1361-6463/ab3b2c.

[68] Nitrogen Statistics and Information, U.S. Geological Survey, (n.d.). https://www.usgs.gov/centers/national-minerals-information-center/nitrogen-statistics-and-information (accessed February 22, 2022).

[69] World Population Prospects 2019, Department of Economic and Social Affairs, Population Dynamics, United Nations, https://population.un.org/wpp/ (accessed February 22, 2022).

[70] T.E. Bell, L. Torrente-Murciano, H_2 Production via Ammonia Decomposition Using Non-Noble Metal Catalysts: A Review, Topics in Catalysis. 59 (2016) 1438–1457. https://doi.org/10.1007/s11244-016-0653-4.

[71] A. Yapicioglu, I. Dincer, A review on clean ammonia as a potential fuel for power generators, Renewable and Sustainable Energy Reviews. 103 (2019) 96–108. https://doi.org/10.1016/j.rser.2018.12.023.

[72] S. Kelly, A. Bogaerts, Nitrogen fixation in an electrode-free microwave plasma, Joule. 5 (2021) 3006–3030. https://doi.org/10.1016/j.joule.2021.09.009.

[73] K.H.R. Rouwenhorst, L. Lefferts, Feasibility Study of Plasma-Catalytic Ammonia Synthesis for Energy Storage Applications, Catalysts. 10 (9) 999 (2020). https://doi.org/10.3390/catal10090999.

[74] S. Ornes, Green ammonia could produce climate-friendly ways to store energy and fertilize farms, Proceedings of the National Academy of Sciences of the United States of America. 118 (2021). https://doi.org/10.1073/pnas.2119584118.

[75] II. On the direct synthesis of ammonia, Proceedings of the Royal Society of London. 21 (1873) 281–282. https://doi.org/10.1098/RSPL.1872.0057.

[76] A. Keith Brewer, J.W. Westhaver, The Synthesis of Ammonia in the Glow Discharge, The Journal of Physical Chemistry. 33 (2002) 883–895. https://doi.org/10.1021/J150300A008.

[77] D. Zhou, R. Zhou, R. Zhou, B. Liu, T. Zhang, Y. Xian, P.J. Cullen, X. Lu, K. (Ken) Ostrikov, Sustainable ammonia production by non-thermal plasmas: Status, mechanisms, and opportunities, Chemical Engineering Journal. 421 (2021). https://doi.org/10.1016/j.cej.2021.129544.

[78] R. Hawtof, S. Ghosh, E. Guarr, C. Xu, R. Mohan Sankaran, J.N. Renner, Catalyst-free, highly selective synthesis of ammonia from nitrogen and water by a plasma electrolytic system, Science Advances. 5 (2019). https://doi.org/10.1126/sciadv.aat5778.

[79] Y. Gorbanev, E. Vervloessem, A. Nikiforov, A. Bogaerts, Nitrogen Fixation with Water Vapor by Nonequilibrium Plasma: toward Sustainable Ammonia Production, ACS Sustainable Chemistry & Engineering. 8 (2020) 2996–3004. https://doi.org/10.1021/acssuschemeng.9b07849.

[80] J. Sun, D. Alam, R. Daiyan, H. Masood, T. Zhang, R. Zhou, P.J. Cullen, E.C. Lovell, A. Jalili, R. Amal, A hybrid plasma electrocatalytic process for sustainable ammonia production, Energy & Environmental Science. 14 (2021) 865–872. https://doi.org/10.1039/D0EE03769A.

[81] P. Peng, Y. Cheng, R. Hatzenbeller, M. Addy, N. Zhou, C. Schiappacasse, D. Chen, Y. Zhang, E. Anderson, Y. Liu, P. Chen, R. Ruan, Ru-based multifunctional mesoporous catalyst for low-pressure and non-thermal plasma synthesis of ammonia, International Journal of Hydrogen Energy. 42 (2017) 19056–19066. https://doi.org/10.1016/J.IJHYDENE.2017.06.118.

[82] A. Gómez-Ramírez, J. Cotrino, R.M. Lambert, A.R. González-Elipe, Efficient synthesis of ammonia from N_2 and H_2 alone in a ferroelectric packed-bed DBD reactor, Plasma Sources Science and Technology. 24 (2015). https://doi.org/10.1088/0963-0252/24/6/065011.

[83] A. Gómez-Ramírez, A.M. Montoro-Damas, J. Cotrino, R.M. Lambert, A.R. González-Elipe, About the enhancement of chemical yield during the atmospheric plasma synthesis of ammonia in a ferroelectric packed bed reactor, Plasma Processes and Polymers. 14 (2017). https://doi.org/10.1002/ppap.201600081.

[84] G. Akay, K. Zhang, Process intensification in ammonia synthesis using novel coassembled supported microporous catalysts promoted by nonthermal plasma, Industrial and Engineering Chemistry Research. 56 (2017) 457–468. https://doi.org/10.1021/acs.iecr.6b02053.

[85] K.H.R. Rouwenhorst, Y. Engelmann, K. van‘t Veer, R.S. Postma, A. Bogaerts, L. Lefferts, Plasma-driven catalysis: green ammonia synthesis with intermittent electricity, Green Chemistry. 22 (2020) 6258–6287. https://doi.org/10.1039/D0GC02058C.

[86] I. Lucentini, X. Garcia, X. Vendrell, J. Llorca, Review of the Decomposition of Ammonia to Generate Hydrogen, Industrial and Engineering Chemistry Research. 60 (2021) 18560–18611. https://doi.org/10.1021/acs.iecr.1c00843.

[87] A.K. Hill, L. Torrente-Murciano, Low temperature H_2 production from ammonia using ruthenium-based catalysts: Synergetic effect of promoter and support, Applied Catalysis B: Environmental. 172–173 (2015) 129–135. https://doi.org/10.1016/J.APCATB.2015.02.011.

[88] L. Wang, Y. Yi, Y. Zhao, R. Zhang, J. Zhang, H. Guo, NH_3 Decomposition for H_2 Generation: Effects of Cheap Metals and Supports on Plasma-Catalyst Synergy, ACS Catalysis. 5 (2015) 4167–4174. https://doi.org/10.1021/acscatal.5b00728.

[89] M. Akiyama, K. Aihara, T. Sawaguchi, M. Matsukata, M. Iwamoto, Ammonia decomposition to clean hydrogen using non-thermal atmospheric-pressure plasma, International Journal of Hydrogen Energy. 43 (2018) 14493–14497. https://doi.org/10.1016/j.ijhydene.2018.06.022.

[90] Z. Wan, Y. Tao, J. Shao, Y. Zhang, H. You, Ammonia as an effective hydrogen carrier and a clean fuel for solid oxide fuel cells, Energy Conversion and Management. 228 (2021). https://doi.org/10.1016/j.enconman.2020.113729.

[91] E. and M. National Academies of Sciences, A Research Strategy for Ocean-based Carbon Dioxide Removal and Sequestration, A Research Strategy for Ocean-Based Carbon Dioxide Removal and Sequestration. (2021). https://doi.org/10.17226/26278.

[92] Overview of Greenhouse Gases, US EPA, (n.d.). https://www.epa.gov/ghgemissions/overview-greenhouse-gases (accessed February 22, 2022).

[93] S. Liu, L.R. Winter, J.G. Chen, Review of Plasma-Assisted Catalysis for Selective Generation of Oxygenates from CO_2 and CH_4, ACS Catalysis. 10 (2020) 2855–2871. https://doi.org/10.1021/acscatal.9b04811.

[94] A. Bogaerts, E.C. Neyts, Plasma Technology: An Emerging Technology for Energy Storage, ACS Energy Letters. 3 (2018) 1013–1027. https://doi.org/10.1021/acsenergylett.8b00184.

[95] A. Bogaerts, T. Kozák, K. van Laer, R. Snoeckx, Plasma-based conversion of CO_2: current status and future challenges, Faraday Discussions. 183 (2015) 217–232. https://doi.org/10.1039/C5FD00053J.

[96] A. Ozkan, A. Bogaerts, F. Reniers, Routes to increase the conversion and the energy efficiency in the splitting of CO_2 by a dielectric barrier discharge, Journal of Physics D: Applied Physics. 50 (2017). https://doi.org/10.1088/1361-6463/aa562c.

[97] W.C. Chung, M.B. Chang, Review of catalysis and plasma performance on dry reforming of CH_4 and possible synergistic effects, Renewable and Sustainable Energy Reviews. 62 (2016) 13–31. https://doi.org/10.1016/j.rser.2016.04.007.

[98] M.E. Dry, The Fischer–Tropsch process: 1950–2000, Catalysis Today. 71 (2002) 227–241. https://doi.org/10.1016/S0920-5861(01)00453-9.

[99] C. de Bie, J. van Dijk, A. Bogaerts, The Dominant Pathways for the Conversion of Methane into Oxygenates and Syngas in an Atmospheric Pressure Dielectric Barrier Discharge, Journal of Physical Chemistry C. 119 (2015) 22331–22350. https://doi.org/10.1021/acs.jpcc.5b06515.

[100] A. Bogaerts, C. de Bie, R. Snoeckx, T. Kozák, Plasma based CO_2 and CH_4 conversion: A modeling perspective, Plasma Processes and Polymers. 14 (2017). https://doi.org/10.1002/ppap.201600070.

Chapter 2

Objectives and Thesis Structure

1.1. Objectives of the Thesis

The general objective of this thesis is to increase the reaction yield and the energy efficiency of several plasma-driven chemical processes in packed-bed plasma reactors, as well as to gain knowledge about the reaction mechanisms involved in these processes. The chemical processes studied are the ammonia synthesis & decomposition reactions (designated with the general term *ammonia reactions*) and the carbon dioxide elimination & valorization (designated with the general term *CO_2 reactions*). The achievement of this general goal will require to comply with the following specific objectives (SO):

SO.1. Characterize the electrical behavior of the packed-bed plasma reactor using dielectric and ferroelectric materials as barriers under equivalent operating conditions and at different temperatures. Correlate this analysis with the reactor performance for the ammonia synthesis reaction.

SO.2. Determine the reaction mechanisms in plasma-assisted *ammonia reactions* and identify inefficient processes through the application of an isotope labeling methodology. Unravel the effect of plasma bulk and surface processes on the reaction yield and energy efficiency of the reactions.

SO3. Incorporate a ruthenium-based catalyst on the surface of the ferroelectric pellets that form the packed-bed barrier. Electrically characterize the barrier containing the catalyst and study the *ammonia reactions*. Correlate the yield and efficiency with the presence/absence of the catalyst at different temperatures.

SO.4. Optimize the *ammonia to hydrogen* process (i.e., ammonia decomposition reaction) in the packed-bed reactor using a ferroelectric as moderator and a Ru-based catalyst. Analysis of the reaction mechanisms.

SO.5. Determine the reaction rate and energy efficiency of the CO_2 splitting process using ferroelectrics as discharge moderators, as well as for gas mixtures containing small amounts of dry air and oxygen, similar to those existing in real facilities. Identification of the involved reaction mechanisms in each case.

SO.6. Study of the valorization of CO_2 and CH_4 mixtures using PZT as moderator in the packed-bed reactor. Analyze the reaction mechanisms applying the isotope labeling methodology.

1.2. Thesis Structure

Figure 2.1 shows the structure of the thesis work. The discussion of the obtained results responding to the aforementioned objectives proceeds through different Chapters. **Chapter 4** is related to **SO.1** (i.e., the electrical characterization of packed-bed reactors), **Chapters 5-7** to **SO.2** and **SO.3 (**study of *ammonia reactions*), and **Chapters 8-9** to **SO.4** and **SO.5 (**study of *CO_2 reaction*s). Finally, the General Conclusions are provided in **Chapter 10**, followed by a summary of the scientific production of the Ph.D. candidate.

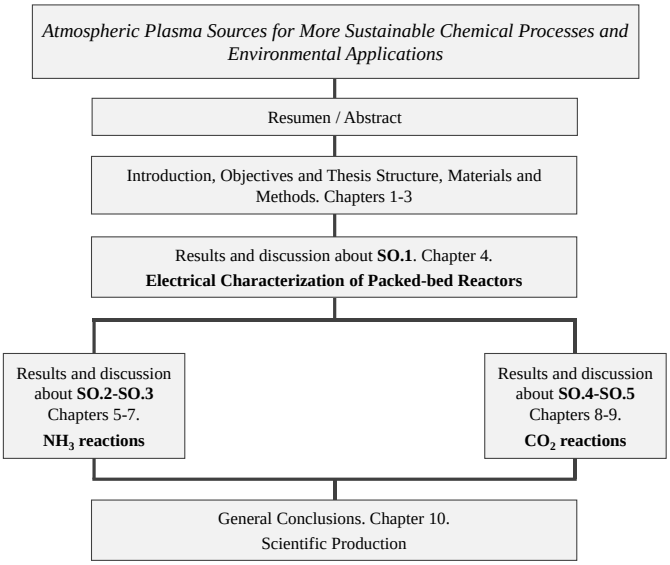

Figure 2.1. Structure of the thesis, divided into the following parts: Abstract (Spanish and English language), **Chapters 1-3**: Introduction, Objectives and Thesis Structure, Materials and Methods, **Chapter 4**: Electrical Characterization of Packed-bed Reactors, **Chapters 5-7**: Study of *ammonia reactions*, **Chapters 8** and **9**: Study of *CO_2 reactions*, **Chapter 10**: General Conclusions, and Scientific Production.

Chapter 3

Materials and Methods

The experiments of this thesis were performed at the laboratories of the *Nanotechnology on Surfaces and Plasma Research Group*, at the Materials Science Institute of Seville. Regarding the experimental setup, the core features are the packed-bed plasma reactor, its connections for gas inlet and outlet supplies, and the power supply to ignite the plasma.

Plasma diagnosis techniques were applied in-situ, i.e., while performing the experiments. They include electrical characterization, Optical Emission Spectroscopy (OES), and Quadrupole Mass Spectrometry (QMS). Occasionally, mass spectrometry analysis was complemented by results obtained with Fourier-Transform Infrared (FTIR) Spectroscopy. In addition, as mentioned in the previous chapter, an isotope labeling method has been applied to analyze reaction mechanisms. This methodology is explained in detail below.

Different material characterization techniques were also used to analyze the surface of the pellets of the packed-bed reactor. These techniques were X-Ray Photoelectron Spectroscopy (XPS), Secondary Electron Microscopy (SEM), Energy Dispersive X-Ray Spectroscopy (EDX), Transmission Electron Microscopy (TEM), and N_2 desorption isotherms (BET method). All of them are briefly discussed in the upcoming pages.

3.1. Packed-bed Plasma Reactor

The packed-bed plasma reactor consisted of a stainless-steel cylindrical vessel, which features four windows. The chamber volume was 310 cm^3 and its inner diameter 10.3 cm. An aluminum electrode of 7.5 cm in diameter is grounded at the bottom of the chamber. It is embedded in an insulating polymer (PEEK) to prevent sparks to the reactor chamber, which is also grounded for safer handling. An analogous upper electrode is connected to the high voltage power supply

attached to the lid in a parallel-plate arrangement. **Figure 3.1** shows photographs of the reactor and its components.

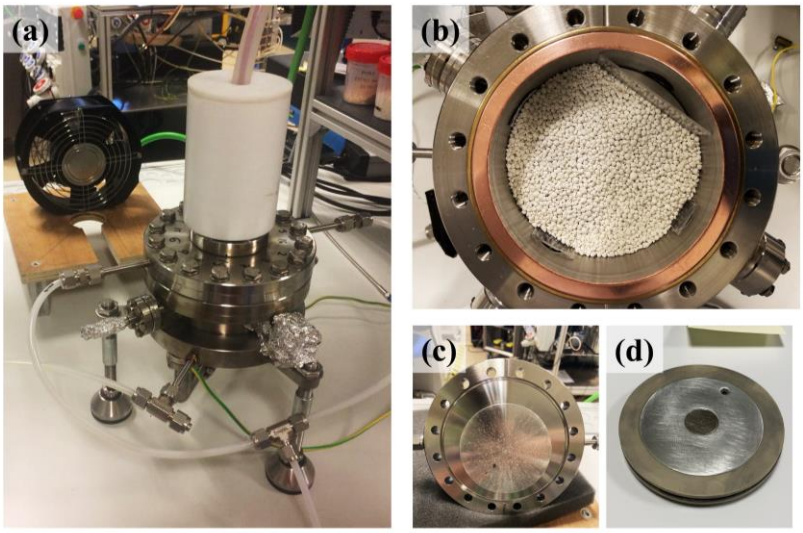

Figure 3.1. (a) Packed-bed plasma reactor. (b) Top view of the opened reactor showing the pellet barrier. (c) Upper electrode connected to the reactor top part. (d) Bottom electrode embedded in PEEK.

The reactor was filled with pellets separating the two electrodes. To vary the inter-electrode distance the controlled parameter was the volume of pellets introduced into the reactor, assuming a homogeneous packing distribution. In this thesis, the inter-electrode distance has been adjusted between 3 and 10 mm. The dielectric and ferroelectric materials utilized to fill the inter-electrode gap are shown in **Figure 3.2**, and their main properties (dielectric constant, geometry, etc.) are indicated in **Table 3.1**

The following materials were used in their final geometry and supplied as: glass spheres (Assistant, Germany); alumina spheres (RGPBALL S.r.l., Italy); $BaTiO_3$ pellets (Catal International Ltd., UK); and $LiNbO_3$ disks (Roditi International Corporation Ltd., UK).

Nevertheless, the principal material used, Lead Zirconate Titanate (PZT), was supplied as powder by APC International Ltd. (US). The PZT pellets were sintered in the laboratories of the Ceramic and Glass Institute (CSIC) following a procedure described in detail in the Thesis Dissertation of Antonio Méndez [1]. PZT pellets in two granulometries have been used, with diameters ranging between 0.5-2 mm and 2-3 mm.

Table 3.1. Main properties of the materials used as discharge moderators in the packed-bed plasma reactor.

Material	ε_r (room temperature)*	Geometry	BET surface (m^2/gr)**	T_C (ºC)*	Size
Glass	3.8	Spheres	(smooth)	-	3 mm
Al_2O_3	$T_{11}=T_{22}=9.34$; $T_{33}=11.54$	Spheres	(smooth)	-	3 mm
$BaTiO_3$	1250	Pellets	0.71	120	2-3 mm
PZT	1900	Pellets	0.74	332	0.5-2 mm; 2-3 mm
$LiNbO_3$	$T_{11}=T_{22}=85.2$; $T_{33}=28.7$	Disk	(smooth)	1210	10 cm (thickness: 0.5 mm)

Note that the Curie Temperature is given only for ferroelectrics. * Information provided by the supplier; ** Measured in our laboratories.

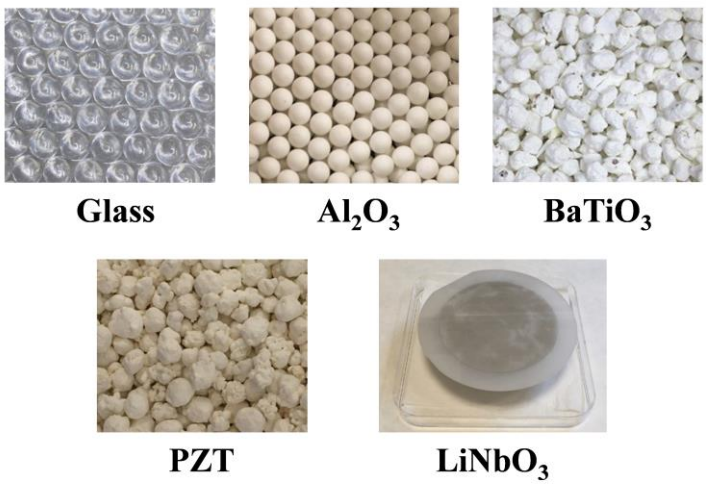

Figure 3.2. Photographs of the different materials utilized as moderators.

In some experiments (**Chapters 4 and 6**), impedance measurements were performed to analyze the electric response of the reactor to the dielectric properties of the materials in **Table 3.1**. These measurements were carried out with the reactor filled with the packed barrier but without operating the plasma. For this purpose, an AUTOLAB 302N potentiostat/galvanostat combined with a FRA32M module was used. The device was operated in a frequency range from 1 MHz to

100 Hz and applying sinusoidal AC signals. In this way, the so-called *Nyquist* plots [2] were obtained. They consist of plots of the imaginary part of the impedance (Z'') versus the real part (Z'), with the standard criterion that moving from high to low frequencies in the diagram means moving from left to right in the X-axis. The shape of this curve (curvature) provides information about the electrical properties (impedance) of solids. The impedance measurements were repeated three times to confirm the reproducibility of the results.

3.2. Experimental Setup: Reactor Operation & Diagnosis in Situ

Reactant gas mixtures were dosed into the reactor through an access port located in the center of the bottom electrode, while the products and the unreacted gas mixture left the reactor chamber through two exhaust tubes connected to its upper part. **Figure 3.3** below illustrates a scheme of the packed-bed reactor highlighting the way how the gases diffuse through the packed bed.

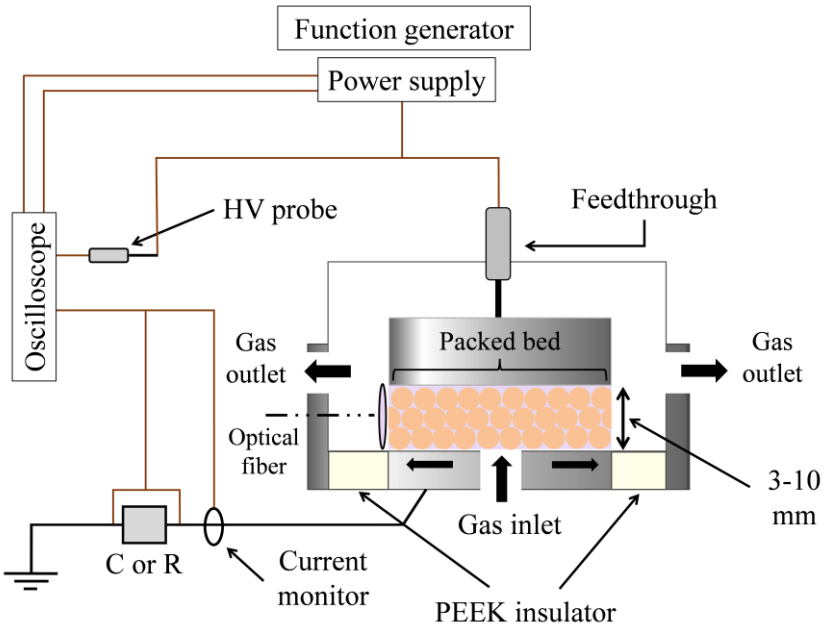

Figure 3.3. Scheme of the parallel plate packed-bed reactor and the electrical excitation/diagnosis system.

The inter-electrode distance, the size of the pellets, and the gas flow rate are used as parameters to control the residence time of the gases in the plasma. Gas flow rates are controlled with mass flow controllers (Bronkhorst, Nederland) or with a rotameter (Aalborg, USA) when using NH_3. Different pure gases and mixtures were used. In all the cases, the total flow rate was varied from 3 to 25 sccm. For the *ammonia reactions* we used N_2, H_2, and NH_3 as inlet gases, as well as D_2 instead of H_2 for isotope labeling studies. For the case of *CO_2 reactions*, we used CO_2, CH_4, N_2, O_2 and dry air, as well as $^{13}CO_2$ as an isotope-labeled molecule. All gases were supplied by Air Liquide (Alphagaz, Spain), except for $^{13}CO_2$, which was supplied by Eurisotop (Cambridge Isotope Laboratories, Inc., UK).

Most experiments were performed at atmospheric pressure and room temperature, except for some electrical characterization experiments in **Chapter 4** and the ammonia synthesis experiments in the presence of a metal catalyst (**Chapter 6**), which required heating the reactor walls using a glass fiber heating tape. The temperature was measured at the reactor walls with a thermocouple (K-type, RS Components). This stabilized temperature measured by the thermocouple is designated as *nominal temperature*. While performing the experiments at room temperature, a small thermal drift in temperature up to 40 °C at the reactor walls can occur after long operating periods. To prevent this phenomenon in *CO_2 reactions*, a fan was used to cool down the metal walls of the reactor.

To ignite the plasma, a high voltage signal was applied between the electrodes (see **Figure 3.3** above). The upper electrode was connected to a high voltage amplifier (Trek Inc. Model PD05034) coupled to an AC sinusoidal function generator (Stanford Research Systems, Model DS345). In this thesis, frequencies between 1 and 10 kHz and voltage amplitudes between 0.25 and 7 kV have been applied. The operating conditions of each study are indicated in the respective Chapters. **Figure 3.4** depicts a scheme of the experimental setup indicating the links between the reactor and analytical techniques utilized. All measurements were repeated at least twice to increase the confidence in the results.

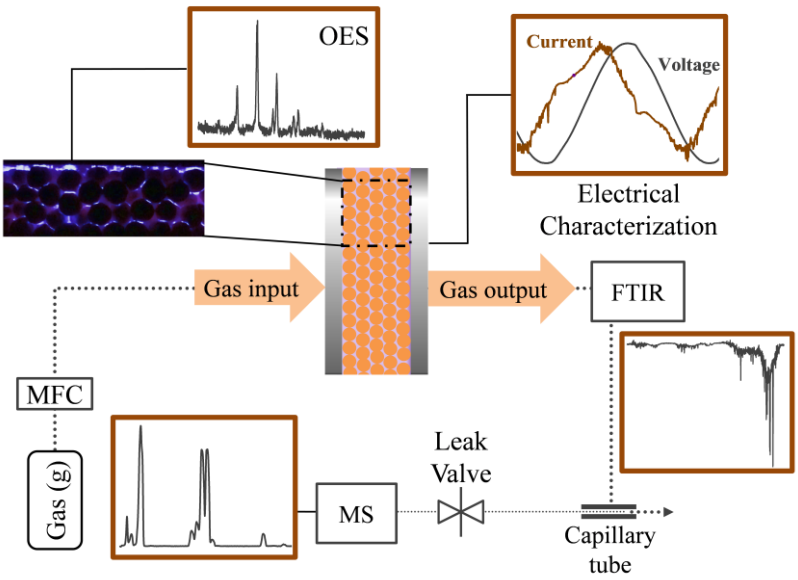

Figure 3.4. Scheme of the experimental setup indicating the links between the reactor and analytical techniques utilized to follow up the plasma-driven chemical processes. MFC refers to mass flow controllers.

3.2.1. Electrical Characterization

The applied voltage was measured using a high voltage probe connected to the active electrode, while the current was determined with a current transformer (Pearson, Current Monitor Model 6585) and/or a resistance (100 and 223 Ω) connected to the ground. To directly quantify the charge transferred through the circuit, a grounded capacitor (2.5 μF) was used in some experiments. All electrical signals were recorded with an oscilloscope (Agilent Tech., Model DSO-X 3024A).

Figure 3.5(a) depicts typical current (*I(t)*) and voltage (*V(t)*) curves measured under plasma ignition conditions. The current intensity shows a filamentary behaviour, characterized by microdischarges. Additionally **Figure 3.5(b)** displays the plot of the transferred charge, *Q(t)*, versus the applied voltage. This plot, referred to as Lissajous figure, illustrates the typical *Q-V* dependence obtained when operating with sinusoidal signals.

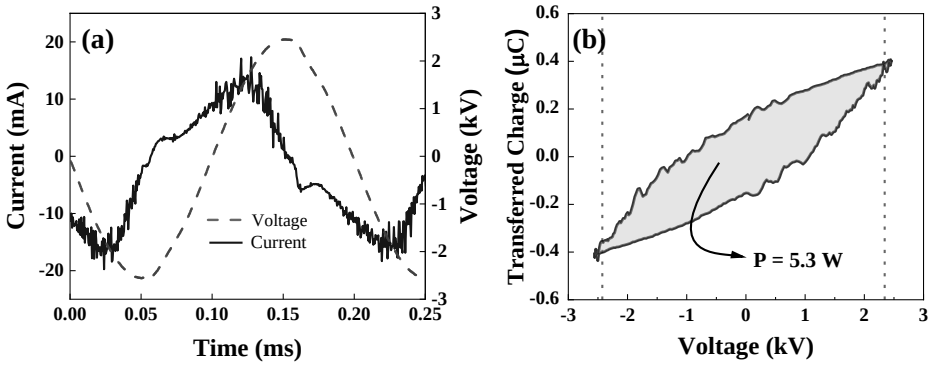

Figure 3.5. Electrical measurements for the following operation conditions: voltage amplitude of 2 kV, frequency of 5 kHz, 6 sccm N_2, and a 5 mm barrier of PZT (pellets of 0.5-2 mm). (a) Voltage and current curves. (b) Lissajous figure for the conditions in (a) with the consumed power indicated.

The power consumed by the reactor was determined from the area of the Lissajous curves, as it is illustrated by the following equation:

$$P = \frac{1}{T} \cdot \int_0^T V \cdot I \cdot dt = \mathrm{f\,[Hz]} \cdot \mathrm{Area}_{Q-V} \qquad (E\ 3.1)$$

The transferred charge was calculated by integrating the current measured through the resistance when the capacitor was not used. To calculate the average power consumed by the reactor, the area of the *Q*-*V* plot is multiplied by the frequency. For all experiments, the electrical measurements were done at least twice – at the beginning and the end of each experiment – to account for an increase in the current because of the heating of the reactor. The average power is used to calculate the energy efficiency of the plasma-driven chemical processes, as explained below.

3.2.2. Optical Emission Spectroscopy (OES)

Nonthermal plasmas can emit electromagnetic radiation over a wavelength range going from ultraviolet to infrared, which can be used for their characterization. Elementary reactions in plasmas lead to a large number of atoms, molecules, ions, and radicals in many different excited states. These excited species emit photons in their de-excitation processes. Taking into account that self-absorption inside the plasma can be considered negligible, the detection of emitted

photons should provide reliable information about the plasma [3]. This technique is known as Optical Emission Spectroscopy (OES).

In this work, the emission spectra were collected with a collimator that was placed at one of the lateral windows of the reactor and connected through an optical fiber to a spectrometer (Horiba Ltd, Jobin-Yvon FHR640). The measurements were taken using two diffraction gratings: one with a density of 1201 lines/cm and centered at 330 nm and another with a density of 900 lines/cm and centered at 600 nm. The integration time was selected between 0.5 or 1 s and the resolution between 0.2 and 1 nm. Since the light emission intensity in packed-bed reactors was low (note that only the light coming from the free space between the pellets contributes to the spectrum), OES is used as a semi-quantitative analysis of the excited species in the plasma. With this assertion, it is meant that, although the main excited species in the plasma could be identified with OES, the low peak to background ratio of some spectral peaks would make the corresponding species hardly quantifiable for the analysis.

Figure 3.6 shows an example of an OES spectrum acquired for a N_2 plasma at atmospheric pressure (voltage amplitude of 2 kV, frequency of 5 kHz and power of 5.3 W). Bands of the second positive system of nitrogen are clearly observed in the spectra. They correspond to the molecular transition $[C^3\Pi \rightarrow B^3\Pi]$, with the main bands appearing at 337.0 and 357.9 nm.

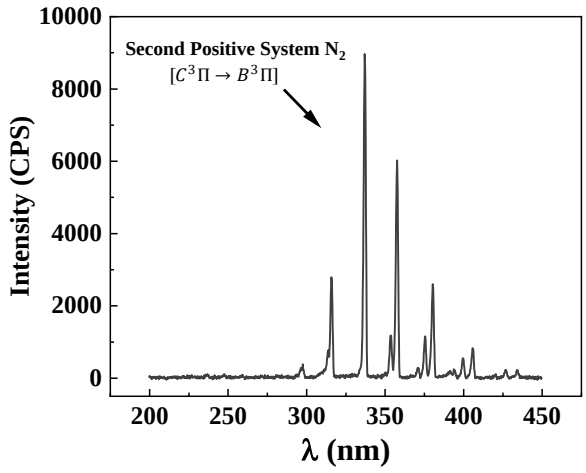

Figure 3.6. OES spectrum acquired for a pure nitrogen plasma (6 sccm N_2) under the same conditions than in **Figure 3.5** (voltage amplitude of 2 kV, frequency of 5 kHz, consumed power of 5.3 W; PZT barrier).

3.2.3. Mass Spectrometry (MS)

The main characterization technique used in this thesis is Mass Spectrometry (MS), utilized to determine the composition of the reactor gas outlet. A quadrupole mass spectrometer (QMS; Pfeiffer Vacuum, QMG 220 Prisma Plus) has been used for this purpose[*].

Mass Spectrometry and nonthermal plasmas are linked since the beginnings of this characterization technique: the first mass spectrometer was built by Thomson in 1913 – the *parabola spectrograph* – using a DC discharge as ion source [3]. A mass spectrometer consists of three components: the ionization chamber, the mass analyzer, and the detector. In this thesis, the mass analyzer is a quadrupole, and the detector is a Faraday collector.

In the ionization chamber, atoms and molecules become ionized by interaction with electrons. These electrons are emitted by a heated filament and accelerated by an electric field and have energies usually comprised between 5 and 100 eV [3]. The produced ion beam enters the quadrupole (analyzer), which is composed of four metal cylinders supplied with a high-frequency RF signal defining the quadrupole structure. The time-varying magnetic field generated during the activation of the quadrupole acts as an ion filter. In this way, only the species with a certain mass-charge ratio (m/z) may reach the detector. In this thesis, a Faraday cup collector (i.e., the detector) is used for the detection of ions at pressures around $1.0 \cdot 10^{-5}$ mbar. The *Quadera* software was used to control the equipment.

When molecules are introduced into the ionization chamber, characteristic fragmentation patterns are obtained. These patterns stem from both the ionization and dissociation of the analyzed species, induced by the electron impact during the ionization stage. **Figure 3.7** shows the fragmentation pattern of NH_3 and CO_2 molecules as detected in the mass spectrometer used in this thesis. Regarding the ammonia spectrum, NH_3^+ (m/z=17) and NH_2^+ (m/z=16) species give rise to the main signals, but contributions of N_2^+ (m/z=28) and H_2^+ (m/z=2) are also detected. On the other hand, for the carbon dioxide pattern the CO_2^+ (m/z=44) is the main signal, but also contributions of CO^+ (m/z=28), O^+ (m/z=16), and C^+ (m/z=12) are obtained.

[*] In this thesis, MS and QMS are indistinctly used to refer to the Quadrupole Mass Spectrometry utilized to analyze the gas composition of the reactor outlet.

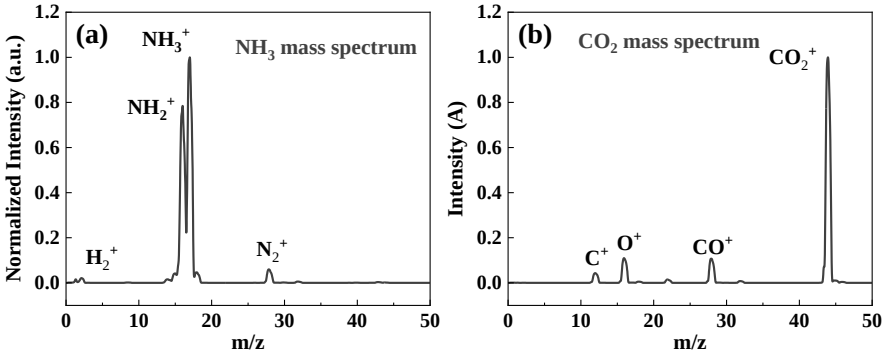

Figure 3.7. Fragmentation patterns obtained in the mass spectrometer for the ammonia molecule (a) and the carbon dioxide molecule (b) with the attribution of the different m/z peaks to the corresponding ionized species.

The NIST dataset provides an extensive collection of molecular patterns for mass spectrometry [4]. Nevertheless, in this thesis, the patterns of the main reactants and products have been obtained by analyzing a known stream of the gases of interest. A similar procedure has been applied to determine the sensitivity factor of the main species, in this case analysing the QMS spectra of gas mixtures containing the corresponding gas and different proportions of N_2. This factor relates the intensity of the signal provided by the detector to the amount of the detected species. For a given species, the sensitivity factor is considered constant under fixed operating conditions.

3.2.4. Fourier-Transform Infrared Spectroscopy (FTIR)

Fourier-Transform Infrared (FTIR) Spectroscopy provides information about the composition of the gas outlet. This technique detects the vibrations of the bonds of a given molecule. In a simplified way, it can be assumed that the characteristic vibration energy of a given bond depends on the mass of the bonded atoms. A simple way of using this technique for the identification of species consists of a fingerprint mode, i.e., associating the energy of a given spectral band to the presence of a given molecule. In this thesis, absorption FTIR spectroscopy is used to complement isotope-labeling studies carried out for the analysis of ammonia reactions. A more detailed explanation about this topic will be presented in the next section. For this purpose, an Agilent Cary 630 FTIR Spectrometer is placed in series with the outlet flow of the gases, before the mass spectrometer, as

indicated in **Figure 3.4**. The IR spectra were recorded in the region between 4000 and 500 cm^{-1} with a resolution of 1 cm^{-1}. **Figure 3.8** provides a characteristic spectrum for the ammonia molecule, with its three groups of main vibrational/rotational band systems in the regions 3600-3100, 1800-1300 and 1250-700 cm^{-1}.

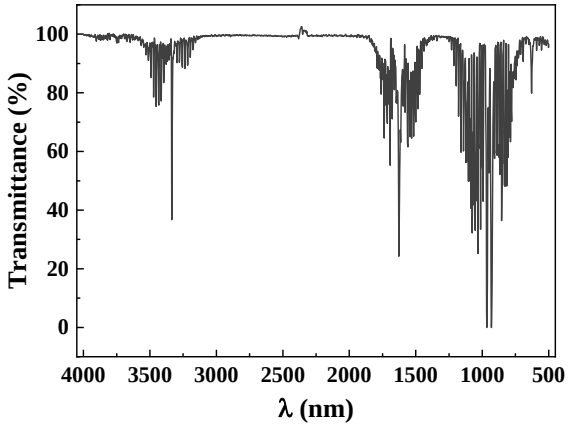

Figure 3.8. FTIR spectrum of the ammonia molecule.

3.3. Isotope Labeling Method

Isotope labeling is a technique conventionally used in thermal catalysis. This experimental method relies on the use of molecules marked with less common isotopes as reactants by the studied chemical reactions. Following the partition of these isotopes among the product molecules may provide interesting information regarding reaction mechanisms. There are different strategies to track isotope marked molecules, for example, by analyzing their mass or their vibrational mode characteristics. In concrete, the evolution of isotope labeled molecules can be followed by mass spectrometry and FTIR spectroscopy.

In this thesis, isotope labeling has been used to analyze chemical reactions in a packed-bed reactor from a plasma-catalysis perspective. This means that reactions are the result of both plasma (gas) phase and surface-mediated processes. Two different isotope labeled molecules have been used. They are D_2 for *ammonia reactions* and $^{13}CO_2$ for *CO_2 reactions*. Specific applications and objectives of the

use of each isotope are explained in the respective Chapters: **Chapter 5** for *ammonia reactions* and **Chapter 9** for *CO_2 reactions*.

Figure 3.9 shows an example of the use of the isotope labeling technique to analyze reaction mechanisms in *ammonia reactions*. The plots consist of mass spectra taken before and after the plasma ignition of a NH_3 + D_2 mixture. It can be observed that before igniting the plasma the main peaks are due to D_2 (m/z=4) and NH_3 (m/z=17 and 16). Nevertheless, when the plasma is ignited, several atom exchange processes can be identified: hydrogen atoms from NH_3 and deuterium atoms from D_2. Therefore, labeled molecules such as HD (m/z=3), NH_2D (m/z=18) and NHD_2 (m/z=19) can be recognized in the spectrum.

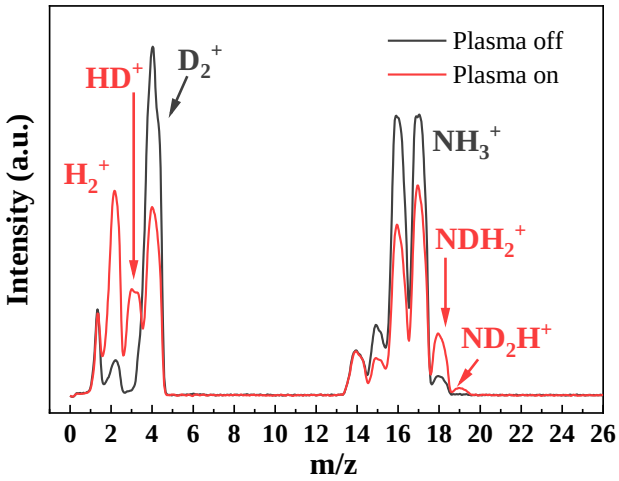

Figure 3.9. QMS spectra of a NH_3+D_2 mixture before (dark gray line) and after (red line) plasma ignition. The assignment of peaks to the different labeled (or not) molecules present in the mixture is included. Spectra were acquired for a total flow rate of 9 sccm with a 2:3 NH_3:D_2 ratio.

Regarding *CO_2 reactions*, $^{13}CO_2$ has been used as reactant for isotope-labeling experiments that are explained in detail in **Chapter 9**. **Figure 3.10** provides a comparison between similar flow rates of $^{12}CO_2$ and $^{13}CO_2$. On the one hand, $^{12}CO_2^+$ (m/z=44), ^{12}CO (m/z=28), and $^{12}C^+$ (m/z=12) ions are detected for the $^{12}CO_2$ flow rate. On the other hand, $^{13}CO_2^+$ (m/z=45), ^{13}CO (m/z=29) and $^{13}C^+$ (m/z=13) ions are detected for the $^{13}CO_2$ flow rate. The O^+ specie (m/z=16) is common for both spectra.

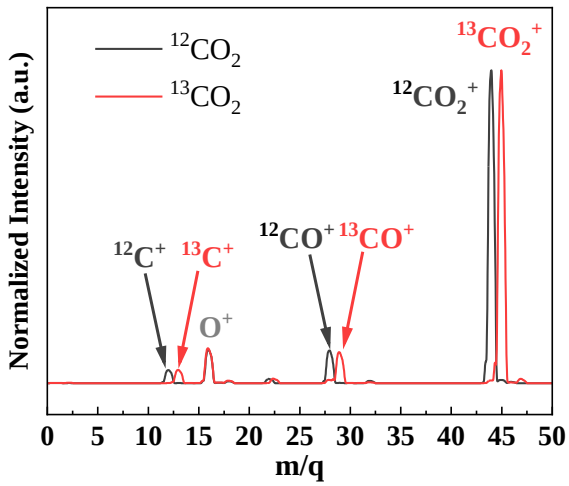

Figure 3.10. QMS normalized spectra for 15 sccm of $^{12}CO_2$ (dark gray line) and $^{13}CO_2$ (red line). The attribution of the different m/z peaks to the ionized species is included.

Two parallel assumptions are made for *ammonia* and *CO_2 reactions* when applying the isotope labeling. These approximations allow us to determine the contribution of each labeled molecule to each particular mass/charge (m/z) peak, and hence, to obtain the relative distribution of labeled molecules in the total flow:

1. The sensitivity factor (see **section 3.2.3**) for similar molecules – isotope-labeled or not – is the same. It means that for *ammonia reactions* the MS sensitivity of NH_3, NH_2D, NHD_2, and ND_3 molecules is equivalent. Moreover, the sensitivity of $^{13}CO_2$ is assumed to be the same than for $^{12}CO_2$. A similar assumption is made for hydrogen (H_2, HD, or D_2) or $^{12}CO/^{13}CO$ (mass 28 and 29).
2. The fragmentation pattern of each molecule in the mass spectrometer is proportionally the same. For example, ammonia and *hydrogen* molecules containing deuterium atoms fragment equally than NH_3 and H_2 do, but they give rise to different m/z peaks. Therefore, the pattern of CO_2 (molecular mass 44) is approximately similar to the pattern of $^{13}CO_2$ (molecular mass 45) (this was experimentally proved in the mass spectrometer).

The isotope labeling methodology has been scarcely utilized in plasma-catalysis before. To our knowledge, only a few studies were reported during the last decades. For example, in 2007 Mizushima *et al.* reported the use of ^{15}N in the

ammonia synthesis reaction to verify the dissociative adsorption of nitrogen on a catalyst surface [5]. The same procedure was applied by L. Wang *et al.* in 2013 to analyze the ammonia decomposition process [6]. In addition, in 2011 H-H Kim *et al.* reported the use of ^{18}O to analyze the role of oxygen in the oxidation of VOCs utilizing different catalysts in a packed-bed reactor.

3.3.1. Study of Inefficient Reaction Events by Isotope Labeling

The concept of inefficient Reaction Events (REs) designates the occurrence of intermediate processes that are ineffective in producing a valuable "product" molecule. Typical examples are the exchange reactions between hydrogen atoms of ammonia molecules and hydrogen atoms of hydrogen molecules in the ammonia synthesis process. **Figure 3.11** shows a scheme to illustrate an inefficient RE between NH_3 and D_2 molecules:

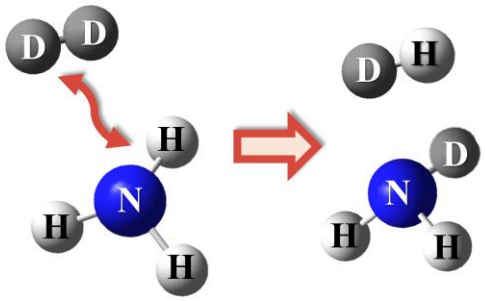

Figure 3.11. Scheme of an exchange reaction between deuterium atoms (of a D_2 molecule) and hydrogen atoms (of a NH_3 molecule). This figure illustrates the potential of isotope labeling to track inefficient plasma processes.

As shown in **Figure 3.11**, this exchange reaction is an example of such an inefficient reaction event, which would be easily monitored by the isotopic exchange technique ($NH_3 + D_2 \rightarrow NDH_2 + HD$). Accordingly, these isotope exchanges can give rise to ammonia-deuterated molecules with one (NDH_2), two (ND_2H), or even three (ND_3) atoms of deuterium.

The minimum number of inefficient REs associated with the formation of a given labeled molecule, such as NDH_2, is defined as:

$$\mathrm{RE}_{\mathrm{NDH_2}} = (\%\mathrm{NDH_2} \cdot 1) \cdot \frac{\mathrm{M}_{\mathrm{NH_3}}(\mathrm{out})\ [\mathrm{sccm}]}{\mathrm{Total\ flow\ (out)[sccm]}} \qquad (E\ 3.2)$$

where $\%NDH_2$ refers to the molecule percentage in the outlet mixture determined by mass spectrometry and M_{NH3} (out) to the flow of NH_3 in the outlet mixture. The multiplying factor 1 takes into account that this molecule requires at least one intermediate reaction event to be formed in a mixture of NH_3 and D_2. This is illustrated in **Figure 3.11** above: one H atom in the ammonia molecule is removed and substituted by a D atom from D_2. Likewise, similar definitions can be made for ND_2H and ND_3:

$$\mathrm{RE}_{\mathrm{ND_2H}} = (\%\mathrm{ND_2H} \cdot 2) \cdot \frac{\mathrm{M}_{\mathrm{NH_3}}(\mathrm{out})\ [\mathrm{sccm}]}{\text{Total flow (out) [sccm]}} \qquad (E\ 3.3)$$

$$\mathrm{RE}_{\mathrm{ND_3}} = (\%\mathrm{ND_3} \cdot 3) \cdot \frac{\mathrm{M}_{\mathrm{NH_3}}(\mathrm{out})\ [\mathrm{sccm}]}{\text{Total flow (out) [sccm]}} \qquad (E\ 3.4)$$

where the multiplying factors 2 and 3 in expressions *E 3.3* and *E 3.4*, respectively, refer that a ND_2H molecule involves at least two intermediate REs for its formation, while ND_3 requires at least three.

Although isotope labeling provides evidence regarding these inefficient processes in plasma reactors, there can be many inefficient reactions that cannot be tracked. For example, the hydrogen atoms exchange between two different NH_3 molecules. Therefore, the minimum number of inefficient Reaction Events in the production of a given total amount of ammonia molecules is defined as:

$$\mathrm{RE}_{\mathrm{Amm.}} = (\%\mathrm{NDH_2} \cdot 1 + \%\mathrm{ND_2H} \cdot 2 + \%\mathrm{ND_3} \cdot 3) \cdot \frac{\mathrm{M}_{\mathrm{NH_3}}(\mathrm{out})\ [\mathrm{sccm}]}{\text{Total flow (out) [sccm]}} \qquad (E\ 3.5)$$

A similar definition can be made for the various forms of labeled hydrogen (i.e., H_2 and HD), when using D_2 as a reactant in the mixture, HD requiring at least one exchange and H_2 two exchanges:

$$\mathrm{RE}_{\mathrm{Hydrogen}} = (\%\mathrm{HD} \cdot 1 + \%\mathrm{H_2} \cdot 2) \cdot \frac{\mathrm{M}_{\mathrm{D_2}}(\mathrm{out})\ [\mathrm{sccm}]}{\text{Total flow (out) [sccm]}} \qquad (E\ 3.6)$$

where M_{D2} (out) refers to the flow of D_2 in the outlet mixture. Therefore, the minimum total number of inefficient Reaction Events (TRE) is defined including events affecting both hydrogen and ammonia:

$$\mathrm{TRE} = \mathrm{RE}_{\mathrm{Ammonia}} + \mathrm{RE}_{\mathrm{Hydrogen}} \qquad (E\ 3.7)$$

3.4. Magnitude Definitions for Reaction Yield and Energy Efficiency

The main magnitudes used in the discussion are defined in this section. The Specific Input Energy (SIE) is defined for all studied plasma-driven chemical processes, while the other expressions are specifically related to each reaction under study.

The SIE, also known as SEI (Specific Energy Input) or SED (Specific Energy Density), is the ratio between the power consumed by the reactor and the gas flow rate:

$$\text{SIE}\ [\text{kJ}\cdot\text{L}^{-1}] = \frac{\text{Power}\ [\text{kW}]}{\text{Total flow rate}\ [\text{L}\cdot\text{s}^{-1}]} = \frac{\text{Power}\ [\text{W}]}{\text{Total flow rate}\ [\text{sccm}]}\cdot\frac{1}{60} \qquad \text{(E 3.8)}$$

where the average power is determined by calculating the area of the Lissajous plot, as explained above (see **section 3.2.1**). The SIE is often used in the literature to describe the energy consumption in a plasma reactor. This parameter will enable a direct comparison of the results obtained in this thesis with other results in literature. At atmospheric pressure and room temperature, the SIE is also commonly expressed in eV per molecule:

$$\text{SIE}\left[{}^{\text{eV}}/_{\text{molec.}}\right] = \text{SIE}\ [\text{kJ/L}]\cdot\frac{C_1\ [\text{eV}\cdot\text{kJ}^{-1}]\cdot C_2\ [\text{L}\cdot\text{mol}^{-1}]}{N_A\ [\text{molec.}\cdot\text{mol}^{-1}]} \qquad \text{(E 3.9)}$$

where C_1 is the kJ to eV equivalence ($6.24\cdot10^{21}$ eV/kJ), C_2 is the L to mol equivalence at ambient conditions – 25ºC, 1 atm – considering the ideal gas molar volume (24.5 L/mol), and N_A is the Avogadro constant ($6.022\cdot10^{23}$ molecules/mol).

In the upcoming pages, different expressions are provided depending on the process studied. Nevertheless, these magnitudes have similar connotations. On the one hand, reaction yields (or chemical yields) are given. These yields are defined in relation to the consumed amount of a key reactant: N_2 for ammonia synthesis, NH_3 for ammonia decomposition, CO_2 for CO_2 splitting, and CO_2 & CH_4 in case of the revaluation process. On the other hand, the energy efficiency of each process is taken proportional to the ratio between the reaction yield and the consumed power in the reactor.

In the discussion Chapters, the obtained results are discussed in terms of the evolution of these magnitudes – yields and efficiencies – with the variation of

operating parameters such as voltage amplitude, frequency, or gas flow rate. Alternatively, also in relation to derived magnitudes like the power consumption or the SIE.

3.4.1. Definitions for Ammonia Reactions

Expressions for the Ammonia Synthesis Reaction

For the ammonia synthesis reaction, the reaction yield is the percentage of nitrogen converted into ammonia, Y_{N2} [%], defined as:

$$Y_{N_2}(\%) = \frac{M_{NH_3}(\text{out})\ [\text{sccm}]}{2 \cdot M_{N_2}(\text{in})\ [\text{sccm}]} \cdot 100 \qquad (E\ 3.10)$$

where M_{NH3} (out) and M_{N2} (in) refer to the flows of these gases in the product and reactant mixtures, respectively.

The energy efficiency of ammonia production is provided in grams of produced ammonia per consumed power. It is named EE-NH_3 [gNH_3/kWh] and defined as:

$$EE - NH_3\ [gNH_3 \cdot (kWh)^{-1}] = \frac{m_{NH_3}(\text{out})\ [g \cdot \text{min}^{-1}] \cdot\ 60\ [\text{min} \cdot \text{h}^{-1}]}{\text{Power}\ [kW]} \qquad (E\ 3.11)$$

where m_{NH3} (out) is the rate of ammonia production expressed in grams per minute. This magnitude accounts for small changes in the reactor temperature during operation. Expression *E 3.11* follows the most common convention to express the energy efficiency in ammonia synthesis [7].

Expressions for the Ammonia Decomposition Reaction

For the ammonia decomposition reaction, the decomposition yield, DY_{NH3} [%] is defined as:

$$DY_{NH_3}\ [\%]\ = \frac{M_{NH_3}(\text{in})\ [\text{sccm}] - M_{NH_3}(\text{out})\ [\text{sccm}]}{M_{NH_3}(\text{in})\ [\text{sccm}]} \cdot 100 \qquad (E\ 3.12)$$

where M_{NH3} (in) and M_{NH3} (out) refer to the inlet and outlet ammonia flows, respectively. The energy efficiency for H_2 production, EE-H_2 [LH_2/kWh] is defined as:

$$EE - H_2\ [LH_2 \cdot (kWh)^{-1}] = \frac{V_{H_2}(\text{out})\ [\text{sccm}] \cdot 60\ [\text{min} \cdot \text{h}^{-1}]}{\text{Power}\ [kW]} \qquad (E\ 3.13)$$

where V_{H2} (out) refers to the volume (in liters) of H_2 that is produced by the decomposition of ammonia.

3.4.2. Definitions for CO_2 Reactions

Expressions for the CO_2 splitting reaction

The CO_2 conversion rate, χ [%], is defined as the percentage of CO_2 molecules that is split in the reactor:

$$\mathrm{CO_2\ Conversion\ Rate}, \chi\ [\%] = \frac{(\mathrm{M_{CO_2}\ (in)} - \mathrm{M_{CO_2}\ (out)})\ [\mathrm{sccm}]}{\mathrm{M_{CO_2}\ (in)}\ [\mathrm{sccm}]} \cdot 100 \qquad (E\ 3.14)$$

where M_{CO2} (in) and (out) refer to the CO_2 flow rate in the reactant and product mixtures respectively. The CO_2 splitting reaction provides CO (m/z=28) and O_2 (m/z=32) as main reaction products. Therefore, the conversion rate can be directly determined following the intensity of the m/z=44 signal (note that CO_2 is the only molecule that contributes to this peak).

For the gas mixtures (i.e., CO_2 plus O_2 or dry air), the conversion rate has to be corrected by multiplying the absolute CO_2 conversion rate, χ [%], by the dilution factor:

$$\mathrm{Effective\ CO_2\ Conversion\ Rate}, \chi_{\mathrm{eff}}\ [\%] = \chi\ (\%) \cdot \frac{\mathrm{CO_2\ flow\ rate\ (sccm)}}{\mathrm{Total\ flow\ rate\ (sccm)}} \qquad (E\ 3.15)$$

The efficiency of the CO_2 splitting process is defined in relation to the standard reaction enthalpy. In this thesis, the energy efficiency term, ζ [%], (equation *E 3.16*) is defined following the same criteria that were applied by Snoeckx and Bogaerts in a recent review [8]. To determine ζ [%], we relate the CO_2 conversion rate (absolute or effective, this latter utilized for CO_2 mixtures with other gases) with the SIE and the standard enthalpy of the CO_2 dissociation reaction into CO and O_2, ΔH_0 (283 kJ/mol):

$$\mathrm{Energy\ Efficiency}, \zeta\ [\%] = \frac{\chi\ [\%] \cdot \Delta \mathrm{H_0(kJ \cdot mol^{-1})}}{\mathrm{SIE\ (kJ \cdot mol^{-1})}} \qquad (E\ 3.16)$$

Although the dissociation of CO_2 into CO and O_2 has been supposed to be the main reaction pathway, other reactions might also take place. In particular, carbon deposition on the packing material and/or on the electrode surfaces. To quantify the amount of deposited carbon, a Carbon Balance parameter, C_B [%], has

been defined as the ratio between the outlet flows of the formed CO and unreacted CO_2 and the inlet flow of CO_2 initially fed into the reactor:

$$\text{Carbon Balance, } C_B\ [\%] = \frac{\left(\text{CO (out)} + \text{CO}_2\text{ (out)}\right)\ [\text{mol}]}{\text{CO}_2\text{ (in)}[\text{mol}]} * 100 \qquad (E\ 3.17)$$

Expressions for the valorization of CO_2 & CH_4

It will be further explained in **Chapter 9** that several types of hydrocarbons can be formed in the revalouation process of CO_2 and CH_4. Therefore, using expressions *E 3.14* and *E 3.15* to determine the absolute and effective CO_2 conversion rate, respectively, the contributions to the m/z=44 signal of these hydrocarbons should be removed to estimate the intensity associated with CO_2.

The absolute and effective conversion rate of methane is determined in the same manner, with M_{CH4} (in) and (out) as the CH_4 flow rate in the inlet and outlet mixture respectively:

$$\text{Absolute } CH_4 \text{ Conversion Rate } [\%] = \frac{\left(\text{M}_{\text{CH}_4}\text{ (in)} - \text{M}_{\text{CH}_4}\text{ (out)}\right)\ [\text{sccm}]}{\text{M}_{\text{CH}_4}\text{ (in)}\ [\text{sccm}]} \cdot 100 \qquad (E\ 3.18)$$

$$\text{Effective } CH_4 \text{ Con. Rate } [\%] = \text{Abs. } CH_4 \text{ Conv. Rate} \cdot \frac{CH_4 \text{ flow rate (sccm)}}{\text{Total flow rate (sccm)}} \qquad (\text{E } 3.19)$$

3.5. Ru/Al_2O_3 Catalyst Incorporation onto the Surface of PZT Pellets

This section describes the experimental procedure followed to cover the PZT pellets with a Ru/Al_2O_3 catalyst (**Chapters 7 and 8**). To assess the specific effects of Ru particles incorporation, a series of pellets coated only with the alumina support (without metal added) were also prepared. The state of the pellet coating in this series of pellets is further referred to as pristine.

Ru was incorporated into the alumina powder (Sigma Aldrich, γ-Al_2O_3, BET surface area of 120 m^2/g) using an incipient wet impregnation technique. For the pristine coating, the powder was impregnated with Milli-Q water. On the other hand, to incorporate Ru the impregnation was carried out using a solution of Ruthenium (III) chloride hydrate (Sigma Aldrich) instead of water.

The volume needed to acquire the incipient impregnation stage of 7 g of Al_2O_3 was experimentally determined (5 mL). Reaching this point, to incorporate a 2 wt% loading of ruthenium, a solution with a concentration of Ruthenium (III) of 63mg/mL was prepared. After the incorporation of the 5 mL into the alumina powder to acquire a wet impregnation state, the PZT pellets were covered with the impregnated powder spreading them in the slurry. Photographs of the different steps of the impregnation process are indicated in **Figure 3.12**.

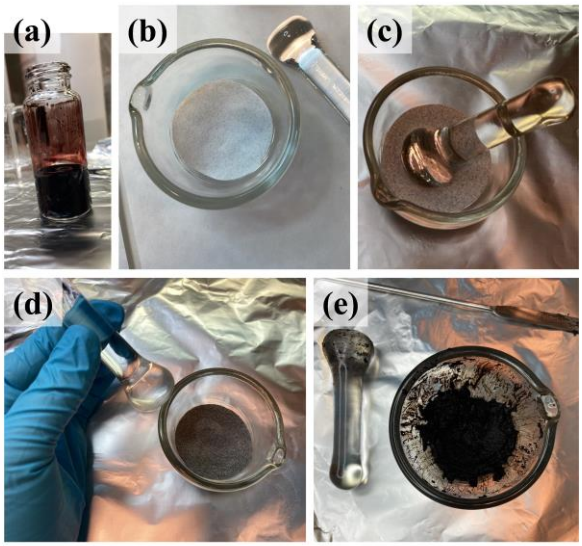

Figure 3.12. Photographs of the wet impregnation process showing the solution containing Ruthenium (III) (a) and the progressive impregnation of the alumina powder (b-d) until obtaining the incipient impregnation state (e).

The impregnated pellets were dried for approximately 12h at room temperature. Then, the covered pellets were dried in air at 120ºC for 4h at a rate of 1ºC/min and subsequently calcined in air at 450ºC for 3 hours at a rate of 2ºC/min, i.e., following the same procedure described by B. Patil [9].

This method provides a way to incorporate a 2 wt% Ru into the powder. The covered pellets and impregnated powders were examined by using the characterization methods explained below, in order to analyze the incorporation of Ru and the formation of metal particles. To avoid PZT contaminations, powder samples – without mixing the pellets and the slurry – were synthesized (impregnated and calcinated) and analyzed separately. Note that this procedure was necessary for a straightforward detection of the Ru particles, avoiding artifacts and interferences coming from signals due to PZT.

3.6. Techniques for Physicochemical Characterization of Packed-bed Materials

The following techniques have been used to characterize the ferroelectric pellets and catalytic powder samples in different conditions:

- X-Ray Photoelectron Spectroscopy (XPS), used to analyze the surface chemistry of the samples. For this purpose, the equipment (PHOIBOS 100, Specs, Germany) was operated at normal incidence using the Kα line of Magnesium as the excitation source.
- Scanning Electron Microscopy (SEM), to acquire morphological information about the microstructure of the surface. It was performed with a S4800 field emission microscope (Hitachi High-Tech Corporation, Japan), applying 2 kV in secondary and backscattered electron modes. The powder samples were suspended in an ethanol drop, which was supported into a grid composed of Cu-Co-Au.
- Transmission Electron Microscopy (TEM), used to characterize the microstructure of the alumina powder suspended in ethanol. For this purpose, a JEOL 2100Plus (Jeol, Japan) microscope equipped with a LaB6 filament and a CCD camera (Gatan, US) was used. The microscope was operated at 200 kV.
- Energy Dispersive X-Ray Spectroscopy (EDX or EDXS), to analyze the chemical composition of the microstructures. Both microscopes previously mentioned are equipped with energy dispersive X-Ray analyzers. Regarding the SEM, a Bruker-X Flash-4010 (Bruker, US) equipment was used to obtain element composition maps with an acceleration voltage set between 10-30 kV. Regarding the TEM, an X-Max 80T (Oxford Instruments, UK) analyzer was used at 200 kV.
- N_2 adsorption, to study the Brunauer-Emmett-Teller (BET) surface area of the samples. The nitrogen adsorption technique at 77 K was performed with a TriStar II 3020 analyzer (Micromeritics Instruments Corporation, US). Prior to the analysis, samples were outgassed at 150ºC for 2 hours.

3.7. References

[1] A. Méndez Montoro de Damas, *Plasmas de Descarga de Barrera Dieléctrica con Empaquetamiento Ferroeléctrico a Presión Atmosférica Aplicados a la Producción de Hidrógeno, Amoníaco y a la Descontaminación de Aire*, Sevilla: Universidad de Sevilla, 2017.

[2] W. Bolton, Nyquist Diagrams, Instrumentation and Control Systems. (2015) 271–279. https://doi.org/10.1016/B978-0-08-100613-9.00012-2.

[3] J. Meichsner, M. Schmidt, R. Schneider and H.E. Wagner (2013), Nonthermal plasma chemistry and physics, CRC Press. https://doi.org/10.1201/b12956.

[4] National Institute of Standards and Technology (NIST), Mass Spectrometer Data Center, (n.d.). https://chemdata.nist.gov/.

[5] T. Mizushima, K. Matsumoto, H. Ohkita, N. Kakuta, Catalytic Effects of Metal-loaded Membrane-like Alumina Tubes on Ammonia Synthesis in Atmospheric Pressure Plasma by Dielectric Barrier Discharge, Plasma Chemistry and Plasma Processing 2006 27:1. 27 (2006) 1–11. https://doi.org/10.1007/S11090-006-9034-2.

[6] L. Wang, Y. Zhao, C. Liu, W. Gong, H. Guo, Plasma driven ammonia decomposition on a Fe-catalyst: eliminating surface nitrogen poisoning, Chemical Communications. 49 (2013) 3787–3789. https://doi.org/10.1039/C3CC41301B.

[7] M.L. Carreon, Plasma catalytic ammonia synthesis: State of the art and future directions, Journal of Physics D: Applied Physics. 52 (2019). https://doi.org/10.1088/1361-6463/ab3b2c.

[8] R. Snoeckx, A. Bogaerts, Plasma technology: a novel solution for CO_2 conversion?, Chemical Society Reviews. 46 (2017) 5805–5863. https://doi.org/10.1039/c6cs00066e.

[9] B.S. Patil, *Plasma (catalyst) - assisted nitrogen fixation: reactor development for nitric oxide and ammonia production*, Eindhoven: Technische Universiteit Eindhoven, 2017.

Chapter 4

Electrical Characterization of Ferroelectric Packed-bed Reactors*

4.1. Introduction

Plasma reactors with a packed-bed configuration are efficiently and increasingly utilized for different plasma-driven chemical processes. These processes are, for example, the reforming of hydrocarbons [1–3], the abatement of pollution [4,5], or the synthesis of ammonia [6–8], processes of enormous environmental and energetic relevance for different industrial strategic sectors. As discussed in **Chapter 1**, the characteristics of the barrier materials – i.e., the discharge moderator – constitute one of the most critical variables for the control of the reactor electrical behavior and, therefore, its power consumption, a working parameter that is strictly related with the energy efficiency. However, the large variety of reported product selectivities, process efficiencies, reactor configurations (geometry, size, distance between electrodes, size, and type of pellet material, etc.) or operating conditions (voltage, frequency, temperature, etc.) makes it difficult to account for the effect of discharge moderators reported in the numerous studies carried out in this research area [9–11].

It has been empirically realized that the use of ferroelectrics (i.e., Ferroelectric Barrier Discharge reactors, FBD) instead of conventional dielectrics (i.e., Dielectric Barrier Discharge reactors, DBD) as interelectrode material may contribute to increasing the yield and energy efficiency of plasma processes in packed-bed reactors [12–14]. In particular, previous results from our research group have demonstrated that the energy efficiency for ammonia synthesis or pollutant removal processes could be increased using a ferroelectric material like

* The content of this chapter has been published in: A. Gómez-Ramírez, R. Álvarez, **P. Navascués**, F. J. Garcia-García, A. Palmero, J. Cotrino, A. R. González-Elipe, Electrical and reaction performances of packed-bed plasma reactors moderated with ferroelectric or dielectric materials. *Plasma Processes and Polymers*. 18 (3) (2021) 2000193. https://doi.org/10.1002/ppap.202000193

PZT (lead zirconate titanate) as moderator in a packed-bed FBD plasma reactor [5,8]. Other authors have proved similar effects, as Michielsen *et al.*, who, for the CO_2 dissociation, compared the effect of $BaTiO_3$ pellets with that of SiO_2, Al_2O_3 and ZrO_2 beds [14]. Similarly, G. Akay and K. Zhang reported an increase in the reaction yield for the ammonia synthesis reaction filling a packed-bed reactor with $BaTiO_3$ instead of glass beds [12].

This chapter aims at clarifying the effect of the dielectric constant of the moderator material on the reactor efficiency. Therefore, the electrical behavior of the plasma reactor has been systematically studied as a function of voltage amplitude and frequency, filling the reactor with either dielectric (alumina and glass) or ferroelectric ($BaTiO_3$ and PZT) pellets of similar size. Despite its relatively low Curie temperature [15], $BaTiO_3$ is the ferroelectric material most widely used in plasma-catalysis [16–18]. As a consequence, in this thesis the electrical behavior of the reactor filled with this material has been studied as a function of temperature, a variable that is usually varied in plasma-catalysis processes to promote the efficiency and selectivity of many reactions [19].

The discussion of the results obtained in this chapter justifies the use of PZT as moderator for the different plasma-catalysis processes studied in this thesis. The phenomenological analysis has shown that ferroelectrics are more efficient than dielectrics to operate packed-bed reactors. The reactor performance has been discussed according to previous results of our research group regarding the ammonia synthesis reaction.

4.2. Experimental Details

The packed-bed reactor was filled with a *single packed layer* of 3 mm of dielectric (alumina and glass beads) and ferroelectric (PZT and $BaTiO_3$) pellets of similar size (see **Table 3.1** in **Chapter 3** for the material properties). The selection of this configuration, where the electrodes are in direct contact with the *single packed layer*, ensures that the electrical behavior of the set-up is exclusively controlled by the dielectric properties of the pellets (note that in typical DBD reactors the metal electrodes are generally covered by a dielectric plate [20]).

The voltage amplitude was varied between 0.5 and 7 kV and the frequency between 0.5 and 10 kHz. A dry air flow of 25 sccm was passing through the reactor during all electrical characterization experiments.

Most experiments of this study have been carried out at room temperature. Therefore, they were performed for very short periods of time to avoid that an uncontrolled increase in temperature due to plasma operation could affect the electrical characterization results. For completeness, some experiments were also carried out controlling the temperature with an external heater (see **Chapter 3**). The heater was positioned around the reactor until the temperature reached the targeted steady state value (i.e., *nominal temperature*). *V(t)* and *I(t)* data were acquired after reaching a stable steady state at each given *nominal temperature*. A temperature gradient is expected between the inner parts and the external reactor walls. The *nominal temperature* measured at the reactor wall is likely to be smaller than the actual temperature inside the reactor where plasma is another source of heat. This is due to that local hot points can develop at the contact points between pellets and between pellets and electrodes where plasma intensity is maximum.

This study encompasses impedance measurements performed in the reactor filled with the *single packed layer* of $BaTiO_3$ in the absence of plasma to acquire *Nyquist* plots. The potentiostat/galvanostat was operated in a frequency range from 1 MHz to 1 Hz applying an alternating voltage of $0.2 \cdot V_{rms}$ between the electrodes of the reactor. The resolution of the measurements was twenty points per decade. The measurements were taken at different imposed temperatures, from 25 ºC up to 144 ºC, respectively, lower and higher temperatures than the Curie point of $BaTiO_3$ (120 ºC) [15]. Impedance measurements were repeated three times to confirm the reproducibility of the results.

4.3. Results and Discussion

4.3.1. Current Dependence on Applied Voltage and Frequency

Common models to describe the electrical behavior of DBD reactors rely on RC (resistor-capacitor) circuit models, where the reactor behavior is assumed to be equivalent to that of a circuit composed of a variable resistor (plasma) and, usually, two capacitances (one for the gap between the electrodes and another for the dielectric material used as barrier). However, as recently pointed out by Butterwoth and Allen [21], applying such kind of RC models to packed-bed reactors can be misleading. For example, at low voltages plasma ignites in the contact points between pellets and between pellets and electrodes, and only spreads from there to fill the whole gap when voltage increases. In other words, the actual volume of plasma is not constant and varies with the applied voltage. Moreover, the evolution of dielectric properties of the barrier material with operating variables such as voltage or frequency can be critical to properly describe these models, but they are rarely included in the analysis [22–24]. Therefore, a careful electrical characterization of packed-bed reactors should take into account all these facts.

The first issue in this study is to determine the evolution of the current in the reactor at room temperature as a function of the applied voltage and frequency: *I(V)* and *I(f)*. **Figure 4.1** shows plots of the root mean square (rms) current measured as a function of the applied voltage at a frequency of 3 kHz (**Figure 4.1(a)**) and as a function of frequency at a fixed voltage of 2 kV (**Figure 4.1(b)**). **Figure 4.1(a)** shows that, for Al_2O_3 and glass, the current varies linearly with voltage, the two materials showing similar curves. Unlike this behavior, particularly at voltages higher than 1.5 kV, the current follows a polynomial variation with the frequency, and it is more intense for the two ferroelectrics than for the two dielectrics, with a higher intensity for $BaTiO_3$ than for PZT in the studied voltage range. It is also noteworthy that the direct observation of the plasma shows that, even at the highest applied voltages, discharges are mainly located at the contact points between pellets and electrodes, and do not extend through the interpellet void space of the single pellet layer utilized in this study.

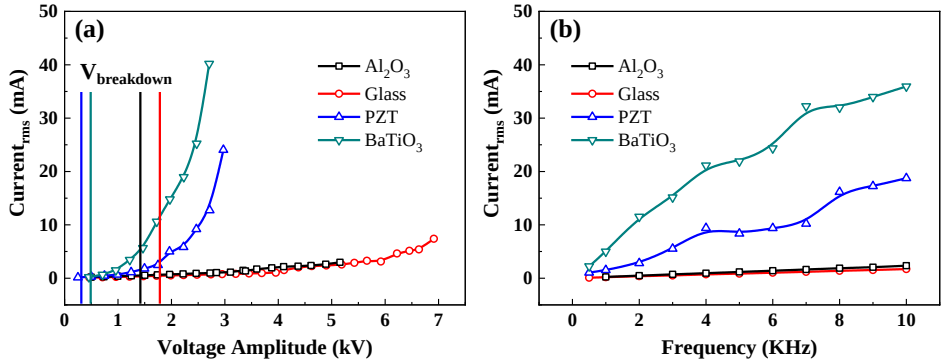

Figure 4.1. Plots of the root mean square (rms) current measured as a function of the applied voltage for f= 3kHz (with the average *breakdown voltage* indicated for each configuration) (a) and as a function of the operating frequency for V=2kV (b). Plots are presented for dielectric (Al_2O_3 and glass) and ferroelectric (PZT and $BaTiO_3$) materials. Experiments were performed at ambient temperature.

The plots in **Figure 4.1,** showing a different *I-V* dependence for the four moderator materials, confirm that the reactor efficiency depends on the dielectric constant of the materials and, therefore, on the known dependence of this parameter with applied voltage and frequency [25]. Whereas a direct (although not lineal) frequency dependence is the typical expected behavior of this kind of packed-bed systems as documented in electromagnetism books, [26] the voltage dependence, which is related with the ferroelectric hysteresis loop of ferroelectric materials (polarization vs. electric field representation), is currently under research [27,28]. Since variations with frequency and voltage may affect the evolution of the energy efficiency in a large variety of plasma-catalysis processes [4,29–34], we deem it critical to carry out systematic comparative studies to obtain clear evidence about the effect of the dielectric constant of moderator materials on the reactor performance.

The vertical lines in **Figure 4.1(a)** highlight the average *breakdown voltage* determined for each barrier configuration: 1.8 kV for glass, 1.4 kV for Al_2O_3, 0.5 kV for $BaTiO_3$, and 0.3 kV for PZT. As illustrated in **Figure 4.2,** the procedure used to determine the *breakdown voltage* entails the selection of the voltage at which a first filament is observed. The values of the *breakdown voltage* were determined at 3 kHz for each applied voltage, selecting the average value with its standard deviation as indicated in **Table 4.1**. This table includes the value of the

dielectric constant of each material, the average *breakdown voltage* at 3 kHz, and the power consumed by the reactor under the indicated experimental conditions.

Table 4.1. Dielectric constant, average *breakdown voltage*, and consumed power reated to the four moderator materials.

	Moderator material	**Dielectric constant, ε**	**Breakdown voltage** (kV)	**Power** (W)*
DBD	Glass	3.8	1.79 ± 0.17	0.5
	Al_2O_3	10	1.4 ± 0.3	2.6
FBD	$BaTiO_3$	1250-10000	0.5 ± 0.13	47.6
	PZT	1900	0.29 ± 0.07	12.6

*Consumed power calculated for an applied voltage of 2.75 kV (FBD-mode) and 5.2 kV (DBD-mode) (see **Figure 4.4**). The frequency was 3 kHz in all cases.

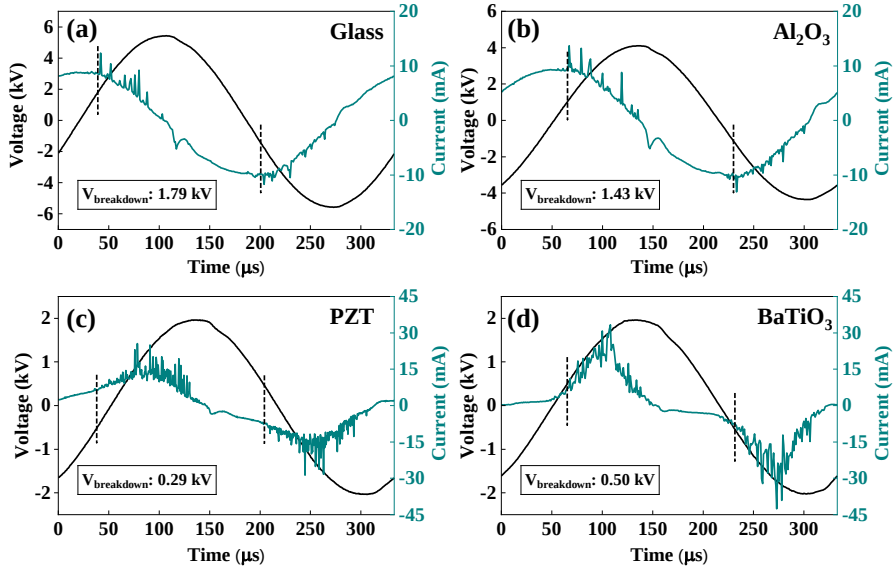

Figure 4.2. *I(t)* and *V(t)* curves with the procedure utilized to determine the *breakdown voltage* indicated (in bracket the applied voltage amplitude in each case): (a) Glass (V=5.5kV), (b) Al_2O_3 (V=4kV), (c) PZT (V=2kV), and (d) $BaTiO_3$ (V=2kV). The frequency was fixed at 3 kHz.

It is apparent in the previous table that plasma ignites at lower voltages using ferroelectrics. Owing to the higher dielectric constant and more efficient polarization switching of these materials, this feature can be associated with an enhancement of the electric field at the contact points between pellets, as well as between pellets and electrodes [35]. Similarly, plots in **Figure 4.1(b)** show that current increases with the operating frequency and reaches maximum values for the ferroelectric materials. It is also apparent in this set of *I(f)* plots that $BaTiO_3$ induces higher rms current values than PZT and, therefore, should produce an enhancement of plasma intensity.

In general, the relative dielectric permittivity of typical dielectrics does not vary significantly with the applied voltage. Nevertheless, the strong dependence of reactor current on voltage in ferroelectrics must be attributed to a non-linear and strong variation of the function $\varepsilon(V)$ [36–38]. **Figure 4.1(a)** also shows that the *I(V)* curve depicts higher values for $BaTiO_3$ than for PZT pellets, in agreement with the higher dielectric constant of the former at temperatures lower than 120 ºC (Curie temperature of $BaTiO_3$ [15]). Similarly, the higher values in **Figure 4.1(b)** depicted by the *I(f)* plots of the two ferroelectrics, particularly for $BaTiO_3$, must be attributed to the characteristic evolution of the $\varepsilon(f)$ functions of these two materials [37,39].

A close look at the shape of the *I(t)* curves also reveals significant differences between DBD-like and FBD-like modes of reactor operation. **Figures 4.2** and **4.3** show that the current waveform with dielectrics depicts a sine-like curve with superimposed filaments once the plasma ignites. However, for ferroelectrics, the *I(t)* curves depict a narrower alternant behavior, with zero or close to zero intensity periods of time between subsequent positive and negative values. Moreover, **Figure 4.3** shows that, at increasing values of the applied voltage, the *I(t)* curves recorded for the four materials depict a progressive increase of amplitude with this parameter. In addition to the differences in the shape of the *I(t)* curves of dielectrics and ferroelectrics, the plasma intensity is much higher in the FBD-mode of operation, as further demonstrated by the Lissajous curves plotted in **Figure 4.4**.

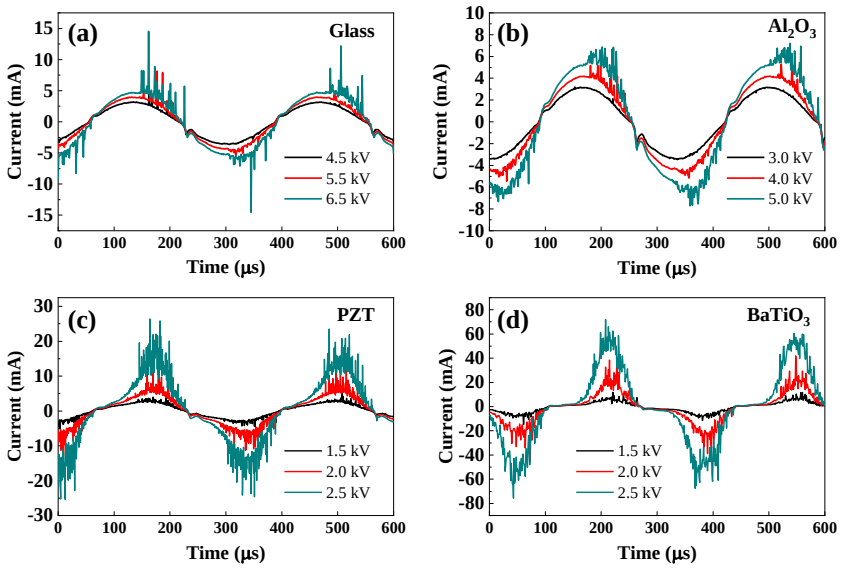

Figure 4.3. *I(t)* curves: glass (a), Al_2O_3 (b), PZT (c), and $BaTiO_3$ (d) as packed materials, for an operating frequency of 3 kHz and the indicated applied voltages.

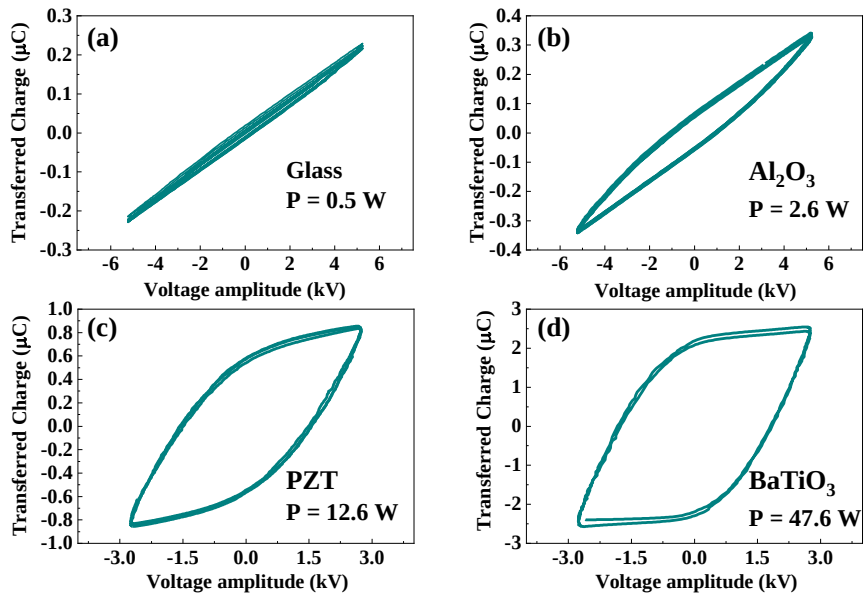

Figure 4.4. Lissajous figures: glass (a), Al_2O_3 (b), PZT (c), and $BaTiO_3$ (d) for an operating frequency of 3 kHz and different applied voltages: 2.75 kV for the FBD-mode and 5.2 kV for the DBD-mode.

The consumed power values deduced from these Lissajous curves and gathered in **Table 4.1** clearly evidence the operating differences between the different packed bed barriers, with values that are one or two orders of magnitude higher for PZT and $BaTiO_3$ than for glass or Al_2O_3. Data shown in **Table 4.1** indicates that operating the reactor with PZT requires a smaller average *breakdown voltage* than $BaTiO_3$. This fact can be related to the higher rugosity of the laboratory sintered PZT pellets in comparison with that of the $BaTiO_3$ ones, which were supplied by the manufacturer in pellet form (see **Figure 3.2** in **Chapter 3**). A high surface rugosity will induce an intensification of the reduced electric field at these points, reducing the relative distances and promoting the breakdown of the gas at lower voltages. This feature is discussed using some modeling results in **Chapter 6**.

4.3.2. Current Dependence on Temperature

Temperature is a typical running parameter to improve reaction selectivity in plasma-catalysis [40–42]. To study the effect of this parameter on the electrical behavior of packed-bed reactors, the rms current has been measured as a function of the *nominal temperature* for a constant voltage of 2.5 kV and a frequency of 3 kHz. **Figure 4.5** shows the results obtained as a function of the *nominal temperature* measured on the reactor external wall for the packed-bed reactor filled with Al_2O_3, PZT and $BaTiO_3$ pellets. It can be observed that the current did not vary when operated with alumina. However, it increased constantly for PZT, while for $BaTiO_3$ it reached a maximum at about 60ºC of wall *nominal temperature* and then decreased. These distinct variations with temperature can be related with the different $\varepsilon(T)$ functions of the materials under study [25,36,37,39,43–47]. For dielectrics, $\varepsilon(T)$ does not vary significantly in the interval explored in this study. However, the value of the dielectric constant of PZT increases continuously with the temperature, whereas for $BaTiO_3$, there is a sharp drop in ε due to the ferroelectric-to-paraelectric phase transition occurring at the Curie Temperature (120 ºC) [37,45]. Regarding the $BaTiO_3$ curve in **Figure 4.5**, it is noteworthy that the current does not depict a sharp variation as it should be expected for the variation of the dielectric constant with the temperature of a perfect crystalline material [48]. Therefore, we attribute the observed broad dependence on *nominal temperature* depicted in **Figure 4.5** (i.e., the appearance of a wider peak around 60 ºC) to the polycrystalline character of the pellets. Additionally, the temperature

distribution inside the reactor might be inhomogeneous due to gas flow disturbances and localized heat release processes. Therefore, the fact that the *I(t)* maximum appears around a wall *nominal temperature* of 60-70 ºC suggests the existence of temperature gradients between the pellets inside and the reactor walls.

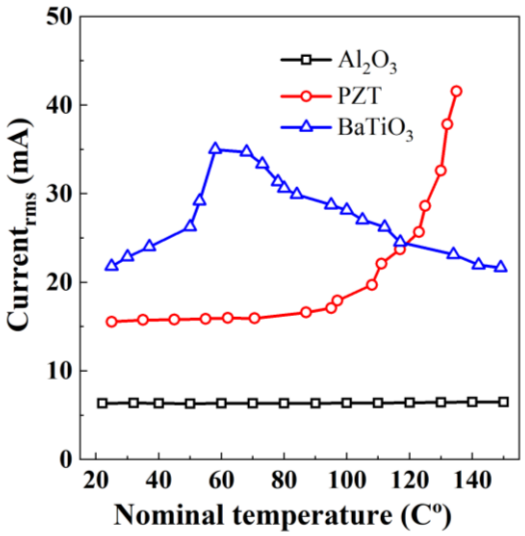

Figure 4.5. Variation of the rms current as a function of the temperature measured on the external wall of the reactor (i.e., *nominal temperature*) for a voltage of 2.5 kV and a frequency of 3kHz.

The association of the maximum in **Figure 4.5** with that the $BaTiO_3$ pellets are progressively reaching their Curie point is further supported by the *Nyquist* plots [49,50] in **Figure 4.6**, determined at different *nominal temperatures* with the reactor filled with pellets of this material. As it has been mentioned in **Chapter 3**, the shape of the curvature in a typical *Nyquist* plot provides information about the electrical properties (i.e., impedance) of solids.

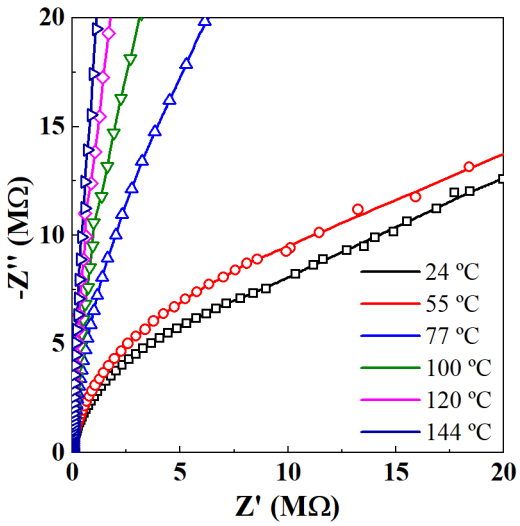

Figure 4.6. Z"-Z' (*Nyquist*) plot for the reactor moderated with $BaTiO_3$ at the indicated *nominal temperatures*.

Clearly, the curves in **Figure 4.6** can be grouped in two sets, for *nominal temperatures* higher or lower than 55 ºC. For *nominal temperatures* higher than 55ºC, the curves are characterized by high slopes (i.e., as expected for a high radius Z"-Z´ ideal hemispherical curve), a characteristic of dielectric materials with a constant value of the relative dielectric permittivity. This behavior suggests a paraelectric state for $BaTiO_3$. On the other hand, for *nominal temperatures* lower than 55ºC, the behavior is closer to that of ferroelectric materials (i.e., an ideal hemisphere of small radius [51]). The different tendencies found analyzing the electrical behavior indicate that temperature is a parameter that not only plays a very important role to promote certain catalytic reaction mechanisms but also introduces important variations in the current intensity when operating with ferroelectrics. In relation to the previously mentioned RC-circuit modeling to describe the electrical behavior of DBD reactors [23,52], the findings herein support the need to incorporate the dependence with the temperature of the capacitances that are used in these models.

4.3.3. Curie Temperature and Packed-bed Reactor Efficiency

The observed dependence of electrical properties of the reactor filled with $BaTiO_3$ in comparison with Al_2O_3 pellets (FBD-like vs. DBD-like modes of operation, **Figure 4.1**) correlates well with previous results from our research group about pollutant removal experiments carried out with the same packed-bed reactor configuration [5]. In that study, it was shown that using alumina as moderator material rendered a negligible removal of pollutants as compared with the results achieved with $BaTiO_3$. According to the discussion in **section 4.3.1**, the much lower efficiency found with Al_2O_3 can be associated with the lower current and power values obtained for this moderator material (**Figures 4.1-4.4**).

In principle, $BaTiO_3$ would perform better than PZT as a moderator of plasma discharges in FBD packed-bed reactors. However, comparative ammonia synthesis experiments carried out with the same packed-bed reactor using pellets of either $BaTiO_3$ or PZT showed that, above a certain voltage, the reaction yield was inferior for the former [53]. The results of these experiments, reported in **Figure 4.7**, show that the reaction yield was only higher for $BaTiO_3$ when working at voltages smaller than 2.5 kV and the maximum temperature measured at the reactor wall, due solely to plasma heating, was 25ºC. At higher voltages, wall temperatures in the steady state due to plasma heating were higher, the yield for the ammonia synthesis reversed, and PZT resulted in a much more efficient moderator material for this reaction (e.g., when the external temperature of the reactor wall reached 35º or higher temperatures). The difference between the two configurations progressively increased for higher voltages and wall temperatures up to 50-60º. Although the reaction yield increases for the two moderator materials, there is a loss of efficiency for $BaTiO_3$ with respect to PZT. These results can be explained under the assumption that certain parts of the $BaTiO_3$ pellets have reached the Curie Temperature at which the ferroelectric-to-paraelectric phase transition occurs. Under these conditions, these pellets would be less efficient for the generation of highly intense plasma discharges. In general terms, results in **Figure 4.7** also highlight the importance of carefully controlling reactor temperature (and temperature drifts) during plasma-catalysis experiments, even at relatively low temperatures. Specifically, when temperature control is an issue, this investigation supports the use of ferroelectric materials with a high Curie Temperature that would not be affected by uncontrolled phase transformation phenomena at the reactor operating temperature.

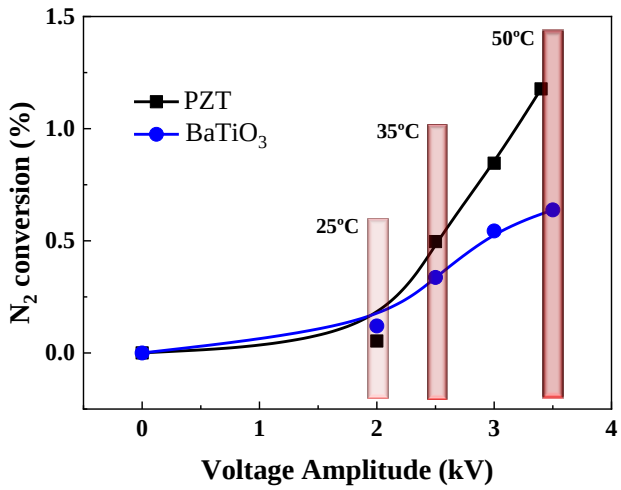

Figure 4.7. Reaction yield of the ammonia synthesis process (expressed in percentage of reacted nitrogen) vs. the applied voltage in the ferroelectric packed-bed reactor. The vertical lines indicate the *nominal temperature* determined at the walls of the reactor after 1 h of operation in steady state conditions. Yield values taken from [53].

The explanation of these results exclusively in terms of a $BaTiO_3$ phase transition should be taken cautiously and as an object of debate. Effectively, several studies carried out with $BaTiO_3$ and glass as moderator materials revealed that the former performs better, even at temperatures above its Curie point [54–56]. Since ferroelectric materials may act as catalysts for the ammonia synthesis and other plasma-catalysis processes [54,55,57,58], the higher reaction yield obtained with PZT could also be due to a higher catalytic activity of this material as compared with that of $BaTiO_3$. In addition, the highest $BaTiO_3$ current values in **Figure 4.5** for the same temperature range than for the experiment in **Figure 4.7** supports that, in certain situations, the high intensity of the plasma can have detrimental effects on the reaction efficiency. Just a tentative possibility in this particular case, we can claim that electron impact processes directly related with the decomposition of ammonia [59] can be more probable for $BaTiO_3$ than for PZT. These mechanisms, named *back-reactions*, might contribute to decreasing the reaction efficiency. This and other types of reaction mechanisms are discussed in detail in the upcoming Chapters of this thesis.

Finally, it should be mentioned that apart from the right choice of moderator in terms of their dielectric properties, the incorporation of classic catalysts in

packed-bed plasma reactors and the design of new reactor configurations are current challenges that will enable increasing the energy efficiency and yield of the processes [57,60]. In this regard, the incorporation of Ruthenium catalyst onto PZT pellets to moderate plasma-assisted *ammonia reactions* has been proposed in this thesis as a means to improve the reaction efficiency (see **Chapters 6 and 7**).

4.4. Conclusions

The previous results have provided empirical evidence that may contribute to understand the distinct phenomenology reported in the literature regarding packed-bed plasma reactors. It has been demonstrated that, for similar applied voltages, the plasma current is much higher when operating the reactor with ferroelectrics instead of dielectrics as discharge moderators. As a general conclusion, we state that plasma-catalysis or, in general, gas processing with packed-bed reactors, should be more effective with a ferroelectric barrier. The selection of the specific ferroelectric material can be critical if the operating temperature during the process reaches values higher than its Curie Temperature. Hints of such a dependence have been found for the ammonia synthesis reaction with $BaTiO_3$ as moderator. The observed evolution of efficiency justifies the choice of PZT as moderator to carry out plasma-catalysis processes, as it will be illustrated in the upcoming Chapters of this thesis.

4.5. References

[1] X. Tu, J.C. Whitehead, Plasma-catalytic dry reforming of methane in an atmospheric dielectric barrier discharge: Understanding the synergistic effect at low temperature, Applied Catalysis B: Environmental. 125 (2012) 439–448. https://doi.org/10.1016/J.APCATB.2012.06.006.

[2] A.M. Montoro-Damas, J.J. Brey, M.A. Rodríguez, A.R. González-Elipe, J. Cotrino, Plasma reforming of methane in a tunable ferroelectric packed-bed dielectric barrier discharge reactor, Journal of Power Sources. 296 (2015) 268–275. https://doi.org/10.1016/J.JPOWSOUR.2015.07.038.

[3] H.L. Chen, H.M. Lee, S.H. Chen, Y. Chao, M.B. Chang, Review of plasma catalysis on hydrocarbon reforming for hydrogen production—Interaction, integration, and prospects, Applied Catalysis B: Environmental. 85 (2008) 1–9. https://doi.org/10.1016/J.APCATB.2008.06.021.

[4] K. Hyun-Ha, Nonthermal Plasma Processing for Air-Pollution Control: A Historical Review, Current Issues, and Future Prospects, Plasma Processes and Polymers. 1 (2004) 91–110. https://doi.org/10.1002/ppap.200400028.

[5] A. Gómez-Ramírez, A. M. Montoro-Damas, M.A. Rodríguez, A. R. González-Elipe, J. Cotrino, Improving the pollutant removal efficiency of packed-bed plasma reactors incorporating ferroelectric components, Chemical Engineering Journal. 314 (2017) 311–319. https://doi.org/https://doi.org/10.1016/j.cej.2016.11.065.

[6] P. Peng, P. Chen, C. Schiappacasse, N. Zhou, E. Anderson, D. Chen, J. Liu, Y. Cheng, R. Hatzenbeller, M. Addy, Y. Zhang, Y. Liu, R. Ruan, A review on the non-thermal plasma-assisted ammonia synthesis technologies, Journal of Cleaner Production. 177 (2018) 597–609. https://doi.org/https://doi.org/10.1016/j.jclepro.2017.12.229.

[7] A. Gómez-Ramírez, A.M. Montoro-Damas, J. Cotrino, R.M. Lambert, A.R. González-Elipe, About the enhancement of chemical yield during the atmospheric plasma synthesis of ammonia in a ferroelectric packed bed reactor, Plasma Processes and Polymers. 14 (2016) 1600081. https://doi.org/10.1002/ppap.201600081.

[8] A.R. Gómez-Ramírez, A; Cotrino, J; Lambert, R. M. and González-Elipe, Efficient synthesis of ammonia from N_2 and H_2 alone in a ferroelectric packed-bed DBD reactor, Plasma Sources Science and Technology. 24 (2015) 65011. https://doi.org/10.1088/0963-0252/24/6/065011.

[9] R. Snoeckx, A. Bogaerts, Plasma technology - a novel solution for CO_2 conversion?, Chemical Society Reviews. 46 (2017) 5805–5863. https://doi.org/10.1039/C6CS00066E.

[10] J. Hong, S. Prawer, A.B. Murphy, Plasma Catalysis as an Alternative Route for Ammonia Production: Status, Mechanisms, and Prospects for Progress, ACS Sustainable Chemistry & Engineering. 6 (2018) 15–31. https://doi.org/10.1021/acssuschemeng.7b02381.

[11] M.L. Carreon, Plasma catalysis: A brief tutorial, Plasma Research Express. 1 (2019). https://doi.org/10.1088/2516-1067/ab5a30.

[12] G. Akay, K. Zhang, Process intensification in ammonia synthesis using novel coassembled supported microporous catalysts promoted by nonthermal plasma, Industrial and Engineering Chemistry Research. 56 (2017) 457–468. https://doi.org/10.1021/acs.iecr.6b02053.

[13] W.C. Chung, K.L. Pan, H.M. Lee, M.B. Chang, Dry reforming of methane with dielectric barrier discharge and ferroelectric packed-bed reactors, Energy and Fuels. 28 (2014) 7621–7631. https://doi.org/10.1021/ef5020555.

[14] I. Michielsen, Y. Uytdenhouwen, J. Pype, B. Michielsen, J. Mertens, F. Reniers, V. Meynen, A. Bogaerts, CO_2 dissociation in a packed bed DBD reactor: First steps towards a better understanding of plasma catalysis, Chemical Engineering Journal. 326 (2017) 477–488. https://doi.org/10.1016/j.cej.2017.05.177.

[15] K. Sakayori, Y. Matsui, H. Abe, E. Nakamura, M. Kenmoku, T. Hara, D. Ishikawa, A. Kokubu, K. Hirota and T. Ikeda, Curie Temperature of $BaTiO_3$, Japanese Journal of Applied Physics. 34 (1995) 5443. https://doi.org/10.1143/JJAP.34.5443.

[16] T. Butterworth, R. Elder, R. Allen, Effects of particle size on CO_2 reduction and discharge characteristics in a packed bed plasma reactor, Chemical Engineering Journal. 293 (2016) 55–67. https://doi.org/https://doi.org/10.1016/j.cej.2016.02.047.

[17] I. Michielsen, Y. Uytdenhouwen, J. Pype, B. Michielsen, J. Mertens, F. Reniers, V. Meynen, A. Bogaerts, CO_2 dissociation in a packed bed DBD reactor: First steps towards a better understanding of plasma catalysis, Chemical Engineering Journal. 326 (2017) 477–488. https://doi.org/https://doi.org/10.1016/j.cej.2017.05.177.

[18] S. Xu, J.C. Whitehead, P.A. Martin, CO_2 conversion in a non-thermal, barium titanate packed bed plasma reactor: The effect of dilution by Ar and N_2, Chemical Engineering Journal. 327 (2017) 764–773. https://doi.org/10.1016/j.cej.2017.06.090.

[19] P. Mehta, P. Barboun, D.B. Go, J.C. Hicks, W.F. Schneider, Catalysis Enabled by Plasma Activation of Strong Chemical Bonds: A Review, ACS Energy Letters. 4 (2019) 1115–1133. https://doi.org/10.1021/acsenergylett.9b00263.

[20] Whitehead J.C. (2019) Plasma Catalysis: Introduction and History. In: Tu X., Whitehead J., Nozaki T. (eds) Plasma Catalysis. Springer Series on Atomic, Optical, and Plasma Physics, vol 106. Springer, Cham. https://doi.org/10.1007/978-3-030-05189-1_1.

[21] T. Butterworth, R.W.K. Allen, Plasma-catalyst interaction studied in a single pellet DBD reactor: dielectric constant effect on plasma dynamics, Plasma Sources Science and Technology. 26 (2017) 65008. https://doi.org/10.1088/1361-6595/aa6c35.

[22] A. V Pipa, J. Koskulics, R. Brandenburg, T. Hoder, The simplest equivalent circuit of a pulsed dielectric barrier discharge and the determination of the gas gap charge transfer, Review of Scientific Instruments. 83 (2012) 115112. https://doi.org/10.1063/1.4767637.

[23] V.A. Pipa, R. Brandenburg, The Equivalent Circuit Approach for the Electrical Diagnostics of Dielectric Barrier Discharges: The Classical Theory and Recent Developments, Atoms. 7 (2019). https://doi.org/10.3390/atoms7010014.

[24] M. Archambault-Caron, H. Gagnon, B. Nisol, K. Piyakis, M.R. Wertheimer, Precise energy and temperature measurements in dielectric barrier discharges at atmospheric pressure, Plasma Sources Science and Technology. 24 (2015) 45004. https://doi.org/10.1088/0963-0252/24/4/045004.

[25] K.C. Kao, 2 - Electric Polarization and Relaxation, in: K.C.B.T.-D.P. in S. Kao (Ed.), Academic Press, San Diego, 2004: pp. 41–114. https://doi.org/https://doi.org/10.1016/B978-012396561-5/50012-8.

[26] J.D. Jackson (1998), Classical Electrodynamics, 3rd ed., John Wiley & Sons, Ltd.

[27] H. Li, G. Subramanyam, Capacitance of thin-film ferroelectrics under different drive signals, IEEE Transactions on Ultrasonics, Ferroelectrics, and Frequency Control. 56 (2009) 1861–1867. https://doi.org/10.1109/TUFFC.2009.1262.

[28] O. Emelyanov, A. Plotnikov, Ferroelectric capacitors in pulsed modes: Experimental study and analytical calculations, in: 2016 IEEE International Conference on Dielectrics (ICD), 2016: pp. 893–896. https://doi.org/10.1109/ICD.2016.7547760.

[29] D. Mei, X. Zhu, Y.-L. He, J. D. Yan and X. Tu, Plasma-assisted conversion of CO_2 in a dielectric barrier discharge reactor: understanding the effect of packing materials, Plasma Sources Science and Technology. 24 (2015) 15011. https://doi.org/10.1088/0963-0252/24/1/015011.

[30] A. Gómez-Ramírez, V.J. Rico, J. Cotrino, A.R. González-Elipe, R.M. Lambert, Low Temperature Production of Formaldehyde from Carbon Dioxide and Ethane by Plasma-Assisted Catalysis in a Ferroelectrically Moderated Dielectric Barrier Discharge Reactor, ACS Catalysis. 4 (2014) 402–408. https://doi.org/10.1021/cs4008528.

[31] W.-C. Chung, K.-L. Pan, H.-M. Lee, M.-B. Chang, Dry reforming of methane with dielectric barrier discharge and ferroelectric packed-bed reactors, Energy and Fuels. 28 (2014) 7621–7631. https://doi.org/10.1021/ef5020555.

[32] V.J. Rico, J.L. Hueso, J. Cotrino, A.R. González-Elipe, Evaluation of Different Dielectric Barrier Discharge Plasma Configurations as an Alternative Technology for Green C1 Chemistry in the Carbon Dioxide Reforming of Methane and the Direct Decomposition of Methanol, The Journal of Physical Chemistry A. 114 (2010) 4009–4016. https://doi.org/10.1021/jp100346q.

[33] D. Ray, Ch. Subrahmanyam, CO_2 decomposition in a packed DBD plasma reactor: influence of packing materials, RSC Advances. 6 (2016) 39492–39499. https://doi.org/10.1039/C5RA27085E.

[34] W. Lu, Y. Abbas, M.F. Mustafa, C. Pan, H. Wang, A review on application of dielectric barrier discharge plasma technology on the abatement of volatile organic compounds, Frontiers of Environmental Science & Engineering. 13 (2019) 30. https://doi.org/10.1007/s11783-019-1108-5.

[35] A. Gómez-Ramírez, A.M. Montoro-Damas, J. Cotrino, R.M. Lambert, A.R. González-Elipe, About the enhancement of chemical yield during the atmospheric plasma synthesis of ammonia in a ferroelectric packed bed reactor, Plasma Processes and Polymers. 14 (2017). https://doi.org/10.1002/ppap.201600081.

[36] L. Jin, *Broadband Dielectric Response in Hard and Soft PZT: Understanding Softening and Hardening Mechanisms*, Lausanne: École Polytechnique Fédérale de Lausanne (EPFL), 2011.

[37] K.C. Kao, 4 - Ferroelectrics, Piezoelectrics, and Pyroelectrics, in: K.C.B.T.-D.P. in S. Kao (Ed.), Academic Press, San Diego, 2004: pp. 213–282. https://doi.org/https://doi.org/10.1016/B978-012396561-5/50014-1.

[38] C.-C. Chung, *Microstructural Evolution in Lead Zirconate Titanate (PZT) Piezoelectric Ceramics*, Connecticut: University of Connecticut, 2014.

[39] M. W. Hooker (1998), Properties of PZT-Based Piezoelectric Ceramics Between -150 and 250°C, National Aeronautics and Space Administration (NASA), Langley Research Center.

[40] A.M. Vandenbroucke, R. Morent, N. De Geyter, C. Leys, Non-thermal plasmas for non-catalytic and catalytic VOC abatement, Journal of Hazardous Materials. 195 (2011) 30–54. https://doi.org/https://doi.org/10.1016/j.jhazmat.2011.08.060.

[41] J.-L. Liu, Z. Li, J.-H. Liu, K. Li, H.-Y. Lian, X.-S. Li, X. Zhu, A.-M. Zhu, Warm-plasma catalytic reduction of CO_2 with CH_4, Catalysis Today. 330 (2019) 54–60. https://doi.org/https://doi.org/10.1016/j.cattod.2018.05.046.

[42] P. Barboun, P. Mehta, F.A. Herrera, D.B. Go, W.F. Schneider, J.C. Hicks, Distinguishing Plasma Contributions to Catalyst Performance in Plasma-Assisted Ammonia Synthesis, ACS Sustainable Chemistry & Engineering. 7 (2019) 8621–8630. https://doi.org/10.1021/acssuschemeng.9b00406.

[43] N.M. Alford and S.J. Penn, Sintered alumina with low dielectric loss, Journal of Applied Physics. 80 (1996) 5895–5898. https://doi.org/10.1063/1.363584.

[44] R. Doering and Y. Nishi (2008), Handbook of Semiconductor Manufacturing Technology, 2nd ed, CRC Press, https://doi.org/10.1201/9781420017663.

[45] G. Arlt, D. Hennings, G. de With, Dielectric properties of fine-grained barium titanate ceramics, Journal of Applied Physics. 58 (1985) 1619–1625. https://doi.org/10.1063/1.336051.

[46] Q.M. Zhang, H. Wang, N. Kim, L.E. Cross, Direct evaluation of domain-wall and intrinsic contributions to the dielectric and piezoelectric response and their temperature dependence on lead zirconate-titanate ceramics, Journal of Applied Physics. 75 (1994) 454–459. https://doi.org/10.1063/1.355874.

[47] A. Von Hippel, Ferroelectricity, domain structure, and phase transitions of barium titanate, Reviews of Modern Physics. 22 (1950) 221–237. https://doi.org/10.1103/RevModPhys.22.221.

[48] N. Ashcroft and D.N. Mermin (1976), Solid state physics, Saunders College Publishing.

[49] S. Devi and A.K. Jha, Dielectric and complex impedance studies of $BaTi_{0.85}W_{0.15}O_{3+\delta}$ ferroelectric ceramics, Bulletin of Materials Science. 33 (2010) 683–690. https://doi.org/10.1007/s12034-011-0144-y.

[50] F.J. Garcia-Garcia, Y. Tang, F.J. Gotor, M.J. Sayagués, Development by Mechanochemistry of $La_{0.8}Sr_{0.2}Ga_{0.8}Mg_{0.2}O_{2.8}$ Electrolyte for SOFCs, Materials. 13 (2020) 1366. https://doi.org/10.3390/ma13061366.

[51] J.F. Rubinson, Y.P. Kayinamura, Charge transport in conducting polymers: insights from impedance spectroscopy, Chemical Society Reviews. 38 (2009) 3339–3347. https://doi.org/10.1039/B904083H.

[52] Peeters, F., & Butterworth, T. (2018). Electrical Diagnostics of Dielectric Barrier Discharges. In A. Nikiforov, & Z. Chen (Eds.), Atmospheric Pressure Plasma - from Diagnostics to Applications. IntechOpen. https://doi.org/10.5772/intechopen.80433.

[53] A. Gómez-Ramírez, J. Cotrino, R.M. Lambert, A.R. González-Elipe, Efficient synthesis of ammonia from N_2 and H_2 alone in a ferroelectric packed-bed DBD reactor, Plasma Sources Science and Technology. 24 (2015). https://doi.org/10.1088/0963-0252/24/6/065011.

[54] E. Chiremba, K. Zhang, C. Kazak, G. Akay, Direct nonoxidative conversion of methane to hydrogen and higher hydrocarbons by dielectric barrier discharge plasma with plasma catalysis promoters, AIChE Journal. 63 (2017) 4418–4429. https://doi.org/10.1002/aic.15769.

[55] K. Zhang, G. Zhang, X. Liu, A.N. Phan, K. Luo, G. Akay, Correction to "A Study on CO_2 Decomposition to CO and O_2 by the Combination of Catalysis and Dielectric-Barrier Discharges at Low Temperatures and Ambient Pressure," Industrial & Engineering Chemistry Research. 59 (2020) 502. https://doi.org/10.1021/acs.iecr.9b06637.

[56] G. Akay, Sustainable Ammonia and Advanced Symbiotic Fertilizer Production Using Catalytic Multi-Reaction-Zone Reactors with Nonthermal Plasma and Simultaneous Reactive Separation, ACS Sustainable Chemistry & Engineering. 5 (2017) 11588–11606. https://doi.org/10.1021/acssuschemeng.7b02962.

[57] K.H.R. Rouwenhorst, Y. Engelmann, K. van 't Veer, R.S. Postma, A. Bogaerts, L. Lefferts, Plasma-driven catalysis: green ammonia synthesis with intermittent electricity, Green Chemistry. 22 (2020) 6258–6287. https://doi.org/10.1039/D0GC02058C.

[58] K. Zhang, G. Zhang, X. Liu, A.N. Phan, K. Luo, A Study on CO_2 Decomposition to CO and O_2 by the Combination of Catalysis and Dielectric-Barrier Discharges at Low Temperatures and Ambient Pressure, Industrial & Engineering Chemistry Research. 56 (2017) 3204–3216. https://doi.org/10.1021/acs.iecr.6b04570.

[59] P. Navascués, J.M. Obrero-Pérez, J. Cotrino, A.R. González-Elipe, A. Gómez-Ramírez, Unraveling Discharge and Surface Mechanisms in Plasma-Assisted Ammonia Reactions, ACS Sustainable Chemistry & Engineering. 8 (2020) 14855–14866. https://doi.org/10.1021/acssuschemeng.0c04461.

[60] G. Akay, Plasma Generating-Chemical Looping Catalyst Synthesis by Microwave Plasma Shock for Nitrogen Fixation from Air and Hydrogen Production from Water for Agriculture and Energy Technologies in Global Warming Prevention, Catalysts. 10 (2020) 152. https://doi.org/10.3390/catal10020152.

Chapter 5

Discharge and Surface Mechanisms in Plasma-assisted Ammonia Reactions*

5.1. Introduction

The study presented in this chapter is primarily driven by the need of improving the performance of the plasma-assisted ammonia synthesis in a scenario where, as discussed in **Chapter 1**, the catalytic Haber-Bosch (H-B) process is responsible for ca. 1.2% of the global CO_2 emissions [1]. The requisite of combining the reduction of energy consumption with the production of ammonia in a distributed way close to final users has called for an active investigation of alternative reaction processes, including plasma-catalysis [1–26]. Another motivation in this line is the use of ammonia as a suitable hydrogen storage vector and the advantages, with respect to classical catalysis [27–29], of small plasma reactors for its low-temperature decomposition into hydrogen, as required for mobile device applications.

Although remarkable reaction yields have been obtained for ammonia production during the last years (e.g., Akay and Zhang *et al* reported values of 12% using a silica-supported nickel catalyst [13] and Gómez-Ramírez *et al* [12] values of 7% in the absence of catalyst) the reported energy efficiencies are still far from those required to outperform the H-B process. Trying to approach this problem from a novel perspective, the present investigation proposes a first study at fundamental level of the ammonia synthesis and decomposition reactions. In particular, it has tried to determine the extent of intermediate plasma processes that, consuming energy, do not contribute to increasing the reaction yield. A

* The content of this chapter has been published in: **P. Navascués**, J.M. Obrero-Pérez, J. Cotrino, A.R. González-Elipe, A. Gómez-Ramírez, Unraveling Discharge and Surface Mechanisms in Plasma-Assisted Ammonia Reactions. *ACS Sustainable Chemistry & Engineering*, 8, 39 (2020) 14855–14866. https://doi.org/10.1021/acssuschemeng.0c04461

conceptual approach of determining the participation of these types of plasma processes has not been systematically used in the field of atmospheric-pressure plasmas, even if it could provide valuable information for improving the reactor design and the operational conditions.

To analyze the reaction mechanisms, an isotope labeling methodology has been applied in this study (see **Chapter 3**). This technique, although widely used in conventional catalysis, has been scarcely utilized in plasma-catalysis. Herein, the isotope labeling methodology has been applied to study mixtures of the type NH_3+D_2 and N_2+D_2+NH_3. From this analysis, it has been possible to detect the extent of the ammonia decomposition reaction (i.e., $2NH_3 \rightarrow N_2 + 3H_2$), as well as other inefficient hydrogen exchange processes occurring simultaneously to the ammonia synthesis. These processes detract plasma energy and contribute to the reduction of the energy efficiency of the synthesis process.

Additionally, it has been realized that the isotope labeling may provide information about reaction mechanisms taking place on the surface of the pellets. Processes of this type, accepted to occur in the plasma-catalytic synthesis of ammonia [30–36], have been discussed in different modeling studies [9,37], but scarcely analyzed experimentally (in this regard, it is noteworthy the study of Lea Winter *et al.*, who at the end of 2020 presented direct evidence of surface reactions and reaction intermediates using FTIR spectroscopy [38]). In this chapter, through the ignition of N_2+D_2 and N_2+H_2 mixtures it has been proved the occurrence of surface processes, for the latter mixture after prolonged exposure of the PZT barrier to a D_2 plasma, and in both cases following the H/D isotope distribution in the outlet gas mixture. The evolution of the isotope-labeled products, together with the analysis of the emission spectra of intermediate species formed in the plasma, have permitted to propose a series of reaction mechanisms, both in the plasma and on the surface of the moderator material that take place during the ammonia synthesis reaction.

In the curse of this investigation, it turned out that the interest in the ammonia decomposition reaction, initially investigated from the perspective of its impact on the efficiency of the ammonia-synthesis process, is of interest by itself under the perspective of the hydrogen production. Therefore, pure NH_3 plasmas have been ignited to analyze the hydrogen production rate and the energy efficiency of this process.

In the light of the conclusions reached in the present study, the ammonia synthesis and decomposition reactions have been separately studied in **Chapters 6 and 7** of this thesis, incorporating a Ru-based catalyst in the packed-bed reactor.

5.2. Experimental Details

In all the experiments discussed in this chapter, PZT has been used as discharge moderator. The experiments have been performed with two different barrier gaps of 3 and 10 mm filled with pellets with diameters between 0.5-2 mm and 2-3 mm, respectively. Regarding the electrical operating conditions, the voltage amplitude was varied between 2 and 4 kV, while the frequency was fixed at 5 kHz, if not otherwise stated. The reactor was operated at atmospheric pressure and ambient temperature, although a small thermal drift in temperature up to 40ºC was detected at the reactor walls after long operating periods.

In this study, N_2, H_2, D_2, and NH_3 have been used as inlet gases. The following mixtures have been studied: N_2+H_2, N_2+D_2, N_2+D_2+NH_3, NH_3+D_2, and NH_3+N_2. Pure discharges of NH_3, N_2 and D_2 have been also ignited. The gas flow was varied between 2.9 and 8.2 sccm for N_2, between 1.5 and 25.8 sccm for D_2 (H_2), and between 1.2 and 9 sccm for NH_3. The gas ratio was 1:3 and 2:3 for the N_2:H_2 and NH_3:D_2 mixtures, respectively. For the ternary mixture (NH_3+N_2+D_2), the N_2:D_2 ratio was fixed at 1:3 and the NH_3 flow rate at 3.7 sccm. Therefore, to evaluate the effect of the residence time on the reaction mechanisms, the total gas flow rate of reactants was varied while keeping constant the mentioned proportion between gas mixture components.

Hereafter, molecules, compounds, and molecular fragments are designated with their formulas, considering the presence of either H or D atoms in their structure (e.g., HD, ND_2H, etc.). However, the terms *hydrogen* and *ammonia* in cursive script are used when referring to the complete set of labeled molecules of each specific compound. For more details about the fundamentals of the isotope labeling methodology see **Chapter 3**.

5.3. Results and Discussion

5.3.1. Ammonia Decomposition and Hydrogen Production

In previous studies from our research group it was demonstrated that experimental parameters such as the electrical input or the residence time of the gases affect the performance of the ammonia synthesis reaction in N_2+H_2 plasmas [11,12]. For example, as the residence time increases, besides the ammonia synthesis reaction, other plasma processes inefficient to produce ammonia may be favored. One of these inefficient processes is the partial decomposition of the previously formed ammonia into nitrogen and hydrogen. In terms of the classical H-B catalytic synthesis of ammonia, which is controlled by thermodynamics, ammonia decomposition implies the back-transformation of products into reactants, a process that would occur up to redressing the equilibrium conditions if these had been altered (e.g., by changing pressure or removing reactants). However, in plasma-catalysis the processes do not reach equilibrium and it is better to refer to them as reactions in two directions than as reversible reactions. Nonetheless, if ammonia decomposes into N_2 and H_2, it will reduce the total ammonia synthesis rate and the energy efficiency of the ammonia production process. However, promoting the ammonia decomposition process would be desirable if the interest resides in the hydrogen production.

Herein, pure ammonia plasmas have been ignited to investigate the capability of our reactor for hydrogen production. The obtained results are shown in **Figure 5.1** and **Table 5.1**. Data in this figure show that more than 30% of the pure ammonia fed into the reactor can be decomposed in this experiment. In addition, the decomposition yield only decreased by 7-8% for a three times higher flow. It is noteworthy that the energy efficiency for hydrogen production in this experiment is similar or even higher than the yields previously reported by our research group for the wet reforming of methane in the same reactor [39].

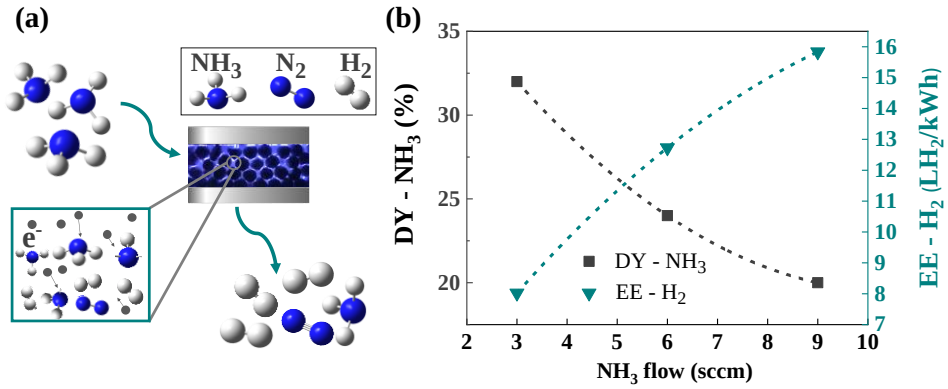

Figure 5.1. (a) Scheme of the decomposition of ammonia indicating that three H_2 and one N_2 molecules are formed by the decomposition of two ammonia molecules due to plasma processes triggered by the interaction with plasma electrons (see the square inset for illustration). (b) Plots of NH_3 Decomposition Yield (DY-NH_3) and Energy Efficiency for H_2 production (EE-H_2) versus NH_3 flow rate. The experiments were carried out at a frequency of 5 kHz and a voltage amplitude of 2 kV (consumed power 10 ± 1 W) with a PZT barrier of 3 mm.

The relatively high energy efficiency of the decomposition reaction supports that the process $N_2 + H_2 \Leftrightarrow NH_3$, readily occurs in the two directions in the packed-bed plasma reactor when igniting N_2+H_2 plasmas and that electron interactions with either NH_3, N_2, or H_2 is likely the main mechanistic factor controlling yields and efficiencies. This assessment is also supported by the decomposition yield and energy efficiency values found for NH_3+N_2 and NH_3+H_2 mixtures as summarized in **Table 5.1**. Since values of these two parameters were similar for pure NH_3 and a mixture of NH_3+N_2 (1:2 ratio), it can be concluded that plasma electrons preferentially activate ammonia over nitrogen molecules. However, data in this table for the NH_3+H_2 (2:3 ratio) mixture reveal a net loss of energy efficiency, suggesting that hydrogen competes more efficiently than nitrogen (and as efficiently as ammonia) for the plasma electrons. This inference agrees with the lower impact dissociation energy of H_2 vs. N_2 (4.5 eV [40] and 9.8 eV [41], respectively) and its relatively lower ionization threshold energy (13.6 eV [40] and 15.6 eV [42], respectively]). This experiment with NH_3+H_2 mixtures also suggests that hydrogen radicals or excited di-hydrogen species may be very reactive. They can recombine with hydrogen atoms in the ammonia molecules or fragments, i.e., leading to exchange processes that do not contribute to increasing the decomposition yield and, therefore, reducing the energy efficiency for H_2 production. This would occur through a series of *inefficient reaction events* that do

not contribute to the net formation of hydrogen molecules. These events will be studied in the next sections of this chapter using the isotope labeling technique with mixtures of NH_3+D_2 and N_2+D_2+NH_3.

Table 5.1. Ammonia Decomposition Yield (DY-NH_3) and Energy Efficiency associated with H_2 production (EE-H_2) for pure NH_3 plasmas and mixtures of this gas with N_2 or H_2. The current amplitude was kept constant at 25 mA.

Gas or mixture	Total flow rate (sccm)	DY-NH_3 (%)	EE-H_2 (LH_2/kWh)
NH_3 $^{(*)}$	3	32	8.0
	6	24	13
	9	20	16
NH_3 +N_2 $^{(*)}$	9 (ratio 1:2)	19	16
NH_3 + H_2 $^{(**)}$	9 (ratio 2:3)	17	6.0

Experiments performed using a PZT barrier of $^{(*)}$ 3 mm and $^{(**)}$ 10 mm

5.3.2. Inefficient Reaction Mechanisms: Ammonia Decomposition vs. Hydrogen Atom Exchange (NH_3+D_2 Mixtures)

It has been mentioned in the previous section that hydrogen atom exchange processes between NH_3 and H_2(D_2) molecules are inefficient from the point of view of ammonia synthesis and decomposition reactions. To assess in detail the involved *reaction events*, a series of experiments have been carried out with NH_3+D_2 plasmas. A summary of the results obtained is reported in **Figure 5.2**. **Figure 5.2(a)** indicates a clear evolution in the intensity of the recorded *m/z* peaks as a function of power, showing a progressive decrease in the intensity of peaks associated to D_2 and NH_3 and an increase of those due to H_2, HD, NDH_2, and ND_2H. As illustrated by the schemes in **Figure 5.2(b),** this evolution sustains that isotopic exchange process of the type:

$$NH_3 + D_2 \rightarrow ND_XH_Y + HD\ (H_2) \quad (E\ 5.1)$$

become more likely with the applied plasma power.

From the analysis of the intensity of the different *m/z* peaks, it is possible to estimate the partition of the different labeled molecules in each compound (i.e., H_2, HD, and D_2 for *hydrogen* and NH_3, NDH_2, ND_2H, and ND_3 for *ammonia*). The

histogram plots in **Figures 5.2(c)** and **(d)** represent the percentages of the different labeled molecules as a function of plasma power for a fixed flow of reactants (9 sccm), or as a function of the total flow of reactants at constant power (9 ± 1 W).

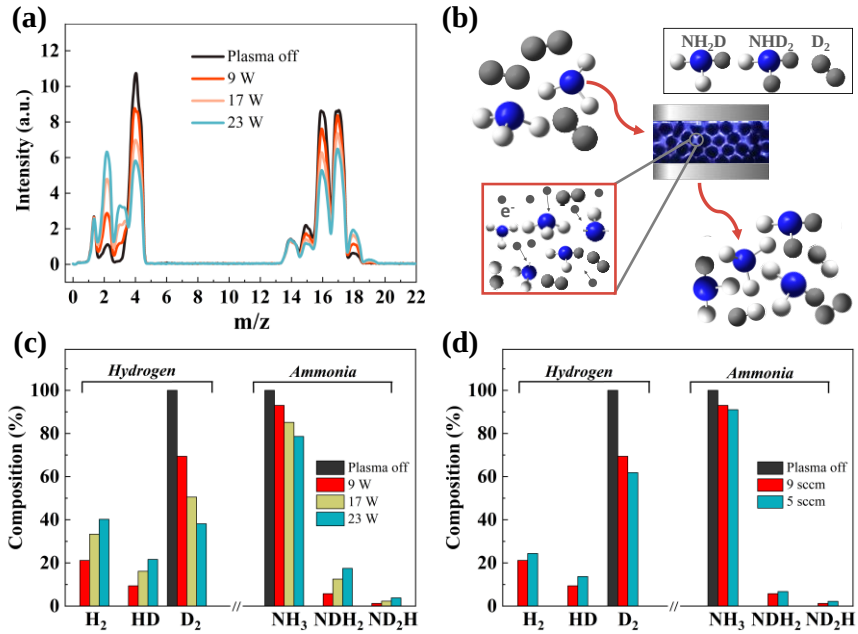

Figure 5.2. (a) Series of mass spectra recorded for plasma-activated NH_3+D_2 mixtures at increasing powers from 9 to 23 W (total flow fixed at 9 sccm). (b) Scheme showing plasma exchange processes leading to the formation of deuterium-labeled molecules of ammonia and hydrogen. (c) Histogram from (a), showing the percentage of the different molecules as a function of plasma power. (d) Idem as a function of total flow (power fixed at 9 ± 1 W). The experiments were carried out using a 10mm-PZT barrier at a frequency of 5 kHz and varying the voltage amplitude between 2.5 and 4 kV.

It can be observed that the amount of NH_3 and D_2 progressively decreases in the outlet gas mixture because they progressively exchange their constituent H/D atoms according to processes such as that represented in *E 5.1*. According to **Figures 5.2(c)** and **(d)**, these exchange *reaction events* are more frequent when increasing power and decreasing the reactant flow (i.e., increasing the residence time) and may produce up to 60% reduction of D_2 molecules in the total amount of *hydrogen* in the outlet mixture.

Additionally, it has been found a little but progressive increase with power in the *m/z=28* peak intensity, directly related to the formation of N_2, as indicated in the zoomed QMS spectra plotted in **Figure 5.3**. This evidence, as well as the

observed decrease in the total amount of *ammonia* molecules in the outlet with respect to the inlet flow, proves that a fraction of ammonia is effectively decomposed into nitrogen and hydrogen. **Table 5.2** summarizes the results for various experimental conditions. Data include the NH_3 decomposition yield and the partition between the "reacted" NH_3 molecules that have led to N_2 (and *hydrogen*) and the "reacted" NH_3 molecules that have exchanged H by D. It is interesting that, under certain conditions, more NH_3 molecules have undergone exchange processes (fifth column) than decomposition into N_2 and *hydrogen* (fourth column).

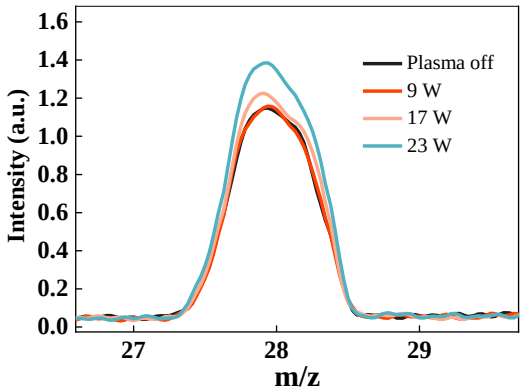

Figure 5.3. (a) Evolution with the increasing power of the *m/z=28* QMS signal for the NH_3+D_2 mixture (operating conditions similar to those in **Figure 5.2(a)**).

Moreover, **Table 5.2** shows that the fraction of NH_3 molecules decomposed into N_2 and *hydrogen* (HD can be formed through secondary processes) increases with power and decreases with the reactant flow, while the fraction of ammonia molecules that undergoes inefficient H-D exchange processes follows an opposite trend. From a practical point of view, these opposed tendencies show that *operating packed-bed reactors at high input powers and low flow rates favor the decomposition of ammonia into hydrogen and nitrogen with respect to the occurrence of hydrogen exchange reaction events.* This experimental evidence supports the direct involvement of high-energy plasma electrons in the decomposition of ammonia molecules, in agreement with the proposals of Hong *et al*. [2] for back-reactions during the plasma-catalytic synthesis of ammonia.

Table 5.2. Evolution of the ammonia decomposition yield and fractions of ammonia decomposed molecules and H-D exchange processes. Experimental conditions are similar to those in the experiments shown in **Figure 5.2**.

NH_3 flow rate (sccm)	**Power (±1 W)**	**DY-NH_3 (%)**	**Fraction of "reacted" NH_3 molecules decomposed into N_2 and *hydrogen***	**Fraction of "reacted" NH_3 molecules that have exchanged H by D**
9	9	0.24	0.03	0.97
	17	8.9	0.40	0.60
	23	17	0.49	0.51
5	9	12	0.47	0.53
3	5	11	0.58	0.42

5.3.3. *Hydrogen* Isotopic Exchange Reactions under Steady State Conditions (N_2+D_2+NH_3 Mixtures)

Mixtures of nitrogen, hydrogen, and ammonia represent the typical composition of outlet gases during both ammonia synthesis and decomposition experiments. The ternary inlet mixture N_2+D_2+NH_3 has been studied to quantitatively estimate to which extent hydrogen exchange and similar intermediate *reaction events* waste energy without contributing to the desired processes. Molecular ratios have been adjusted to avoid any net nitrogen reaction, i.e., adjusting the inlets in such a way that the inlet ratio N_2/NH_3 is the same as the outlet ratio $N_2/(NH_3+NDH_2+ND_2H+ND_3)$. Accordingly, for these conditions, the yield of *ammonia* formation is equivalent to that of *ammonia* decomposition. Such conditions were satisfied for inlet mixtures with a N_2:D_2 constant ratio of 1:3, a NH_3 flow of 3.7 sccm and total flows of 15, 27 and 38 sccm.

The bar diagrams in **Figure 5.4** show the partitions of the different labeled molecules in each compound (i.e., *hydrogen* or *ammonia*), either as a function of power or the total flow of reactants. The diagrams indicate that the relative concentrations of NDH_2 and ND_2H, as well as some hints of ND_3, increase with the consumed power (**Figure 5.4(a)**) and for smaller flow rates (**Figure 5.4(b)**). A similar tendency was found for the evolution of H_2 and HD molecules. These

results confirm that, under the investigated conditions, H-D exchange reactions are massively taking place with zero energy efficiency for the two plasma-assisted *ammonia reactions* of interest (synthesis and decomposition).

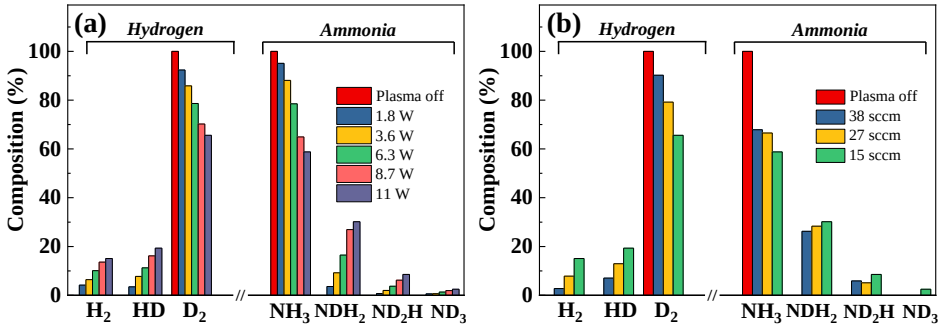

Figure 5.4. Percentages of the different *hydrogen* and *ammonia* molecules detected for the mixture N_2+D_2+NH_3 as a function of (a) the applied power (for V=2.5 kV, flow rate of 15 sccm, and frequencies between 1 and 5 kHz) and (b) the total input flow of reactants (i.e., 38, 27 and 15 sccm) for a consumed power of 11 ± 1 W (2.5 kV, 5 kHz). Experiments were carried out for a PZT barrier of 3 mm.

To more precisely assess how plasma energy is consumed in promoting plasma exchange reactions we apply the *Reaction Events* concept (RE, see **Chapter 3**). **Figure 5.5** shows the evolution of the different *Reaction Events* as a function of the total flow rate for an applied power of 11 W (same conditions as for the histogram in **Figure 5.4(b)**). In these plots, overall data are also provided for *hydrogen* production (i.e., the sum of RE leading to the formation of HD and H_2), for *ammonia* production (i.e., the sum of RE leading to the formation of NDH_2, ND_2H, and ND_3) and for the sum of these two *Reaction Events* (Total Reaction Events, TRE). Clearly, there is a progressive decrease in the number of inefficient *Reaction Events* when the total flow rate increases (i.e., when the residence time decreases).

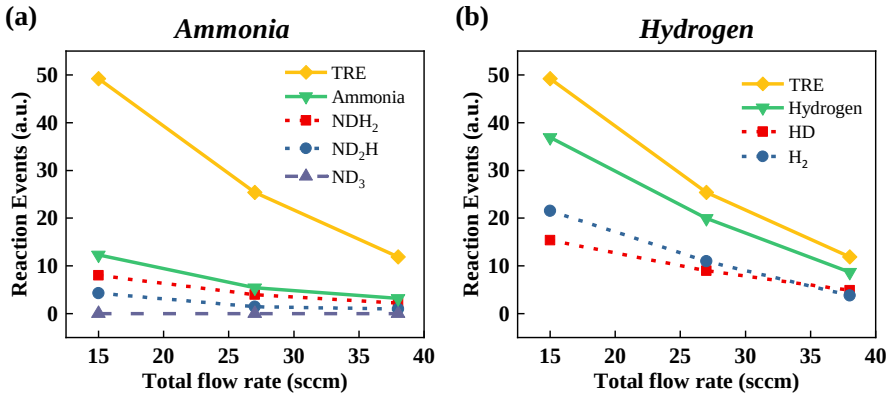

Figure 5.5. Representation of the number of *Reaction Events* for (a) *ammonia* and (b) *hydrogen* molecules detected in the outlet mixture during the analysis of the stationary mixture N_2+D_2+NH_3 as a function of the total flow rate. Experimental conditions were similar to those in **Figure 5.4(b)**.

Similarly, a progressive increase in the number of inefficient *Reaction Events* was found when increasing the consumed power, as shown in **Figure 5.6**. Interestingly, **Figures 5.5** and **5.6** show that hydrogen is more likely to undergo exchange RE than ammonia. This fact agrees with the results summarized in **Table 5.1** and the discussion thereof about the influence of hydrogen in the ammonia decomposition reaction. From a practical point of view, gathered *evidence suggests that a suitable strategy to increase the energy efficiency for the synthesis of ammonia would consist of properly adjusting the hydrogen flow, while if the objective is to decompose ammonia, produced hydrogen should be immediately removed from reaction medium after its formation* (e.g., using selective diffusion membranes) [43]. These conclusions agree with those of an article published by our research group in 2019 specifically focused on the use of the isotope labeling method to analyze N_2+D_2+NH_3 mixtures [22].

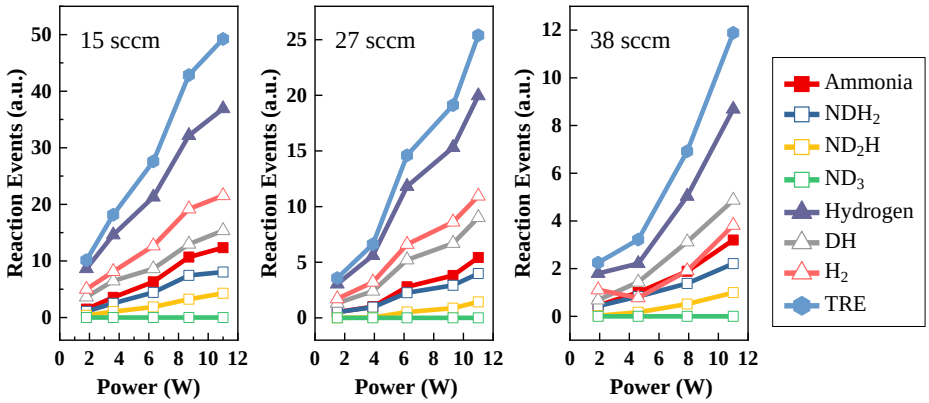

Figure 5.6. Representation of the number of *Reaction Events* for (left to right) 15, 27, and 38 sccm total flows during the analysis of the stationary mixture N_2+D_2+NH_3 as a function of applied power. Experimental conditions were similar to those in **Figure 5.4(a)**.

5.3.4. Intermediate Plasma Species During the Synthesis & Decomposition of Ammonia

Exchange *Reaction Events* taking place during the synthesis and the decomposition of ammonia must involve plasma excited species. The role of surface-adsorbed intermediates in these processes also forms part of the current models proposed to account for the plasma-catalytic synthesis of ammonia [9,37,44]. There is still much discussion in the literature about the relative importance of pure plasma processes vs. mechanisms mediated by the adsorption and surface reactions of gas species and plasma intermediates. Unlike conventional heterogeneous catalysis, where *in situ* and *in operando* techniques for the characterization of intermediate adsorbed species are well established, in plasma-catalysis *in situ* analysis of these species has been scarcely developed and only exceptionally applied [38]. Therefore, the analysis of intermediate species is usually restricted to the plasma phase, most commonly using OES measurements.

Trying to shed some light on the reaction mechanisms for *ammonia reactions* under our experimental conditions, we carried out a systematic analysis by OES of the NH_3+D_2 mixture studied in **section 5.3.2**. Typical OES spectra of this mixture as a function of power are shown in **Figure 5.7(a)**, where the emission bands can be attributed to excited states of N_2^* and $NH^*(ND^*)$ [45]. This assignment relies on similar plasma investigations where signals between 290-385

nm were attributed to the second positive system of N_2^* [$C^3\Pi \rightarrow B^3\Pi$] and the signal at 336.0 nm to NH^* species [$A^3\Pi \rightarrow X^3\Sigma^-$] [11,12]. The detection of these bands confirms that these species are formed in the plasma, although other excited species formed might not be detected by OES. Interestingly, unlike the spectra recorded for N_2+H_2 mixtures [11,12], no hints at 391.4 nm and 427.8 nm can be attributed to N_2^+ excited species [$B^2\Sigma_u^+ \rightarrow X^2\Sigma_g^+$].

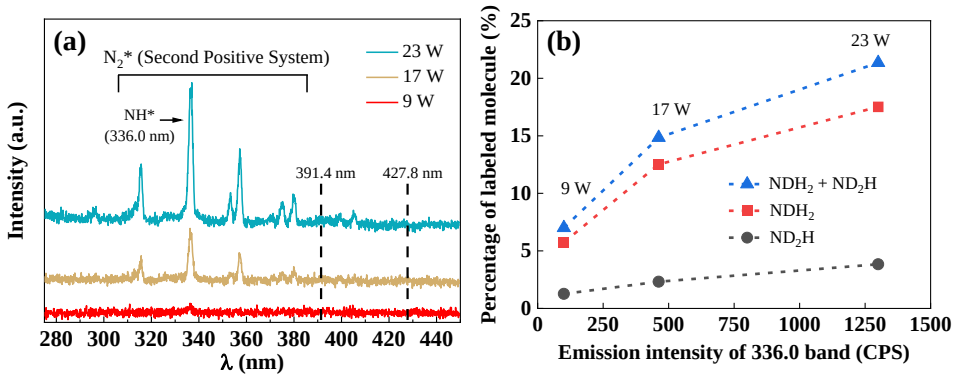

Figure 5.7. (a) OES spectra recorded for the NH_3+D_2 plasma mixture (same conditions that in **Figures 5.2(a)** and **(c)**) as a function of the applied power. (b) Plot of the percentage of ammonia molecules containing deuterium (data taken from **Figure 5.2(c)**) against the intensity of the 336.0 nm band (associated with NH^*) for the indicated applied powers.

The slight increase in the spectral background at lower wavelengths observed in the high-power (23 W) spectrum in **Figure 5.7(a)** can be related to the presence of excited deuterium species (D_2^*) in the plasma. This characteristic emission of H_2 (or D_2) [46] is very common in N_2+H_2 (D_2) plasmas, as illustrated in **Figure 5.8** for the OES spectra of a N_2+D_2 (1:3) mixture.

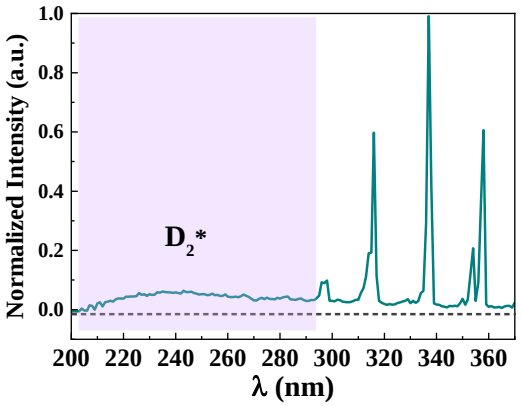

Figure 5.8. Emission spectrum of a N_2+D_2 (1:3) plasma for the following operating conditions: PZT barrier of 10 mm, total flow rate of 12 sccm, 5 kHz, 4 kV, and 42 W. The horizontal dashed line at y = 0 is drawn to highlight the spectrum background.

The progressive formation of NH^*(ND^*) species as the power increases and its correlation with the detected percentage of labeled molecules NDH_2 and ND_2H (c.f., **Figure 5.7(b)**) suggests that deuterium exchange reactions are involved in the formation of NH^* (ND^*) and NH_2^* (ND_2^* or NDH^*) intermediate radicals via processes *E 5.2 - E 5.6*, implying the initial formation of NH^* and NH_2^*:

$$NH_3 + e^- \rightarrow NH^* + 2H^* \quad (E\ 5.2)$$

$$NH_3 + e^- \rightarrow NH_2^* + H^* \quad (E\ 5.3)$$

Then, once NH^* and NH_2^* radicals are formed, it is likely their interaction with D_2 according to:

$$NH^* + D_2 \rightarrow NDH^* + D^* \quad (E\ 5.4)$$

$$NH_2^* + D_2 \rightarrow NDH_2 + D^* \quad (E\ 5.5)$$

or, in a second step:

$$NDH^* + D_2 \rightarrow ND_2H + D^* \quad (E\ 5.6)$$

The fact that OES detects the emission of NH^*(ND^*) but not of NH_2^* (ND_2^*, NDH^*) suggests a higher reactivity and a shorter lifetime for NH_2^* species; in other words, that reactions *E 5.5* and *E 5.6* should be very fast, drastically contributing to removing these intermediate species from the plasma. Previous investigations in other types of plasmas as inductively coupled radiofrequency discharges [47] or

plasma jets [48] also support a higher stability for NH^* species with respect to NH_2^*.

In addition, D^* radicals probably formed by electron-impact dissociation (*E 5.7*) are expected to react with NH_3 (NDH_2, ND_2H) molecules and contribute to isotopic exchange processes such as:

$$D_2 + e^- \rightarrow 2D^* \quad (E\ 5.7)$$

$$NH_3 + D^* \rightarrow NDH_2 + H^* \quad (E\ 5.8)$$

The drift in the spectral background in **Figure 5.7(a)** (and **Figure 5.8**) is an indirect evidence of dideuterium (dihydrogen) radicals formation but does not discard the occurrence of dissociation reactions [46]. In **Figure 5.7(a)**, the absence of spectral features due to N_2^+ species is noteworthy. The formation of this molecular ion has been reported in previous studies dedicated to the synthesis of ammonia in nitrogen-rich conditions (i.e., feeding the reactor with N_2 and H_2) [11,12]. The absence of this emission in NH_3+D_2 plasmas must be due to the relatively small concentration of nitrogen molecules formed in the mixture through ammonia decomposition, as well as the high electron energy required for the ionization of N_2 molecules (15.6 eV) [2].

This OES experiment strongly supports the occurrence of processes *E 5.2* - *E 5.6* in the plasma phase but does not provide any direct experimental evidence about the involvement of the barrier material in the reaction mechanisms. However, some inferences can be made based on the known reactivity of the different species involved in the process. For example, excited species and fragments of ammonia, such as NH^*, which are inferred by the OES analysis, can be adsorbed on the surface of the PZT pellets and subsequently react with surface-adsorbed hydrogen or deuterium atomic species. In this regard, it can be a reasonable assumption that the cross-section of a NH_XD_Y+H(D) direct reaction is higher if these species are adsorbed on a surface than if they collide in the plasma.

5.3.5. Surface vs. Plasma Reaction Mechanisms (N_2+H_2(D_2) Mixtures)

A key feature in plasma and plasma-catalysis reactions is to determine the involvement of surface-mediated processes. Although evidence of these processes exist for the low-pressure plasma-catalytic synthesis of ammonia [49] and are a common assumption in plasma-catalysis [50,51], there is little direct evidence about surface mechanisms and/or intermediate species participating in the reaction for a given experimental configuration, i.e., without varying the initial reactor configuration (for example, adding a catalyst) [38]. Herein, using the isotope labeling technique, it has been proved that, under the utilized experimental conditions, surface processes actively participate in the ammonia synthesis reaction.

In a first experiment, using a mixture N_2+D_2 (ratio 1:3), it has been found that besides the expected ND_3 molecules, labeled molecules such as NH_3, NDH_2, and ND_2H (together with HD) were detected in the outlet flow. The series of mass spectra in **Figure 5.9(a)** taken before and after igniting the plasma clearly show the formation of these labeled molecules upon plasma ignition. Analogously, the FTIR spectra in **Figure 5.9(b)** shows the appearance of bands attributed to NH_3 (3335 cm^{-1}), NDH_2 (2505 cm^{-1}), ND_2H (2558 cm^{-1}), and ND_3 (2420 cm^{-1}) species [52–54], whose intensity increases with the applied power [22].

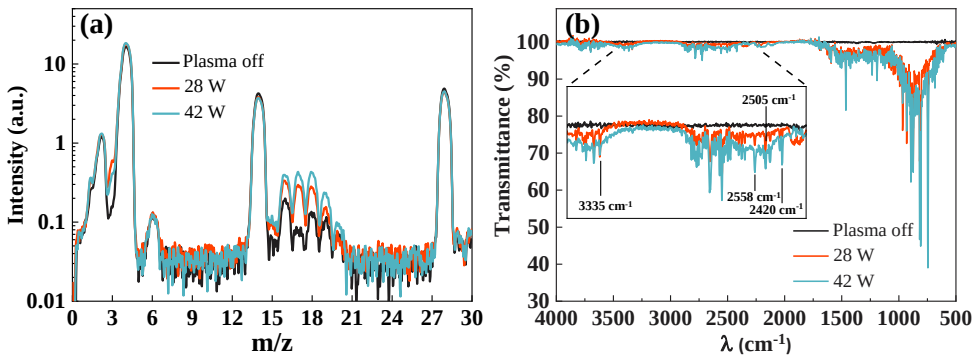

Figure 5.9. (a) QMS and (b) FTIR spectra taken at increasing consumed powers for the N_2+D_2 mixture ignited under the following operating conditions: PZT barrier of 10 mm, total flow rate of 12 sccm, frequency of 5 kHz, and voltage amplitudes of 3.4 (28 W) and 4 kV (42 W).

In this experiment, it has been found that the partition of labeled molecules changed with the total flow of gases (see **Table 5.3**). For the lowest flow rate, the concentration of H-containing molecules was higher, showing that H atoms – apparently from an unknown source inside the reactor – intervene in the ammonia synthesis reaction (these H atoms can proceed from the PZT barrier). On the one hand, these hydrogen atoms can react with ND^* or ND_2^* excited species (or these species in the ground state) of the plasma by direct interaction according to an Eley-Rideal (E-R) mechanism. On the other hand, the plasma species can be adsorbed on the surface where they may react with hydrogen atoms and lead to the formation of partially deuterated ammonia according to a Langmuir-Hinshelwood (L-H) mechanism:

$$ND^* \text{ (s or plasma phase)} + H(s) \rightarrow NDH^*(s) \quad (E\ 5.9)$$

$$NDH^* \text{ (s or plasma phase)} + H(s) \rightarrow NDH_2 \quad (E\ 5.10)$$

$$ND_2^* \text{ (s or plasma phase)} + H(s) \rightarrow ND_2H \quad (E\ 5.11)$$

where (s) denotes adsorbed species and A^* denotes that the species can be in electronically excited states.

Reactions *E 5.9* - *E 5.11* take place on the surface and can occur simultaneously as similar processes in the plasma phase. The evolution of ND_XH_Y concentration as a function of the flow rate (**Table 5.3**) permits one to assess qualitatively the relative importance of surface-mediated versus direct plasma interactions as responsible for each process. For example, the fact that the NDH_2 relative concentration was higher for a lower reactant flow rate (i.e., for longer residence times) suggests that reaction steps *E 5.9* and *E 5.10* at the surface are more likely to occur under these conditions. This possibility agrees with the common assumption in plasma-catalysis about the longer time-scale of surface reactions with respect to other processes in the plasma phase [55]. Accordingly, the relatively higher concentration of ND_2H with respect to NDH_2 found at higher flow rates (i.e., shorter residence times) seems to indicate that surface processes are less probable for these conditions. Therefore, the formation of ammonia through the intervention of ND_2 intermediate species is more likely to occur for shorter residence times, either directly in the plasma phase or through a one-step E-R mechanism (*E 5.11*).

Table 5.3. Percentages of the different *ammonia* molecules detected one hour after igniting the plasma for two input flow rates of N_2+D_2 (ratio 1:3). Experiments were carried out using a PZT barrier of 10 mm, at 5 kHz and 4 kV (42 W).

Total flow rate of N_2+D_2	**12 sccm**	**34 sccm**
Molecular specie	Relative (%)	Relative (%)
ND_3	7	60
ND_2H	22	28
NDH_2	42	1
NH_3	29	11

A complementary experiment to check the previous hypothesis about surface processes was carried out as follows. First, a 10mm-PZT barrier was exposed for 3 hours to a plasma of pure deuterium. During the treatment, as reported in **Figure 5.10**, the QMS spectrum showed the formation of HD molecules, indicating the existence of H-D exchange processes. Reaching this point, the experiment suggested that, before plasma ignition, there were H atoms and –OH groups incorporated in the bulk and on the surface of the pellets, respectively.

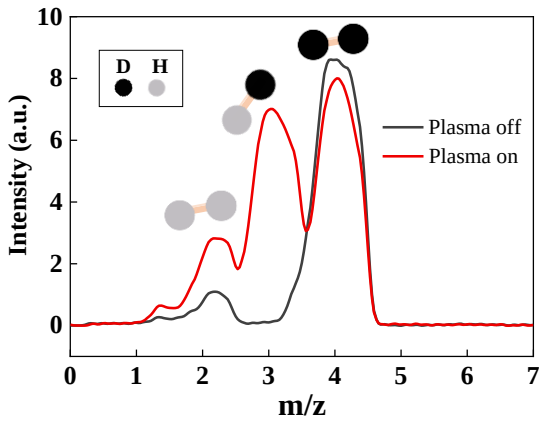

Figure 5.10. QMS spectra recorded before and during the D_2 plasma activation of the PZT barrier. Operating conditions: PZT barrier of 10 mm, D_2 flow rate of 1.5 sccm, 4 kHz, 3.7 kV, and average consumed power of 23 W.

The experiment continued with the verification that, upon subsequently igniting a plasma of pure N_2, no traces of *ammonia* molecules could be detected (**Figure 5.11(a)**). However, when shortly thereafter a N_2+H_2 plasma was ignited, NDH_2 and ND_2H molecules were detected by mass spectrometry (see **Figure 5.11(b)**). These findings confirm the involvement of deuterium, probably incorporated in the ferroelectric pellets, in the generation of D-labeled ammonia molecules. Therefore, the three following hypotheses can be proposed: (1) a source of hydrogen exists in the PZT pellets utilized to moderate *ammonia reactions*, (2) this hydrogen can be mobilized when the pellets are exposed to a plasma containing either H_2 or D_2, and (3) H/D exchange reactions between the plasma gas and the surface may take place for N_2+H_2(D_2) plasmas.

A condition enabling these three working hypotheses is the incorporation of hydrogen or deuterium atoms into the PZT pellets when they are exposed to a *hydrogen* plasma. Under these conditions, the direct interaction of PZT with H(D) radicals and, possibly, molecular *hydrogen* and excited states of the molecule, seems to promote the incorporation of H(D) onto the surface (e.g., in the form of –OH/D groups), and likely also in the interior of the PZT pellets. Although the mechanisms for such a hydrogen plasma-driven incorporation process are still unknown, it is noteworthy that atomic hydrogen can be incorporated in PZT by thermal or electrochemical treatments [56,57]. According to the literature, the capacity of PZT to incorporate hydrogen is very high and can amount to one atom per lattice octahedral unit of its structure (i.e., a maximum 1H:1Pb ratio) [58,59].

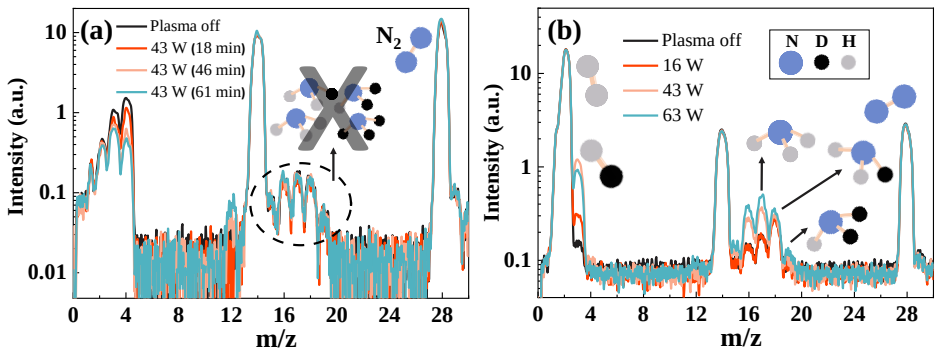

Figure 5.11. (a) QMS spectra for N_2 plasma (3 sccm of N_2; 5 kHz, 4.3 kV, 43 W) taken at different times after the ignition of the D_2-plasma during 3h. Note that signals m/z=2 and m/z=3 decrease with time because they are residual species present in the QMS chamber from the previous activation experiment. (b) Idem for N_2+H_2 plasma

(total flow of 34 sccm; 5 kHz, and voltage amplitudes between 3.3 and 4.1 kV) after the subsequent ignition of the D_2 and the N_2 plasmas.

Therefore, considering the absence of ammonia after the ignition of the pure-N_2 plasma over deuterium-saturated PZT, we propose that nitrogen dissociation and excitation, as well as the formation of NH^* and NH_2^* species, which are reaction intermediates for the synthesis of ammonia, occur mainly in the plasma phase according to processes such as:

$$N_2 + e^- \rightarrow N_2^* + e^- \quad (E\ 5.12)$$

$$N_2^* + N_2^* \rightarrow N + N + N_2^* \quad (E\ 5.13)$$

$$N_2 + e^- \rightarrow N^* + N^* + e^- \quad (E\ 5.14)$$

$$H_2 + e^- \rightarrow H_2^* + e^- \quad (E\ 5.15)$$

$$N^* + H_2^* \rightarrow NH^* + H \quad (E\ 5.16)$$

$$NH^* + H_2^* \rightarrow NH_2 + H \quad (E\ 5.17)$$

where A^* species indicate that they can be electronically excited.

Although processes *E 5.12- E 5.17* are proposed to occur in the plasma phase, the discussed experiment proves that alternative processes can also take place on the surface. For example, the dissociative surface adsorption of *hydrogen* or other molecular excited species [37], as well as the *hydrogenation* of reaction intermediates (NH and NH_2) [51]. It is accepted that the formation of NH or NH_2 intermediates may also involve N_2^+ species, which are usually detected by OES in N_2+H_2 plasmas [11], and could interact with H_2^* in the plasma according to:

$$N_2^{+*} + H_2^* \rightarrow 2\ NH^* \quad (E\ 5.18)$$

The direct interaction of N_2^{+*} with the surface might also lead to the generation of activated adsorbed species of nitrogen (i.e., $N^*(s)$). Nevertheless, since no ammonia was detected when PZT pellets containing hydrogen/deuterium were exposed to a plasma of pure N_2 (**Figure 5.11(a)**), dissociative adsorption of nitrogen molecules must be discarded under these experimental conditions.

5.4. Overview of the Reaction Mechanisms for the Ammonia Synthesis in a PZT-moderated Packed-bed Reactor

The scheme in **Figure 5.12** systematizes the most probable surface reaction pathways involved in the ammonia synthesis reaction under our experimental conditions. They have been proposed based on the previous results and considerations. However, it should be mentioned that the processes in this scheme do not disregard the occurrence of pure plasma reactions with the same results. Therefore, according to reactions *E 5.12 - E 5.17*, the NH^* and NH_2^* intermediates formed in the plasma become adsorbed or directly interact with atomic hydrogen species attached onto the surface of PZT.

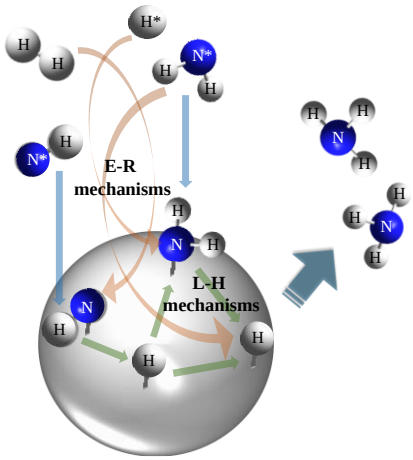

Figure 5.12. Scheme of reaction mechanism leading to the ammonia synthesis in the PZT-moderated packed-bed reactor. Orange arrows indicate Eley-Rideal mechanisms while green ones Langmuir-Hinshelwood mechanisms.

According to **Figure 5.12** both E-R and L-H type surface mechanisms may be involved in the ammonia synthesis, whereby NH^* and NH_2^* intermediates from the plasma can react with hydrogen atoms on the surface leading to the formation of ammonia (the former in a two-step hydrogenation process). This surface reaction model assumes that the rate-limiting step under our experimental conditions are: (1) the dissociation of nitrogen in the plasma (*E 5.12 - E 5.14*) and (2) the subsequent formation of NH^* and NH_2^* intermediates also in the plasma phase. This assumption is different than that of Aihara *et al.* [35]; these authors,

utilizing a completely different experimental configuration (therefore, a distinct electron energy distribution function) propose the dissociative surface adsorption of N_2 or N_2^* as the key process for ammonia synthesis. The dissociative adsorption of vibrationally excited states of the nitrogen molecule is also the mechanism proposed by Metha *et al.* [9,44,60], who studied the plasma-catalysis synthesis of ammonia at different temperatures. On the other hand, Akay and Zhang [13] proposed that both paths are possible (i.e., the nitrogen dissociation by electron impact in the plasma and the dissociative adsorption), working with Ni-based catalyst incorporated in a packed-bed reactor operated at 140ºC.

Although the results discussed in this chapter and summarized in **Figure 5.12**, corresponding to bare PZT, support that NH species are formed in the plasma as proposed by Hong *et al.* [37], the occurrence of other mechanisms cannot be discarded. For example, Metha *et al.* [9,60] have proved that the use of metal catalysts in the reactor can enhance ammonia production through the activation of surface mechanisms different from those proposed in the scheme of **Figure 5.12** (e.g., involving the dissociative adsorption of N_2). Therefore, in **Chapters 6 and 7** the ammonia synthesis and decomposition reactions have been studied introducing a metal catalyst into the ferroelectric packed-bed barrier.

5.5. Conclusions

The experiments discussed in this chapter have provided valuable information regarding both the ammonia synthesis and decomposition reactions in a PZT-moderated packed-bed reactor. On the one hand, the ignition of pure NH_3 plasmas has proved that the decomposition of ammonia can be a suitable and an energetically efficient process for hydrogen production. However, the isotope labeling method has shown that, besides the main reaction pathways, in NH_3+D_2 plasmas hydrogen exchange reactions consume energy but do not contribute to the hydrogen formation. These *inefficient Reaction Events* have also been detected when igniting N_2+D_2+NH_3 plasmas, simulating steady state conditions for the ammonia synthesis reaction. Therefore, the decomposition of an ammonia molecule previously formed is also interpreted as a back-reaction that contributes to reducing both the yield and the efficiency of the process. Valuable information regarding the power consumption or the residence time of the gases in the discharge has been deduced from isotope exchange experiments. Accordingly, proposals such as the selective separation of given reactants or products or the

control of the electrical and flow operating conditions have been suggested as possibilities to improve reaction yields and energy efficiencies of *ammonia reactions*.

In addition, we have shown that the combined use of plasma diagnosis and the isotope labeling methodology constitutes a powerful approach to analyze reaction mechanisms. In this line, it has been verified that, in addition to plasma reactions, plasma-surface interaction processes directly intervene in the ammonia synthesis reaction. In concrete, it has been verified that hydrogen atoms incorporated in the PZT pellets can appear in the outlet gases as resulting from surface exchange processes involving intermediate plasma species.

Finally, a scheme of reaction mechanisms has been proposed for the ammonia synthesis in the PZT-moderated packed-bed reactor. The dissociation of nitrogen molecules, as well as the formation of NH and NH_2 species in the plasma phase, have been proposed as rate-limiting steps of the synthesis process. According to the discussion of surface processes, it has been proposed that NH^* and NH_2^* intermediates formed in the plasma can be hydrogenated at the surface of the pellets following Eley-Rideal and Langmuir-Hinshelwood mechanisms to render NH_3 molecules.

5.5. References

[1] C. Smith, A.K. Hill, L. Torrente-Murciano, Current and future role of Haber–Bosch ammonia in a carbon-free energy landscape, Energy Environ. Sci. 13 (2020) 331–344. https://doi.org/10.1039/C9EE02873K.

[2] J. Hong, S. Prawer, A.B. Murphy, Plasma Catalysis as an Alternative Route for Ammonia Production: Status, Mechanisms, and Prospects for Progress, ACS Sustainable Chem. Eng. 6 (2018) 15–31. https://doi.org/10.1021/acssuschemeng.7b02381.

[3] P. Peng, P. Chen, C. Schiappacasse, N. Zhou, E. Anderson, D. Chen, J. Liu, Y. Cheng, R. Hatzenbeller, M. Addy, Y. Zhang, Y. Liu, R. Ruan, A review on the non-thermal plasma-assisted ammonia synthesis technologies, J. Clean. Prod. 177 (2018) 597–609. https://doi.org/10.1016/j.jclepro.2017.12.229.

[4] M.L. Carreon, Plasma catalytic ammonia synthesis: state of the art and future directions, J. Phys. D: Appl. Phys. 52 (2019) 483001. https://doi.org/10.1088/1361-6463/ab3b2c.

[5] Y. Gorbanev, E. Vervloessem, A. Nikiforov, A. Bogaerts, Nitrogen Fixation with Water Vapor by Nonequilibrium Plasma: toward Sustainable Ammonia Production, ACS Sustainable Chem. Eng. 8 (2020) 2996–3004. https://doi.org/10.1021/acssuschemeng.9b07849.

[6] J. Hong, M. Aramesh, O. Shimoni, D.H. Seo, S. Yick, A. Greig, C. Charles, S. Prawer, A.B. Murphy, Plasma Catalytic Synthesis of Ammonia Using Functionalized-Carbon Coatings in an Atmospheric-Pressure Non-equilibrium Discharge, Plasma Chem. Plasma Process. 36 (2016) 917–940. https://doi.org/10.1007/s11090-016-9711-8.

[7] W. Wang, B. Patil, S. Heijkers, V. Hessel, A. Bogaerts, Nitrogen Fixation by Gliding Arc Plasma: Better Insight by Chemical Kinetics Modelling, ChemSusChem. 10 (2017) 2145–2157. https://doi.org/10.1002/cssc.201700095.

[8] P. Peng, P. Chen, M. Addy, Y. Cheng, E. Anderson, N. Zhou, C. Schiappacasse, Y. Zhang, D. Chen, R. Hatzenbeller, Y. Liu, R. Ruan, Atmospheric Plasma-Assisted Ammonia Synthesis Enhanced via Synergistic Catalytic Absorption, ACS Sustainable Chem. Eng. 7 (2019) 100–104. https://doi.org/10.1021/acssuschemeng.8b03887.

[9] P. Mehta, P. Barboun, F.A. Herrera, J. Kim, P. Rumbach, D.B. Go, J.C. Hicks, W.F. Schneider, Overcoming ammonia synthesis scaling relations with plasma-enabled catalysis, Nat. Catal. 1 (2018) 269–275. https://doi.org/10.1038/s41929-018-0045-1.

[10] X. Zhu, X. Hu, X. Wu, Y. Cai, H. Zhang, X. Tu, Ammonia synthesis over γ-Al_2O_3 pellets in a packed-bed dielectric barrier discharge reactor, J. Phys. D: Appl. Phys. 53 (2020) 164002. https://doi.org/10.1088/1361-6463/ab6cd1.

[11] A. Gómez-Ramírez, J. Cotrino, R.M. Lambert, A.R. González-Elipe, Efficient synthesis of ammonia from N_2 and H_2 alone in a ferroelectric packed-bed DBD reactor, Plasma Sources Sci. Technol. 24 (2015) 065011. https://doi.org/10.1088/0963-0252/24/6/065011.

[12] A. Gómez-Ramírez, A.M. Montoro-Damas, J. Cotrino, R.M. Lambert, A.R. González-Elipe, About the enhancement of chemical yield during the atmospheric plasma synthesis of ammonia in a ferroelectric packed bed reactor, Plasma Process. Polym. 14 (2017) 1600081. https://doi.org/10.1002/ppap.201600081.

[13] G. Akay, K. Zhang, Process Intensification in Ammonia Synthesis Using Novel Coassembled Supported Microporous Catalysts Promoted by Nonthermal Plasma, Ind. Eng. Chem. Res. 56 (2017) 457–468. https://doi.org/10.1021/acs.iecr.6b02053.

[14] H.-H. Kim, Y. Teramoto, A. Ogata, H. Takagi, T. Nanba, Atmospheric-pressure nonthermal plasma synthesis of ammonia over ruthenium catalysts, Plasma. Process. Polym. 14 (2017) 1600157. https://doi.org/10.1002/ppap.201600157.

[15] P. Peng, Y. Cheng, R. Hatzenbeller, M. Addy, N. Zhou, C. Schiappacasse, D. Chen, Y. Zhang, E. Anderson, Y. Liu, P. Chen, R. Ruan, Ru-based multifunctional mesoporous catalyst for low-pressure and non-thermal plasma synthesis of ammonia, Int J. Hydrogen Energ. 42 (2017) 19056–19066. https://doi.org/10.1016/j.ijhydene.2017.06.118.

[16] B.S. Patil, *Plasma (catalyst) - assisted nitrogen fixation: reactor development for nitric oxide and ammonia production*, Eindhoven: Technische Universiteit Eindhoven, 2017.

[17] J.R. Shah, F. Gorky, J. Lucero, M.A. Carreon, M.L. Carreon, Ammonia Synthesis via Atmospheric Plasma Catalysis: Zeolite 5A, a Case of Study, Ind. Eng. Chem. Res. 59 (2020) 5167–5176. https://doi.org/10.1021/acs.iecr.9b05220.

[18] Y. Wang, M. Craven, X. Yu, J. Ding, P. Bryant, J. Huang, X. Tu, Plasma-Enhanced Catalytic Synthesis of Ammonia over a Ni/Al_2O_3 Catalyst at Near-Room Temperature: Insights into the Importance of the Catalyst Surface on the Reaction Mechanism, ACS Catal. 9 (2019) 10780–10793. https://doi.org/10.1021/acscatal.9b02538.

[19] J. Shah, W. Wang, A. Bogaerts, M.L. Carreon, Ammonia Synthesis by Radio Frequency Plasma Catalysis: Revealing the Underlying Mechanisms, ACS Appl. Energy Mater. 1 (2018) 4824–4839. https://doi.org/10.1021/acsaem.8b00898.

[20] M.B. Yaala, A. Saeedi, D.-F. Scherrer, L. Moser, R. Steiner, M. Zutter, M. Oberkofler, G.D. Temmerman, L. Marot, E. Meyer, Plasma-assisted catalytic formation of ammonia in N_2–H_2 plasma on a tungsten surface, Phys. Chem. Chem. Phys. 21 (2019) 16623–16633. https://doi.org/10.1039/C9CP01139K.

[21] J. Shah, F. Gorky, P. Psarras, B. Seong, D.A. Gómez-Gualdrón, M.L. Carreon, Enhancement of the Yield of Ammonia by Hydrogen-Sink Effect during Plasma Catalysis, ChemCatChem. 12 (2020) 1200–1211. https://doi.org/10.1002/cctc.201901769.

[22] P. Navascués, J.M. Obrero-Pérez, J. Cotrino, A.R. González-Elipe, A. Gómez-Ramírez, Isotope Labelling for Reaction Mechanism Analysis in DBD Plasma Processes, Catalysts. 9 (2019) 45. https://doi.org/10.3390/catal9010045.

[23] P. Barboun, P. Mehta, F.A. Herrera, D.B. Go, W.F. Schneider, J.C. Hicks, Distinguishing Plasma Contributions to Catalyst Performance in Plasma-Assisted Ammonia Synthesis, ACS Sustainable Chem. Eng. 7 (2019) 8621–8630. https://doi.org/10.1021/acssuschemeng.9b00406.

[24] P. Peng, Y. Li, Y. Cheng, S. Deng, P. Chen, R. Ruan, Atmospheric Pressure Ammonia Synthesis Using Non-thermal Plasma Assisted Catalysis, Plasma Chem. Plasma Process. 36 (2016) 1201–1210. https://doi.org/10.1007/s11090-016-9713-6.

[25] P. Peng, P. Chen, M. Addy, Y. Cheng, Y. Zhang, E. Anderson, N. Zhou, C. Schiappacasse, R. Hatzenbeller, L. Fan, S. Liu, D. Chen, J. Liu, Y. Liu, R. Ruan, In situ plasma-assisted atmospheric nitrogen fixation using water and spray-type jet plasma, Chem. Commun. 54 (2018) 2886–2889. https://doi.org/10.1039/C8CC00697K.

[26] J.R. Shah, *Non-thermal Plasma Catalytic Synthesis of Ammonia*, Tulsa: University of Tulsa, 2019.

[27] Y. Hayakawa, T. Miura, K. Shizuya, S. Wakazono, K. Tokunaga, S. Kambara, Hydrogen production system combined with a catalytic reactor and a plasma membrane reactor from ammonia, Int. J. Hydrogen Energ. 44 (2019) 9987–9993. https://doi.org/10.1016/j.ijhydene.2018.12.141.

[28] Y. Yi, L. Wang, Y. Guo, S. Sun, H. Guo, Plasma-Assisted ammonia decomposition over Fe–Ni alloy catalysts for CO_x-Free hydrogen, AIChE J. (2018) aic.16479. https://doi.org/10.1002/aic.16479.

[29] Yi Y., Wang L., Guo H. (2019) Plasma-Catalytic Decomposition of Ammonia for Hydrogen Energy. In: Tu X., Whitehead J., Nozaki T. (eds) Plasma Catalysis. Springer Series on Atomic, Optical, and Plasma Physics, vol 106. Springer, Cham. https://doi.org/10.1007/978-3-030-05189-1_7.

[30] B. Mingdong, B. Xiyao, Z. Zhitao, B. Mindi, Synthesis of Ammonia in a Strong Electric Field Discharge at Ambient Pressure, Plasma Chem. Plasma Process. 20 (2000) 511–520. https://doi.org/10.1023/A:1007031906589.

[31] Mindong Bai, Zhitao Zhang, Xiyao Bai, Mindi Bai, Wang Ning, Plasma synthesis of ammonia with a microgap dielectric barrier discharge at ambient pressure, IEEE Trans. Plasma Sci. 31 (2003) 1285–1291. https://doi.org/10.1109/TPS.2003.818761.

[32] T. Mizushima, K. Matsumoto, J. Sugoh, H. Ohkita, N. Kakuta, Tubular membrane-like catalyst for reactor with dielectric-barrier-discharge plasma and its performance in ammonia synthesis, Applied Catalysis A: General. 265 (2004) 53–59. https://doi.org/10.1016/j.apcata.2004.01.002.

[33] M. Bai, Z. Zhang, M. Bai, X. Bai, H. Gao, Synthesis of Ammonia Using CH_4/N_2 Plasmas Based on Micro-Gap Discharge under Environmentally Friendly Condition, Plasma Chem. Plasma Process. 28 (2008) 405–414. https://doi.org/10.1007/s11090-008-9132-4.

[34] M. Bai, Z. Zhang, M. Bai, X. Bai, H. Gao, Conversion of Methane to Liquid Products, Hydrogen, and Ammonia with Environmentally Friendly Condition-Based Microgap Discharge, J. Air Waste Manage. Assoc. 58 (2008) 1616–1621. https://doi.org/10.3155/1047-3289.58.12.1616.

[35] K. Aihara, M. Akiyama, T. Deguchi, M. Tanaka, R. Hagiwara, M. Iwamoto, Remarkable catalysis of a wool-like copper electrode for NH_3 synthesis from N_2 and H_2 in non-thermal atmospheric plasma, Chem. Commun. 52 (2016) 13560–13563. https://doi.org/10.1039/C6CC06752B.

[36] D. Xie, Y. Sun, T. Zhu, X. Fan, X. Hong, W. Yang, Ammonia synthesis and by-product formation from H_2O, H_2 and N_2 by dielectric barrier discharge combined with an Ru/Al_2O_3 catalyst, RSC Adv. 6 (2016) 105338–105346. https://doi.org/10.1039/C6RA21351K.

[37] J. Hong, S. Pancheshnyi, E. Tam, J.J. Lowke, S. Prawer, A.B. Murphy, Kinetic modelling of NH_3 production in N_2–H_2 non-equilibrium atmospheric-pressure plasma catalysis, J. Phys. D: Appl. Phys. 50 (2017) 154005. https://doi.org/10.1088/1361-6463/aa6229.

[38] L.R. Winter, B. Ashford, J. Hong, A.B. Murphy, J.G. Chen, Identifying Surface Reaction Intermediates in Plasma Catalytic Ammonia Synthesis, ACS Catal. 10 (2020) 14763–14774. https://doi.org/10.1021/acscatal.0c03166.

[39] A.M. Montoro-Damas, J.J. Brey, M.A. Rodríguez, A.R. González-Elipe, J. Cotrino, Plasma reforming of methane in a tunable ferroelectric packed-bed dielectric barrier discharge reactor, J. Power Sources. 296 (2015) 268–275. https://doi.org/10.1016/j.jpowsour.2015.07.038.

[40] Y.P. Zhang, C.H. Cheng, J.T. Kim, J. Stanojevic, E.E. Eyler, Dissociation Energies of Molecular Hydrogen and the Hydrogen Molecular Ion, Phys. Rev. Lett. 92 (2004) 203003. https://doi.org/10.1103/PhysRevLett.92.203003.

[41] D.C. Frost, C.A. McDowell, C.E.H. Bawn, The dissociation energy of the nitrogen molecule, Proceedings of the Royal Society of London. Series A. Mathematical and Physical Sciences. 236 (1956) 278–284. https://doi.org/10.1098/rspa.1956.0135.

[42] T. Trickl, E.F. Cromwell, Y.T. Lee, A.H. Kung, State-selective ionization of nitrogen in the $X^2\Sigma^+_g v_+=0$ and $v_+=1$ states by two-color (1+ 1) photon excitation near threshold, J. Chem. Phys. 91 (1989) 6006–6012. https://doi.org/10.1063/1.457417.

[43] S. Yun, S. Ted Oyama, Correlations in palladium membranes for hydrogen separation: A review, J. Membrane Sci. 375 (2011) 28–45. https://doi.org/10.1016/j.memsci.2011.03.057.

[44] P. Mehta, P.M. Barboun, Y. Engelmann, D.B. Go, A. Bogaerts, W.F. Schneider, J.C. Hicks, Plasma-Catalytic Ammonia Synthesis beyond the Equilibrium Limit, ACS Catal. 10 (2020) 6726–6734. https://doi.org/10.1021/acscatal.0c00684.

[45] R.W.B. Pearse and A.G. Gaydon (1965), The Identification of Molecular Spectra, 3rd ed., Chapman and Hall Ltd., England.

[46] K. Stapelmann, J.-W. Lackmann, I. Buerger, J.E. Bandow, P. Awakowicz, A H_2 very high frequency capacitively coupled plasma inactivates glyceraldehyde 3-phosphate dehydrogenase (GapDH) more efficiently than UV photons and heat combined, J. Phys. D: Appl. Phys. 47 (2014) 085402. https://doi.org/10.1088/0022-3727/47/8/085402.

[47] J.R. Shah, J.M. Harrison, M.L. Carreon, Ammonia Plasma-Catalytic Synthesis Using Low Melting Point Alloys, Catalysts. 8 (2018) 437. https://doi.org/10.3390/catal8100437.

[48] P.J. van den Oever, J.H. van Helden, C.C.H. Lamers, R. Engeln, D.C. Schram, M.C.M. van de Sanden, W.M.M. Kessels, Density and production of NH and NH_2 in an Ar–NH_3 expanding plasma jet, J. Appl. Phys. 98 (2005) 093301. https://doi.org/10.1063/1.2123371.

[49] K.S. Yin, M. Venugopalan, Plasma chemical synthesis. I. Effect of electrode material on the synthesis of ammonia, Plasma Chem. Plasma Process. 3 (1983) 343–350. https://doi.org/10.1007/BF00564632.

[50] A. Bogaerts, Q.-Z. Zhang, Y.-R. Zhang, K. Van Laer, W. Wang, Burning questions of plasma catalysis: Answers by modeling, Catal. Today. 337 (2019) 3–14. https://doi.org/10.1016/j.cattod.2019.04.077.

[51] K.H.R. Rouwenhorst, H.-H. Kim, L. Lefferts, Vibrationally Excited Activation of N_2 in Plasma-Enhanced Catalytic Ammonia Synthesis: A Kinetic Analysis, ACS Sustainable Chem. Eng. 7 (2019) 17515–17522. https://doi.org/10.1021/acssuschemeng.9b04997.

[52] M. Snels, L. Fusina, H. Hollenstein, M. Quack, The v_1 and v_3 bands of ND_3, Mol. Phys. 98 (2000) 837–854. https://doi.org/10.1080/00268970050025457.

[53] M. Snels, H. Hollenstein, M. Quack, The NH and ND stretching fundamentals of $^{14}ND_2H$, J. Chem. Phys. 119 (2003) 7893–7902. https://doi.org/10.1063/1.1592506.

[54] T. Shimanouchi, Tables of Molecular Vibrational Frequencies, in: NIST Standard Reference Database, USA, 1972.

[55] Kim HH., Teramoto Y., Ogata A. (2019) Plasma-Catalyst Interactions. In: Tu X., Whitehead J., Nozaki T. (eds) Plasma Catalysis. Springer Series on Atomic, Optical, and Plasma Physics, vol 106. Springer, Cham. https://doi.org/10.1007/978-3-030-05189-1_3.

[56] C.-K. Huang, T.-B. Wu, Plasma etching and hydrogen blocking characteristics of PtOx thin films in ferroelectric capacitor fabrication, Appl. Phys. Lett. 83 (2003) 3147–3149. https://doi.org/10.1063/1.1610250.

[57] K. Drogowska, S. Flege, D. Rogalla, H.-W. Becker, E. Ionescu, N.-T.H. Kim-Ngan, A.G. Balogh, Hydrogen content analysis in hydrogen-charged PZT ferroelectric ceramics, Solid State Ionics. 235 (2013) 32–35. https://doi.org/10.1016/j.ssi.2013.01.009.

[58] A.S. Mohammadabadi, Hydrogen-induced damage of lead-zirconate-titanate (PZT), University of British Columbia, 2013. https://doi.org/10.14288/1.0073678.

[59] M. Liyanage, R. Miller, R. Rajapakse, First principles study of hydrogen in lead zirconate titanate, Smart Mater. Struct. 28 (2019) 034002. https://doi.org/10.1088/1361-665X/aafeed.

[60] P. Mehta, P. Barboun, D.B. Go, J.C. Hicks, W.F. Schneider, Catalysis Enabled by Plasma Activation of Strong Chemical Bonds: A Review, ACS Energy Lett. 4 (2019) 1115–1133. https://doi.org/10.1021/acsenergylett.9b00263.

Chapter 6

Ammonia Synthesis by Plasma-Catalysis. Role of a Metal Catalyst*

6.1. Introduction

The incorporation of catalysts into plasma reactors (mainly in a packed-bed configuration) has been demonstrated to be a useful strategy to increase the performance of different plasma-driven chemical processes [1–3]. In this chapter, we analyze the effect of a Ru-catalyst on the plasma-assisted ammonia synthesis, with the intention of proving possible effects of this incorporation into the overall reaction process. Determining the role of pure catalytic or plasma interactions in the reaction mechanisms of ammonia synthesis has become a key issue to overcome the current energy efficiency limitations of this reaction [4–6]. Many authors have tried to select an appropriated catalysts for its incorporation in packed-bed plasma reactors for the synthesis of ammonia. For example, G. Akay and K. Zhang studied the incorporation of a porous Ni-based catalyst into a packed-bed reactor moderated by glass and $BaTiO_3$ pellets, obtaining reaction yield values (i.e., molecular percentage of converted nitrogen) as high as 12% [7]. Similarly, M. Carreon and coworkers have reported that porous materials such as zeolites seem to favor the ammonia synthesis into their pores [8,9]. They have also demonstrated that perovskites with electronegative alkaline-earth cations (e.g., $MgTiO_3$) contribute to weaken the nitrogen bond (N≡N) and thereby favor the ammonia synthesis reaction [10]. However, there are not yet clear criteria for the choice of the best catalyst, mainly because its function under plasma interaction conditions may be different than its typical activity at high pressures and temperatures.

* The content of this chapter will be sent for publication as an invited article: **P. Navascués**, J. Garrido-García, J. Cotrino, A. R. González-Elipe, A. Gómez-Ramírez, Energy Efficiency and Reaction Mechanisms by the Ammonia Synthesis in a Ferroelectric Packed-bed Plasma Reactor Adding Ruthenium Catalyst. Journal *ACS Sustainable Chemistry & Engineering*.

Focusing on the reaction mechanisms, Rouwenhorst *et al.* made a clear distinction between the different processes that could take place in a packed-bed plasma reactor either in the plasma bulk or at the surface of an embedded catalyst [5]. They distinguish four types of interactions: (1) *plasma-phase ammonia synthesis*, with all processes taking place in the plasma phase; (2) *surface-enhanced plasma-driven ammonia synthesis*, characterized by the dissociation of N_2 and H_2 in the plasma phase, followed by surface reactions; (3) *plasma-enhanced semicatalytic ammonia synthesis*, with the dissociation of N_2 taking place in the plasma phase and the dissociation of H_2 happening in the catalyst, followed by surface reactions; and (4) *plasma-enhanced catalytic ammonia synthesis*, involving an initial step of N_2 vibrational excitation by interaction with the electrons of the plasma, followed by the dissociation of the excited molecule onto the surface of the catalyst (where also hydrogen may become dissociated), the occurrence of surface reactions to produce ammonia and, finally, the ammonia desorption.

Trying to shed some light into the reaction mechanisms and the relative importance of these interactions, Bogaerts and coworkers have recently combined a catalytic reaction microkinetic model with a plasma chemical kinetics description [11]. Thanks to the incorporation of these two perspectives, these authors have concluded that the NH_3 turnover frequency (TOF)[†] does not depend on the catalytic material for plasmas with a high concentration of radical species and that E-R type elemental reactions are then favored. This idea differs from other studies proposing that the NH_3 TOF depends on the type of catalyst [12,13], thus stressing the importance of selecting the catalyst in terms of cost and stability. A confirmation of this view has been experimentally provided by Gorbanev *et al.* using Al_2O_3-supported Fe, Ru, Co, and Cu catalysts, reporting increases up to four times in the amount of produced ammonia when comparing the metal catalyst results with those obtained using Al_2O_3 beds as barrier [14]. However, these results and their interpretation are controversial since these authors obtained NH_3 concentrations around 8000 ppm upon the incorporation of 10 wt% metal loaded catalysts, a meager result corresponding to small reaction yields around 1%. In a similar way, Gorky *et al.*, studying the effect of adding Ni nanoparticles of different sizes into a packed-bed reactor filled by SiO_2 and feeding the reactor with a 1:3 N_2:H_2 gas

[†] The turnover frequency (TOF) is defined as the number of moles of substrate that a mole of catalyst can convert per unit time before becoming inactivated. Accordingly, an ideal catalyst would have an infinite TOF.

flow ratio, found an increase in the energy efficiency of ammonia production from 0.8 to 3.1 g NH_3/kWh, but in a range of reaction yields around 0.5% [15]. It is noteworthy for these two studies that the incorporation of metal catalysts produces and increase in reaction yield as compared with the use of classic dielectrics as moderators: Al_2O_3 (Gorbanev *et al.*) and SiO_2 (Gorky *et al.*). All the same, these are low reaction rates when compared to previous results of our research group working at ambient temperature with PZT as moderator (i.e., 7% of nitrogen conversion) [16] or the aforementioned results of Akay and Zhang for reactions carried out at 140ºC (i.e., 12% of nitrogen conversion) [7].

Despite the considerable efforts illustrated by these works in literature aiming at understanding the links between surface reactions and bulk plasma processes involved in the synthesis of ammonia, various unexplored questions still require a critical assessment. For example, a missing aspect is to determine the extent and mechanisms by which the metal catalytic particles are involved in the reaction process and/or how they may affect the plasma properties and behavior [3]. In this chapter we analyze these aspects, using the reaction yield and the energy efficiency of the plasma process as parameters to discuss the possible effects of the incorporation of a metallic phase on the packed-bed plasma reactor and, eventually, on the overall synthesis process. Based on previous studies of our research group about the ammonia synthesis reaction [16,17], experiments have been designed to easily study possible differences appearing when adding the metal catalyst. In this regard, it is important to remark that the selected operating conditions are not those optimized to obtain the aforementioned reaction yield of 7% [16], but others properly designed to address the main objective of this study: the analysis of the effects of the metal catalyst on the plasma and on the reactor performance.

For this purpose, we study the effect of incorporating a metal catalyst into a ferroelectric PZT barrier, a reactor configuration that, already provides reaction yield values higher than those obtained with classic dielectrics even without the incorporation of a metal catalyst [16,17]. In concrete, the ammonia synthesis reaction has been carried out in a packed-bed reactor using three configurations of the packed bed: i) using pure PZT pellets as discharge moderator (designed as PZT configuration); ii) with these pellets covered by an Al_2O_3 coating (Al_2O_3/PZT configuration), and iii) with this coating containing Ruthenium (Ru) nanoparticles (Ru-Al_2O_3/PZT configuration). Ruthenium is the most widely used metal catalyst for the plasma-catalytic synthesis of ammonia [6,11,12,14,18,19], as well as very

common in thermal catalysis [20]. A similar design strategy of the pellet's characteristics using core-shell structures as catalyst was applied by Uytdenhouwen *et al.* for the plasma-based CO_2 splitting process [21]. Furthermore, a similar configuration was also used in the previously mentioned study of Gorbanev *et al.*, where Ru nanoparticles were directly incorporated by a wet impregnation method onto γ-Al_2O_3 dielectric pellets [14].

As discussed in **Chapter 4**, the use of ferroelectrics instead of dielectrics results in higher current densities and generally provides a better trade-off between reaction yield and energy efficiency. In this chapter, a systematic study has been carried out for the three selected barrier configurations (PZT, Al_2O_3/PZT, and Ru-Al_2O_3/PZT) and two different temperatures: ambient temperature and 190ºC, considering that for this latter value certain catalytic effects may take place in the plasma reactor [6]. The study has primarily disclosed the effect of the alumina support and the metal catalyst phase on the plasma discharge. Thus, we show that alumina, with a dielectric constant smaller than that of the PZT (see **Chapter 4**) tends to *cool down* the plasma. In addition, we also prove that the incorporation of Ru contributes to compensate this *cooling* effect in the line proposed by Kushner and collaborators for catalytic moieties dispersed onto dielectric pellets [22]. However, our experiments demonstrate that the incorporation of a ruthenium catalyst when using ferroelectrics as moderators does not provide a significant enhancement (or this is negligible) either in reaction yield or in energy efficiency with respect to the PZT ferroelectric barrier. This assessment is confirmed by a critical evaluation of reaction mechanisms involved in the ammonia synthesis reaction, its back decomposition into H_2 and N_2, and/or additional processes that, occurring to a different extent at ambient temperature or 190ºC, may be detrimental for the overall reaction performance in the presence of a metal catalyst.

6.2. Experimental Details

All the experiments have been performed using PZT pellets (with diameters between 0.5-2 mm) and a barrier length of 5 mm. Seeking for plasma-catalysis synergies and taking into account the possible benefits of operating the reactor with ferroelectric pellets incorporating metal particles, a Al_2O_3-supported Ru catalyst powder was coated onto the PZT pellets (Ru-Al_2O_3/PZT configuration) using an incipient wetting impregnation technique (for more details see **section 3.5** in **Chapter 3**). For comparative purposes, the PZT pellets were also coated with Al_2O_3 powders (Al_2O_3/PZT configuration). Non-coated pellets have been also used as barrier (PZT configuration). The coatings (in powder and/or once deposited onto the pellets) were characterized by Scanning Electron Microscopy (SEM), Transmission Electron Microscopy (TEM), Energy Dispersive X-Ray Spectroscopy (EDX), X-ray Photoelectron Spectrometry (XPS), and the nitrogen adsorption BET technique (for more details about these characterization techniques, see **section 3.6** in **Chapter 3**). It should be mentioned that powders and coated pellets have been analyzed before plasma exposure, with the ruthenium particles in an oxidized state due to a precursor pretreatment consisting of calcination in air at elevated temperatures (see the preparation procedure in **section 3.5** in **Chapter 3**). However, it is expected that interactions with the hydrogen-rich plasma produced by ignition of the N_2:H_2 reaction mixture will reduce these ruthenium oxide particles to a metallic state [23].

The coated pellets were introduced in the packed-bed as a middle layer of the barrier, where they were sandwiched by two layers of PZT pellets. This configuration permits avoiding the short-circuits that often occur due to direct contacts between Ru particles and the metal electrodes. Therefore, the packed-bed consisted of three layers of pellets (38.5 cm^3) arranged as illustrated in **Figure 6.1**. The central layer occupies 11.5 cm^3 of coated pellets, while the top and bottom layers of PZT pellets have a total volume of 27 cm^3. The sketches in **Figure 6.1** also represent the expected differences between the external surface of the three kinds of pellets due to their coating with the Ru-Al_2O_3 catalyst and Al_2O_3 support. The three different barrier configurations have been analyzed via impedance measurements. For this analysis, the required potentiostat/galvanostat was operated in a frequency range from 1 MHz to 100 Hz applying an alternating voltage of 5 V_{rms} between the electrodes of the reactor.

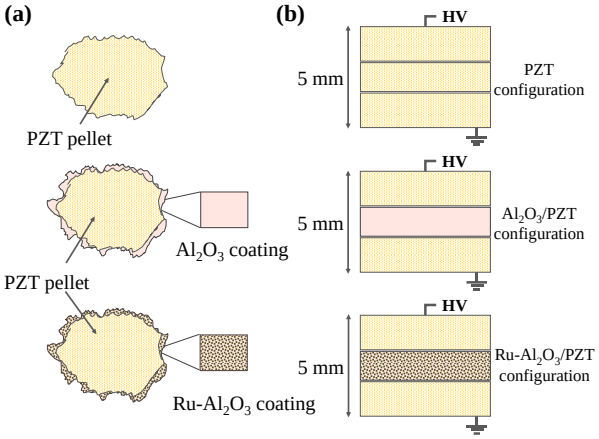

Figure 6.1. (a) Schematic of the PZT, Al_2O_3/PZT, and Ru-Al_2O_3/PZT pellets. (b) Barrier configurations when using coated pellets.

According to Kruszelnicki *et al.*, [3] when metal particles are added to dielectric beds in packed-bed reactors operated at atmospheric pressure, there is an enhancement in plasma density in the proximity of the metallic catalysts. This description relies on a computational model and has been experimentally confirmed by iCCD imaging analysis by the authors. Therefore, it is expected that the intensity of plasma generated with the Ru-Al_2O_3/PZT configuration is higher than that for the other two configurations at the same operating voltage. However, the situation is less clear for the Al_2O_3/PZT against the PZT configuration, the former including pellets formed by a PZT core coated by an irregular layer of Al_2O_3. The effect in the electric field distribution of covering the PZT pellets with an alumina coating has been analyzed with the AC/DC module of Comsol Multiphysics [24]. Simulations have been carried out for an inter-electrode distance of 3.695 mm, assuming that the PZT pellets are irregular and have a mean diameter of 0.6 mm. For the calculations, to disregard any tip effect, the external shape profile of the Al_2O_3/PZT is taken identical to that of the PZT pellets, but incorporating an irregular alumina coating with a mean thickness of 0.05 mm. The applied voltage between the electrodes was 2.5 kV at a frequency of 5 kHz. An extremely fine mesh was used for the calculations, rendering a computing time of approximately 90 seconds. The color maps in **Figure 6.2(a)** depict the electrical field distribution between two PZT pellets (i.e., PZT configuration) and between adjacent PZT and Al_2O_3/PZT pellets (note that in the Al_2O_3/PZT and Ru-Al_2O_3/PZT configurations, only the middle layer in the packed-bed is filled with coated pellets, see **Figure 6.1(b)**). These color maps evidence that, for similar

outer topographies and distances, the electric field in the inter-pellet space is higher between two PZT pellets than between two adjacent PZT and Al_2O_3/PZT pellets. **Figure 6.2(b)** provides a detailed evaluation of the electric field along a line "r" connecting two pellets.

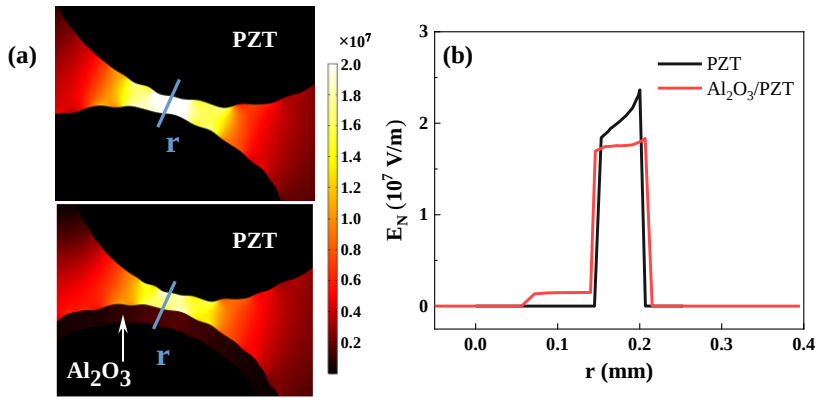

Figure 6.2. Analysis of the electric field distribution in the packed-bed barrier by means of Comsol Multiphysics simulations [24]. (a) Distribution of the electric field between two equally separated pellets of PZT (top) and a PZT and a Al_2O_3/PZT pellet (bottom). The "r" line indicates the pathway selected to evaluate the electric field. (b) Electric field distribution along the line "r" for the PZT and Al_2O_3/PZT configurations.

The difference in electric field distribution between the PZT and PZT-Al_2O_3/PZT configurations responds to the distinct dielectric constants of the ferroelectric PZT and dielectric Al_2O_3 materials (1900 and 10, respectively, see **Chapter 4**). It is also noteworthy that the electric field intensity appears enhanced at locations where either the Al_2O_3 or the PZT surfaces present irregularities. This behavior is usually overlooked in similar simulations reported in the literature, where perfectly spherical inter-electrode pellets are considered for the calculations [25,26]. These simulations of electrical field distribution forecast that the lower electric field distribution in the inter-pellet space for the Al_2O_3/PZT configuration may affect the electrical behavior of the reactor. In concrete, according to these results, this configuration is expected to *cool down* the plasma, reducing both the electron temperature and density.

Experiments in this chapter have been carried out at atmospheric pressure and two different temperatures: ambient temperature (with a slightly drift in this parameter during the experiments up to a maximum of 35ºC, a value that has been considered for the energy efficiency calculations) and at a *nominal temperature* of

190ºC measured at the reactor walls. At ambient temperature, experiments have been performed in two ways: i) varying the voltage amplitude between 1.75 and 3 kV at a fixed frequency of 5 kHz, and ii) varying the frequency between 1 and 5 kHz at a fixed voltage of 2.5 kV. In this latter mode, plasma current varied with the frequency of operation and was chosen as a method to vary systematically the plasma power without modifying the electric field distribution in the packed-bed reactor. At 190ºC only mode i) was used applying a fixed voltage amplitude of 2.5 kV, while the frequency was varied between 1 and 3 kHz. The repetition of measurements between two and three times showed that the experimental error was in the order of 10%.

Since this study focuses on the ammonia synthesis reaction, a N_2+H_2 mixture has been used as inlet gas. A total *effective* flow rate of 23 sccm (1:3 N_2:H_2 ratio) was kept constant during all the experiments. To ensure that the residence time of reactant gases in the reactor was similar when increasing the temperature, the inlet gas flow was adjusted considering the expected volume expansion of gases due to their heating in the reactor (i.e., the effective residence time will be affected by the reactor temperature). Therefore, N_2 and H_2 gas flows were set at 5.75 sccm and 17.25 sccm at room temperature and at 3.7 sccm and 11.1 sccm, at 190ºC.

6.3. Results and Discussion

6.3.1. Characterization of Al_2O_3/PZT and Ru-Al_2O_3/PZT Pellets

Al_2O_3 and Ru-Al_2O_3 powders were characterized before coating. **Figure 6.3** displays TEM micrographs and EDX spectra taken for the two types of powder samples, showing that Ru containing nanoparticles have been effectively incorporated onto the Al_2O_3 phase. This effective incorporation was revealed by the EDX spectrum and the dark spots that, with an average length of 120 nm, are observed in the TEM micrograph of a grain of the Ru-Al_2O_3 catalyst powder (see **Figure 6.3(b)**).

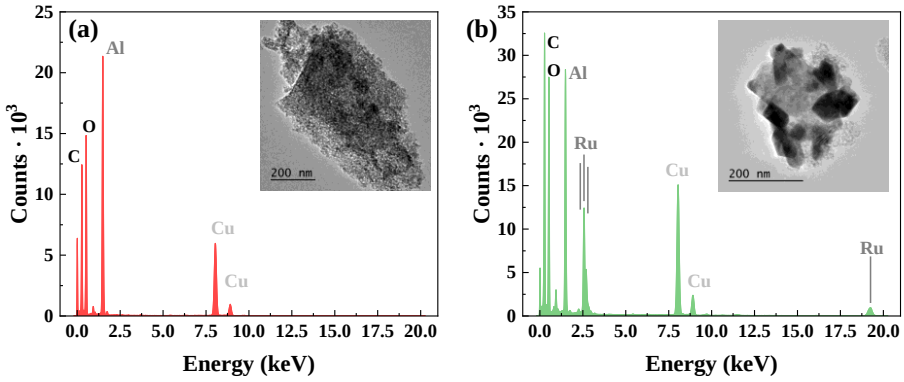

Figure 6.3. TEM micrographs and EDX spectra of Al_2O_3 (a) and Ru-Al_2O_3 (b) powder samples. The Cu signals in the EDX spectra are due to the sample holder.

The presence of Ru containing nanoparticles onto the Al_2O_3 support was also demonstrated by XPS analysis. **Figure 6.4** shows the XPS spectra of Al_2O_3 and Ru-Al_2O_3 powders. In both cases, signals associated to Al (Al2p, Al2s), O (O1s) and C (C1s) can be observed. The signal marked with C1s in the spectrum of the Ru-Al_2O_3 sample overlaps with that of Ru3d (c.f., **Figure 6.4(b)**), the most intense photoelectron peak of this element. Despite the overlapping of the Ru3d and C1s peaks, the concentration of this element can be estimated in 0.9% from the analysis of the less intense Ru3p signal. This is a reasonable value considering the agglomeration and partial distribution of the ruthenium (2% wt. added) in the Al_2O_3 powder internal pores. According to the position of the Ru3p3/2 signal (462 eV), it is expected that Ru nanoparticles are in an oxidized form, as expected from the calcination treatment in air of the Ru containing precursor powder (see **Chapter 3**).

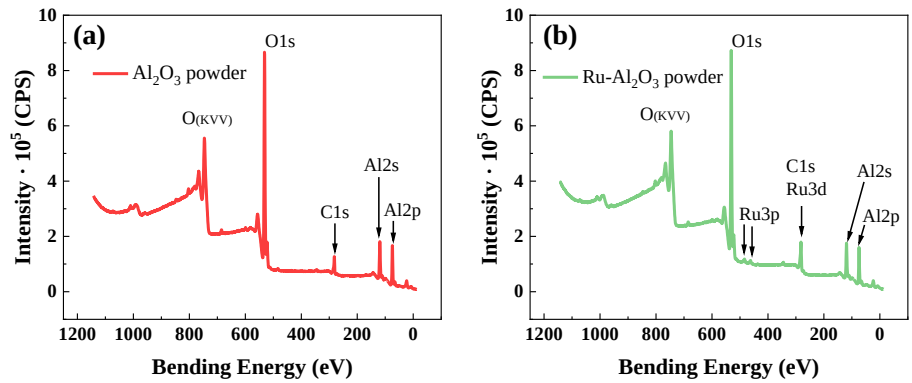

Figure 6.4. XPS survey spectra of Al_2O_3 (a) and Ru-Al_2O_3 (b) powder samples.

The surface area of the powders was determined by means of the BET nitrogen adsorption technique. Similar values of 107.9 and 112.7 m^2/g were obtained for the Al_2O_3 and the Ru-Al_2O_3 powder samples, respectively.

As evidenced in **Figures 6.5(a)** and **(b),** the SEM characterization of the Ru-Al_2O_3 powder also demonstrated that Ru was enriched in certain zones of the Al_2O_3 support forming particles or patches with sizes ranging from 100 to 200 nm (see also **Figure 6.3(b)**). The SEM micrograph in **Figure 6.5(a)**, obtained in backscattered electron mode at 2 kV, shows that Ru containing particles are intermingled with the Al_2O_3 grains, although some aggregation of these particles occurs at certain regions, as indicated by arrows in the figure. This is clearly seen in **Figure 6.5(b)** showing the EDX maps of the same powders demonstrating that, in certain zones, Ru containing particles may form clusters onto the alumina support.

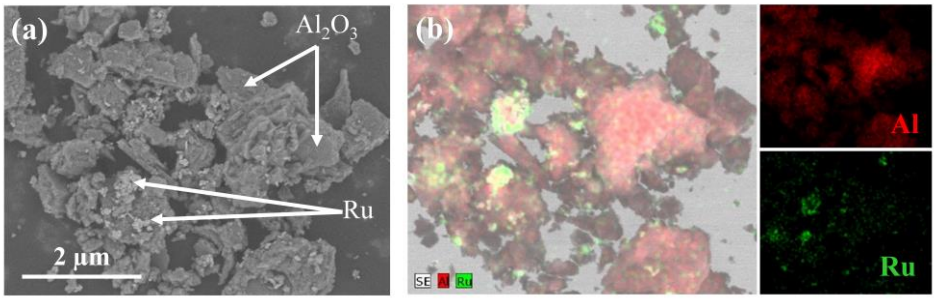

Figure 6.5. SEM characterization of the Al_2O_3-supported Ru catalyst powder. (a) SEM micrograph (backscattered electrons). (b) EDX analysis (electron beam energy of 30 kV) of the sample region in (a).

After the impregnation and calcination of the PZT pellets, their morphological characteristics were also determined. **Figure 6.6(a)** displays a scheme of the Ru-Al_2O_3/PZT pellets showing its irregular coating and that the Ru containing nanoparticles are not only located at the external zones of the coating, but also distributed within the irregular alumina coating layer formed by the agglomeration of the Al_2O_3 support powder. The SEM micrographs in **Figure 6.6(b)** confirms that the coating is not entirely conformal and that the pellet may expose areas of uncovered PZT. The topography and shape of the Ru-Al_2O_3/PZT pellets was similar to that of Al_2O_3/PZT.

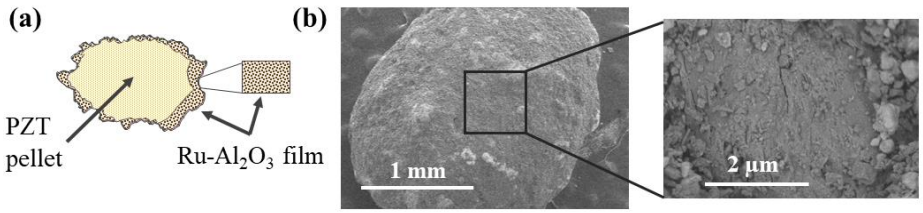

Figure 6.6. (a) Sketch of the coating of a Ru-Al_2O_3 pellet. (b) SEM micrographs of a pellet sample at 2 kV with secondary (left) and backscattered (right) electron modes.

The XPS analysis of the Al_2O_3/PZT pellets indicates that, although Al and O are the most abundant elements, signals of PZT can be also detected (see **Figure 6.7**). The evaluation in the table in **Figure 6.7** of the atomic percentage at the surface of the examined samples renders a minority contribution of the PZT elements (i.e., Pb, Zr, Ti), thus suggesting that although the coverage of the pellet surface is almost complete very small zones of PZT are not fully covered by the alumina (c.f., **Figure 6.6(b)**). Similar evidence could be inferred for to the Ru-Al_2O_3/PZT pellets.

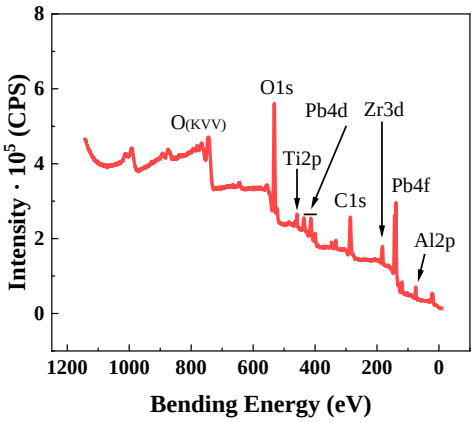

	Al	O	C	N
%at	18.8	39.4	29.3	3.2
	Pb	Zr	Ti	
%at	4.5	2.9	1.9	

Figure 6.7. XPS analysis of a set of Al_2O_3/PZT samples: survey spectrum (left) and atomic concentration (right) of each element.

6.3.2. Electrical Behavior of the Packed-bed Reactor

The electrical behavior of the packed-bed reactor operating in the PZT, Al_2O_3/PZT and Ru-Al_2O_3/PZT configurations was firstly assessed by means of impedance spectroscopy. The measurements were carried out in the absence of plasma but after performing series of plasma experiments to reach steady state operating conditions of the reactor.

The Nyquist curves depicted in **Figure 6.8(a)** determined by impedance spectroscopy analysis can be interpreted considering that the curvature is related to the electrical properties of the barrier. As discussed in **Chapter 4**, high resistive materials are characterized by a high radius Z"-Z' hemispherical plot, while the radius becomes smaller for less insulating materials. The lines in **Figure 6.8(a)** correspond to the first part of the Z"-Z' hemispherical plots obtained for the three configurations of the reactor. The evolution of the slopes of these lines indicates that the curvature radius of the Nyquist plots, and therefore the resistance of the reactor, follows the order PZT>Al_2O_3/PZT>Ru-Al_2O_3/PZT. This tendency agrees with the lower dielectric constant of Al_2O_3 in comparison with that of PZT (and therefore of a barrier where some PZT pellets are coated by Al_2O_3). Meanwhile, the incorporation of a metallic phase (ruthenium must have been reduced in the steady state after exposure to a reducing plasma discharge), even if it is in the form of dispersed particles, seems to substantially decrease the resistance of the barrier.

The previous impedance spectroscopy evaluation has been complemented with the analysis of the characteristic *V(t)* and *I(t)* curves recorded under different plasma operating conditions. The *V(t)* and *I(t)* curves recorded during plasma operation (c.f., **Figure 6.8(b))** show a clear evolution for the three analyzed configurations (applied voltage of 2.5 kV and frequency of 5 kHz). Thus, although the three *I(t)* curves show the microdischarge features typical of packed-bed reactors (discussed in detail in **Chapter 4**), they depict a different overall intensity, following the order Ru-Al_2O_3/PZT>PZT>Al_2O_3/PZT. These *I(t)* curves give rise to the Lissajous curves in **Figure 6.8(c)**, whose shape indicate that the discharge power, taken as proportional to their areas, is maximum for the reactor containing Ru-Al_2O_3/PZT pellets, followed by PZT and Al_2O_3/PZT pellets, as indicated in **Figure 6.8(d)**. The minimum current intensity and consumed power found for the Al_2O_3/PZT configuration agrees with the Comsol analysis discussed in **section 6.2**: the Al_2O_3 coating tends to *cool down* the plasma, decreasing the electric field intensity in the inter-pellet space.

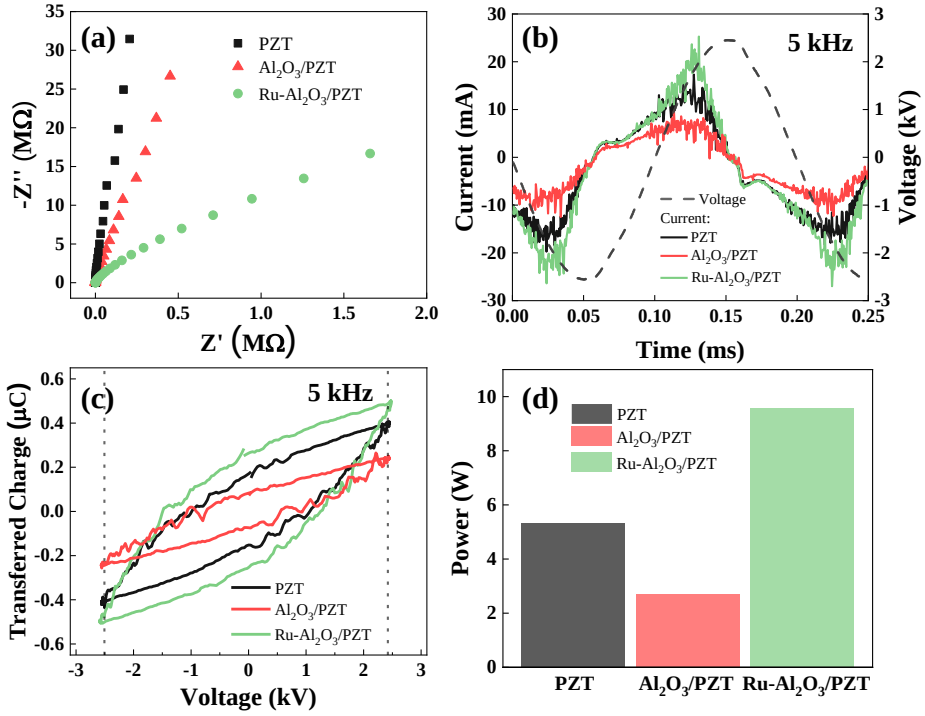

Figure 6.8. Electrical characterization of the reactor with the three barrier configurations (PZT, Al_2O_3/PZT and Ru-Al_2O_3/PZT): (a) *Nyquist* plots measured for the reactor applying 5V, (b) *V(t)* and *I(t)* curves during plasma ignition (2.5 kV, 5kHz), (c) Lissajous figures determined from the curves in (b), and (d) consumed power from the conditions in plots (b)-(c).

6.3.3. Ammonia Synthesis at Ambient Temperature

The synthesis of ammonia by igniting N_2+H_2 plasmas was firstly investigated at room temperature for the three barrier configurations of the reactor. **Figure 6.9** shows the evolution with applied voltage of reaction yield (i.e., N_2 conversion) and energy efficiency. **Figure 6.9(a)** shows that, at low voltages, reaction yields smaller than 0.5% were obtained for the different barriers. The uncertainty in accurately determining these small values and the low power consumed at these conditions make that the energy efficiency magnitude may be subjected to large experimental errors (see **Figure 6.9(b)**). Therefore, these points in the plots are represented with empty dots joined by dashed lines to clearly distinguish these points from those that are meaningful for the analysis of the reactor performance.

According to the data in **Figure 6(a),** the reaction yield is higher for the reactor filled with PZT pellets, particularly for voltages higher than 2.25 kV. Interestingly, there is a similar high yield for the Ru-Al_2O_3/PZT configuration, except for the highest accessible voltage at which the conversion yield tends to decrease. The lowest yield values are obtained for the Al_2O_3/PZT reactor configuration, a result that can be related to the lower current and electric field distribution characterizing this barrier.

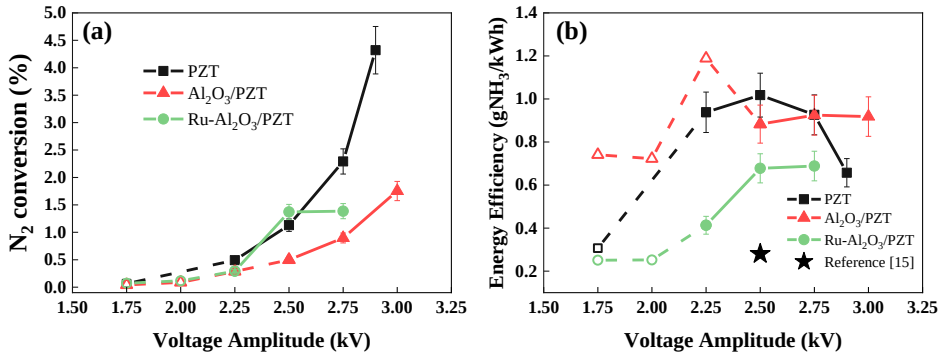

Figure 6.9. Evolution of the reaction yield (a) and energy efficiency (b) for the ammonia synthesis reaction as a function of the applied voltage. Data corresponding to low reaction yields are plotted with empty dots and dash lines, while the other data are plotted with solid markers and lines. Experiments were carried out at ambient temperature and a frequency of 5 kHz. The star dot corresponds to data taken from ref. [16].

From a practical point of view, the energy efficiency of a plasma-catalysis process defines its actual capacity to compete with other established technologies [27]. It is noteworthy in this regard that high conversion yields do not warrant high energy efficiencies, and that an opposite evolution of these two magnitudes is a common behavior for other plasma catalysis processes [2,21]. An example illustrating this dysfunctional tendency is included in **Figure 6.9(b)**. The star dot in the diagram corresponds to operating conditions taken from a previous study of our research group [16] (i.e., a PZT barrier of 3 mm, flow rate of 11.5 sccm, frequency of 5 kHz and voltage amplitude of 2.5 kV), where a N_2 conversion yield of 7% was obtained. We realize here that this high conversion rate occurs at expenses of relatively small energy efficiency in comparison with the conditions described in this chapter, where a barrier of 5 mm has been selected to including a middle layer of pellets loaded with the metal catalyst and support, as explained in **section 6.2** (c.f., **Figure 6.1**).

The evolution of the energy efficiency with the applied voltage shown in **Figure 6.9(b)** reveals a different behavior depending on reactor configuration, also suggesting some differences in reaction mechanisms. The Al_2O_3/PZT configuration depicts an approximately constant value of the energy efficiency for voltages higher than 2.25 kV, indicating that reaction mechanisms do not significantly change with the applied voltage. Meanwhile, the PZT barrier depicts an energy efficiency maximum at 2.5 kV, followed by a progressive small decrease at higher voltages. We tentatively attribute this decrease to the occurrence of *inefficient processes* as those discussed in **Chapter 5**, i.e., decomposition of ammonia and hydrogen exchange reactions. The tendency is similar for the Ru-Al_2O_3/PZT configuration for voltages higher than 2.25 kV, but always with lower efficiencies than for the PZT case. Since the reaction was carried out at ambient temperature, *pure catalytic* mechanisms induced by the Ru particles can be discarded. This systematic lower efficiency can be related to a higher probability of ammonia decomposition reactions induced by the impact with high energy electrons [26] that, generated in the microdischarges, are more abundant due to the presence of the metal phase [22]. Meanwhile, for the Al_2O_3/PZT configuration, we propose that ammonia decomposition and/or hydrogen exchange reactions responsible to diminish the energy efficiency for the ammonia synthesis are less probable because of the claimed *cooling down* of the plasma.

The previous considerations gain further credit examining the evolution of reaction yield and energy efficiency as a function of operating frequency (c.f., **Figure 6.10)**. The frequency was varied systematically (1-5 kHz) at constant voltage (2.5 kV) as a way to modify the power consumed in the reactor as illustrated in **Figure 6.10(a)**. **Figure 6.10(b)** shows that, in the three cases, the reaction yield progressively increases with frequency (i.e., power) and that the actual values follow the order Ru-Al_2O_3/PZT>PZT>Al_2O_3/PZT. Additionally, the evolution of the energy efficiency shown in **Figure 6.10(c)** reveals that this magnitude continuously increases for the PZT configuration, but it passes through a maximum (at around 2.5 kV) for the Ru-Al_2O_3/PZT; more noticeably, for the Al_2O_3/PZT configuration the energy efficiency reaches a maximum at a frequency of 3 kHz. This behavior supports that, for these two latter configurations, *inefficient reaction mechanisms* are favored at increasing frequencies (i.e., powers), something that is less evident for the PZT configuration, where the energy efficiency continuously increase with frequency. In this experiment, for the PZT configuration the maximum efficiency of 1g NH_3/kWh was found at 5 kHz.

According to previous considerations, the maximum energy efficiency found for the Al_2O_3/PZT configuration at 3 kHz (1.3 g NH_3/kWh) can be linked with a relatively lower probability of decomposition reactions under these conditions.

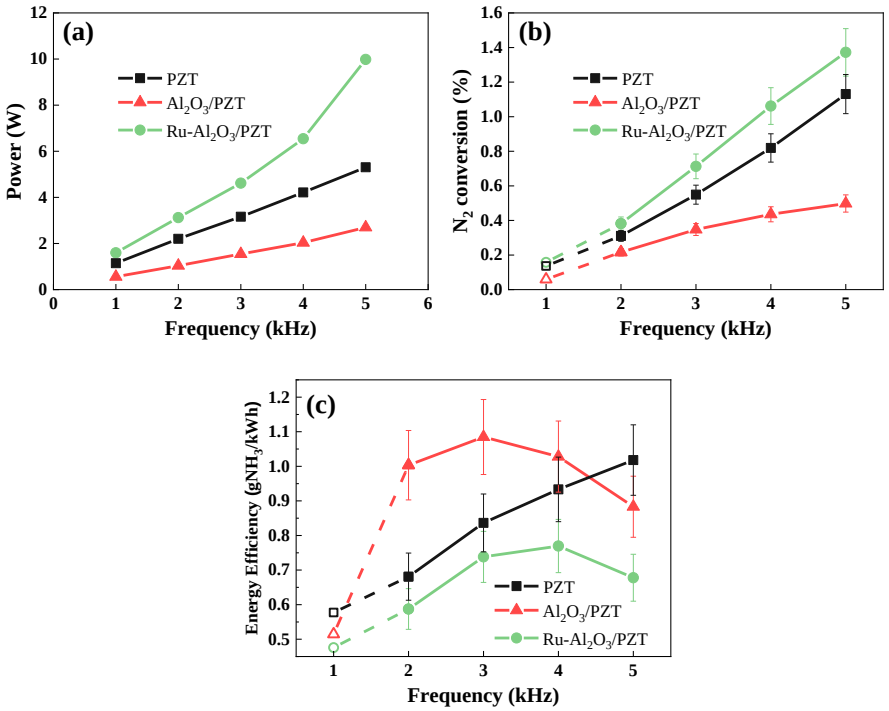

Figure 6.10. Evolution of power consumption (a), reaction yield (b), and energy efficiency (c) for the ammonia synthesis reaction as a function of frequency. For the experiments at 1 kHz, results are plotted with empty dots and dash lines indicating a possible inaccuracy in the determination of these values. Experiments were carried out at ambient temperature, a voltage amplitude of 2.5 kV and a variable frequency between 1 and 5 kHz.

6.3.4. Ammonia Synthesis at Elevated Temperature

Within a plasma-catalysis perspective, a catalytic effect of the Ru particles might be expected at elevated temperatures [6]. Therefore, similar experiments than those described in the previous section were carried out at a *nominal temperature* of 190ºC. According to Rouwenhorst *et al.*, this temperature is a kind of threshold for the catalytic promotion of the ammonia synthesis in plasma reactors incorporating a Ru-based catalyst [6]. Owing to the special conditions of our experiment it is expected that the temperature inside the packed-bed zone may be higher that this nominal value at the reactor wall (see similar considerations in **Chapter 4)**.

Since an applied voltage of 2.5 kV provided the highest energy efficiencies at ambient temperature (c.f., **Figure 6.9(b)**), the 190ºC-experiments were carried out varying the frequency between 1 and 3 kHz at this voltage and the three reactor configurations. This frequency range was chosen because of experimental limitations: at high temperatures the appearance of sparks and short-circuits affect the stability of the discharges at higher frequencies (>3kHz).

Figure 6.11(a) shows the *I(t)* curves recorded for the three barrier configurations at 190ºC. Unlike the relatively large differences observed at room temperature (see **Figure 6.8(b)**), the *I(t)* curves for the three configurations have a relatively higher amplitude and, with the exception of the curve for the Al_2O_3/PZT configuration, they tend to overlap (note that the curves are plotted for a frequency of 2 kHz and not 5 kHz as for the experiments at ambient temperature). As discussed in **Chapter 4**, we attribute this behavior to the progressive non-linear increase with temperature of the dielectric constant of PZT. In other words, the significantly higher value of the PZT dielectric constant at 190ºC would be the predominant factor controlling the discharge. Accordingly, **Figure 6.11(b)** shows that at a fixed frequency, the Lissajous plots for the three configurations are rather similar, though the curve for the Al_2O_3/PZT configuration has a slightly lower area. Consequently, **Figure 6.11(c**) shows that the increasing evolution of discharge power with frequency is rather similar for the PZT and Ru-Al_2O_3/PZT configurations, but slightly smaller for the Al_2O_3/PZT case.

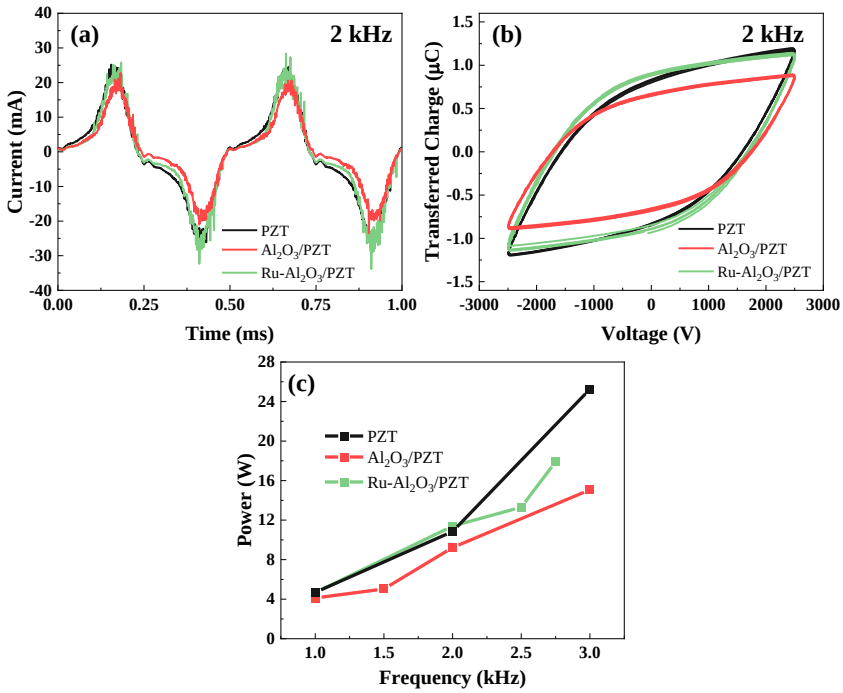

Figure 6.11. Electrical characterization of the three reactor configurations at 190ºC and 2.5 kV. (a) *I(t)* curves measured at 2 kHz, (b) Lissajous figures of the discharge for the same conditions than in (a), and (c) consumed power for frequencies between 1 and 3 kHz.

Figure 6.12 shows the evolution with frequency of the reaction yield and energy efficiency at 190 ºC (values obtained at ambient temperature are also plotted for comparative purposes). It can be observed in **Figure 6.12(a)**) that reaction yields significantly increase with respect to the results at ambient temperature for the three configurations, with values five times higher at 3 kHz and practically no differences between the three configurations. Meanwhile, energy efficiency (see **Figure 6.12(b)**) presents larger differences following the order Ru-Al_2O_3/PZT<PZT<Al_2O_3/PZT, particularly for frequencies smaller than 3 kHz. For the PZT and Al_2O_3/PZT configurations, there is a decrease in the energy efficiency at this frequency. However, for the Ru-Al_2O_3/PZT configuration the energy efficiency, though smaller at low frequencies than in the other two cases, progressively and continuously increases with frequency. For PZT the observed decrease in energy efficiency at 3 kHz is likely due to a progressive increase in the occurrence of *inefficient reactions* (i.e., hydrogen atom exchanges and ammonia decomposition) at high temperature. A similar small decrease is obtained at this

frequency for the Al_2O_3/PZT configuration. On the other hand, the different evolution consisting of a continuous increase in energy efficiency found for Ru-Al_2O_3/PZT configuration suggests a certain difference in reaction mechanism with respect to the other two cases. However, the small differences found in reaction yield with respect to the other two cases (c.f., **Figure 6.12(a)**) suggests that possible catalytic effects should be considered second-order or negligible. This behavior differs from that of typical catalytic processes involving the dissociation of nitrogen and/or hydrogen on metal surfaces claimed as critical steps by the thermal catalytic synthesis of ammonia [5,6,19,20,29].

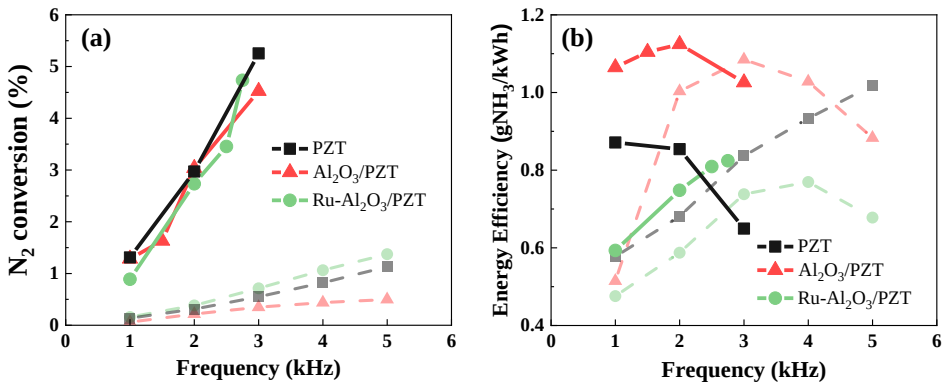

Figure 6.12. Evolution of reaction yield (a) and energy efficiency (b) for the ammonia synthesis reaction as a function of frequency. Experiments were carried out at 190ºC for a voltage amplitude of 2.5 kV and variable frequencies between 1 and 3 kHz.

To further analyze the differences between the three configurations at ambient and high temperatures, we have completed the study with optical emission measurements.

6.3.5. OES Analysis: Intermediate Plasma Species at Ambient and Elevated Temperature

Figure 6.13 shows a series of OES spectra recorded for the three investigated configurations at ambient (a) and high temperatures (b). The detected bands can be attributed to: NH^* (transition $[A^3\Pi \rightarrow X^3\Sigma^-]$ at 336 nm), the first negative system of N_2^+ (transition $[B^2\Sigma_u^+ \rightarrow X^2\Sigma_g^+]$, with main bands at 391.4 and 427.8 nm), and the second positive system of N_2 (transition $[C^3\Pi \rightarrow B^3\Pi]$, with main bands at 337 and 357.9 nm.

Although at first glance the spectra look similar, there are appreciable differences in the ratio between bands, a fact that can be related to the relative concentration of each species in the plasma phase. With this purpose, intensity ratios between N_2^{+*} (391.4 nm) and N_2^{*} (357.9 nm) bands have been evaluated ‡. This normalization criterion is justified because the electronic excitation of N_2 to render N_2^{*} species is a common elementary plasma-process occurring in the three configurations. The calculated ratios are presented in **Table 6.1**.

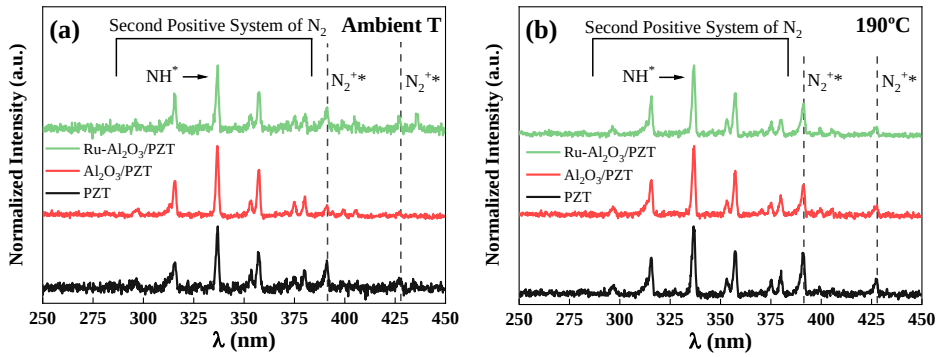

Figure 6.13. OES spectra recorded at ambient temperature (2.5 kV, 5 kHz) (a) and 190ºC (2.5 kV, 2 kHz) (b).

Table 6.1. N_2^{+*}/N_2^{*} intensity ratios calculated from the OES spectra acquired at ambient temperature (5 kHz) and 190ºC (2 kHz). Data taken from spectra plotted in **Figure 6.13**.

Configuration	**Ambient Temperature**	**190ºC**
PZT	0.90	0.98
Al_2O_3/PZT	0.49	0.75
Ru-Al_2O_3/PZT	0.82	0.87

‡ The 357.9 nm band of the Second Positive System of N_2^{*} is usually chosen to calculate the emission ratio of the species of interest because it does not overlap with bands of other species. Since this occurs for the main band of the Second Positive System of N_2 (337 nm), partially overlapping with the NH^{*} band (336 nm), this ratio has not been considered for evaluation.

The most significant result from the data in **Table 6.1** is that, at ambient temperature, the N_2^+ relative emission intensity is significantly smaller for the Al_2O_3/PZT configuration. Since, as discussed in **Chapter 5**, the formation of N_2^+ species requires electrons with energies equal or higher than 15.6 eV [30], the relatively lower intensity of N_2^+ species found for the Al_2O_3/PZT configuration agrees with the claimed *cooling down* effect of plasma due to the alumina coating (c.f., **Figure 6.2**). Another consequence of this *cooling effect* is the decrease in reaction yield obtained at 5 kHz and ambient temperature for the Al_2O_3/PZT (0.5%) with respect to the other configurations (around 1.3%) (c.f., **Figure 6.9**). The reduction in the electron energy due to the lower electric field obtained when using the alumina coating might also contribute to decrease the importance of the back-reactions (i.e., ammonia decomposition), and therefore contribute to increase the generally higher energy efficiency for the Al_2O_3/PZT configuration for all studied operating conditions.

As discussed in **Chapter 5**, the formation of N_2^+ and NH species by electron impact in the plasma phase has been interpreted as rate-limiting steps when using a PZT barrier. In this regard, the results obtained here for the three barriers suggest that, at the essayed operating conditions, new catalytic reaction pathways do not significantly contribute to the reaction, even at high temperature and with ruthenium particles. According to these inferences, the incorporation of metal catalyst particles does not seem to provide any significant enhancement in reaction yield. Therefore, rather than to a catalytic effect of the metal particles (not discarded, but comparatively negligible), the rather high reaction yield and energy efficient values obtained with the three configurations, generally higher than recently reported values from literature (see, for example, review publications [31,32]), should be primarily attributed to the enhancement of plasma intensity by the PZT ferroelectric barrier.

6.5. Conclusions

In the study carried out in this chapter, three different barrier configurations (PZT, Al_2O_3/PZT, and Ru-Al_2O_3/PZT) have been systematically essayed to study the effect of the incorporation of a ruthenium metal catalyst in a ferroelectric packed-bed reactor for the synthesis of ammonia. Ferroelectric packed-bed reactors are characterized by high plasma intensities due to the high dielectric constant of these materials. The operation of plasma reactors moderated with

ferroelectric materials, both at ambient and high temperatures, has allowed us to conclude that catalyst metal nanoparticles are not particularly beneficial for the ammonia synthesis under the experimental conditions herein analyzed, even at high temperatures at which a certain catalytic activity is expected to contribute to the formation of ammonia. We relate the apparent lack of catalytic activity to that the NH_3 decomposition reaction is also promoted by interactions with high-energy electrons formed in the high-intense plasma microdischarges induced as an effect of metal particles. We should remark that this enhancement of detrimental plasma reactions does not discard that the ammonia synthesis reaction may be favored by pure catalytically-driven processes occurring at the surface of the metal catalyst. However, the overall consequence is that the final production of ammonia is similar for the three configurations, that the energy efficiency is always smaller for the Ru-Al_2O_3/PZT than for the Al_2O_3/PZT configuration and, for certain values of frequency, also for the PZT configuration.

It has been also demonstrated that a pristine alumina coating on the PZT pellets tends to *cool down* the plasma due to the decrease in the electric field intensity in the inter-pellet space. Additionally, we propose that the alumina coating can decrease the occurrence of inefficient reactions taking place at the PZT surface at elevated temperatures. As a general conclusion, unlike different studies reported in the literature using dielectrics as moderators [6,11,12,14,18,19], the incorporation of metal catalysts – even activated at high temperatures – in ferroelectric packed-bed reactors does not seem to be the best strategy to improve the plasma-catalytic performance towards the ammonia synthesis reaction.

6.6. References

[1] A. Bogaerts, X. Tu, J.C. Whitehead, G. Centi, L. Lefferts, O. Guaitella, F. Azzolina-Jury, H.H. Kim, A.B. Murphy, W.F. Schneider, T. Nozaki, J.C. Hicks, A. Rousseau, F. Thevenet, A. Khacef, M. Carreon, The 2020 plasma catalysis roadmap, Journal of Physics D: Applied Physics. 53 (2020). https://doi.org/10.1088/1361-6463/ab9048.

[2] Whitehead J.C. (2019) Plasma Catalysis: Introduction and History. In: Tu X., Whitehead J., Nozaki T. (eds) Plasma Catalysis. Springer Series on Atomic, Optical, and Plasma Physics, vol 106. Springer, Cham. https://doi.org/10.1007/978-3-030-05189-1_1.

[3] M.L. Carreon, Plasma catalysis: A brief tutorial, Plasma Research Express. 1 (2019). https://doi.org/10.1088/2516-1067/ab5a30.

[4] Mizuno A., Craven M. (2019) Plasma Catalysis Systems. In: Tu X., Whitehead J., Nozaki T. (eds) Plasma Catalysis. Springer Series on Atomic, Optical, and Plasma Physics, vol 106. Springer, Cham. https://doi.org/10.1007/978-3-030-05189-1_2.

[5] K.H.R. Rouwenhorst, H.-H. Kim, L. Lefferts, Vibrationally Excited Activation of N_2 in Plasma-Enhanced Catalytic Ammonia Synthesis: A Kinetic Analysis, ACS Sustainable Chemistry & Engineering. 7 (2019) 17515–17522. https://doi.org/10.1021/acssuschemeng.9b04997.

[6] K.H.R. Rouwenhorst, H.G.B. Burbach, D.W. Vogel, J. Núñez Paulí, B. Geerdink, L. Lefferts, Plasma-catalytic ammonia synthesis beyond thermal equilibrium on Ru-based catalysts in non-thermal plasma, Catalysis Science and Technology. 11 (2021) 2834–2843. https://doi.org/10.1039/d0cy02189j.

[7] G. Akay, K. Zhang, Process intensification in ammonia synthesis using novel coassembled supported microporous catalysts promoted by nonthermal plasma, Industrial and Engineering Chemistry Research. 56 (2017) 457–468. https://doi.org/10.1021/acs.iecr.6b02053.

[8] F. Gorky, J.M. Lucero, J.M. Crawford, B. Blake, M.A. Carreon, M.L. Carreon, Plasma-Induced Catalytic Conversion of Nitrogen and Hydrogen to Ammonia over Zeolitic Imidazolate Frameworks ZIF-8 and ZIF-67, ACS Applied Materials and Interfaces. 13 (2021) 21338–21348. https://doi.org/10.1021/acsami.1c03115.

[9] F. Gorky, S.R. Guthrie, C.S. Smoljan, J.M. Crawford, M.A. Carreon, M.L. Carreon, Plasma ammonia synthesis over mesoporous silica SBA-15, Journal of Physics D: Applied Physics. 54 (2021). https://doi.org/10.1088/1361-6463/abefbc.

[10] F. Gorky, J.M. Lucero, J.M. Crawford, B.A. Blake, S.R. Guthrie, M.A. Carreon, M.L. Carreon, Insights on cold plasma ammonia synthesis and decomposition using alkaline earth metal-based perovskites, Catalysis Science and Technology. 11 (2021) 5109–5118. https://doi.org/10.1039/d1cy00729g.

[11] Y. Engelmann, K. Van'T Veer, Y. Gorbanev, E.C. Neyts, W.F. Schneider, A. Bogaerts, Plasma Catalysis for Ammonia Synthesis: A Microkinetic Modeling Study on the Contributions of Eley-Rideal Reactions, ACS Sustainable Chemistry and Engineering. 9 (2021) 13151–13163. https://doi.org/10.1021/acssuschemeng.1c02713.

[12] P. Mehta, P. Barboun, F.A. Herrera, J. Kim, P. Rumbach, D.B. Go, J.C. Hicks, W.F. Schneider, Overcoming ammonia synthesis scaling relations with plasma-enabled catalysis, Nature Catalysis 2018 1:4. 1 (2018) 269–275. https://doi.org/10.1038/s41929-018-0045-1.

[13] P. Mehta, P.M. Barboun, Y. Engelmann, D.B. Go, A. Bogaerts, W.F. Schneider, J.C. Hicks, Plasma-Catalytic Ammonia Synthesis beyond the Equilibrium Limit, ACS Catalysis. 10 (2020) 6726–6734. https://doi.org/10.1021/acscatal.0c00684.

[14] Y. Gorbanev, Y. Engelmann, K. Van'T Veer, E. Vlasov, C. Ndayirinde, Y. Yi, S. Bals, A. Bogaerts, Al_2O_3-supported transition metals for plasma-catalytic NH_3 synthesis in a DBD plasma: Metal activity and insights into mechanisms, Catalysts. 11 (2021). https://doi.org/10.3390/catal11101230.

[15] A. Gómez-Ramírez, A.M. Montoro-Damas, J. Cotrino, R.M. Lambert, A.R. González-Elipe, About the enhancement of chemical yield during the atmospheric plasma synthesis of ammonia in a ferroelectric packed bed reactor, Plasma Processes and Polymers. 14 (2017). https://doi.org/10.1002/ppap.201600081 .

[16] F. Gorky, A. Best, J. Jasinski, B.J. Allen, A.C. Alba-Rubio, M.L. Carreon, Plasma catalytic ammonia synthesis on Ni nanoparticles: The size effect, Journal of Catalysis. 393 (2021) 369–380. https://doi.org/10.1016/j.jcat.2020.11.030.

[17] A. Gómez-Ramírez, J. Cotrino, R.M. Lambert, A.R. González-Elipe, Efficient synthesis of ammonia from N_2 and H_2 alone in a ferroelectric packed-bed DBD reactor, Plasma Sources Science and Technology. 24 (2015). https://doi.org/10.1088/0963-0252/24/6/065011.

[18] X. Hu, X. Zhu, X. Wu, Y. Cai, X. Tu, Plasma-enhanced NH_3 synthesis over activated carbon-based catalysts: Effect of active metal phase, Plasma Processes and Polymers. 17 (2020). https://doi.org/10.1002/ppap.202000072.

[19] K.H.R. Rouwenhorst, L. Lefferts, On the mechanism for the plasma-activated N_2 dissociation on Ru surfaces, Journal of Physics D: Applied Physics. 54 (2021). https://doi.org/10.1088/1361-6463/ac1226 .

[20] C. Smith, A.K. Hill, L. Torrente-Murciano, Current and future role of Haber-Bosch ammonia in a carbon-free energy landscape, Energy and Environmental Science. 13 (2020) 331–344. https://doi.org/10.1039/c9ee02873k.

[21] Y. Uytdenhouwen, V. Meynen, P. Cool, A. Bogaerts, The potential use of core-shell structured spheres in a packed-bed DBD plasma reactor for CO_2 conversion, Catalysts. 10 (2020). https://doi.org/10.3390/catal10050530.

[22] J. Kruszelnicki, K.W. Engeling, J.E. Foster, M.J. Kushner, Interactions between atmospheric pressure plasmas and metallic catalyst particles in packed bed reactors, Journal of Physics D: Applied Physics. 54 (2020) 104001. https://doi.org/10.1088/1361-6463/abcc92.

[23] B.S. Patil, *Plasma (catalyst) - assisted nitrogen fixation: reactor development for nitric oxide and ammonia production*, Eindhoven: Technische Universiteit Eindhoven, 2017.

[24] COMSOL Multiphysics v.5.5. www.comsol.com (2019).

[25] K. van Laer, A. Bogaerts, How bead size and dielectric constant affect the plasma behaviour in a packed bed plasma reactor: A modelling study, Plasma Sources Science and Technology. 26 (2017) 085007. https://doi.org/10.1088/1361-6595/aa7c59.

[26] K. van Laer, A. Bogaerts, Fluid modelling of a packed bed dielectric barrier discharge plasma reactor, Plasma Sources Science and Technology. 25 (2015) 015002. https://doi.org/10.1088/0963-0252/25/1/015002.

[27] K.H.R. Rouwenhorst, L. Lefferts, Feasibility Study of Plasma-Catalytic Ammonia Synthesis for Energy Storage Applications, Catalysts 2020, Vol. 10, Page 999. 10 (2020) 999. https://doi.org/10.3390/catal10090999.

[28] J. Hong, S. Pancheshnyi, E. Tam, J.J. Lowke, S. Prawer, A.B. Murphy, Kinetic modelling of NH_3 production in N_2–H_2 non-equilibrium atmospheric-pressure plasma catalysis, Journal of Physics D: Applied Physics. 50 (2017) 154005. https://doi.org/10.1088/1361-6463/aa6229.

[29] T.E. Bell, L. Torrente-Murciano, H_2 Production via Ammonia Decomposition Using Non-Noble Metal Catalysts: A Review, Topics in Catalysis. 59 (2016) 1438–1457. https://doi.org/10.1007/s11244-016-0653-4.

[30] T. Trickl, E.F. Cromwell, Y.T. Lee, A.H. Kung, State-selective ionization of nitrogen in the $X^2\Sigma^+_g v_+=0$ and $v_+=1$ states by two-color (1+ 1) photon excitation near threshold, The Journal of Chemical Physics. 91 (1998) 6006. https://doi.org/10.1063/1.457417.

[31] D. Zhou, R. Zhou, R. Zhou, B. Liu, T. Zhang, Y. Xian, P.J. Cullen, X. Lu, K. (Ken) Ostrikov, Sustainable ammonia production by non-thermal plasmas: Status, mechanisms, and opportunities, Chemical Engineering Journal. 421 (2021). https://doi.org/10.1016/j.cej.2021.129544.

[32] M.L. Carreon, Plasma catalytic ammonia synthesis: State of the art and future directions, Journal of Physics D: Applied Physics. 52 (2019). https://doi.org/10.1088/1361-6463/ab3b2c.

Chapter 7

Ammonia Decomposition by Plasma-Catalysis. Role of a Metal Catalyst*

7.1. Introduction

As mentioned in **Chapter 1**, the so-called *second ammonia revolution* is concerned with the use of ammonia as a hydrogen vector for its use in fuel cells [1]. The easier handling and transportation of ammonia with respect to that hydrogen itself offers advantages for the use of this compound as a source of hydrogen. Therefore, the envisaged back-transformation of ammonia justifies the interest in ammonia for hydrogen production, a decomposition process also known as the *ammonia to hydrogen* process. This reaction is characterized by a standard molar enthalpy of 54.4 kJ/mol, much lower than that of the water splitting reaction (285.8 kJ/mol) [2].

The ammonia decomposition process has been traditionally done at high temperatures, particularly when carrying out this process at atmospheric pressure. For example, S.-F. Yin *et al.* reported in 2004 that 99.9% decomposition of ammonia is induced by a Ru-based catalyst working at around 1000 ºC [3]. Novel catalysts based on metals such as ruthenium (Ru), iron (Fe), or nickel (Ni) have been proposed to reduce the operating temperature [4]. For example, Ru-based catalysts with potassium (K) as promoter have been reported to reduce the operating temperature up to 300 ºC [5]. However, these thermocatalytic strategies are not suitable to work at temperatures close to the operation temperature of PEM fuel cells (below 180ºC) [4] or ambient temperature. In addition, these catalytic processes require long stabilization times to reach steady-state conditions while the reactors should be large enough to be competitive from an energetic point of

* The content of this chapter is in preparation to be published as: **P. Navascués**, J. Cotrino, A. R. González-Elipe, A. Gómez-Ramírez, Ammonia to Hydrogen by Plasma-Catalysis in a Ferroelectric Packed-Bed Reactor at Ambient Conditions.

view. These restrictions do not apply to plasma-catalysis processes that can operate at small scales, have a practically zero induction time, and operate at ambient or, if required, mild temperatures.

The first studies about the ammonia decomposition using plasmas were reported in the second half of the previous century, using glow [6] and radiofrequency (RF) discharges [7,8] at low pressures. However, the interest of these investigations was mainly academic, focusing on the study of reaction mechanisms and/or the formation of hydrazine (N_2H_4), and not on the implementation of a reliable hydrogen production procedure. Due to the increasing interest in hydrogen applications, the last few years have witnessed the appearance of new plasma studies about ammonia decomposition [2], in parallel to more classical ones related to ammonia synthesis [9–11]. Thus, the *ammonia to hydrogen* process has been studied at atmospheric pressure using different plasma sources such as microwave (MW) [12,13], arc torch (GA) [14–17], and Dielectric Barrier Discharge (DBD) reactors [9,10,18–24]. Related to the latter technology, remarkable results have been obtained by L. Wang and collaborators working with cylindrical packed-bed reactors and different catalysts. However, to obtain meaningful results in terms of total decomposition yields (i.e., higher than 15%), these authors had to operate the DBD reactors at temperatures higher than 300 ºC [20–22]. To overcome this restrictive requirement, other studies have proposed the use of DBD reactors at ambient conditions of temperature and pressure but incorporating Pd-Cu membranes to separate hydrogen and unreacted ammonia [23,25]. In another approach, the addition of carrier gases to the reactant mixture has been reported to enhance the plasma activation in cylindrical DBD reactors [9–11]. However, most of these studies have an academic focus since they do not deal with pure-ammonia flows but proceed through the ignition of mixtures of ammonia and nitrogen [9,24] or helium [10] as carrier gases.

In this chapter, we study the ammonia decomposition reaction in a packed-bed reactor moderated with PZT pellets. Similarly to the study of the ammonia synthesis reaction in **Chapter 6**, the same Ru-based catalyst has been incorporated on the surface of the PZT pellets to perform the *ammonia to hydrogen* process. The ammonia decomposition yield and the energy efficiency of hydrogen production have been studied for the three experimental configurations previously discussed in **Chapter 6**. To make compatible the ammonia decomposition technology for fuel cells operation, the decomposition process has been carried out igniting pure-ammonia flows at ambient conditions of pressure and temperature.

Optical emission spectroscopy has been also used to unravel possible differences in the reaction mechanisms when a Ru-Al_2O_3 catalyst is incorporated into the barrier. Finally, the process performance of the three studied configurations has been compared with other state-of-the-art results obtained with plasma reactors. It has been concluded that the PZT-moderated packed-bed reactor can efficiently decompose ammonia at ambient conditions and that the reaction yield can be improved by adding a Ru-based catalyst to the barrier. Therefore, it is concluded that ferroelectric plasma reactors are a promising technology for hydrogen production, although further improvements in reactor performance and in the coupling of plasma discharge with hydrogen diffusion membranes will be still required to make feasible the practical use of this technology [26].

7.2. Experimental Details

The experiments have been performed with 5mm-barriers similar to those utilized in the previous chapter. The utilized barrier configurations have been designated as PZT, Al_2O_3/PZT, and Ru-Al_2O_3/PZT. The reader is referred to **section 6.3.1** in **Chapter 6** for a thorough description of the experimental details of the barriers and the physicochemical characterization of the modified pellets.

This study has been carried out at atmospheric pressure and ambient temperature (note that a slight drift in temperature up to 30º was detected during operation). The experiments were carried out at a fixed frequency of 5 kHz, varying the voltage amplitude between 1 and 2.5 kV to analyze the ammonia decomposition process as a function of the effective distribution of electric field in the packed-bed barrier. Repeated measurements showed that the experimental error was in the order of 10%. Pure-ammonia discharges have been ignited for a flow rate of 9 sccm.

7.3. Results and Discussion

7.3.1. Electrical Behavior of the Packed-bed Reactor

In **sections 6.2** and **6.3.2** of the previous chapter, the electrical behavior and electric field distribution within the barrier have been assessed based on impedance measurements and Comsol Multiphysics simulations. We concluded the following: (1) the incorporation of Ru particles seems to decrease the equivalent resistance through the barrier and (2) the alumina coating in the Al_2O_3/PZT configuration reduces the effective electric field intensity in the inter-pellet space. In addition to this electrical characterization in the absence of plasma, in this chapter, we analyze the electrical response (i.e., *V(t)* and *I(t)* curves) of the reactor for pure-ammonia plasma discharges. **Figure 7.1(a)** shows the *I(t)* plots acquired for the three reactor configurations at the maximum applied voltage of 2.5 kV. The evolution of the current intensity of these curves follows the same trend that for N_2+H_2 mixtures: Ru-Al_2O_3/PZT>PZT>Al_2O_3/PZT. This tendency was also obtained for all the applied voltages, as shown in the bar-plots of **Figure 7.1(b)** representing the average power as a function of applied voltage. It is noteworthy in this plot that no data are provided for the PZT and Al_2O_3/PZT configurations for the lowest essayed voltages (equal or lower than 1.25 kV), simply because plasma was not ignited under these operating conditions. This means that the addition of Ru particles, likely in metallic form, promotes the ignition of plasma discharges at lower applied voltages.

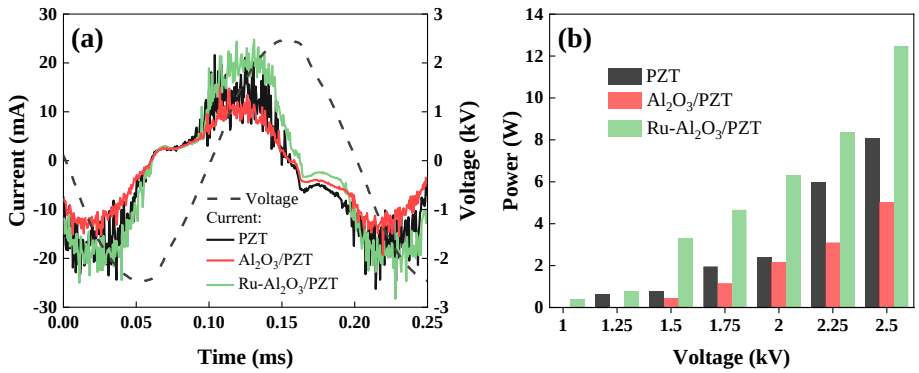

Figure 7.1. Electrical characterization of pure-ammonia discharges at ambient temperature for the three barrier configurations: (a) *V(t)* and *I(t)* curves during plasma ignition at 2.5 kV. (b) Power values obtained for the entire range of voltage amplitudes applied in this study (power values are not provided when no ignition was detected). Operating conditions: 9 sccm NH_3 and frequency fixed at 5kHz.

7.3.2. Ammonia Decomposition at Ambient Temperature

Pure-ammonia discharges have been ignited for the electrical operating conditions described in the previous section. N_2 and H_2 are obtained as unique reaction products, as can be observed in the QMS spectra in **Figure 7.2**. In comparison with the spectrum of ammonia flow before the plasma ignition, the mass spectrum acquired after plasma ignition shows an increase in the intensity of the peaks associated to H_2 (m/z=2) and N_2 (m/z=28), as well as a decrease in the peaks associated to NH_3 (m/z=17 and 16). **Figure 7.2** also shows that no signals due to hydrazine (N_2H_4, m/z=32) are detected, indicating that this is not a reaction product under our operating conditions. This result agrees with those obtained at atmospheric pressure by Wang *et al.* [15,16] or M. Akiyama *et al.* [9] and stresses the interest and potential of the plasma technology to produce pure hydrogen to feed fuel cells.

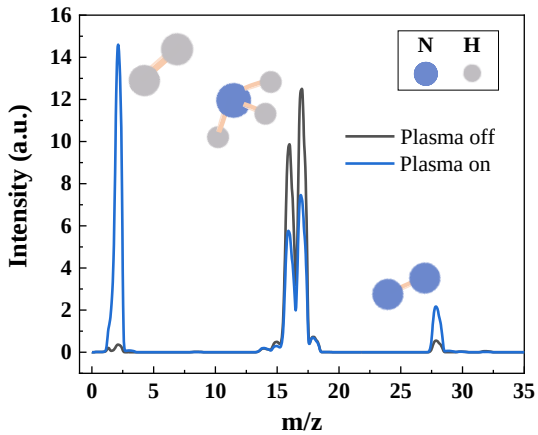

Figure 7.2. QMS spectra recorded at ambient temperature before and after igniting a discharge of pure ammonia. Spectra show the increase in the signals associated to H_2 (m/z=2) and N_2 (m/z=28) and the decrease in the bands associated to NH_3 (m/z=17 and 16). Operating conditions: Ru-Al_2O_3/PZT configuration, 5 kHz, and 2.5 kV (12.5 W).

The *ammonia to hydrogen* reaction has been studied in this thesis for the three selected barrier configurations. **Figure 7.3** shows the evolution with the applied voltage of the ammonia decomposition yield and the energy efficiency for hydrogen production. It is apparent in these plots that, for the three packed-beds, the decomposition rate clearly increases with voltage (see **Figure 7.3(a)**), while the energy efficiency decreases slightly (see **Figure 7.3(b)**). These tendencies are

similar to those obtained for other plasma-assisted decomposition reactions such as the CO_2 splitting reaction [27], a process that is also studied in this thesis (**Chapter 8**). The Ru-Al_2O_3/PZT configuration renders the highest decomposition rate, reaching 40% of ammonia decomposition at the maximum applied voltage (see **Figure 7.3(a)**). Under similar conditions, the PZT and Al_2O_3/PZT configurations render lower decomposition rate values, reaching maxima of 34% and 26% at the highest voltage, respectively. Meanwhile, curves in **Figure 7.3(b)** show that for the three configurations the process is characterized by similar energy efficiencies ranging between 30 and 40 LH_2/kWh for operation voltages higher than 1.5 kV. This is highlighted by a yellow band in the figure (i.e., corresponding to reaction yields higher than 5%; for lower decomposition yields, small errors in this parameter highly affect the EE values).

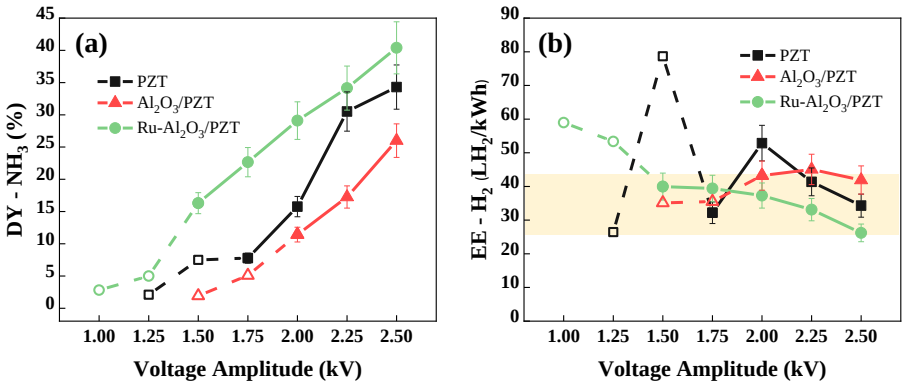

Figure 7.3. Evolution of the ammonia decomposition yield (a) and the energy efficiency for hydrogen production (b) as a function of the applied voltage amplitude. Data corresponding to low reaction yields are plotted with empty dots and dash lines, while the other data are plotted with solid markers and lines. The yellow band in this plot highlights the energy yield range obtained for the three configurations for voltages higher than 1.5 kV. Experiments were carried out at ambient temperature, a 9 sccm NH_3 flow rate, and a frequency of 5 kHz.

Interestingly, when decomposition yield and energy efficiency are plotted as a function of the applied power, overlapped curves were obtained (see **Figure 7.4**). The overlapping of the three curves observed in **Figure 7.4(a)** suggests that, in first instance, the percentage of ammonia decomposition depends on the intensity of the discharge, i.e., it is mainly affected by the differences in the electric field distribution from a configuration to another, as discussed in **Chapter 6**. Accordingly, it can be suggested that the involved mechanistic processes do not require very high electron energies to induce the decomposition of the ammonia

molecule. Several facts support this assessment. For example, the dissociation energy of the first H-NH_2 bond of the ammonia molecule is 4.7 eV, followed by 4.0 and 3.4 for the H-NH and N-H bonds in the NH_2 and NH intermediates, respectively [2]. These energy barriers are low in comparison with the dissociation of the N-N bond in the N_2 molecule (i.e., 9.8 eV) [28], which was considered a limiting step for the synthesis of ammonia (c.f., **Chapters 5 and 6)**. This hypothesis also agrees with the fact that electrons promoting intermediate reactions (*E 7.1 - E 7.3*) require relatively low threshold energies of 4, 5.6, and 8.6 eV, respectively [29]:

$$e^- + NH_3 \rightarrow NH + H_2 + e^- \quad (E\ 7.1)$$

$$e^- + NH_3 \rightarrow NH_2 + H + e^- \quad (E\ 7.2)$$

$$e^- + NH_3 \rightarrow NH + 2H + e^- \quad (E\ 7.3)$$

It is noteworthy in this regard that the EEDFs for the three studied configurations should be characterized by average values equal or higher than the threshold energies of these reactions and that, therefore, some of the secondary electrons appearing at the right hand of reactions *E 7.1 - E 7.3* may effectively intervene in new N-H breaking processes.

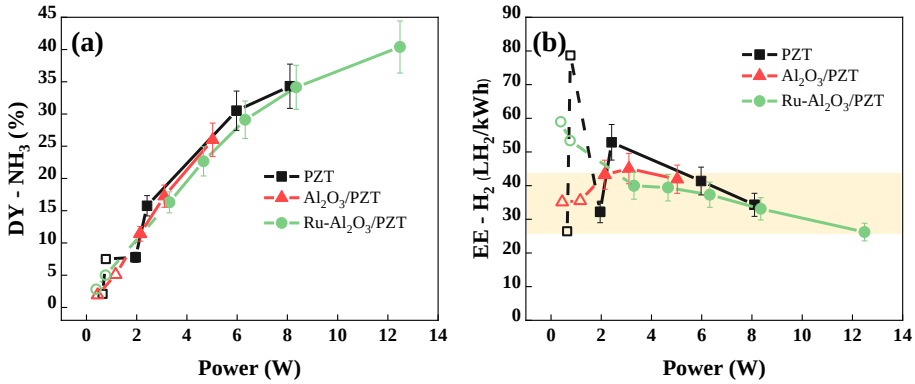

Figure 7.4. Evolution of the ammonia decomposition yield (a) and the energy efficiency for hydrogen production (b) as a function of the consumed power. Data corresponding to low reaction yields are plotted with empty dots and dash lines, while data at higher power are plotted with solid markers and lines. The yellow band in the energy efficiency plot highlights the energy yield range obtained for the three configurations for powers higher than 2 W. Experiments were carried out at ambient temperature, a 9 sccm NH_3 flow rate, a frequency of 5 kHz, and voltage amplitudes between 1 and 2.5 kV.

The previous assessment only considers electron-impact pathways occurring in the plasma phase. However, plasma reactions do not disregard the possibility of other processes taking place at the surface of pellets. To shed some light on this possibility, NH_3 discharges for the PZT and the Ru-Al_2O_3/PZT configurations have been examined by OES. The Al_2O_3/PZT configuration – which rendered the lowest decomposition rate values – has been discarded for this analysis to simplify the discussion.

7.3.3. Intermediate Species Involved in the Decomposition of Ammonia at Ambient Temperature

Figures 7.5(a) and (c) show a series of emission spectra obtained in pure-ammonia discharges for the PZT and Ru-Al_2O_3/PZT configurations at increasingly higher voltages. Similarly than in the ammonia synthesis reaction (see **Chapter 6**), these spectra are characterized by bands due to NH ($[A^3\Pi \rightarrow X^3\Sigma^-]$), N_2 (second positive system), and N_2^+ (first negative system) excited species, likely formed by the excitation of intermediates resulting from the NH_3 decomposition (i.e., NH species) and reaction products (i.e., N_2). Note that for the lower voltage amplitudes employed in this study, i.e., 1.0 kV and 1.25 kV, the emission intensity was negligible. **Figures 7.5(b)** and **7.5(d)** show the evolution of the emission intensity of the NH-band (336 nm) and the ammonia decomposition yield as a function of consumed power. It is apparent in these plots that the NH-band emission intensity increases with the consumed power, following in both configurations a tendency similar to that found for the ammonia decomposition yield (c.f., **Figures 7.5(b)** and **7.5(d)**).

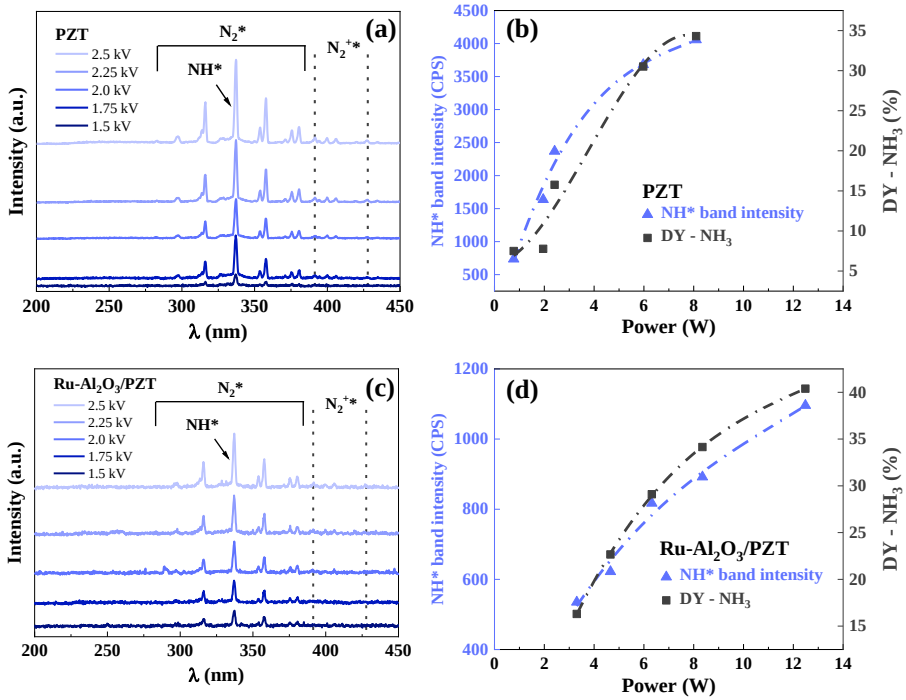

Figure 7.5. OES analysis of the 200-450 nm spectral zone for the (a-b) PZT and (c-d) Ru-Al_2O_3/PZT configurations: (a-c) Spectrum acquired at different voltage amplitudes and (b-d) evolution of the intensity of the NH-band (336.0 nm) and the ammonia decomposition yield with the consumed power. Operating conditions: 9 sccm NH_3, 5 kHz, voltage varied between 1.5 and 2.5 kV, ambient temperature.

In first instance, the similar evolution of the NH^* emission intensity for the two configurations supports that this species is a common reaction intermediate of the ammonia decomposition reaction. However, to properly assess possible differences between the two experimental conditions, i.e., PZT and Ru-Al_2O_3/PZT configurations, relative intensity and not absolute intensity values should be compared. With this purpose, we have analyzed the emission spectra in the 450-800 nm range where signals stemming from NH_3^* species can be monitored [30]. Relying on these spectral lines and working with a Fe-based catalyst in a packed-bed reactor at 400 ºC, L. Wang *et al.* [20] found a first continuous increase with power in the intensity of NH_3^* bands – an evolution that runs parallel to the NH_3 decomposition rate – that then decreases at high powers. This evidence was claimed by these authors as a hint of the involvement of the metal Fe catalyst in the reaction process. For the two reactor configurations considered in our experiment, **Figures 7.6(a)** and **7.6(c)** show that NH_3 Schuster's bands located

between 564 and 567 nm [30] are also detected. Additionally, the H_α line (656.3 nm [31]) is clearly detected for the PZT configuration, while hints of it are also observed in the less-resolved spectra recorded for the Ru-Al_2O_3/PZT configuration. The other bands between 560 and 900 nm in these spectra are second order N_2-bands. For the two configurations, the plots in **Figures 7.6(b)** and **7.6(d)** of the evolution with the consumed power of the emission intensity of the NH_3^* Schuster's bands show an initial increase with power (as the NH_3 production increases) and a flattering at high power values, a tendency that is particularly clear for the Ru-Al_2O_3/PZT configuration, where these bands depict a practically constant intensity for powers higher than 4 W. Regarding this intensity evolution, it is also noteworthy that for the PZT configuration the NH_3^* intensity increases from 500 CPS at 1 W to around 900 CPS at 8 W, while for the Ru-Al_2O_3/PZT configuration it only increases by a meager amount from 410 CPS at 3 W to 480 CPS at 12 W.

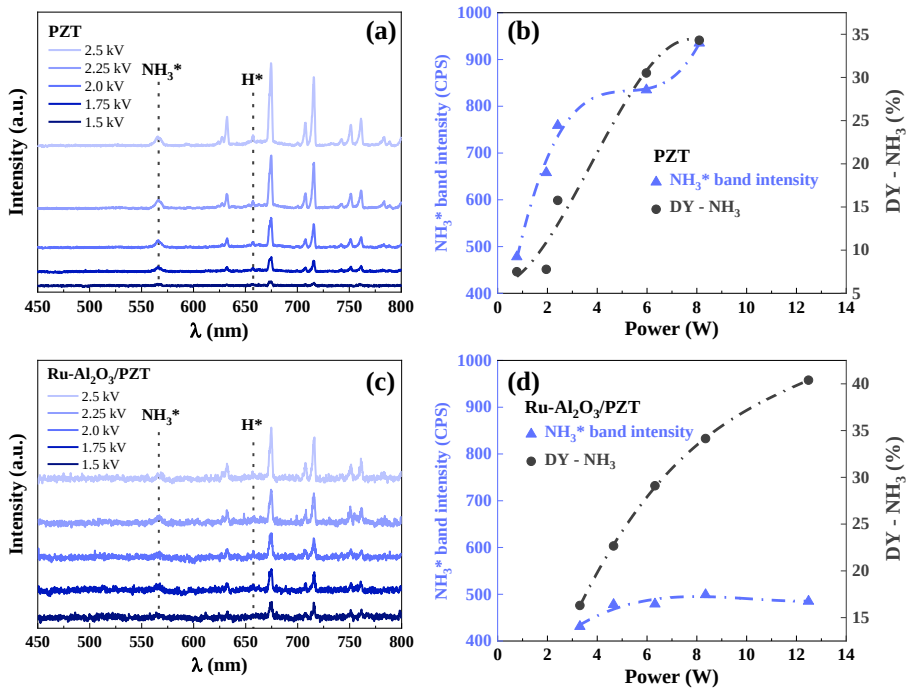

Figure 7.6. OES analysis of the 450-800 nm spectral zone for the (a-b) PZT and (c-d) Ru-Al_2O_3/PZT configurations: (a-c) Spectrum acquired at different voltage amplitudes and (b-d) evolution of the intensity of the NH_3 Schuster's bands (564-567 nm) and the ammonia decomposition yield with the consumed power. Operating conditions: 9 sccm NH_3, 5 kHz, voltage varied between 1.5 and 2.5 kV, ambient temperature.

The evolution of the intensities of the NH^* (**Figures 7.5(b-d)**) and NH_3^* (**Figures 7.6(b-d)**) bands with power, particularly the flattening of the intensity of the latter for the Ru-Al_2O_3/PZT configuration, suggests that the probability for the direct excitation of the NH_3 molecule is relatively higher at low power and for the PZT configuration, while other processes should gain importance for other operating conditions. Therefore, we propose that for low applied voltages (i.e., low consumed power in our experiment), the *ammonia to hydrogen* process might also involve reaction pathways such as:

$$e^- + NH_3 \rightarrow NH_3^* + e^- \quad (E\ 7.4)$$

$$e^- + NH_3^* \rightarrow NH_X + H_Y + e^- \quad (E\ 7.5)$$

However, at higher voltages (i.e., high power in our experiment), while the energy of the plasma electrons increases, the ammonia decomposition mechanism might also involve dehydrogenation reactions by electron impact such as *E 7.1 - E 7.3* discussed in the previous section. It is also likely that the relatively higher energy of the electrons expected for the Ru-Al_2O_3/PZT configuration would favor processes *E 7.1 - E 7.3* as the main responsible for the ammonia decomposition, which would take place without requiring the previous formation of NH_3^*. This would agree with the practically constant intensity of the NH_3^* bands depicted in **Figure 7.6(d)**.

Furthermore, the analysis of the ratio between the intensities of the two reaction intermediates, NH^* and NH_3^*, with the applied power provides additional information about the reaction mechanisms. **Figure 7.7** shows the plots of the NH^*/NH_3^* band intensity ratio against the power for the two studied configurations. The plots indicate that for similar consumed powers, the band intensity ratio for PZT doubles the value for the Ru-Al_2O_3/PZT configuration. It is also apparent that, for the whole interval of considered powers, the ratio varies by a factor of 3 for the PZT (interval from 1.5 to 8 W), but only by a factor of 2 or for the Ru-Al_2O_3/PZT configuration (interval from 2.5 to 12 W). These differences not only support the proposal above of a different involvement degree of intermediate processes (*E 7.1 - E 7.3* vs *E 7.4 - E 7.5*) but also the possibility that specific surface reactions may take place for the Ru-Al_2O_3/PZT configuration. In concrete, we propose that part of the plasma activated NH_3^* and, with a higher probability, NH^* species, would be removed from the plasma phase by adsorption on the surface of the metal particles where they will decompose into N_2 and H_2 molecules, which would be subsequently desorbed.

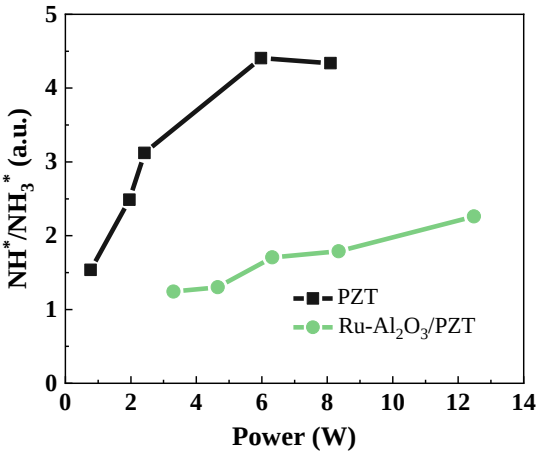

Figure 7.7. NH^* to NH_3^* intensity ratio (i.e., NH^*/NH_3^*) for the PZT and the Ru-Al_2O_3/PZT configurations versus the consumed power. Operating conditions: 9 sccm NH_3, 5 kHz, voltage varied between 1.5 and 2.5 kV, ambient temperature.

The involvement of the metal catalyst particles in the reaction mechanism was indirectly proved by L. Wang *et al.* showing the formation of Fe_3N and Fe_4N compounds by X-ray diffraction [2] and through desorption measurements using the ^{15}N isotope [19]. Involvement of ruthenium particles in the reaction mechanism was also suggested in our case by the XPS analysis of Ru-Al_2O_3/PZT used pellets. **Figure 7.8** shows the N1s spectral zones corresponding to pellets before and after successive plasma ammonia-decomposition experiments. The pellets exposed to the pure-ammonia plasma depict a small but not negligible contribution at around 397-398 eV, superimposed on a spurious common feature at around 400 eV. This feature at 397-398 eV is compatible with a metal nitride [32] and supports the formation of a ruthenium nitride upon exposure to an ammonia plasma.

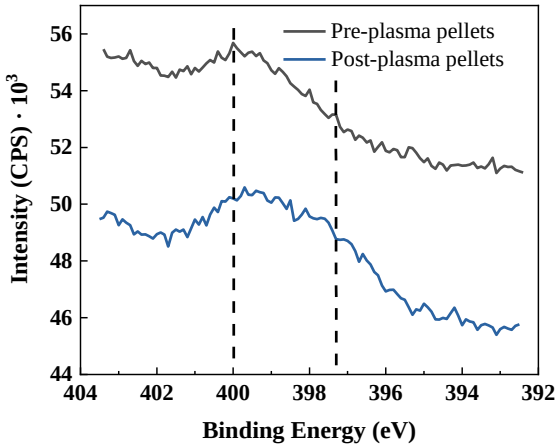

Figure 7.8. XPS analysis of the N1s signal of a set of Ru-Al_2O_3/PZT pellets acquired before (gray line) and after (blue line) successive plasma exposures.

Therefore, although the involvement of surface reaction pathways cannot be discarded for the PZT configuration as proposed in **Chapter 5** of this thesis work, a specific surface contribution would exist for the Ru-Al_2O_3/PZT configuration due to the presence of metal particles. In practical terms, the involvement of metal particles in the ammonia decomposition reactions would be responsible for the observed increase in ammonia decomposition yield at 12 W for the Ru-Al_2O_3/PZT configuration (c.f., **Figure 7.4(a)**). Additionally, this could be the main factor making that the similar energy efficiency for H_2 production found for the PZT and Ru-Al_2O_3/PZT configurations up to 8 W (c.f., **Figure 7.4(b)**) still decreases at 12 W for the latter configuration.

7.4. State-of-the-art Assessment of Efficiency of Plasma-assisted *Ammonia to Hydrogen* Processes

The efficiency of the *ammonia to hydrogen* conversion by means of thermal catalysis is still limited by the temperature of operation. This restriction is clearly evidenced in the recent review of I. Lucentini *et al.*, who summarized the use of different catalysts at temperatures around 300 and 500 ºC [4]. Taking into account the temperature requirements to make this technology compatible with the operation of a PEM fuel cell [2] (working temperature lower than 180 ºC [32]), much work is being carried out trying to decrease the operating temperature and to replace expensive noble metal catalysts by cheaper and more abundant elements like iron (Fe), cobalt (Co), and nickel (Ni) [33]. Additional requirements are the design of processes working with pure flows of ammonia (not with mixtures of other gases), the increase of the NH_3 decomposition yield and the decrease of the operation temperature [34]. A summary of results by using different plasma technologies is included in **Table 7.1**, indicating the operating temperature, the catalyst utilized, the decomposition yield, and the consumed power in each case.

Table 7.1. Overview of some *ammonia to hydrogen* results reported in the literature with different plasma technologies, including those of this study. Pure flows of ammonia were treated at atmospheric pressure and different temperatures.

Plasma technology	T (ºC)	Catalyst	DY-NH_3 (%)	Power (W)	Ref.
Packed-bed reactors	25	Ru-Al_2O_3/PZT	40	13	This chapter
	25	PZT	34	8	This chapter
	450	Co/SiO_2	99	30	[18]
	400	Improved Co/SiO_2	98	34	[21]
	350	Improved Co/SiO_2	40	27	[21]
Microwave (MW)	350	Co/AC*	98	100-120	[12]
Arc Torch	25 (1400)**	NiO/Al_2O_3	26	700	[17]

* Amorphous carbon; ** The gas temperature increases up to this value.

An outstanding result in this table corresponds to the studies of L. Wang and collaborators, who using cylindrical packed-bed reactors at 350ºC with a Co/SiO_2 catalyst obtained a 40% of ammonia decomposition [21]. In comparison with this series of results, it is remarkable the similar decomposition yield results obtained in this thesis work at ambient temperature and much lower consumed power. The results obtained in this chapter are also remarkable when compared with other DBD and packed-bed reactors results, as shown in **Table 7.2**. The interest of our approach is further highlighted by the fact that most papers in this table study non-pure ammonia streams, which is a clear drawback from the point of view of practical applications [9,10,24].

Table 7.2. Overview of selected *ammonia to hydrogen* results obtained with DBD and packed-bed reactors during the last few years at ambient conditions of pressure and temperature (pure-ammonia and mixtures).

Configuration	**Catalyst**	**Gas**	**DY-NH_3 (%)**	**Power (W)**	**Ref.**
Packed-bed reactor	Ru-Al_2O_3/PZT pellets	100% NH_3	40.4	13	This chapter
	PZT pellets		34.3	8	This chapter
	Wool-like wires	5% NH_3, 95 % N_2	99	50	[9]
	$MgTiO_3$ powder*	2.4 % NH_3, 97.6 % N_2	44.4	20	[24]
	Ni/SiO_2 powder**	9% NH_3, 91% N_2 (+He)	42.0	11	[10]
DBD membrane reactor	-	100% NH_3	24	400	[23]

The temperature of the reactor chamber can increase up to (*) 172ºC and (**) 155 ºC.

The efficiency of the *ammonia to hydrogen* process studied in this chapter can be compared with other *hydrogen-production* plasma processes carried out using DBD plasmas (for example, the reforming of methane, previously studied by our research group using PZT as moderator in a packed-bed reactor [35]). **Table 7.3** shows a comparison between the results in this chapter and others for wet, oxidative, and dry reforming of methane. These data correspond to the maximum rate of H_2 produced (LH_2/h) and include the required energy efficiency values for

hydrogen production (LH_2/kWh). Clearly, the *ammonia to hydrogen* process outperforms the methane reforming reactions and positions this plasma reaction as a promising zero-CO_X emission hydrogen production technology.

Table 7.3. Comparison between the results of this chapter and previous studies of our research group regarding H_2 production using PZT as discharge moderator in packed-bed reactors. The "H_2 production rate" column shows the maximum values obtained for each process.

Process	**Discharge moderator**	**H_2 production rate (LH_2/h)**	**Energy efficiency (LH_2/kWh)**	**Ref.**
Ammonia decomposition	Ru-Al_2O_3/PZT	0.33	27	This chapter
	PZT	0.28	34	This chapter
Wet reforming of methane	PZT	0.19	9.6	[35]
Oxidative reforming of methane	PZT	0.36	20	[35]
Dry reforming of methane	PZT	0.17	6.8	[35]

We would like to conclude this comparative analysis indicating that to envisage an improvement in process efficiency would imply the separation of hydrogen molecules from the mixture of unreacted ammonia and nitrogen. This would be possible incorporating a hydrogen selective membrane to the reactor, as in studies of Hayakawa *et al.* using a DBD *membrane reactor* [23,25], or in other studies in thermal catalysis [26].

7.5. Conclusions

The *ammonia to hydrogen* process (i.e., the decomposition of NH_3 into N_2 and H_2) has been studied in a ferroelectric-moderated packed-bed reactor at ambient conditions of pressure and temperature. As in **Chapter 6**, three different barriers (PZT, Al_2O_3/PZT, and Ru-Al_2O_3/PZT configurations) have been essayed to properly study the effect of the incorporation of a metal catalyst onto the surface of the ferroelectric pellets. The Ru-Al_2O_3/PZT configuration provides the highest

reaction yield, with 40% of ammonia decomposition, followed by decomposition rates of 34% and 26% for the PZT and the Al_2O_3/PZT configurations, respectively. Values of reaction yield have been correlated with the consumed power for each experimental condition. Similar tendencies with the consumed power have been obtained both for reaction yield and energy efficiency in the three studied barriers. This fact suggests that the essayed experimental configurations are characterized by EEDFs with energies high enough to efficiently promote the plasma decomposition of the NH_3 molecules by electron-impact processes. Maximum energy efficiency values ranging from 30 and 40 LH_2/kWh have been obtained for the three studied configurations.

The plasma has been examined by OES to analyze possible differences in the reaction mechanisms between a ferroelectric barrier (i.e., PZT configuration) and the barrier with a catalyst added (i.e., Ru-Al_2O_3/PZT configuration). The evolution of the emission intensity of NH^* and NH_3^* intermediates with the consumed power (and related to the decomposition yield) depicts a similar behavior for the NH^* emission bands for both configurations, while the emission of NH_3^* tends to a plateau for the Ru-Al_2O_3/PZT configuration. Additionally, relying on the analysis of the NH^*/NH_3^* emission intensity ratio as a function of power, we suggest that the relatively smaller population of NH^* species for the Ru-Al_2O_3/PZT configuration is related to surface dehydrogenation processes taking place on the surface of the metal catalyst.

Finally, the decomposition results obtained in this study have been compared with those reported by other authors using the plasma technology for the *ammonia to hydrogen* process, as well as with previous results of our research group regarding the reforming of methane in a PZT-moderated packed-bed reactor. It is concluded that the *ammonia to hydrogen* process working with pure ammonia flows at ambient conditions of pressure and temperature is an efficient route to produce H_2 at moderate power values without producing CO_x emissions.

7.6. References

[1] C. Smith, A.K. Hill, L. Torrente-Murciano, Current and future role of Haber-Bosch ammonia in a carbon-free energy landscape, Energy and Environmental Science. 13 (2020) 331–344. https://doi.org/10.1039/c9ee02873k.

[2] Yi Y., Wang L., Guo H. (2019) Plasma-Catalytic Decomposition of Ammonia for Hydrogen Energy. In: Tu X., Whitehead J., Nozaki T. (eds) Plasma Catalysis. Springer Series on Atomic, Optical, and Plasma Physics, vol 106. Springer, Cham. https://doi.org/10.1007/978-3-030-05189-1_7.

[3] S.F. Yin, Q.H. Zhang, B.Q. Xu, W.X. Zhu, C.F. Ng, C.T. Au, Investigation on the catalysis of COx-free hydrogen generation from ammonia, Journal of Catalysis. 224 (2004) 384–396. https://doi.org/10.1016/J.JCAT.2004.03.008.

[4] I. Lucentini, X. Garcia, X. Vendrell, J. Llorca, Review of the Decomposition of Ammonia to Generate Hydrogen, Industrial and Engineering Chemistry Research. 60 (2021) 18560–18611. https://doi.org/10.1021/acs.iecr.1c00843.

[5] M. Pinzón, E. Ruiz-López, A. Romero, A.R. de la Osa, P. Sánchez, A. de Lucas-Consuegra, Electrochemical activation of Ru catalyst with alkaline ion conductors for the catalytic decomposition of ammonia, Molecular Catalysis. 511 (2021) 111721. https://doi.org/10.1016/J.MCAT.2021.111721.

[6] J.C. Devins, M. Burton, Formation of Hydrazine in Electric Discharge Decomposition of Ammonia, Journal of the American Chemical Society. 76 (2002) 2618–2626. https://doi.org/10.1021/JA01639A006.

[7] R. d'Agostino, F. Cramarossa, S. de Benedictis, G. Ferraro, Kinetic and spectroscopic analysis of NH_3 decomposition under R.F. Plasma at moderate pressures, Plasma Chemistry and Plasma Processing 1981 1:1. 1 (1981) 19–35. https://doi.org/10.1007/BF00566373.

[8] J.E. Nicholas, A.I. Spiers, N.A. Martin, Kinetics and mechanism in the decomposition of NH_3 in a radio-frequency pulse discharge, Plasma Chemistry and Plasma Processing 1986 6:1. 6 (1986) 39–51. https://doi.org/10.1007/BF00573820.

[9] M. Akiyama, K. Aihara, T. Sawaguchi, M. Matsukata, M. Iwamoto, Ammonia decomposition to clean hydrogen using non-thermal atmospheric-pressure plasma, International Journal of Hydrogen Energy. 43 (2018) 14493–14497. https://doi.org/10.1016/j.ijhydene.2018.06.022.

[10] F. Gorky, A. Best, J. Jasinski, B.J. Allen, A.C. Alba-Rubio, M.L. Carreon, Plasma catalytic ammonia synthesis on Ni nanoparticles: The size effect, Journal of Catalysis. 393 (2021) 369–380. https://doi.org/10.1016/j.jcat.2020.11.030.

[11] F. Gorky, J.M. Lucero, J.M. Crawford, B.A. Blake, S.R. Guthrie, M.A. Carreon, M.L. Carreon, Insights on cold plasma ammonia synthesis and decomposition using alkaline earth metal-based perovskites, Catalysis Science and Technology. 11 (2021) 5109–5118. https://doi.org/10.1039/d1cy00729g.

[12] R. Can Seyfeli, D. Varisli, Ammonia decomposition reaction to produce COx-free hydrogen using carbon supported cobalt catalysts in microwave heated reactor system, International Journal of Hydrogen Energy. 45 (2020) 34867–34878. https://doi.org/10.1016/j.ijhydene.2020.01.124.

[13] M. Akca, D. Varisli, Performance of Co-Fe@Alumina catalysts in comparison to monometallic Co@Alumina and Fe@Alumina catalysts for microwave assisted COx-free hydrogen production, Molecular Catalysis. 485 (2020). https://doi.org/10.1016/j.mcat.2020.110823.

[14] M. Młotek, M. Perron, K. Krawczyk, Ammonia Decomposition in a Gliding Discharge Plasma, Energy Technology. 9 (2021). https://doi.org/10.1002/ente.202100677.

[15] Y. Zhao, L. Wang, J. Zhang, H. Guo, Enhancing the ammonia to hydrogen (ATH) energy efficiency of alternating current arc discharge, International Journal of Hydrogen Energy. 39 (2014) 7655–7663. https://doi.org/10.1016/j.ijhydene.2014.03.128.

[16] Y. Zhao, L. Wang, J. Zhang, W. Gong, H. Guo, Decomposition of ammonia by atmospheric pressure AC discharge: Catalytic effect of the electrodes, Catalysis Today. 211 (2013) 72–77. https://doi.org/10.1016/j.cattod.2013.03.027.

[17] Q.F. Lin, Y.M. Jiang, C.Z. Liu, L.W. Chen, W.J. Zhang, J. Ding, J.G. Li, Instantaneous hydrogen production from ammonia by non-thermal arc plasma combining with catalyst, Energy Reports. 7 (2021) 4064–4070. https://doi.org/10.1016/j.egyr.2021.06.087.

[18] L. Wang, Y. Yi, Y. Zhao, R. Zhang, J. Zhang, H. Guo, NH_3 Decomposition for H_2 Generation: Effects of Cheap Metals and Supports on Plasma-Catalyst Synergy, ACS Catalysis. 5 (2015) 4167–4174. https://doi.org/10.1021/acscatal.5b00728.

[19] L. Wang, Y. Zhao, C. Liu, W. Gong, H. Guo, Plasma driven ammonia decomposition on a Fe-catalyst: Eliminating surface nitrogen poisoning, Chemical Communications. 49 (2013) 3787–3789. https://doi.org/10.1039/c3cc41301b.

[20] L. Wang, Y. Yi, Y. Guo, Y. Zhao, J. Zhang, H. Guo, Synergy of DBD plasma and Fe-based catalyst in NH_3 decomposition: Plasma enhancing adsorption step, Plasma Processes and Polymers. 14 (2017). https://doi.org/10.1002/ppap.201600111.

[21] L. Wang, Y.H. Yi, H.C. Guo, X.M. Du, B. Zhu, Y.M. Zhu, Highly dispersed co nanoparticles prepared by an improved method for plasma-driven NH_3 decomposition to produce H_2, Catalysts. 9 (2019). https://doi.org/10.3390/catal9020107.

[22] Y. Yi, L. Wang, Y. Guo, S. Sun, H. Guo, Plasma-assisted ammonia decomposition over Fe–Ni alloy catalysts for COx-Free hydrogen, AIChE Journal. 65 (2019) 691–701. https://doi.org/10.1002/aic.16479.

[23] Y. Hayakawa, S. Kambara, T. Miura, Hydrogen production from ammonia by the plasma membrane reactor, International Journal of Hydrogen Energy. 45 (2020) 32082–32088. https://doi.org/10.1016/j.ijhydene.2020.08.178.

[24] F. Gorky, J.M. Lucero, J.M. Crawford, B.A. Blake, S.R. Guthrie, M.A. Carreon, M.L. Carreon, Insights on cold plasma ammonia synthesis and decomposition using alkaline earth metal-based perovskites, Catalysis Science and Technology. 11 (2021) 5109–5118. https://doi.org/10.1039/d1cy00729g.

[25] Y. Hayakawa, T. Miura, K. Shizuya, S. Wakazono, K. Tokunaga, S. Kambara, Hydrogen production system combined with a catalytic reactor and a plasma membrane reactor from ammonia, International Journal of Hydrogen Energy. 44 (2019) 9987–9993. https://doi.org/10.1016/j.ijhydene.2018.12.141.

[26] J.P. Collins, J.D. Way, Catalytic decomposition of ammonia in a membrane reactor, Journal of Membrane Science. 96 (1994) 259–274. https://doi.org/10.1016/0376-7388(94)00138-3.

[27] R. Snoeckx, A. Bogaerts, Plasma technology: a novel solution for CO_2 conversion?, Chemical Society Reviews. 46 (2017) 5805–5863. https://doi.org/10.1039/c6cs00066e.

[28] The dissociation energy of the nitrogen molecule, Proceedings of the Royal Society of London. Series A. Mathematical and Physical Sciences. 236 (1956) 278–284. https://doi.org/10.1098/RSPA.1956.0135.

[29] M. Yousfi, M.D. Benabdessadok, Boltzmann equation analysis of electron-molecule collision cross sections in water vapor and ammonia, Journal of Applied Physics. 80 (1998) 6619. https://doi.org/10.1063/1.363785.

[30] J.K.G. Watson, W.A. Majewski, J.H. Glownia, Assignment of the Schuster band of ammonia, Journal of Molecular Spectroscopy. 115 (1986) 82–87. https://doi.org/10.1016/0022-2852(86)90277-8.

[31] R.W.B. Pearse and A.G. Gaydon (1965), The Identification of Molecular Spectra, 3rd ed., Chapman and Hall Ltd., England.

[32] M.G. Moreno-Armenta, J. Diaz, A. Martinez-Ruiz, G. Soto, Synthesis of cubic ruthenium nitride by reactive pulsed laser ablation, Journal of Physics and Chemistry of Solids. 68 (2007) 1989–1994. https://doi.org/10.1016/j.jpcs.2007.06.002.

[33] T.E. Bell, L. Torrente-Murciano, H_2 Production via Ammonia Decomposition Using Non-Noble Metal Catalysts: A Review, Topics in Catalysis. 59 (2016) 1438–1457. https://doi.org/10.1007/s11244-016-0653-4.

[34] Z. Wan, Y. Tao, J. Shao, Y. Zhang, H. You, Ammonia as an effective hydrogen carrier and a clean fuel for solid oxide fuel cells, Energy Conversion and Management. 228 (2021). https://doi.org/10.1016/j.enconman.2020.113729.

[35] A.M. Montoro-Damas, J.J. Brey, M.A. Rodríguez, A.R. González-Elipe, J. Cotrino, Plasma reforming of methane in a tunable ferroelectric packed-bed dielectric barrier discharge reactor, Journal of Power Sources. 296 (2015) 268–275. https://doi.org/10.1016/j.jpowsour.2015.07.038.

Chapter 8

Packed-bed Plasma Reactors as a CCU Technology to Eliminate CO_2*

8.1. Introduction

The concern about the continuous increase in carbon dioxide concentration and other greenhouse gases in Earth's atmosphere has fostered the development of new remediation strategies and technologies. One possible way to reverse this situation consists of applying Carbon Capture Storage (CCS) or Utilization (CCU) systems to either hold back or transform carbon emissions into valuable products before their release to the atmosphere [1]. Moreover, carbon dioxide conversion processes have gained much attention for the oxygen production in the CO_2 rich (95%) Mars atmosphere, where promising results have been recently obtained by the Moxie experiment carried out in the red planet applying a high temperature decomposition technique [2].

Current strategies for CO_2 elimination and revaluation face the problem of the high stability of the molecule. From a thermodynamic point of view, either its dissociation breaking or just its activation are highly demanding energetic processes (e.g., C=O doubled bound energy is 783 kJ/mol, while the Gibbs free energy of CO_2 formation is 394 kJ/mol [3]). The energetic requirements imposed by these internal energy parameters are particularly relevant if the intended process is the splitting of CO_2 into CO and O_2 induced by plasma. Plasma technologies promote this splitting through the excitation of CO_2 molecules by different elemental processes followed by a series of subsequent intermediate reactions ending up in the production of the desired products. In particular, in Dielectric Barrier Discharges (DBDs) at atmospheric pressure, electron temperatures typically vary between 1 and 20 eV [4]. This wide range enables the direct

* The content of this chapter has been published in: P. Navascués, J. Cotrino, A. R. González-Elipe, A. Gómez-Ramírez, Plasma assisted CO_2 dissociation in pure and gas mixture streams with a ferroelectric packed-bed reactor in ambient conditions. *Chemical Engineering Journal*, 430 (2022) 133066, https://doi.org/10.1016/j.cej.2021.133066

activation of the CO_2 molecule by different electron impact mechanisms through electronic excitation, ionization, or dissociation processes [5].

Due to their operational advantages, DBD reactors and packed-bed systems filled with different materials have been extensively utilized during the last decade to induce various CO_2 conversion or decomposition processes [6–11]. Examples of dielectric materials used to moderate the CO_2 plasma splitting reaction include Al_2O_3, ZrO_2, or SiO_2 beds [3,12–14]. In general, energy efficiencies around 5% have been obtained with these conventional dielectrics, with some exceptions like the 12% obtained by Ozkan *et al.* operating in burst mode instead of a conventional AC mode [15,16]. More recently, non-conventional materials such as polyurethane foams or core-shell structures have been utilized to moderate the discharges. However, their reported energy efficiencies only reach ca. 5% for meaningful splitting rates [17–19].

To overcome such an apparent energy efficiency limit of packed-bed reactors moderated with dielectric materials, ferroelectrics, particularly the most common $BaTiO_3$, and/or catalytically active beds, have been essayed as moderator materials for the splitting of CO_2 [7,11,13,20–27]. Using some of these approaches, the CO_2 plasma splitting mechanism has been analyzed seeking for procedures favoring the most efficient processes. For example, Xin Tu and collaborators have reported that catalyst surfaces with oxygen vacancies can efficiently promote the dissociation of the CO_2 molecule. Based on additional evidence, the authors proposed a decomposition mechanism triggered by the breaking of the C=O bond upon interaction with plasma electrons [20,25,26]. This mechanism differs from that proposed for the CO_2 decomposition induced in microwave (MW) and gliding arc (GA) reactors that, operating at boundary conditions between thermal and nonthermal plasmas, seem to favor a CO_2 decomposition mechanism mediated by the vibrational excitation of the molecule [28–30]. Nevertheless, in DBD and packed-bed reactors the average electron temperature is very high to efficiently induce the dissociation through vibrationally excitations, a fact that partially explains the efficiency limitations of this technology [5,31].

In this thesis, according to the conclusions of **Chapter 4** and in line with the study of *ammonia reactions* (see **Chapters 5-7**), the decomposition of CO_2 into CO and O_2 has been carried out using a PZT-moderated packed-bed reactor. The choice of this material has been guided by the intention to overcome the aforementioned energetic limit.

The motivation of the study reported in this chapter is twofold. Firstly, determining the efficiency of PZT-moderated packed-bed reactors for the splitting of CO_2. Secondly, to advance in the understanding of the basic mechanisms involved in this reaction. With this aim, $CO_2 + O_2$ mixtures have been analyzed to check the occurrence of back-reactions (i.e., the recombination of CO and O_2 to render CO_2). Furthermore, considering that in real facilities a CCU technology will deal with CO_2 combined with other gases, mixtures of CO_2 with dry air have also been studied. The results obtained show that, in the mixture containing oxygen, recombination reactions reduce the reaction yield, while an increasing energy efficiency is obtained for a mixture with 15% air. Unlike previous results in literature, where harmful N_XO_Y compounds were found as by-product of a plasma reaction of nitrogen and CO_2 [11,32], no traces of nitrogen oxides have been found under our working conditions.

8.2. Experimental Details

This study was carried out in the already described packed-bed reactor with three different barrier architectures (see **Table 8.1**). Although the main experiments were performed with a PZT barrier, for comparison, pellets of $BaTiO_3$ have been also used as discharge moderator for the CO_2 splitting reaction (BT configuration). Additionally, for some experiments with PZT, the upper electrode was covered with a ferroelectric $LiNbO_3$ plate (PZT-D configuration). As is shown in **Figure 8.1(a)**, the incorporation of this extra ferroelectric plate reduces the electric field intensity in the free space between pellets for a constant operating voltage.

Table 8.1. Experimental configurations and packed-bed characteristics utilized for the experiments in this chapter.

Configuration	Pellets diameter	Active electrode covered by the ferroelectric plate	Inter-electrode (metal-metal) distance
PZT	2 – 3 mm	No	5 mm
PZT-D	2 – 3 mm	$LiNbO_3$	5.5 mm*
BT	2 mm	No	5 mm

*Note that when incorporating the $LiNbO_3$ ferroelectric plate, the inter-electrode (metal-metal) distance is lengthened to compensate the incorporation of the plate in order to keep constant the residence time of the gases in the reactor.

Figure 8.1 shows the electric field distribution calculated using the AC/DC module of Comsol Multiphysics [33]. Electric field simulations have been done in a simplified way, as they are intended for comparison purposes. The input parameters/model design were an inter-electrode distance of 5 mm, spherical pellets with a diameter of 2 mm (applying an extra-fine mesh), and a voltage of 3.25 kV applied between the electrodes. The calculation time was around 9 seconds. Both for the PZT-D and BT configurations it was found that the electric field intensity in the inter-pellet space is smaller than in the PZT configuration. This effect can be observed in **Figure 8.1(b)**, showing anevaluation of the electric field (V/m) along the line connecting two pellets (marked as 'r' in the colour maps of **Figure 8.1(a)**). Differences in the electric field intensity in the PZT and BT configurations are due to the different value of the dielectric constant of these materials, i.e., 1900 and 1250 respectively for these two materials operating at ambient temperature (see **Chapter 4**).

The different magnitudes used for the discussion of results are: the Specific Input Energy (SIE [kJ/L]), the absolute (χ[%]) and effective (χ_{eff}[%]) CO_2 conversion rates, the energy efficiency (ζ[%]), and the carbon balance (C_B[%]) (see **Chapter 3** for the definitions).

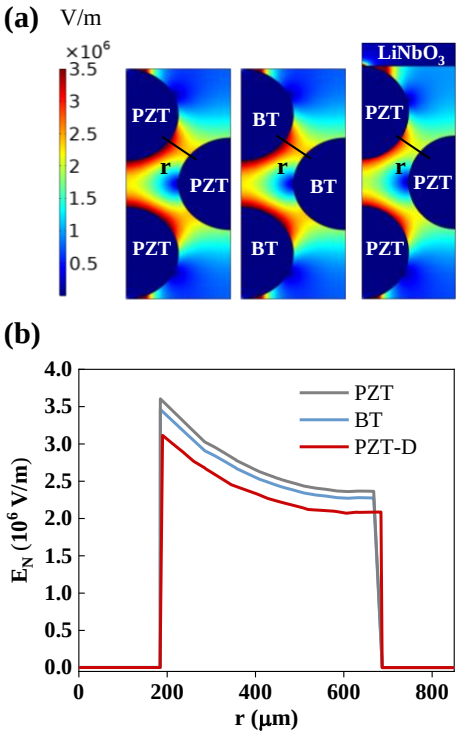

Figure 8.1. (a) Electric field distribution for the PZT (left), BT (middle), and PZT-D (right) configurations (the "r" line indicates the race points selected to evaluate the electric field). (b) Electric field distribution along the "r" line for PZT, BT, and PZT-D configurations.

All the experiments discussed in this chapter have been carried out at atmospheric pressure and ambient temperature. A fan was used to cool down the metal walls of the reactor. The voltage amplitude was varied between 2.5 and 4 kV. Most experiments were carried out for an operating frequency fixed at 1 kHz, although frequencies between 1 and 3 kHz were also used for an applied voltage of 3.25 kV. The CO_2 flow rate was fixed at 15, 25, and 40 sccm. Gas mixtures of CO_2 with O_2 and dry air were analyzed for a total flow rate of 25 sccm; CO_2 concentrations varied from 100 to 90% for O_2 mixtures and from 100% to 80% for air mixtures.

Finally, OES measurements were taken with the diffraction grating centered at 330 nm. The integration time was 0.5 s and the resolution 0.2 nm. **Table 8.2** summarizes the characteristic emission bands recorded for typical CO_2 plasmas and their association to the corresponding excited species and electronic transitions [11,34–39].

Table 8.2. Emission bands for pure CO_2 plasmas taken from [35–38].

System	Transition	λ (nm)
CO_2^+ (B)	$B^2\,\Sigma^+ \rightarrow X^2\,\Pi$	288.3 - 289.6
CO_2^+ (A): Fox, Duffendack and Barker's (FDB) System [1]	$A^2\,\Pi \rightarrow X^2\,\Pi$	304.8, 324.6, 313.9, 337.0, 337.7, 355.1, 356.5, 362.1, 369.1, 383.8, 387.0, 396.0, 412.0, 413.7
Third Positive System of CO	$b^3\,\Sigma^+ \rightarrow a^3\,\Pi$	283.3, 297.7, 313.4, 330.5, 349.3, 369.9

[1]For the Fox, Duffendack and Barker's System, only high intensity bands are shown (i.e., bands whose intensity is higher than 0.6 in a scale normalized to the most intense line)

8.3. Results and Discussion

8.3.1. Effect of PZT as Packing Material

In **Chapter 4**, it has been shown that operating packed-bed reactors with PZT reduces the breakdown voltage and enhances the electric field distribution with respect to the operation with $BaTiO_3$. It was discussed that both features contribute to reduce the power consumption and, therefore, PZT-moderated packed-bed reactors provide higher yields and efficiencies for the ammonia synthesis reaction. A first issue in the present investigation is to determine whether similar effects intervene for the CO_2 splitting process. **Figure 8.2** shows comparative experiments carried out for the PZT and BT configurations. The voltage amplitude was fixed at 3.25 kV and the frequency was varied between 1 and 3 kHz for a CO_2 flow rate of 25 sccm. As it can be observed in the plots, higher values of the CO_2 conversion rate and energy efficiency were obtained with the PZT configuration for all operating conditions. Although the PZT configuration is characterized by a decrease in energy efficiency as frequency increases, the values obtained for this magnitude were always higher than for the BT configuration.

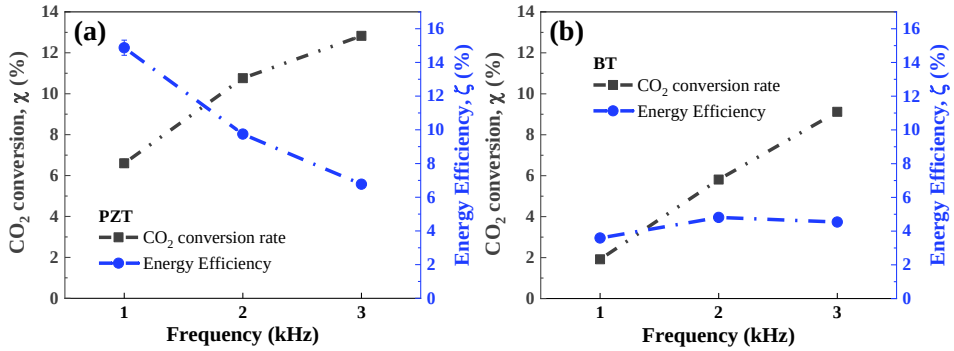

Figure 8.2. CO_2 conversion rate and energy efficiency represented versus the operating frequency for the PZT (a) and BT (b) configurations. Experiments were carried out for a CO_2 flow rate of 25 sccm, a voltage amplitude of 3.25 kV, and frequencies between 1 and 3 kHz.

By the carried-out experiments, voltage amplitude and the CO_2 flow rate were varied to study the performance of the PZT barrier. **Figure 8.3** shows the CO_2 conversion rate and the energy efficiency for the CO_2 splitting process using the PZT configuration. Conversion rate has been plotted as a function of the SIE for three gas flow rates (15, 25, and 40 sccm). The SIE has been chosen as x-axis variable to properly compare the effect of different flow rates and configurations. The SIE was changed varying the power for a given flow rate while increasing the applied voltage between 2.5 and 4 kV. The plots in **Figure 8.3** clearly show an increase in the conversion rate and a sharp drop in the energy efficiency for increasing values of SIE. This behavior is common in plasma-driven CO_2 decomposition processes operated in AC mode [19,20,40–44] and agrees with results obtained by numerical modeling [45].

Another interesting finding evidenced by the plot in **Figure 8.3(a)** is that the conversion rate increases with the gas flow (or analogously when the residence time decreases). This behavior differs from that found by other authors that usually report maximum conversion rates for lower CO_2 flows (i.e., for higher resident times) [12,14,43]. We tentatively attribute this difference to the occurrence of back-reactions taken place on the pellet's surfaces and/or in the plasma bulk (e.g., $CO + O \rightarrow CO_2$). Other authors have claimed similar back-reaction effects for the CO_2 plasma splitting reaction [18,46]. From the plots in **Figure 8.3(a)** it is also remarkable that conversion curves almost converge into a single trend for flow rates higher than 25 sccm. Conversely, the fact that the energy efficiency decreases with the SIE and for lower gas flow rates (higher resident time) (c.f. **Figure 8.3(b)**)

further supports that back-reactions may be involved and detrimentally affect the process efficiency.

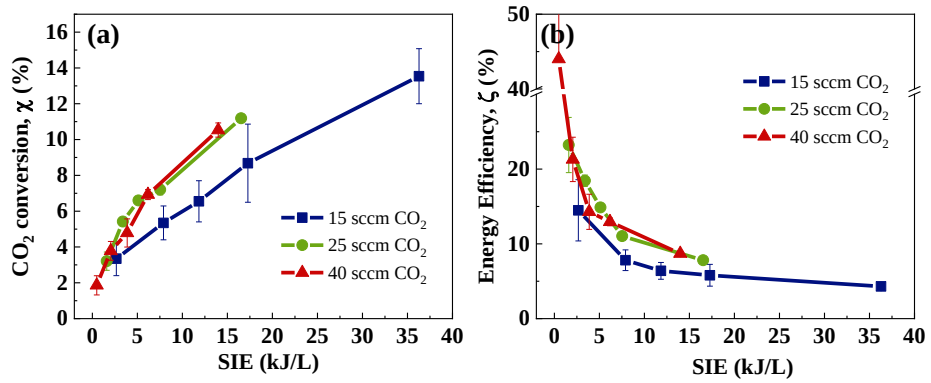

Figure 8.3. CO_2 conversion rate (a) and energy efficiency (b) versus the SIE values for the PZT configuration. Experiments were carried out for CO_2 flow rates of 15, 25, and 40 sccm, a frequency of 1 kHz, and voltage amplitudes between 2.5-4.0 kV.

Results plotted in **Figure 8.3** show that, for the PZT configuration, a conversion rate of 11% and an energy efficiency of 10% were reached for a SIE of 17 kJ/L, a response representing a good trade-off between these two magnitudes. Remarkably, these energy efficiencies were obtained with PZT as packing material, in the absence of a carrier gas or another catalytic material. The corresponding *I(t)* curves plotted in **Figure 8.4(a)** show that, in agreement with other authors under similar working conditions [15,41], the CO_2 plasmas present a significantly high amount of microdischarges.

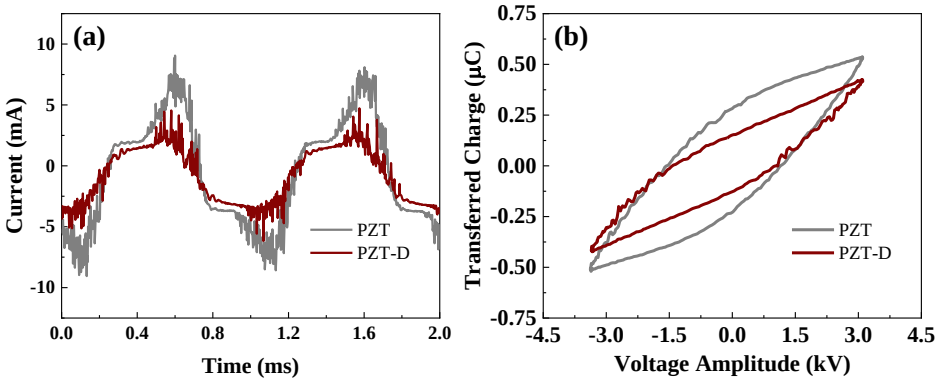

Figure 8.4. Measured current (a) and Lissajous curves (b) determined for the PZT and PZT-D configurations for a CO_2 flow rate of 25 sccm, an applied voltage of 4.0 kV, and a frequency of 1 kHz.

8.3.2. Insights into the Reaction Mechanisms

Figure 8.5 shows the optical emission spectrum recorded for the reactor in the PZT configuration, an applied voltage of 3.25 kV, a frequency of 3 kHz, and a CO_2 flow rate of 25 sccm. The assignment of the recorded bands, gathered in **Table 8.2**, confirms the presence in the plasma of CO^* and CO_2^{+*} excited species. Following this assignment, the third Positive System of CO and the FDB System of CO_2^+ (i.e., CO_2^+(A)) are marked with different solid lines in the figure (black and blue respectively), while the double band located between 288 and 290 nm, attributed to CO_2^+(B) emissions, is marked with a dashed line. Differentiating the 288.3 nm and 289.6 nm bands associated with CO_2^+(B) was not possible because of their small intensity and the low spectral resolution available in the packed-bed reactor, where only the light coming from the free space between the pellets contributes to the spectrum.

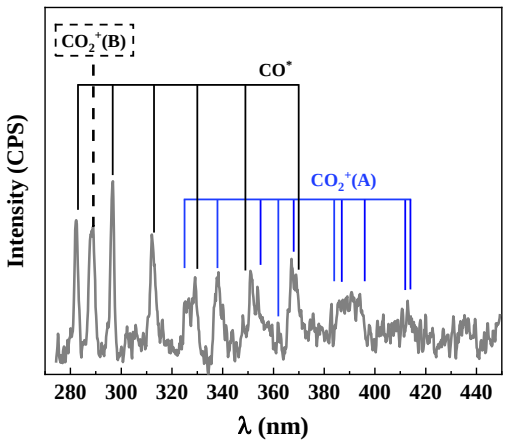

Figure 8.5. Characteristic emission spectrum obtained for the PZT configuration, an applied voltage of 3.25 kV, a frequency of 3 kHz, and a CO_2 flow rate of 25 sccm. Bands are assigned according to **Table 8.2**.

According to Snoeckx and Bogaerts, the partition of the available electron energy between electronic excitations, dissociation, ionization, and vibrational excitations processes is 70-80%, 5%, 5%, and 10%, respectively, for the CO_2 splitting reaction under DBD conditions (for a reduced electric field higher than 200 Td) [3]. Moreover, because of the high dielectric permittivity of ferroelectrics, packed-bed plasmas filled with these materials are characterized by an EEDF that extends to rather high energies. In these conditions, even if both surface reactions involving excited species [47] and CO_2 vibrational excitation might contribute to

the dissociation reaction (e.g., as in MW plasmas [28,30,48]), it is the most likely that electron impact dissociation induced by electronic excitation is the dominant mechanism for the CO_2 splitting reaction. The detection in the plasma of both the CO_2^+(B) and the CO_2^+(A) emission bands supports this assumption (CO_2^+ formation from CO_2 requires ionization energies around 18 eV [40]). Likewise, the recording of the characteristic fingerprint bands of CO^* species, characterized by a relative intensity much higher than in spectra recorded by other authors [11,34,39]), further supports the involvement of high-energy electrons in the reaction process. In literature there is not agreement about the spectral characteristics and formation routes of CO^* species in CO_2 plasmas. For example, Brehmer *et al.* proposed that the detection of CO^* emission bands is the result of reactions directly leading to the formation of CO in this excited electronic state [34]. Conversely, Du *et al.* proposed that CO is initially formed in its ground state and becomes subsequentially excited through electron impact processes [49]. In the PZT moderated packed-bed reactor, we assume that, in addition to other processes, the interaction of CO_2 molecules and CO_2^+ species with high-energy electrons efficiently contribute to the CO_2 decomposition through intermediate reactions that lead to the formation of CO^* species (i.e., reactions *E 8.1i - 8.3i*, where *i* stands for "intermediate reaction"):

$$CO_2 + e^- \text{ (high energy)} \rightarrow CO_2^+ (CO_2^{+*}) + 2e^- \quad \textit{(E 8.1i)}$$

$$CO_2 + e^- \text{ (high energy)} \rightarrow CO^* + O + e^- \quad \textit{(E 8.2i)}$$

$$CO_2^+ (CO_2^{+*}) + e^- \text{ (high energy)} \rightarrow CO^* + O \quad \textit{(E 8.3i)}$$

where CO_2^{+*} refers to ionized carbon dioxide molecules in the A or B excited states.

To further support the involvement of high-energy electrons in these intermediate reactions, the results obtained with the PZT configuration was compared with those of two additional barrier architectures: those in the PZT-D and the BT configurations (see **Table 8.1**). For comparative purposes, and based on the simulations plotted in **Figure 8.1**, the applied voltage was kept constant (3.25 kV) while the frequency was varied. As can be observed in the Comsol simulations plotted in **Figure 8.1(a)**, for the investigated geometries, electric field distributions are identified by *channel of voids* between the pellets, in agreement with recent studies of Van Laer and Bogaerts [50,51]. These authors also demonstrated that the electron temperature follows a spatial distribution similar to

that of the electric field. In relation with the present study, simulations suggest that for the PZT-D and BT configurations there is a reduction in the electron energy with respect to the energy for the PZT configuration. The following two comparative experiments also support such a conclusion.

The first experiment consisted of adding an extra ferroelectric barrier in the form of a plate, i.e., PZT-D configuration. A previous study from our research group dealing with the removal of air contaminants proved that the incorporation of a ferroelectric disk served to modify the EEDF, keeping constant the current and increasing the applied voltage [52]. Herein a different strategy has been followed consisting of operating at constant voltage to decrease the electric field intensity between the pellets. As a result (c.f., **Figure 8.1**) the electric field in the *channel of voids* zone is reduced when the upper electrode was covered with a ferroelectric plate of $LiNbO_3$. Accordingly, measured *I(t)* and Lissajous curves present lower intensities for the PZT-D configuration, as shown in **Figure 8.4**.

To illustrate that a decrease in the electric field intensity induces a decrease in the mean electron energy, the EEDFs have been calculated using the BOLSIG+ code [53] (see **Figure 8.6**). For this purpose, the maximum values of the reduced electric field plotted in **Figure 8.1(b)** have been introduced in the simulations: 360 and 300 Td for the PZT and PZT-D configurations, respectively. Other input parameters for these computations were a gas temperature of 300 K and a gas composition of 100% CO_2. Electron-electron and electron-ion collisions were explicitly considered, while the ratio between the electrical input frequency and the gas density was very low and can be approximated to zero. **Figure 8.6** shows that the EEDF curves have a similar shape and that for the PZT configuration the population of high energy electrons (Te>30/40 eV) should be higher. As a result, a slightly higher mean electron energy has been obtained for this configuration, 8.2 eV, against an energy of 7.4 eV obtained for the PZT-D configuration.

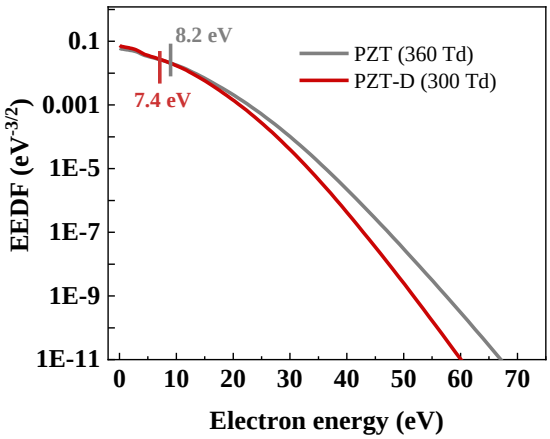

Figure 8.6. Electron Energy Distribution Function (EEDF) simulated using the BOLSIG+ code [53] for the PZT and PZT-D configurations.

Table 8.3 shows the conversion rate and energy efficiency obtained for the PZT, PZT-D and BT configurations working at 3.25 kV when varying the frequency between 1 and 3 kHz. In addition, for the three barrier configurations, **Figure 8.7** shows a normalized representation of the OES spectra zoomed at the 280-300 nm zone.

Table 8.3. Conversion rate, energy efficiency, and SIE values for the PZT, PZT-D, and BT reactor configurations at frequencies between 1-3 kHz, a constant applied voltage of 3.25 kV, and a flow rate of 25 sccm CO_2.

	PZT			**PZT-D**			**BT**		
f (kHz)	χ (%)	ζ (%)	**SIE (kJ/L)**	χ (%)	ζ (%)	**SIE (kJ/L)**	χ (%)	ζ (%)	**SIE (kJ/L)**
1	6.6	15	5.1	2.7	11	2.9	1.9	3.6	6.2
2	11	9.7	13	3.8	6.5	3.2	5.8	4.8	14
3	13	6.8	20	4.7	9.3	6.9	9.1	4.5	23

According to this table, conversion rate and SIE values were smaller for the PZT-D in comparison with the PZT configuration. Furthermore, the OES analysis suggests the existence of considerable mechanistic differences for the splitting reaction for these two configurations. **Figure 8.7(a)** shows that, for the PZT case,

the higher the frequency (or SIE) the higher the intensity of the CO^* band. Nevertheless, this tendency is not observed for PZT-D (**Figure 8.7(b)**). We attribute these differences to that a larger population of high-energy electrons in the inter-pellet space for the PZT case will efficiently contribute to increase the probability of reactions *E 8.2i* and *E 8.3i*. Conversely, for the PZT-D configuration, the fact that the intensity of the CO^* emission bands remains constant (c.f. **Figure 8.7(b)**) while the conversion rate increases supports that this emission intensity is not only related to the CO concentration in the outlet flow (i.e., related to the CO_2 conversion rate), as proposed in [49], but rather to the population of high-energy electrons in the plasma. In other words, we attribute the lower and almost invariable CO^* population found for the PZT-D configuration to the lower concentration of energetic electrons in this case.

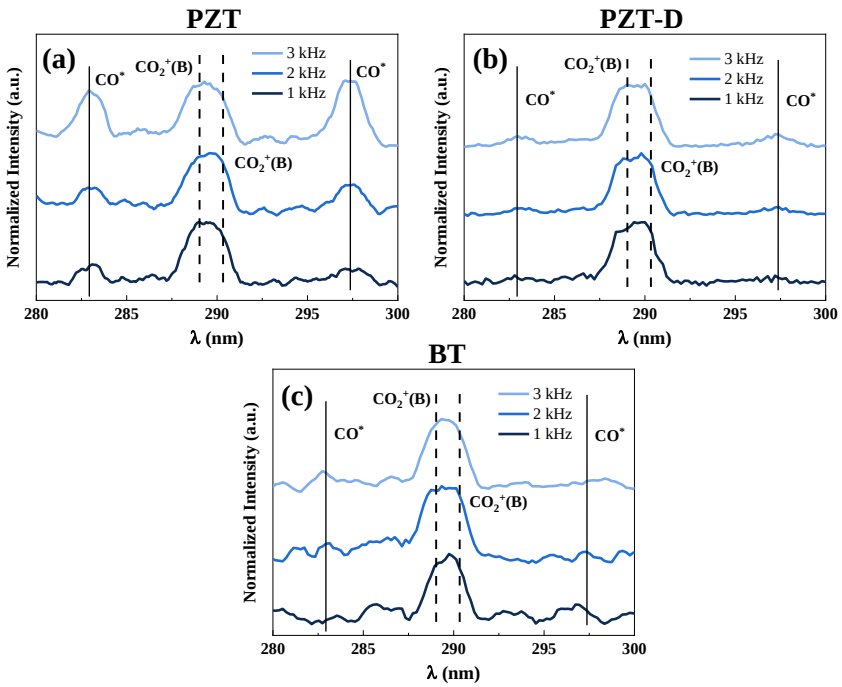

Figure 8.7. Optical emission spectra normalized to the intensity of the 288/290 nm band recorded for the PZT (a), PZT-D (b), and BT (c) reactor configurations at different frequencies, a constant applied voltage of 3.25 kV and 25 sccm of CO_2.

Figure 8.7(c) shows the OES spectra of the second complementary experiment, consisting of the use of $BaTiO_3$ instead of PZT as packing material. As indicated in **Table 8.3**, both conversion and energy efficiency were lower for the BT than for the PZT reactor configuration. These findings support the

hypothesis that a high dielectric constant contributes to intensify the electric field strength in a packed-bed reactor and, consequently, to increase the mean electron energy of plasma electrons [51]. As mentioned in **Chapter 1**, the discharge mode may also depend on the dielectric constant of the pellets. By fluid modeling and iCCD imaging, Wang *et al*. have demonstrated that the discharge mode may evolve from surface discharges over the whole packing material to a local filamentary mode as the dielectric constant of the material increases [54]. This evolution would also favor the CO_2 splitting process in the PZT moderated packed-bed reactor due to an increase in the average electron energy in the filamentary mode. The existence of different EEDFs for the BT and PZT reactor configurations is supported by the comparison of the OES spectra recorded in each case (c.f., **Figure 8.7**). The absence of high intensity bands of the Third Positive System of CO for the BT case (i.e., a similar behavior than with the PZT-D configuration) agrees with a lower electric field and, consequently, a lower concentration of high-energy electrons in the plasma phase in this case.

8.3.3. Minority and Side-reaction Processes

In addition to the direct splitting of CO_2 into CO and O, other minority global processes might also take place under our reaction conditions. Examples include the direct transformation of CO_2 into carbon and oxygen:

$$CO_2 \rightarrow C + O_2 \quad (E\ 8.4)$$

or the Boudouard reaction [55]:

$$2\ CO \rightarrow CO_2 + C \quad (E\ 8.5)$$

It is noteworthy that chemical reactions *E 8.4* and *E 8.5* denote global processes that may encompass intermediate reactions taking place in the plasma bulk or on the surface of the pellets and, consequently, involving quite different reactions pathways. As it is illustrated in **Figure 8.8,** direct evidence of such minority processes was gained by the X-Ray Photoelectron Spectroscopy (XPS) analysis of the packing material before and after plasma exposure. This surface analysis revealed the formation of a carbon deposit, evidenced by a significant increase of the C1s band at 284.6 eV attributed to graphite-like carbon, and a considerable incorporation of carbonate like species, deduced by the deployment of an intense C1s contribution at around 290 eV [56].

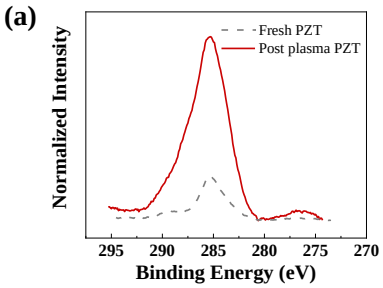

Sample	Ti2p (%At)	C1s (%At)	Ti2p/C1s
Fresh PZT	4.8	2.5	1.9
Post plasma PZT	1.5	45	0.033

Figure 8.8. (a) Normalized C1s signal (with respect to the Ti2p peak) for PZT pellets before and after successive plasma exposures (left) and atomic composition table in terms of atomic percentages of Ti and C (right). (b) Photographs of PZT pellets, before (left)and after (right) plasma exposure.

The data included in the table in **Figure 8.8(a)** can provide a rough estimation of the amount of carbon deposited on the pellet's surfaces and the volume of CO_2 that would be necessary for this process. For this estimate, we rely on the atomic concentration of Ti determined through the assessment of the Ti2p peak intensities (I_{Ti2p}). In concrete, assuming that the attenuation of the Ti2p signal is due to a carbon layer formed on the surface of pellets, the attenuation degree in the intensity of Ti2p peak must be related to the thickness of the carbon deposited layer. The simplest model would be that of a conformal homogenous layer (note, however, that an inhomogeneous distribution is clearly suggested by the photograph in **Figure 8.8(b)**). Under these assumptions it holds that:

$$\frac{I_{Ti2p}\ (\text{post plasma PZT})}{I_{Ti2p}(\text{fresh PZT})} \alpha\ e^{-L/\lambda} \quad (E\ 8.6)$$

where L is the thickness of the carbonaceous layer and λ the mean free path of the Ti2p photoelectrons (we assume that λ is approximately 2 nm). This assessment of L renders a thickness of 2.3 nm. This thickness would correspond to approximately 6 monolayers of carbon under the assumption of a graphitic thin film and a homogeneous surface distribution. This thickness estimation can be related to the volume of carbon dioxide that, upon decomposition, would be needed

to coat the PZT surface with such a carbon deposit (i.e., assuming that one CO_2 molecule will give rise to one deposited carbon atom). A rough estimation reveals that, considering the specific surface of PZT pellets (0.74 m^2/g) and the weight of the PZT barrier, we would need a total volume of about 2 liters of CO_2 to saturate the surface with this 2.3 nm graphitic layer. This value is within the order of magnitude of the expected amount of graphite formed for more than 20 hours of operation for a CO_2 flow rate between 15-40 sccm and a maximum of 15% of reacted CO_2 decomposed into C (see **Figure 8.9** below).

Additionally, the analysis of the evolution of carbon balance for the CO_2 splitting reaction indicates that not all the CO_2 entering the reactor gets out in the form of CO or unreacted CO_2. The results reported in **Figure 8.9** show that carbon balance is never 100% and decreases up to values around 85% at higher SIEs. We propose that the occurrence of alternative reactions other than CO_2 splitting is related with deposition of carbon deduced from the XPS analysis above.

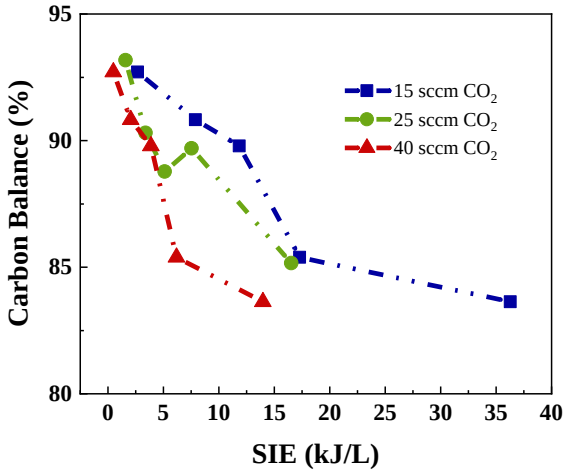

Figure 8.9. Carbon balance versus the SIE for the PZT configuration and the same experimental conditions that those used for the experiments in **Figure 8.3**.

8.3.4. CO_2+O_2 Mixtures

In real outlets, small percentages of oxygen usually appear mixed with CO_2. For example, in outlet gases from power plants it is common to find 5% of O_2 after water removal [57]. Therefore, to analyze the CO_2 splitting process under more realistic conditions (as those required for a realistic CCU technology), we studied

the CO_2 decomposition reaction using mixtures of CO_2 and O_2. Moreover, from a mechanistic point of view, we must note that O_2 is a product of the CO_2 splitting reaction. In the plasma, oxygen is also a potential source of O atoms and other excited species of oxygen that might trigger reaction pathways leading to the formation of CO_2. Considering the C deposition mentioned in the previous section and the main reaction products of CO_2 splitting (CO and O_2), various reaction pathways could be considered to intervene in the following chemical processes:

$$C + O_2 \rightarrow CO_2 \quad (E\ 8.7)$$

$$CO + O + M \rightarrow CO_2 + M \quad (E\ 8.8)$$

$$O_2 + CO \rightarrow CO_2 + O \quad (E\ 8.9)$$

where *E 8.7* refers to a global process that considers the interaction between oxygen molecules and the carbon deposited on the pellet surfaces, while processes *E 8.8* and *E 8.9* are the most important intermediate recombination reactions (at high pressures) considered by Berthelot and Bogaerts for a zero-dimensional chemical kinetics model [58]. The occurrence of these processes would contribute to decrease the overall CO_2 conversion rate.

Figure 8.10 depicts the evolution of CO_2 conversion rate and energy efficiency working with CO_2 + O_2 mixtures and the reactor in the PZT configuration. Although the energy efficiency is determined by using the effective conversion rate (see **Chapter 3**, **section 3.4.2**), the absolute conversion rate is also plotted because results reported in the literature are sometimes discussed in terms of this magnitude. The experiments were carried out varying the oxygen percentage in the mixture (5 and 10%) at a constant flow rate (25 sccm). The voltage amplitude and frequency were 3.25 kV and 3 kHz, conditions that ensured a considerable conversion and a high intensity of the OES spectra. It is noteworthy that, for the CO_2+O_2 mixtures, it was not possible to work at constant SIE (constant power) because the measured current through the reactor changed when oxygen was added to the gas mixture. These changes in electrical measurements suggest that the addition of oxygen may affect both the reaction mechanisms and the physical (and consequently electrical) properties of the discharge.

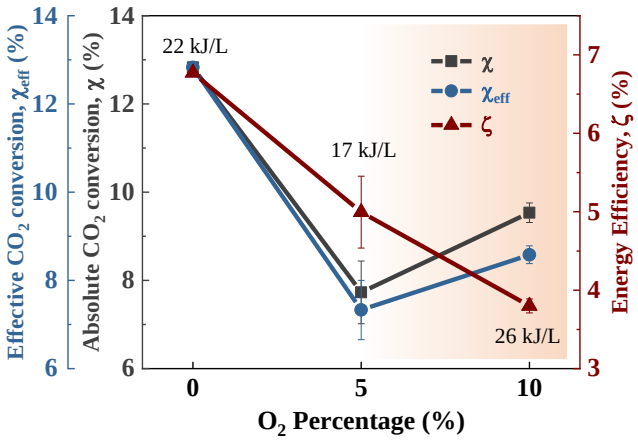

Figure 8.10. Evolution with the O_2 percentage of absolute and effective CO_2 conversion rates (left), and energy efficiency (right). SIE values are indicated for each O_2 percentage (3 kHz, 3.25 kV, and total flow rate of 25 sccm).

Figure 8.10 shows that the effective CO_2 conversion rate decreases from 13% to 8.5% upon addition of 10% O_2. Absolute CO_2 conversion rate and energy efficiency follow an analogous tendency, decreasing from 13% to 9.5% and from 6.8% to 3.8%, respectively. Zhang and Harvey obtained a similar decreasing tendency in a cylindrical packed-bed reactor with $BaTiO_3$ as packing material [21]. However, it is noteworthy that the efficiencies found here are higher (5% for 95/5 mixtures - SIE of 17 kJ/L - versus the 2% reported by these authors - SIE of 103.2 kJ/L).

To wrap up this part of the study, **Figure 8.11** shows the optical emission spectra recorded for the O_2 containing mixtures. It is apparent that, as the proportion of oxygen in the mixture increases, the relative intensity of the CO^* species decreases with respect to that of CO_2^+(B). This tendency agrees with the lower CO_2 splitting yield obtained for the mixture and supports that reaction pathways involving oxygen species could contribute to processes such as *E 8.6* and *E 8.7*, both contributing to decrease the global reaction yield.

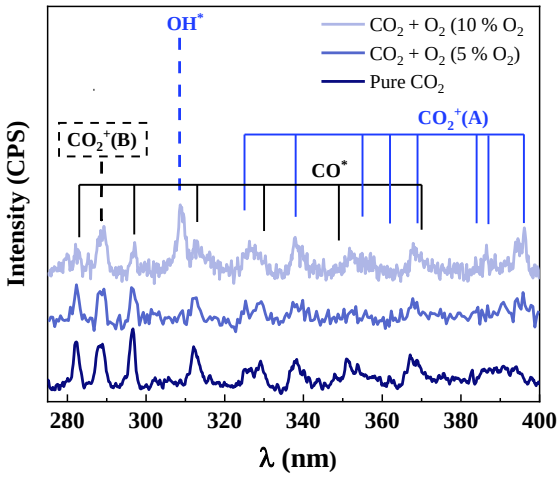

Figure 8.11. Emission spectra for the experimental conditions utilized for the experiments in **Figure 8.10** (3 kHz, 3.25 kV, and total flow rate of 25 sccm).

In the spectra of **Figure 8.11** it is also noteworthy the detection of a band around 308-309 nm that can be attributed to OH^* species (common emission at 308.9 nm) [38]. This impurity presumably comes from the interaction between O_2 and the pellets, in agreement with the known capacity of PZT to incorporate hydrogen (e.g., as OH^- or in other forms) onto their surface and in its bulk, as discussed in **Chapter 5** of this thesis.

8.3.5. CO_2 + Air Mixtures

The CO_2 plasma-splitting process has been widely studied using mixtures of CO_2 with other gases usually referred to as "carrier gases". Data are available for mixtures CO_2 + O_2 [21,59], CO_2 + N_2 [11,32,60,61], CO_2 + Ar [11,19,60,62] and CO_2 + He [60,62]. However, despite that the typical industrial and direct air capture CO_2 outlets include air as a component, to our knowledge no previous studies in DBD reactors have been carried out for mixtures of CO_2 and air. Herein, we have studied the plasma reaction of mixtures of CO_2 with up to 20% dry air (total flow rate of 25 sccm) at constant voltage amplitude of 3.25 kV and a frequency of 3 kHz. Results are shown in **Figure 8.12**, where both the absolute and effective conversion rates and the energy efficiency are plotted as a function of air percentage. These plots show that the effective CO_2 conversion rate changes from 13 to 9.9% when the air percentage varies from 0 to 20%. The energy

efficiency increases from 6.8 to 8.1% for the 15% air mixture. Looking at the absolute CO_2 conversion rate, values vary between 7 and 13%. It is important to remark that, as in the case of mixtures with oxygen, SIE was not maintained constant for the experiments (we kept constant the voltage and frequency and let vary the current).

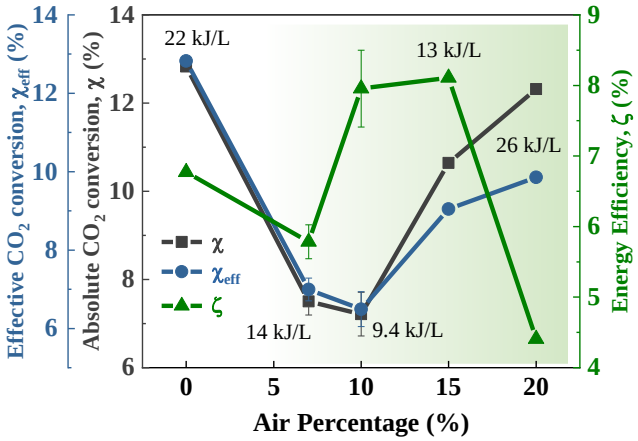

Figure 8.12. Evolution with the air percentage of the absolute and effective CO_2 conversion rates (left) and energy efficiency (right). SIE values are indicated for each experiment (3 kHz, 3.25 kV, and total flow rate of 25 sccm).

It is reported the literature that adding small percentages of nitrogen to a CO_2 plasma modifies the electrical response of a DBD discharge process. Snoeckx *et al.* attributed this behavior upon N_2 addition to a transition from a filamentary discharge mode (pure CO_2) to a more diffuse discharge [32]. Additionally, these authors studied the effect of a larger range of N_2 contents and reported a good agreement between simulation and experimental results. For low nitrogen percentages, similar to those existing in the air mixtures used in this work, they obtained a negligible variation in the energy efficiency of the reaction and concluded that the presence of metastable nitrogen species could influence the reaction mechanisms and compensate the lower CO_2 proportion in the mixture. These authors obtained an energy efficiency of 4.5%, for a mixture of 15% N_2 and a SIE of about 12 kJ/L, while we have reached an efficiency of 8.1% for similar operation conditions [32]. On the other hand, S. Xu *et al.* studied highly diluted N_2 mixtures (from 30% up to 80% of N_2) in a $BaTiO_3$ packed-bed reactor, obtaining that the absolute CO_2 conversion rate increased with the amount of nitrogen in the mixture, though at the expense of a decrease in energy efficiency [11].

Although the results in the previous section showed that the presence of oxygen contributes to diminish conversion and energy efficiency, for the 15% air mixture the combined effect of the air components results in a reduction of the CO_2 conversion rate but in an increase in energy efficiency by more than 20% with respect the initial value without air. This behavior can be attributed to the occurrence of more efficient reaction pathways involving nitrogen species (discussed in more detail below). For an air percentage of 20%, the conversion rate still increases but at expenses of a drastic decrease in the energy efficiency that drops to 4.3% (this reflects the drastic increase in the SIE to 26 kJ/L, due to an increase in the current intensity for this gas mixture). A similar behavior has been reported for CO_2 + N_2 mixtures and attributed to the increase in the nitrogen concentration in the mixture [32].

The addition of air significantly modifies the plasma emission spectrum compared to pure CO_2 discharges. **Figure 8.13** shows that the CO^* signal significantly decreased for a 10% mixture to disappear for a 15% percentage. Meanwhile, no traces of CO_2^+(B) emissions could be detected for these mixtures. These bands are replaced by those of the second positive system of N_2^* (i.e., $[C^3\Pi \rightarrow B^3\Pi]$ transition), characterized by a main band at 357.9 nm. Additionally, the spectra did not provide any hint of the formation of the common N_2^+ species, characteristically identified by its first negative system at 391.4 nm. These changes in the OES spectra prove that N_2 in air affects radically the plasma excitation mechanisms and, as a result, the CO_2 splitting pathways. Since processes like the excitation mechanisms to obtain CO_2^+ species (evidenced by band systems (B) and (A)) require a substantial energy cost (between 17-18 eV), we propose that their occurrence might have been partially replaced by other lower-energy reaction pathways. These can be, for example, the electron impact excitation of N_2 and the formation of metastable states of nitrogen able to promote an efficient dissociation of CO_2 [32].

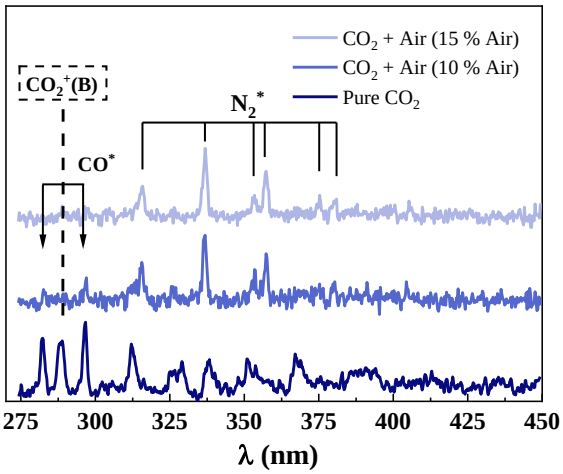

Figure 8.13. Emission spectra for the experimental conditions utilized for the experiments in **Figure 8.12** (3 kHz, 3.25 kV, and total flow rate of 25 sccm).

An important feature by these experiments with CO_2 + air mixtures is that, unlike other author´s reported results for CO_2 + N_2 mixtures in similar reactors [11,32], no N_XO_Y species have been detected as reaction by-products, even if no additional reactants are added to the gas mixture (e.g., Snoeckx *et al.* recently published that CH_4 acts as chemical oxygen scavenger to diminish the NO and NO_2 production in CO_2+N_2 mixtures [63]). The QMS spectra in **Figure 8.14** correspond to the outlet gases of CO_2 + air mixtures recorded before and after plasma ignition. These spectra show the m/q spectral zones related to the formation of N_XO_Y harmful compounds. Key m/q ratios are 30, 46, and 44, attributed to NO, NO_2, and N_2O, respectively. The intensity of these signals remains constant or decrease in intensity (note that the 44 peak is directly related to the CO_2 species), thus proving that no N_XO_Y species are detected in the outlet gas flow after plasma reaction. This outstanding finding can be attributed to the specific conditions of the utilized PZT moderated packed-bed reactor. Although the reasons sustaining this finding are still unclear, we claim several factors that might contribute to it under our experimental conditions. As it is stated in the literature [32], the formation of NO and NO_2 in CO_2 + N_2 plasmas proceeds via oxygen interaction with nitrogen atoms and electronically excited N_2 molecules. Threshold electron energies required to dissociate or excite N_2 molecules are 18.5 eV [66] or 7.7 eV [11], respectively. Taking into account these values and since the results in **Figure 8.13** only show the emission bands of the N_2^* system, we can hypothesize that electron energy is not enough to induce the formation of N^* and N_2^{+*} species. This

is another way of saying that plasma interaction with the air components effectively decreases the electron temperature, making that neither CO_2^{+*} nor N^* species can be formed in our experiment. In addition to this proposal, we can also hypothesize that oxygen molecules of air may prevent the required interaction between oxygen and nitrogen atoms to produce N_xO_y species. In this regard, Brandenburg *et al.* claimed that nitrogen metastable states can be efficiently quenched by O_2 molecules [65], a fact that can hamper the reaction between excited nitrogen and oxygen species. Similarly, in a recent study by Slaets *et al.*, no traces of N_xO_y species were detected in a gliding arc plasmatron working with methane and carbon dioxide in mixtures containing nitrogen and oxygen [66].

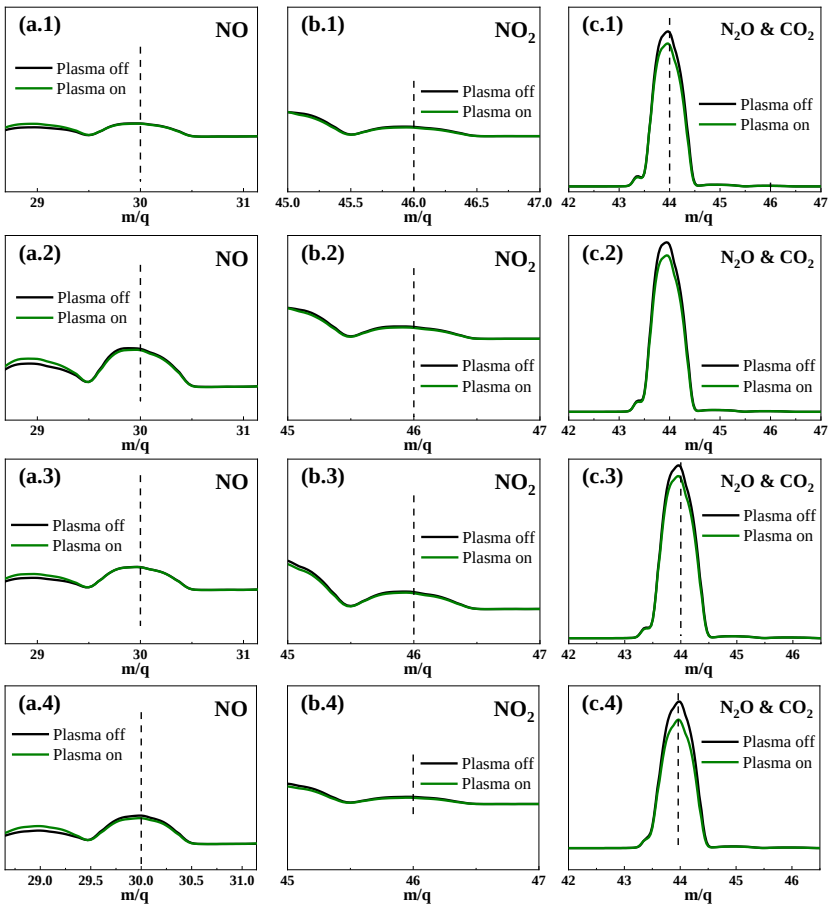

Figure 8.14. QMS spectra recorded before and after plasma discharges for the zones characteristic of NO, m/q=30 (a), NO_2, m/q=46 (b), and N_2O, m/q=44 (c) (the same as CO_2). CO_2/Air proportion: (1) 93/7, (2) 90/10, (3) 85/15, and (4) 80/20.

8.4. Conclusions

The CO_2 dissociation process into CO and O_2 has been studied in a ferroelectric packed-bed plasma reactor operated at atmospheric pressure and ambient temperature. The obtained results have shown that PZT is an optimum ferroelectric packing material to moderate the discharges in packed-bed reactors, outperforming the more widely used $BaTiO_3$. Its usefulness has been proved not only for the activation of pure CO_2 plasmas, but also for mixtures with air. The high reactor performance achieved with PZT has been attributed to its relatively higher dielectric constant at the temperature of operation. It contributes to enhance the electric field in the channel of voids between pellets, where high energetic electrons will trigger a series of intermediate reactions contributing to the overall reaction yield.

Analyzing the effect of the barrier architecture (PZT vs. PZT-D configurations, see **Table 8.1**) and the CO_2 flow rate (15, 25, and 40 sccm), it is found that the best results are obtained with the PZT configuration and high CO_2 flow rates, i.e., for relatively short residence time of reactants. Moreover, the thorough OES characterization of the plasma and the lower reaction performance obtained when adding a ferroelectric plate to the barrier architecture have been justified in terms of changes in the EEDF and a decrease in the average energy of plasma electrons in this latter case. Therefore, it is concluded that the high-energy electrons generated in the discharge moderated with PZT are decisive to produce CO^* species and to improve the overall reaction efficiency.

The incidence of back-reactions in diminishing the process efficiency has been scarcely studied experimentally. Experiments with $CO_2 + O_2$ mixtures have shown that reactions between excited species of oxygen and CO in the plasma bulk may occur under the studied working conditions, contributing to the observed decrease in the CO_2 conversion rate when using low flow rates. In this regard, the higher energy efficiency obtained when igniting pure CO_2 plasma at higher flow rates, i.e., for lower residence times, further supports the occurrence of back-reactions. It is also possible that these back or recombination reactions take place on the surface of the pellets, involving the carbonaceous residues proved by XPS and suggested by a carbon balance analysis.

Finally, a remarkable result is that CO_2 decomposition was rather efficient when using CO_2 + air mixtures, reproducing common conditions in real facilities for CCU technologies. The good trade-off between conversion rate (9%) and

energy efficiency (8.1%) obtained for a 15% air mixture has been accounted for by the involvement of excited nitrogen species in alternative energetically favorable CO_2 decomposition processes. The absence of any N_XO_Y species as reaction byproduct is a noteworthy result that proves the suitability of packed-bed plasma reactors moderated with PZT for CO_2 splitting at ambient conditions and mixtures with air.

8.5. References

[1] R.M. Cuéllar-Franca, A. Azapagic, Carbon capture, storage and utilisation technologies: A critical analysis and comparison of their life cycle environmental impacts, Journal of CO_2 Utilization. 9 (2015) 82–102. https://doi.org/10.1016/j.jcou.2014.12.001.

[2] MOXIE for Scientists - NASA Mars, (n.d.). https://mars.nasa.gov/mars2020/spacecraft/instruments/moxie/for-scientists/ (accessed June 16, 2021).

[3] R. Snoeckx, A. Bogaerts, Plasma technology-a novel solution for CO_2 conversion?, Chemical Society Reviews. 46 (2017) 5805–5863. https://doi.org/10.1039/c6cs00066e.

[4] M.L. Carreon, Plasma catalysis: A brief tutorial, Plasma Research Express. 1 (2019). https://doi.org/10.1088/2516-1067/ab5a30.

[5] A. George, B. Shen, M. Craven, Y. Wang, D. Kang, C. Wu, X. Tu, A Review of Non-Thermal Plasma Technology: A novel solution for CO_2 conversion and utilization, Renewable and Sustainable Energy Reviews. 135 (2021). https://doi.org/10.1016/j.rser.2020.109702.

[6] M. Mikhail, P. da Costa, J. Amouroux, S. Cavadias, M. Tatoulian, S. Ognier, M.E. Gálvez, Electrocatalytic behaviour of CeZrO: x-supported Ni catalysts in plasma assisted CO_2 methanation, Catalysis Science and Technology. 10 (2020) 4532–4543. https://doi.org/10.1039/d0cy00312c.

[7] D. Mei, X. Zhu, Y.L. He, J.D. Yan, X. Tu, Plasma-assisted conversion of CO_2 in a dielectric barrier discharge reactor: Understanding the effect of packing materials, Plasma Sources Science and Technology. 24 (2015). https://doi.org/10.1088/0963-0252/24/1/015011.

[8] A.M. Montoro-Damas, J.J. Brey, M.A. Rodríguez, A.R. González-Elipe, J. Cotrino, Plasma reforming of methane in a tunable ferroelectric packed-bed dielectric barrier discharge reactor, Journal of Power Sources. 296 (2015) 268–275. https://doi.org/10.1016/j.jpowsour.2015.07.038.

[9] A. Gómez-Ramírez, V.J. Rico, J. Cotrino, A.R. González-Elipe, R.M. Lambert, Low temperature production of formaldehyde from carbon dioxide and ethane by plasma-Assisted catalysis in a ferroelectrically moderated dielectric barrier discharge reactor, ACS Catalysis. 4 (2014) 402–408. https://doi.org/10.1021/cs4008528.

[10] R. Michiels, Y. Engelmann, A. Bogaerts, Plasma Catalysis for CO_2 Hydrogenation: Unlocking New Pathways toward CH_3OH, Journal of Physical Chemistry C. 124 (2020) 25859–25872. https://doi.org/10.1021/acs.jpcc.0c07632.

[11] S. Xu, J.C. Whitehead, P.A. Martin, CO_2 conversion in a non-thermal, barium titanate packed bed plasma reactor: The effect of dilution by Ar and N_2, Chemical Engineering Journal. 327 (2017) 764–773. https://doi.org/10.1016/j.cej.2017.06.090.

[12] Y. Uytdenhouwen, S. van Alphen, I. Michielsen, V. Meynen, P. Cool, A. Bogaerts, A packed-bed DBD micro plasma reactor for CO_2 dissociation: Does size matter?, Chemical Engineering Journal. 348 (2018) 557–568. https://doi.org/10.1016/j.cej.2018.04.210.

[13] I. Michielsen, Y. Uytdenhouwen, J. Pype, B. Michielsen, J. Mertens, F. Reniers, V. Meynen, A. Bogaerts, CO_2 dissociation in a packed bed DBD reactor: First steps towards a better understanding of plasma catalysis, Chemical Engineering Journal. 326 (2017) 477–488. https://doi.org/10.1016/j.cej.2017.05.177.

[14] K. van Laer, A. Bogaerts, Improving the Conversion and Energy Efficiency of Carbon Dioxide Splitting in a Zirconia-Packed Dielectric Barrier Discharge Reactor, Energy Technology. 3 (2015) 1038–1044. https://doi.org/10.1002/ente.201500127.

[15] A. Ozkan, A. Bogaerts, F. Reniers, Routes to increase the conversion and the energy efficiency in the splitting of CO_2 by a dielectric barrier discharge, Journal of Physics D: Applied Physics. 50 (2017). https://doi.org/10.1088/1361-6463/aa562c.

[16] A. Ozkan, T. Dufour, T. Silva, N. Britun, R. Snyders, A. Bogaerts, F. Reniers, The influence of power and frequency on the filamentary behavior of a flowing DBD - Application to the splitting of CO_2, Plasma Sources Science and Technology. 25 (2016). https://doi.org/10.1088/0963-0252/25/2/025013.

[17] Y. Uytdenhouwen, V. Meynen, P. Cool, A. Bogaerts, The potential use of core-shell structured spheres in a packed-bed DBD plasma reactor for CO_2 conversion, Catalysts. 10 (2020). https://doi.org/10.3390/catal10050530.

[18] P. Kaliyappan, A. Paulus, J. D'Haen, P. Samyn, Y. Uytdenhouwen, N. Hafezkhiabani, A. Bogaerts, V. Meynen, K. Elen, A. Hardy, M.K. van Bael, Probing the impact of material properties of core-shell SiO_2@TiO_2 spheres on the plasma-catalytic CO_2 dissociation using a packed bed DBD plasma reactor, Journal of CO_2 Utilization. 46 (2021). https://doi.org/10.1016/j.jcou.2021.101468.

[19] H. Taghvaei, E. Pirzadeh, M. Jahanbakhsh, O. Khalifeh, M.R. Rahimpour, Polyurethane foam: A novel support for metal oxide packing used in the non-thermal plasma decomposition of CO_2, Journal of CO_2 Utilization. 44 (2021). https://doi.org/10.1016/j.jcou.2020.101398.

[20] D. Mei, X. Zhu, C. Wu, B. Ashford, P.T. Williams, X. Tu, Plasma-photocatalytic conversion of CO_2 at low temperatures: Understanding the synergistic effect of plasma-catalysis, Applied Catalysis B: Environmental. 182 (2016) 525–532. https://doi.org/10.1016/j.apcatb.2015.09.052.

[21] K. Zhang, A.P. Harvey, CO_2 decomposition to CO in the presence of up to 50% O_2 using a non-thermal plasma at atmospheric temperature and pressure, Chemical Engineering Journal. 405 (2021). https://doi.org/10.1016/j.cej.2020.126625.

[22] T. Butterworth, R. Elder, R. Allen, Effects of particle size on CO_2 reduction and discharge characteristics in a packed bed plasma reactor, Chemical Engineering Journal. 293 (2016) 55–67. https://doi.org/10.1016/j.cej.2016.02.047.

[23] K. Zhang, G. Zhang, X. Liu, A.N. Phan, K. Luo, A Study on CO_2 Decomposition to CO and O_2 by the Combination of Catalysis and Dielectric-Barrier Discharges at Low Temperatures and Ambient Pressure, Industrial and Engineering Chemistry Research. 56 (2017) 3204–3216. https://doi.org/10.1021/acs.iecr.6b04570.

[24] N. Lu, N. Liu, C. Zhang, Y. Su, K. Shang, N. Jiang, J. Li, Y. Wu, CO_2 conversion promoted by potassium intercalated g-C_3N_4 catalyst in DBD plasma system, Chemical Engineering Journal. 417 (2021) 129283. https://doi.org/10.1016/J.CEJ.2021.129283.

[25] L. Wang, X. Du, Y. Yi, H. Wang, M. Gul, Y. Zhu, X. Tu, Plasma-enhanced direct conversion of CO_2 to CO over oxygen-deficient Mo-doped CeO_2, Chemical Communications. 56 (2020) 14801–14804. https://doi.org/10.1039/d0cc06514e.

[26] B. Ashford, Y. Wang, C.K. Poh, L. Chen, X. Tu, Plasma-catalytic conversion of CO_2 to CO over binary metal oxide catalysts at low temperatures, Applied Catalysis B: Environmental. 276 (2020). https://doi.org/10.1016/j.apcatb.2020.119110.

[27] S. Xu, P.I. Khalaf, P.A. Martin, J.C. Whitehead, CO_2 dissociation in a packed-bed plasma reactor: effects of operating conditions, Plasma Sources Science and Technology. 27 (2018) 075009. https://doi.org/10.1088/1361-6595/aacd6a.

[28] N. Britun, T. Silva, G. Chen, T. Godfroid, J. van der Mullen, R. Snyders, Plasma-assisted CO_2 conversion: Optimizing performance via microwave power modulation, Journal of Physics D: Applied Physics. 51 (2018) 144002. https://doi.org/10.1088/1361-6463/aab1ad.

[29] M. Ramakers, G. Trenchev, S. Heijkers, W. Wang, A. Bogaerts, Gliding Arc Plasmatron: Providing an Alternative Method for Carbon Dioxide Conversion, ChemSusChem. 10 (2017) 2642–2652. https://doi.org/10.1002/cssc.201700589.

[30] N. den Harder, D.C.M. van den Bekerom, R.S. Al, M.F. Graswinckel, J.M. Palomares, F.J.J. Peeters, S. Ponduri, T. Minea, W.A. Bongers, M.C.M. van de Sanden, G.J. van Rooij, Homogeneous CO_2 conversion by microwave plasma: Wave propagation and diagnostics, Plasma Processes and Polymers. 14 (2017) 1600120. https://doi.org/10.1002/ppap.201600120.

[31] V. Vermeiren, A. Bogaerts, Improving the Energy Efficiency of CO_2 Conversion in Nonequilibrium Plasmas through Pulsing, Journal of Physical Chemistry C. 123 (2019) 17650–17665. https://doi.org/10.1021/acs.jpcc.9b02362.

[32] R. Snoeckx, S. Heijkers, K. van Wesenbeeck, S. Lenaerts, A. Bogaerts, CO_2 conversion in a dielectric barrier discharge plasma: N_2 in the mix as a helping hand or problematic impurity?, Energy and Environmental Science. 9 (2016) 999–1011. https://doi.org/10.1039/c5ee03304g.

[33] COMSOL Multiphysics v.5.5. www.comsol.com (2019).

[34] F. Brehmer, S. Welzel, M.C.M. van de Sanden, R. Engeln, CO and byproduct formation during CO_2 reduction in dielectric barrier discharges, Journal of Applied Physics. 116 (2014). https://doi.org/10.1063/1.4896132.

[35] G.W. Fox, O.S. Duffendack, E.F. Barker, The Spectrum of CO_2, Proceedings of the National Academy of Sciences. 13 (1927) 302–307. https://doi.org/10.1073/pnas.13.5.302.

[36] H. Anton, Zur Lumineszenz einiger Molekülgase bei Anregung durch schnelle Elektronen. II, Annalen Der Physik. 473 (1966) 178–193. https://doi.org/10.1002/andp.19664730312.

[37] M.A. Johnson, R.N. Zare, J. Rostas, S. Leach, Resolution of the Ã/B̃ photoionization branching ratio paradox for the $^{12}CO_2^+$B̃(000) state, The Journal of Chemical Physics. 80 (1983) 2407–2428. https://doi.org/10.1063/1.446991.

[38] R.W.B. Pearse and A.G. Gaydon (1965), The Identification of Molecular Spectra, 3rd ed., Chapman and Hall Ltd., England.

[39] N. Lu, C. Zhang, K. Shang, N. Jiang, J. Li, Y. Wu, Dielectric barrier discharge plasma assisted CO_2 conversion: understanding the effects of reactor design and operating parameters, Journal of Physics D: Applied Physics. 52 (2019) 224003. https://doi.org/10.1088/1361-6463/ab0ebb.

[40] H. Taghvaei, E. Pirzadeh, M. Jahanbakhsh, O. Khalifeh, M.R. Rahimpour, Polyurethane foam: A novel support for metal oxide packing used in the non-thermal plasma decomposition of CO_2, Journal of CO_2 Utilization. 44 (2021). https://doi.org/10.1016/j.jcou.2020.101398.

[41] D. Mei, X. Tu, Conversion of CO_2 in a cylindrical dielectric barrier discharge reactor: Effects of plasma processing parameters and reactor design, Journal of CO_2 Utilization. 19 (2017) 68–78. https://doi.org/10.1016/j.jcou.2017.02.015.

[42] D. Mei, X. Zhu, Y.L. He, J.D. Yan, X. Tu, Plasma-assisted conversion of CO_2 in a dielectric barrier discharge reactor: Understanding the effect of packing materials, Plasma Sources Science and Technology. 24 (2015). https://doi.org/10.1088/0963-0252/24/1/015011.

[43] Y. Uytdenhouwen, K.M. Bal, I. Michielsen, E.C. Neyts, V. Meynen, P. Cool, A. Bogaerts, How process parameters and packing materials tune chemical equilibrium and kinetics in plasma-based CO_2 conversion, Chemical Engineering Journal. 372 (2019) 1253–1264. https://doi.org/10.1016/j.cej.2019.05.008.

[44] G. Niu, Y. Qin, W. Li, Y. Duan, Investigation of CO_2 Splitting Process Under Atmospheric Pressure Using Multi-electrode Cylindrical DBD Plasma Reactor, Plasma Chemistry and Plasma Processing. 39 (2019) 809–824. https://doi.org/10.1007/s11090-019-09955-y.

[45] S. Ponduri, M.M. Becker, S. Welzel, M.C.M. van de Sanden, D. Loffhagen, R. Engeln, Fluid modelling of CO_2 dissociation in a dielectric barrier discharge, Journal of Applied Physics. 119 (2016) 093301. https://doi.org/10.1063/1.4941530.

[46] A.J. Wolf, F.J.J. Peeters, P.W.C. Groen, W.A. Bongers, M.C.M. van de Sanden, CO_2 Conversion in Nonuniform Discharges: Disentangling Dissociation and Recombination Mechanisms, Journal of Physical Chemistry C. 124 (2020) 16806–16819. https://doi.org/10.1021/acs.jpcc.0c03637.

[47] H.H. Kim, A.A. Abdelaziz, Y. Teramoto, T. Nozaki, K. Hensel, Y.S. Mok, S. Saud, D.B. Nguyen, D.H. Lee, W.S. Kang, Interim report of plasma catalysis: Footprints in the past and blueprints for the future, International Journal of Plasma Environmental Science and Technology. 15 (2021). https://doi.org/10.34343/ijpest.2021.15.e01004.

[48] T. Silva, N. Britun, T. Godfroid, R. Snyders, Understanding CO_2 decomposition in microwave plasma by means of optical diagnostics, Plasma Processes and Polymers. 14 (2017) 1600103. https://doi.org/10.1002/ppap.201600103.

[49] Y. Du, K. Tamura, S. Moore, Z. Peng, T. Nozaki, P.J. Bruggeman, CO ($B_1\Sigma^+ \rightarrow A_1\Pi$) Angstrom System for Gas Temperature Measurements in CO_2 Containing Plasmas, Plasma Chemistry and Plasma Processing 2016 37:1. 37 (2016) 29–41. https://doi.org/10.1007/S11090-016-9759-5.

[50] K. van Laer, A. Bogaerts, Fluid modelling of a packed bed dielectric barrier discharge plasma reactor, Plasma Sources Science and Technology. 25 (2015) 015002. https://doi.org/10.1088/0963-0252/25/1/015002.

[51] K. van Laer, A. Bogaerts, How bead size and dielectric constant affect the plasma behaviour in a packed bed plasma reactor: A modelling study, Plasma Sources Science and Technology. 26 (2017) 085007. https://doi.org/10.1088/1361-6595/aa7c59.

[52] A. Gómez-Ramírez, A. Montoro-Damas, M.A. Rodríguez, A. González-Elipe, J. Cotrino, Improving the pollutant removal efficiency of packed-bed plasma reactors incorporating ferroelectric components, Chemical Engineering Journal. 314 (2017) 311–319. https://doi.org/10.1016/j.cej.2016.11.065.

[53] G.J.M. Hagelaar, L.C. Pitchford, Solving the Boltzmann equation to obtain electron transport coefficients and rate coefficients for fluid models, Plasma Sources Science and Technology. 14 (2005) 722–733. https://doi.org/10.1088/0963-0252/14/4/011.

[54] W. Wang, H.H. Kim, K. van Laer, A. Bogaerts, Streamer propagation in a packed bed plasma reactor for plasma catalysis applications, Chemical Engineering Journal. 334 (2018) 2467–2479. https://doi.org/10.1016/j.cej.2017.11.139.

[55] D. Ray, P. Chawdhury, K.V.S.S. Bhargavi, S. Thatikonda, N. Lingaiah, C. Subrahmanyam, Ni and Cu oxide supported γ-Al_2O_3packed DBD plasma reactor for CO_2 activation, Journal of CO_2 Utilization. 44 (2021). https://doi.org/10.1016/j.jcou.2020.101400.

[56] C.D. Wagner, W.M. Riggs, L.E. Davis, J.F. Moulder (1979), Handbook of X-Ray Photoelectron Spectroscopy, Perkin-Elmer Corporation, Eden Prairie.

[57] X. Xu, C. Song, R. Wincek, J.M. Andresen, B.G. Miller, A.W. Scaroni, Separation of CO_2 from Power Plant Flue Gas Using a Novel CO_2 "Molecular Basket" Adsorbent, in: ACS Division of Fuel Chemistry, Preprints, 2003: pp. 162–163.

[58] A. Berthelot, A. Bogaerts, Modeling of CO_2 Splitting in a Microwave Plasma: How to Improve the Conversion and Energy Efficiency, Journal of Physical Chemistry C. 121 (2017) 8236–8251. https://doi.org/10.1021/acs.jpcc.6b12840.

[59] T. Mikoviny, M. Kocan, S. Matejcik, N.J. Mason, J.D. Skalny, Experimental study of negative corona discharge in pure carbon dioxide and its mixtures with oxygen, Journal of Physics D: Applied Physics. 37 (2004) 64–73. https://doi.org/10.1088/0022-3727/37/1/011.

[60] D. Ray, R. Saha, C. Subrahmanyam, DBD plasma assisted CO_2 decomposition: Influence of diluent gases, Catalysts. 7 (2017) 244. https://doi.org/10.3390/catal7090244.

[61] L. Terraz, T. Silva, A. Morillo-Candas, O. Guaitella, A. Tejero-del-Caz, L.L. Alves, V. Guerra, Influence of N_2 on the CO_2 vibrational distribution function and dissociation yield in non-equilibrium plasmas, Journal of Physics D: Applied Physics. 53 (2019) 094002. https://doi.org/10.1088/1361-6463/ab55fb.

[62] M. Ramakers, I. Michielsen, R. Aerts, V. Meynen, A. Bogaerts, Effect of argon or helium on the CO_2 conversion in a dielectric barrier discharge, Plasma Processes and Polymers. 12 (2015) 755–763. https://doi.org/10.1002/ppap.201400213.

[63] R. Snoeckx, K. van Wesenbeeck, S. Lenaerts, M.S. Cha, A. Bogaerts, Suppressing the formation of NO_X and N_2O in CO_2/N_2 dielectric barrier discharge plasma by adding CH_4: Scavenger chemistry at work, Sustainable Energy and Fuels. 3 (2019) 1388–1395. https://doi.org/10.1039/c8se00584b.

[64] P.C. Cosby, Electron-impact dissociation of nitrogen, The Journal of Chemical Physics. 98 (1993) 9544–9559. https://doi.org/10.1063/1.464385.

[65] R. Brandenburg, V.A. Maiorov, Y.B. Golubovskii, H.E. Wagner, J. Behnke, J.F. Behnke, Diffuse barrier discharges in nitrogen with small admixtures of oxygen: discharge mechanism and transition to the filamentary regime, Journal of Physics D: Applied Physics. 38 (2005) 2187. https://doi.org/10.1088/0022-3727/38/13/017.

[66] J. Slaets, M. Aghaei, S. Ceulemans, S. van Alphen, A. Bogaerts, CO_2 and CH_4 conversion in "real" gas mixtures in a gliding arc plasmatron: how do N_2 and O_2 affect the performance?, Green Chemistry. 22 (2020) 1366–1377. https://doi.org/10.1039/C9GC03743H.

Chapter 9

Reaction Mechanisms by the Valorization of CO_2 and CH_4 Mixtures*

9.1. Introduction

Due to its high hydrogen content, methane (CH_4) is frequently used as a feedstock in the chemical industry as well as a fuel for energy production. However, the high volatility of this gas dissolved in crude oils makes that around 8% of methane becomes released to the atmosphere – thereby contributing to the global warning [1] –during shale gas extraction and distribution [2]. In this context, the transformation of methane into less volatile compounds, such as liquid organic oxygenates and C_n hydrocarbons, is of paramount importance for the chemical industry [3,4]. A very interesting process for this purpose is the reaction between CH_4 and CO_2, with the latter as an oxygen source and a wide range of possible reaction products. A typical example is the so-called Dry Reforming of Methane (DRM) to produce syngas (i.e., CO and H_2) as main reaction output [5] and with high potential for the synthesis of various high added value chemicals.

The conversion of CH_4 and CO_2 at high temperatures is characterized by relatively low conversion rates and not always by a good selectivity for the production of oxygenates, which may decompose or recombine at high temperatures [6]. During the last few decades, the study of nonthermal plasmas of CH_4+CO_2 mixtures has been a subject of much interest [5,7–9]. In general, syngas is the main reaction product in plasma reactors, although light and heavy hydrocarbons and organic oxygenates can also be obtained. This large variety of possible products precludes a proper definition of an energy efficiency parameter, making that this parameter is not taken into account explicitly, or that energetics

* The content of this chapter is expected to be published as: **P. Navascués**, J. Cotrino, A. R. González-Elipe, A. Gómez-Ramírez, Isotope Labeling for Reaction Mechanisms Analysis in CO_2 + CH_4 Plasmas in a Ferroelectric Packed-Bed Reactor

is only discussed in terms of syngas formation when this is the majority reaction product [5].

In CH_4+CO_2 plasmas, the compositional ratio of reactants is one of the most important factors controlling the reaction. According to R. Snoeckx and A. Bogaerts, this parameter affects both the CH_4 and CO_2 conversion rates and the product selectivity. Generally, the selectivity towards light hydrocarbons and H_2 formation increases and that of CO decreases when the amount of CH_4 increases. Meanwhile, the deposition of carbon diminishes when the amount of CO_2 increases. Another critical factor is the SIE, since it happens for the CO_2 splitting process (**see chapter 8**), the higher the SIE values the higher the conversion rates obtained [5].

Most studies about the plasma-assisted CH_4+CO_2 reaction have been carried out in DBD reactors with coaxial geometries. To improve conversion rates and increase the desired selectivity, a wide range of operating parameters have been varied, such as the power consumed, the flow rate, the feed ratio, the electrode materials, the addition of inert gases like He or N_2, etc. Additionally, different moderator materials have been essayed as barriers in packed-bed reactors [5]. In general, authors have reported syngas as the main reaction product, while the formation of little amounts of C_2 and C_3 hydrocarbons (i.e., C_2H_6>>C_3H_8>C_2H_4>C_2H_2) has been also reported [5,10–12]. Occasionally, C_4-C_{10} hydrocarbons and oxygenates in liquid form have also been obtained [10,13,14]. Catalysts are also utilized to increase the process selectivity [5]. The most common formulation is that of Ni particles as active metallic phase and alumina as support [15–17] (for more details, see the recent review of X. Gao *et al.* about the incorporation of Ni-based catalysts in DBD reactors for the reforming of CH_4+CO_2 mixtures [18]).

Several modeling studies have been also carried out to elucidate plasma reaction mechanisms in CH_4+CO_2 mixtures [11,14,19–21], although the complexity of the mixture and computational limitations preclude the development of accurate models [5]. Bogaerts and coworkers concluded that, in DBD reactors, CH_3 and CH_2 radicals formed from CH_4 are the main intermediate species to render C_2H_6 and C_3H_8 molecules. Similarly, they concluded that the dissociation of CO_2 into CO and O species is the dominant pathway involving this molecule and a required step for the formation of product molecules such as formaldehyde (CH_2O), or acetaldehyde (CH_3COH) [11,21]. However, to confirm the involved

reaction mechanisms, more experimental evidence are needed about these plasma-assisted processes. With this aim, as outlined in **Chapter 3** and utilized in **Chapter 5**, herein we apply the isotope labeling methodology to study plasmas of CH_4+CO_2 mixtures.

In this study, different CH_4+CO_2 mixtures have been ignited in the packed-bed reactor using PZT as moderator material. The main reaction products obtained have been H_2, CO, C_2, C_3, and H_2O, in descending order of concentration. To analyze the reaction mechanisms, the isotope labeling methodology has been applied using $^{13}CO_2$ instead of $^{12}CO_2$ as reactant. The application of this methodology, to our knowledge for the first time in the literature for these plasma processes, has allowed to experimentally demonstrate that, in CH_4+CO_2 mixtures, CH_4 and CO_2 reactants follow parallel reaction pathways, such that the interactions between radicals coming from each reactant scarcely happens. In other words, that intermediates coming from CH_4 and CO_2 do not interact extensively.

9.2. Experimental Details

Experiments have been carried out for a 5mm-PZT barrier (pellets with diameters between 2-3 mm). The applied voltage amplitude was fixed at an average value of 3.15 kV and the frequency at 5 kHz. The reactor was operated at atmospheric pressure and ambient temperature. As in **Chapter 8**, a fan was applied to cool down the reactor walls.

CH_4 and CO_2 have been used as main reactants, with a total inlet flow rate of 20 sccm. We used different CH_4:CO_2 feed ratios: 1:1, 2:1, 3:1, and 4:1, varying the CH_4 and the CO_2 flow rate from 10 to 16 sccm and from 4 to 10 sccm, respectively. These operating conditions (i.e., an equal or higher amount of CH_4 with respect to CO_2) were selected to promote the formation hydrocarbons [5]. Moreover, two additional experiments were designed to analyze the reaction mechanisms. On the one hand, a mixture of 14 sccm CH_4 and 1 sccm O_2 was ignited to study the effect of adding oxygen to a CH_4 plasma. On the other, to get a deeper insight into the reaction pathways, the 2:1 CH_4:CO_2 mixture was studied applying the isotope labeling methodology, using $^{13}CO_2$ instead of $^{12}CO_2$.

9.3. Results and Discussion

9.3.1. PZT-moderated CH_4+CO_2 Discharges

The ignition of CH_4+CO_2 plasmas in packed-bed reactors has been investigated using a broad range of materials to moderate the discharges. These studies include ferroelectrics such as $BaTiO_3$ [22,23], $LaNiO_3$ [24], Barium Zirconate Titanate (BZT) and Barium Ferrite Niobate (BFN) as packing materials [25]. W.-C. Chung *et al.* reported in 2014 that the use of BZT and BFN in a cylindrical packed-bed reactor renders higher CH_4 and CO_2 conversion rates than for the reactor filled with glass beads [25]. Based on the fact that PZT and BFN are characterized by similar dielectric constant values (1900 and 2025, respectively), it is expected that use of PZT can provide high reaction yields.

Figure 9.1 shows the absolute and effective conversion rates obtained as a function of the CH_4:CO_2 ratio. Although most studies in literature report absolute values, a proper assessment of conversion rate requires taking into account the dilution of each reactant in the inlet mixture and, therefore, to express the results in terms of effective conversion rates [5]. According to this figure, absolute and effective CH_4 conversion rates are higher than those of CO_2 for all studied conditions. The highest conversion rates, 34% and 25% for CH_4, and 22% and 5.4% for CO_2, absolute and relative magnitudes, respectively, were obtained for a 3:1 ratio. This difference between CH_4 and CO_2 conversion rates suggests that the probability of electron-impact reactions with CH_4 is higher than with CO_2 molecules, in agreement with reported results by Tu and Whitehead [16].

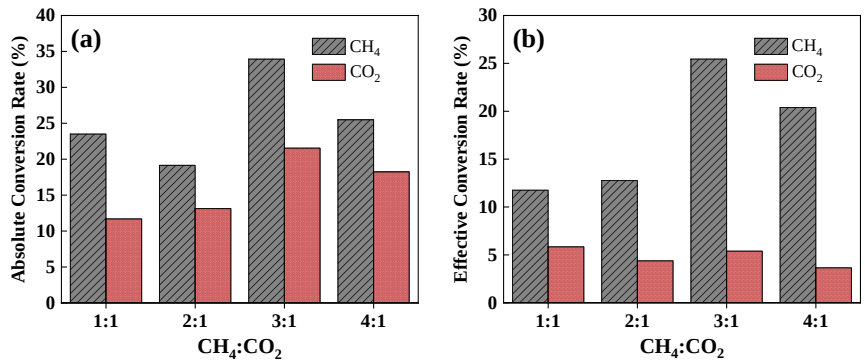

Figure 9.1. Absolute (a) and effective (b) CH_4 and CO_2 conversion rates as a function of the CH_4:CO_2 ratio. Operating conditions: 5 mm-PZT barrier, total flow rate of 20 sccm, voltage amplitude of 3.15 kV, frequency of 5 kHz, and CH_4:CO_2 ratio varied between 1:1 and 4:1.

The SIE is one of the most influential parameters when igniting CH_4+CO_2 plasmas, independently on the type of plasma reactor [5]. As described in **Chapter 3**, this parameter takes into account both the power consumed in the reactor and the flow rate (i.e., the residence time of the gases in the discharge). To rationalize the operating conditions of the experiment, constant flow rates, voltage amplitudes, and operating frequencies have been utilized. However, despite this constant operating conditions, the electrical characterization of the reactor in **Figure 9.2** shows that current and power values vary for the studied CH_4:CO_2 mixtures. **Figure 9.2(a)** shows the *I(t)* curves measured in stationary state conditions, and, in the form of bar plots, **Figure 9.2(b)** shows the power consumed by the reactor. According to **Figure 9.2(a)**, the discharges are characterized by a filamentary behavior, which is more prominent for the 3:1 mixture, which is characterized by current values higher than 100 mA and the highest power consumption of all the series of experiments. These high values agree with the conversion rate values reported in **Figure 9.1**.

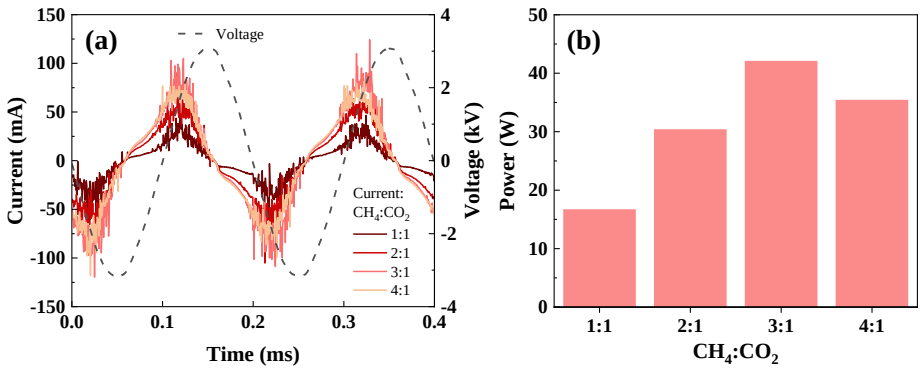

Figure 9.2. Electrical characterization of the plasma reactor fed with CH_4+CO_2 mixtures. Measured current curves (a) and consumed power values (b) as a function of the CH_4:CO_2 ratio. Operating conditions: 5 mm-PZT barrier, total flow rate of 20 sccm, voltage amplitude of 3.15 kV, frequency of 5 kHz, and CH_4:CO_2 ratio varied between 1:1 and 4:1.

To determine the type of products formed upon plasma excitation of the different mixtures, the outlet gases were analyzed by mass spectrometry. Plotted in logarithmic scale, **Figure 9.3** shows the mass spectra acquired for each mixture at stationary state conditions. Mass peaks associated with the reactants, CH_4 (m/z=16) and CO_2 (m/z=44), are indicated with gray dash lines, while mass peaks associated with reaction products are signaled with solid black lines and arrows. The outlet gases detected for the different mixtures consisted of unreacted CH_4 and

CO_2 and the following products: H_2 (m/z=2), CO (m/z=28), H_2O (m/z=18), and C_2 and C_3 hydrocarbons (fragmentation patterns between m/z=25 and m/z=44). In agreement with other authors [12], the formed species have been identified by comparison with the fragmentation patterns reported in the NIST Mass Spectrometer Database [26] (see **Chapter 3**, **section 3.2.3**). For example, for C_2 hydrocarbons, the main contributions due to the fragmentation pattern of acetylene (C_2H_2) are located in mass peaks m/z=25 and 26, while ethane (C_2H_6) peaks are located between m/z=25 and 30. On the other hand, for C_3 hydrocarbons such as propane (C_3H_8), main peaks are located between m/z=27 and 29, as well as for m/z=39, 43, and 44. Additionally, traces of C_4, C_5, and C_6 hydrocarbons can be inferred in the plots, as revealed by the group of peaks around m/z=55, 70, and 80, respectively. Apparently, no significant traces of oxygenated compounds, such as formaldehyde and acetaldehyde, were detected in these experiments, although a minority formation of these compounds cannot be discarded.

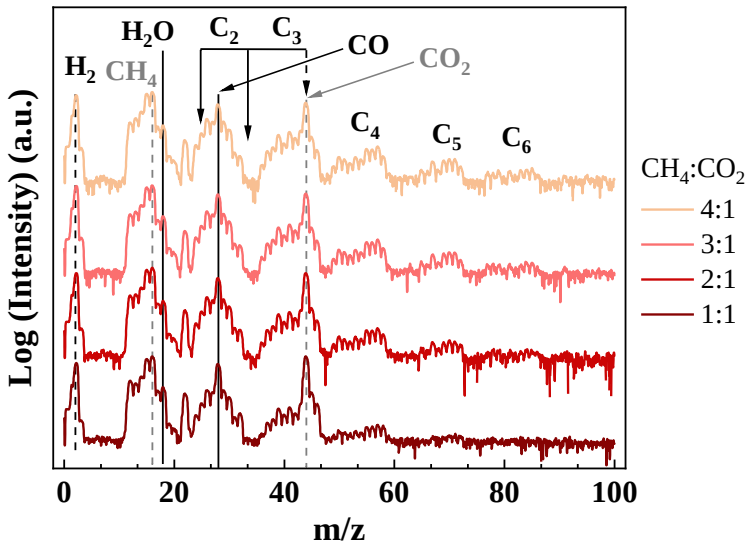

Figure 9.3. QMS spectra (logarithmic scale) acquired after plasma ignition of the indicated mixtures. Mass peaks associated with reactants (m/z=16 and m/z=44 for CH_4 and CO_2, respectively) are indicated with dash gray lines, while those associated with the main products are indicated with solid black lines and arrows (m/z=2 for H_2, m/z=18 for H_2O, m/z=28 for CO, and between m/z=25 and m/z=44 for C_2 and C_3 hydrocarbons). Traces of C_4, C_5, and C_6 hydrocarbons can be also inferred in these spectra. Operating conditions: 5 mm-PZT barrier, total flow rate of 20 sccm, voltage amplitude of 3.15 kV, frequency of 5 kHz, and CH_4:CO_2 ratio varied between 1:1 and 4:1.

A first qualitative analysis of the spectra plotted in **Figure 9.3** suggests that similar products are obtained for the different mixtures. The differences inferred from the mass spectra are probably related to the different power values (i.e., plasma intensity) utilized at each operating condition (c.f., **Figure 9.2(b)**). For example, the formation of minority products such as C_4, C_5 and C_6 hydrocarbons appears to be negligible for the 1:1 mixture, but it is noticeable for the 3:1 and 4:1 mixtures. Therefore, it can be concluded that the formation of long chain hydrocarbons is linked to a higher amount of CH_4 in the discharge and a higher power consumption.

Through the evaluation of the spectra plotted in **Figure 9.3**, it is possible to estimate the composition of the outlet gases. **Figure 9.4** shows this composition expressed in terms of flows of each compound detected by QMS, namely H_2O, H_2, CO, and C_2 and C_3 hydrocarbons. Due to the overlapping of the different m/z signals associated with hydrocarbons with the number of carbons C_n, flow rates of C_2 and C_3 have been determined without differentiating between alkanes, alkenes, or alkynes compounds. The formation of this type of products in the outlet mixture agrees with the results obtained by other authors, such as Tu and Whitehead [16] or M. Kraus *et al.* [19], working with cylindrical packed-bed reactors filled with quartz wool.

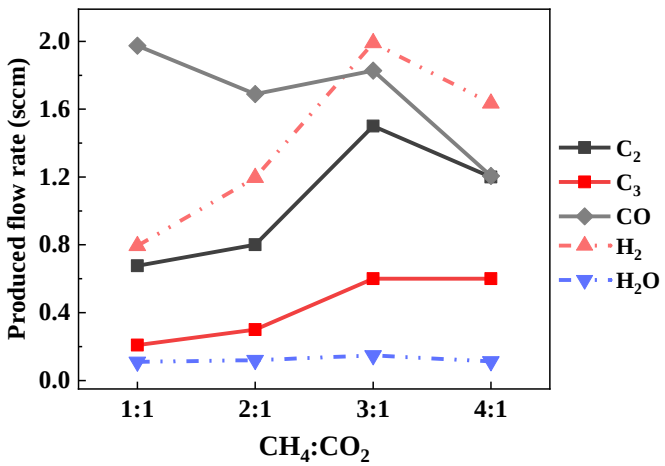

Figure 9.4. Flow rates of the different reaction products as a function of the CH_4:CO_2 ratio. H_2 (green) and H_2O (blue) flow rates are represented with dash lines, while C_2 hydrocarbons (black), C_3 hydrocarbons (red), and CO (gray) flow rates are represented in solid lines. The reported values are obtained by the evaluation of QMS spectra in **Figure 9.3**.

Figure 9.4 shows that syngas components (i.e., H_2 and CO) are the main reaction products [5], followed by C_2 and C_3 hydrocarbons whose production is quite noticeable at the higher (i.e., 3:1 and 4:1) CH_4:CO_2 ratios. The produced amount of H_2 follows a similar tendency than the CH_4 conversion rate (c.f. **Figure 9.1**) as expected from the fact that methane is the unique source of hydrogen atoms available in the system [16]. Flow rates of C_2 and C_3 hydrocarbons follow similar tendencies, although the amount of C_3 slightly varies from the 3:1 to the 4:1 mixture. On the other hand, the evolution of the CO flow follows the effective CO_2 conversion rate and the amount of CO_2 in the inlet mixture, i.e., it decreases with the CH_4:CO_2 reactant ratio. Meanwhile, the H_2O flow rate remained approximately constant at values around 0.12 sccm.

According to the literature, processes *E 9.1* - *E 9.3* are the main electron-impact reaction pathways for the dissociation of the CH_4 molecule [16], with threshold electron energies of 9, 10 and 12 eV, respectively [1]:

$$CH_4 + e^- \rightarrow CH_3 + H + e^- \quad (E\ 9.1)$$

$$CH_4 + e^- \rightarrow CH_2 + H_2 + e^- \quad (E\ 9.2)$$

$$CH_4 + e^- \rightarrow CH + H_2 + H + e^- \quad (E\ 9.3)$$

Different authors have reported that the probability of reactions *E 9.1 – E 9.3* strictly depends on the EEDF of the system [1]. Generally, simulations reveal that, working with dielectrics as DBD moderators, *E 9.1* means around 80% of the electron impact dissociation of CH_4 [21,27]. Due to that, C_2H_6 (i.e., CH_3-CH_3) and C_3H_8 (i.e., CH_3-CH_2-CH_3) are generally reported as the main hydrocarbons produced in CO_2+CH_4 plasmas in DBD reactors [5]. However, the shift to higher energies of the characteristic EEDFs in our experimental configuration – due to the use of PZT as discharge moderator – can justify the formation of a non-negligible amount of acetylene (C_2H_2, CH≡CH) in the outlet gas flow mixture, as revealed by the m/z=25 peak in **Figure 9.3**, mainly due to C_2H_2 [26].

Based on these considerations, we tentatively propose that reactions follow similar reaction pathways for the different mixtures, and that product formation mainly depends on CH_4 and CO_2 conversion rates. To get deeper in the analysis of reaction mechanisms, the different discharges have been characterized by optical emission spectroscopy.

9.3.2. Insights into the Reaction Mechanisms

Optical emission measurements can provide interesting insights into the plasma-chemistry reaction mechanisms. **Figure 9.5** shows the emission spectra recorded for the studied CH_4+CO_2 mixtures. For all the operating conditions, main detected bands correspond to CH^* excited species. The highest CH^* band was found at 314 nm, which is ascribed to the $C^2\Sigma \rightarrow X^2\Pi$ system; in addition, around 430 nm a band corresponding to the $A^2\Delta \rightarrow X^2\Pi$ CH-system is also detected [28]. On the other hand, similarly to other authors [16,19], bands attributed to the C_2 Swan system have been also detected at around 516 nm [28]. According to the literature, C_2 excited species may be formed during hydrocarbons degradation [5] and can contribute to the carbon deposition in the packed-bed pellets and on the surface of the electrodes. No significant contributions of OH^* species (306 nm) can be observed in the spectra, a feature that, in agreement with other authors as M. Kraus *et al.* [19], agrees with the little amounts of water found in the outlet mixture. Meanwhile, bands associated with the Third Positive System of CO are also detected at 283.3, 297.7, and 313.4 nm, the latter overlapping by the emission of CH^* species at 314 nm. Finally, formation of CO_2^+(B) states can be inferred by the detection of bands between 288.3 and 289.6 nm (for comparison, see results for CO_2 mixtures in **Chapter 8**).

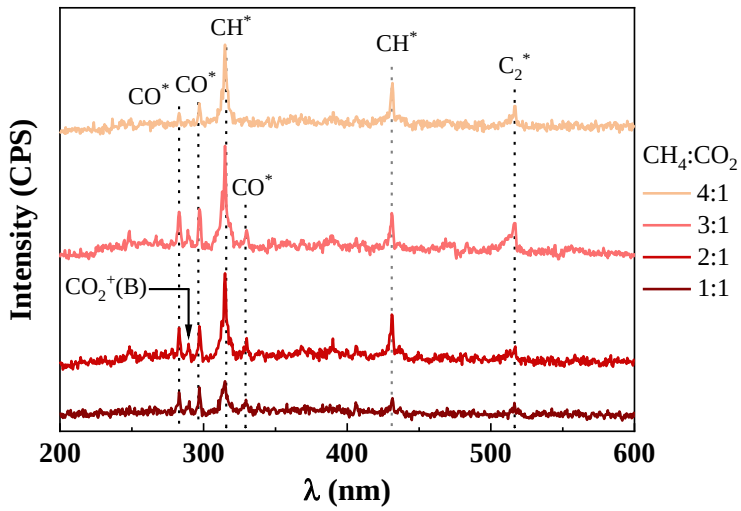

Figure 9.5. Emission spectra acquired for the CH_4+CO_2 plasmas. Main emission bands are indicated. Operating conditions: 5 mm-PZT barrier, total flow rate of 20 sccm, voltage amplitude of 3.15 kV, frequency of 5 kHz, and CH_4:CO_2 ratio varied between 1:1 and 4:1.

It has been mentioned in **Chapter 5** that high hydrogen-contain discharges (in that case, N_2+D_2 plasmas) depict a slight increase in the spectral background at lower wavelengths and that this increase is related to the emission of H_2 excited species. A similar increase can be observed in **Figure 9.5**, which is particularly remarkable for the 3:1 mixture associated with the higher flow of hydrogen produced under these conditions (c.f., **Figure 9.4**). It is also interesting that the CO^* bands present a negligible intensity for the 4:1 mixture, in agreement with the lower flow of CO produced under these operating conditions.

In **Figure 9.5**, it is also apparent the detection of the C_2 Swan system, which has been related to the carbon deposition onto material surfaces in contact with filamentary discharges formed when operating carbon-containing plasmas [5,9]. According to Tu and Whitehead, the deposition of solid carbon can take place through the direct decomposition of CH_4 by reaction *E 9.4*:

$$CH_4 + e^- \rightarrow C + 2H_2 + e^- \quad (E\ 9.4)$$

which is characterized by a threshold energy of 14 eV [16], generally too high for classic DBD configurations, but achievable when working with ferroelectrics in packed-bed reactors as in our experimental system.

The formation of carbon residues is usually associated with instabilities in the discharge or even the impossibility to sustain the plasma. It is noteworthy in this regard that igniting pure-CH_4 plasmas was not possible in the PZT packed-bed reactor, where the production of short-circuits did not enable the stable operation of the reactor. Therefore, it can be proposed that, for CH_4+CO_2 mixtures, oxygen radicals formed in the plasma (gas) due to the splitting of the CO_2 molecules can react with the carbon deposits formed on the surfaces of PZT pellets, according to the E-R mechanisms indicated in *E 9.5*:

$$O\ (\text{gas phase}) + C(s) \rightarrow CO\ (\text{gas phase}) \quad (E\ 9.5)$$

To prove that this reaction may take place in the PZT-moderated packed-bed reactor for CH_4+CO_2 mixtures, a specific experiment with a CH_4+O_2 mixture was designed (1 sccm O_2 and 16 sccm CH_4). Unlike the pure-CH_4 flow, the addition of oxygen enabled the stable ignition of the filamentary discharge. It is remarkable that plasma reaction induced the consumption of most part of the oxygen flow, as indicated with a yellow vertical band in the mass spectra in **Figure 9.6**. It is also observed in this QMS spectrum that peaks attributed to C_n hydrocarbons are also obtained similarly than for the CH_4+CO_2 mixtures (c.f.

Figure 9.3). Furthermore, CO_2 was obtained as an additional product in the outlet mixture (see the increase in the signal m/z=44 in **Figure 9.6**).

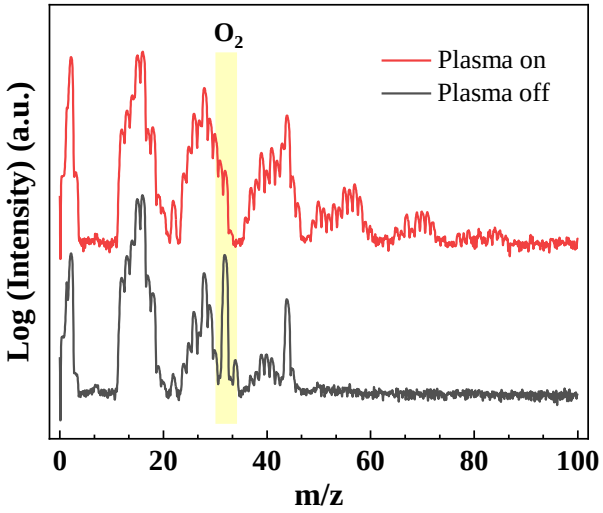

Figure 9.6. QMS spectra (logarithmic scale) acquired before (gray line) and after (red line) plasma ignition for the CH_4+O_2 mixture. The m/z=32 peak, attributed to O_2, is highlighted with a yellow band to show that a major part of the oxygen flow is consumed after 30 minutes of plasma operation (note that residual traces of CO_2 and H_2 were present in the quadrupole chamber before plasma ignition). Operating conditions: 5 mm-PZT barrier, voltage amplitude of 3.15 kV, frequency of 5 kHz, and total flow rate of 17 sccm (16 sccm CH_4 and 1 sccm O_2).

For the CH_4+CO_2 mixtures, reaction *E 9.5* between carbon residues deposited on the pellet surfaces and oxygen atoms from the plasma phase will contribute to the formation of CO in addition to its production by the direct dissociation of CO_2. Furthermore, three body interactions and other more complex processes may be also involved in the production of CO. To further analyze the reaction mechanisms, the isotope labeling methodology has been applied using $^{13}CO_2$ instead of $^{12}CO_2$ as reactant.

9.3.3. Isotope Labeling Analysis with $^{13}CO_2$ as Reactant in CH_4+CO_2 Mixtures

An experiment similar to those discussed in previous sections has been carried out using $^{13}CO_2$ in a CH_4+CO_2 mixture. The experiment was performed for a 2:1 CH_4:CO_2 ratio, a total flow rate of 20 sccm, and similar electrical operating conditions than in **section 9.3.1** (3.15 kV, 5 kHz). **Figure 9.7** illustrates the mass spectra acquired in the steady state after plasma ignition for mixtures with $^{12}CO_2$ and $^{13}CO_2$. **Figure 9.7(a)** shows the QMS spectra for m/z values from 0 to 100 in logarithmic scale. Peaks associated with H_2, H_2O, CH_4, and C_n hydrocarbons are located at the same positions for the two mixtures. However, signals related to CO (m/z=28 and 29) and CO_2 (m/z=44 and 45) are displaced depending on whether $^{12}CO_2$ and $^{13}CO_2$ are used for the experiments. **Figure 9.7(b)** shows the m/z region from 20 to 50 of these spectra, represented in linear scale to clearly illustrate the differences in this mass range. Comparing the two plots, it is apparent the detection of significant differences in the m/z=28 and 29 signals for the $^{12}CO_2$ and the $^{13}CO_2$ experiments.

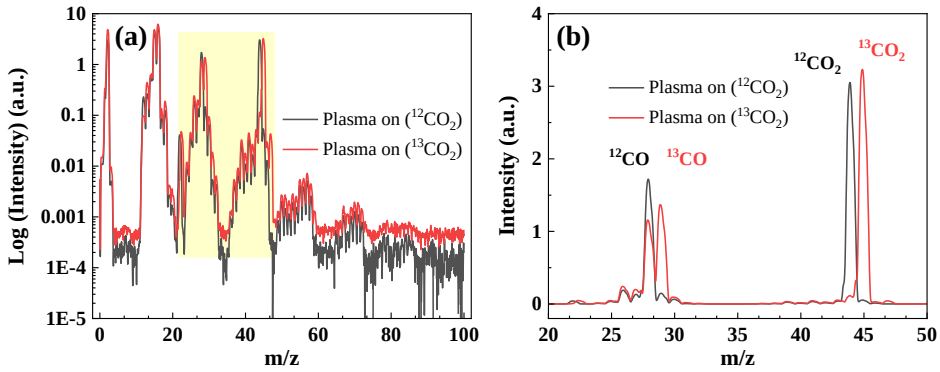

Figure 9.7. QMS spectra acquired using $^{12}CO_2$ (gray line) and $^{13}CO_2$ (red line) for the 2:1 mixture. (a) General spectra in logarithmic scale. (b) Zoomed zone between m/z=20 and m/z=50 in linear scale.

For the isotope-labeled mixture, main contribution to m/z=29 is due to ^{13}CO molecules. Meanwhile the remaining contribution to m/z=28 must stem from ^{12}C atoms in C_2 and C_3 hydrocarbons and in the CH_4 molecules, coinciding with the peak pattern of these hydrocarbons when studying the CH_4+$^{12}CO_2$ mixture. Similarly, for higher m/z values, the CO_2 peaks appears at m/z=44 and m/z=45 for the $^{12}CO_2$ and the $^{13}CO_2$ mixtures, respectively, while the following peaks (C_4 and C_5 hydrocarbons) define a similar pattern.

These observations suggest that, as proposed by model simulations, CH_4 and CO_2 seem to follow independent reaction pathways [11,21,29]. According to our results, these independent chemical routes only intersect under our experimental conditions to form H_2O (see **Figure 9.8**), without giving rise to the formation of oxygenate compounds (CHO, CH_3OH, etc.), as suggested by De Bie *et al.* [29]. Therefore, the applied isotope labeling methodology has allowed us to experimentally track these two general chemical pathways, as summarized in the scheme in **Figure 9.8**. Main reaction products resulting from these pathways are H_2 and hydrocarbons (mainly C_2 and C_3) when stemming from the direct decomposition of CH_4, as indicated with solid arrows in the green zone of the scheme in this figure. Meanwhile, the direct dissociation of the CO_2 molecule into O and CO should be the dominant pathway for this molecule (see the gray zone in **Figure 9.8**). As a result, a non-negligible interaction between H atoms (or the H_2 molecule) from CH_4 and O atoms from the CO_2 pathway should take place to form H_2O as minor reaction product (around 0.1 sccm, as discussed in **section 9.3.1**). Finally, although it may also be a minor reaction pathway, the interaction between C atoms from CH_4 (or even from CO_2) and oxygen atoms formed by the CO_2 splitting cannot be discarded, as indicated with the dash arrows that connect CH_4 and CO_2 reaction pathways.

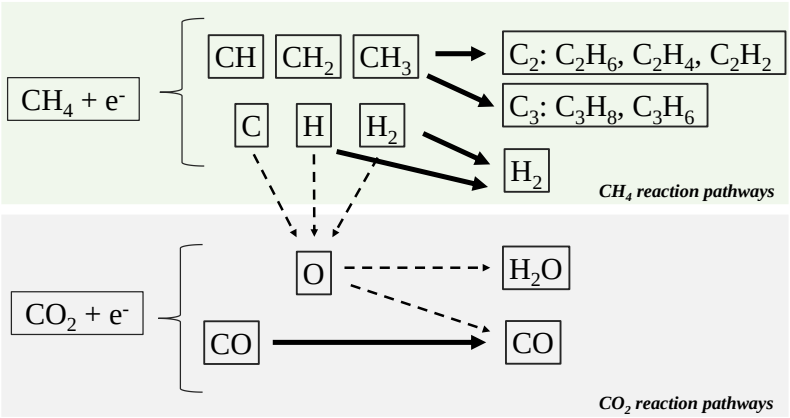

Figure 9.8. Scheme of the independent reaction pathways for CH_4+CO_2 mixtures. CH_4 and CO_2 routes are differentiated in green and gray colors, respectively. Solid arrows illustrate the main reaction pathways, while dashed arrows illustrate minority reaction pathways involving intermediate species of the CH_4 and/or CO_2 pathways.

9.4. Conclusions

In this study, CH_4+CO_2 mixtures have been investigated using a PZT-moderated packed-bed reactor operated at atmospheric pressure and ambient temperature. The CH_4:CO_2 ratio has been adjusted between 1:1 and 4:1, at a fixed voltage amplitude and frequency, obtaining similar types of reaction products. For all the operating conditions, the CH_4 conversion rate was higher than that of CO_2, with a maximum flow of methane converted for the 3:1 mixture, according to the highest power consumption for this mixture. Syngas (CO and H_2), as well as C_2 and C_3 hydrocarbons, are the main reaction products obtained, with a minor contribution of H_2O formed in the reactor. Additionally, slight signals of C_4, C_5 and C_6 hydrocarbons have been detected by mass spectrometry for the 3:1 and the 4:1 mixtures (i.e., with the highest amount of CH_4 in the inlet flow).

The CH_4+CO_2 plasmas have been analyzed with OES, revealing the formation of CH, CO, CO_2 and C_2 excited species. The detection of the C_2 Swan System has been related to the deposition of carbon and to the existence of characteristic high-energy electrons in the PZT-moderated packed-bed reactor. To study the possible carbon deposition, a mixture of CH_4 and a small flow of O_2 has been ignited, showing that a major part of the oxygen inlet flow is consumed, probably due to reactions between the carbon deposited on the surface of pellets and oxygen atoms of the plasma.

The flow of obtained products suggests that, according to the literature, CH_4 and CO_2 mainly follow independent reaction pathways. To analyze these reaction mechanisms, the isotope labeling methodology has been applied, using $^{13}CO_2$ instead of $^{12}CO_2$ in a CH_4+CO_2 mixture. Obtained results indicate that C_2 and C_3 hydrocarbons, as well as H_2, are formed due to the direct dissociation of CH_4, while the flow of CO produced in the reactor mainly comes from the dissociation of the CO_2 molecule, demonstrating that the interaction between species formed by the decomposition of CH_4 and CO_2 molecules represent a minor part of the involved chemical reactions.

9.5. References

[1] H. Puliyalil, D. Lašič Jurković, V.D.B.C. Dasireddy, B. Likozar, A review of plasma-assisted catalytic conversion of gaseous carbon dioxide and methane into value-added platform chemicals and fuels, RSC Advances. 8 (2018) 27481–27508. https://doi.org/10.1039/c8ra03146k.

[2] R.W. Howarth, R. Santoro, A. Ingraffea, R.W. Howarth, R Santoro, A. Ingraffea, Methane and the greenhouse-gas footprint of natural gas from shale formations, Climatic Change 2011 106:4. 106 (2011) 679–690. https://doi.org/10.1007/S10584-011-0061-5.

[3] S. Liu, L.R. Winter, J.G. Chen, Review of Plasma-Assisted Catalysis for Selective Generation of Oxygenates from CO_2 and CH_4, ACS Catalysis. 10 (2020) 2855–2871. https://doi.org/10.1021/acscatal.9b04811.

[4] E. v. Kondratenko, T. Peppel, D. Seeburg, V.A. Kondratenko, N. Kalevaru, A. Martin, S. Wohlrab, Methane conversion into different hydrocarbons or oxygenates: current status and future perspectives in catalyst development and reactor operation, Catalysis Science & Technology. 7 (2017) 366–381. https://doi.org/10.1039/C6CY01879C.

[5] R. Snoeckx, A. Bogaerts, Plasma technology-a novel solution for CO_2 conversion?, Chemical Society Reviews. 46 (2017) 5805–5863. https://doi.org/10.1039/c6cs00066e.

[6] W. Taifan, J. Baltrusaitis, CH_4 conversion to value added products: Potential, limitations and extensions of a single step heterogeneous catalysis, Applied Catalysis B: Environmental. 198 (2016) 525–547. https://doi.org/10.1016/J.APCATB.2016.05.081.

[7] A. Fridman (2008). Plasma Chemistry. Cambridge: Cambridge University Press. https://doi.org/10.1017/CBO9780511546075.

[8] A. Lebouvier, S.A. Iwarere, P. D'Argenlieu, D. Ramjugernath, L. Fulcheri, Assessment of Carbon Dioxide Dissociation as a New Route for Syngas Production: A Comparative Review and Potential of Plasma-Based Technologies, Energy and Fuels. 27 (2013) 2712–2722. https://doi.org/10.1021/EF301991D.

[9] W.C. Chung, M.B. Chang, Review of catalysis and plasma performance on dry reforming of CH_4 and possible synergistic effects, Renewable and Sustainable Energy Reviews. 62 (2016) 13–31. https://doi.org/10.1016/j.rser.2016.04.007.

[10] Y. Li, C.J. Liu, B. Eliasson, Y. Wang, Synthesis of oxygenates and higher hydrocarbons directly from methane and carbon dioxide using dielectric-barrier discharges: Product distribution, Energy and Fuels. 16 (2002) 864–870. https://doi.org/10.1021/ef0102770.

[11] A. Bogaerts, C. de Bie, R. Snoeckx, T. Kozák, Plasma based CO_2 and CH_4 conversion: A modeling perspective, Plasma Processes and Polymers. 14 (2017). https://doi.org/10.1002/ppap.201600070.

[12] A. Majumdar, F. Behnke, R. Hippler, K. Matyash, R. Schneider, Chemical Reaction Studies in CH_4/Ar and CH_4/N_2 Gas Mixtures of a Dielectric Barrier Discharge, Journal of Physical Chemistry A. (2005) 9371–9377. https://doi.org/10.1021/jp053588a.

[13] G. Scarduelli, G. Guella, D. Ascenzi, P. Tosi, Synthesis of Liquid Organic Compounds from CH_4 and CO_2 in a Dielectric Barrier Discharge Operating at Atmospheric Pressure, Plasma Processes and Polymers. 8 (2011) 25–31. https://doi.org/10.1002/PPAP.201000044.

[14] L.M. Martini, G. Dilecce, G. Guella, A. Maranzana, G. Tonachini, P. Tosi, Oxidation of CH_4 by CO_2 in a dielectric barrier discharge, Chemical Physics Letters. 593 (2014) 55–60. https://doi.org/10.1016/J.CPLETT.2013.12.069.

[15] Y. Zeng, X. Zhu, D. Mei, B. Ashford, X. Tu, Plasma-catalytic dry reforming of methane over γ-Al_2O_3 supported metal catalysts, Catalysis Today. 256 (2015) 80–87. https://doi.org/10.1016/J.CATTOD.2015.02.007.

[16] X. Tu, J.C. Whitehead, Plasma-catalytic dry reforming of methane in an atmospheric dielectric barrier discharge: Understanding the synergistic effect at low temperature, Applied Catalysis B: Environmental. 125 (2012) 439–448. https://doi.org/10.1016/J.APCATB.2012.06.006.

[17] A.J. Zhang, A.M. Zhu, J. Guo, Y. Xu, C. Shi, Conversion of greenhouse gases into syngas via combined effects of discharge activation and catalysis, Chemical Engineering Journal. 156 (2010) 601–606. https://doi.org/10.1016/J.CEJ.2009.04.069.

[18] X. Gao, Z. Lin, T. Li, L. Huang, J. Zhang, S. Askari, N. Dewangan, A. Jangam, S. Kawi, Recent Developments in Dielectric Barrier Discharge Plasma-Assisted Catalytic Dry Reforming of Methane over Ni-Based Catalysts, Catalysts 2021, Vol. 11, Page 455. 11 (2021) 455. https://doi.org/10.3390/CATAL11040455.

[19] M. Kraus, W. Egli, K. Haffner, B. Eliasson, U. Kogelschatz, A. Wokaun, Investigation of mechanistic aspects of the catalytic CO_2 reforming of methane in a dielectric-barrier discharge using optical emission spectroscopy and kinetic modeling, Physical Chemistry Chemical Physics. 4 (2002) 668–675. https://doi.org/10.1039/b108040g.

[20] R. Snoeckx, R. Aerts, X. Tu, A. Bogaerts, Plasma-based dry reforming: A computational study ranging from the nanoseconds to seconds time scale, Journal of Physical Chemistry C. 117 (2013) 4957–4970. https://doi.org/10.1021/jp311912b.

[21] C. de Bie, *Fluid Modeling of the Plasma-Assisted Conversion of Greenhouse Gases to Value-Added Chemicals in a Dielectric Barrier Discharge*, Antwerpen: Universiteit Antwerpen, 2016.

[22] V.J. Rico, J.L. Hueso, J. Cotrino, A.R. González-Elipe, Evaluation of Different Dielectric Barrier Discharge Plasma Configurations as an Alternative Technology for Green C1 Chemistry in the Carbon Dioxide Reforming of Methane and the Direct Decomposition of Methanol, Journal of Physical Chemistry A. 114 (2010) 4009–4016. https://doi.org/10.1021/JP100346Q.

[23] K. Zhang, T. Mukhriza, X. Liu, P.P. Greco, E. Chiremba, A study on CO_2 and CH_4 conversion to synthesis gas and higher hydrocarbons by the combination of catalysts and dielectric-barrier discharges, Applied Catalysis A: General. 502 (2015) 138–149. https://doi.org/10.1016/J.APCATA.2015.06.002.

[24] X. Zheng, S. Tan, L. Dong, S. Li, H. Chen, $LaNiO_3$@SiO_2 core–shell nanoparticles for the dry reforming of CH_4 in the dielectric barrier discharge plasma, International Journal of Hydrogen Energy. 39 (2014) 11360–11367. https://doi.org/10.1016/J.IJHYDENE.2014.05.083.

[25] W.C. Chung, K.L. Pan, H.M. Lee, M.B. Chang, Dry reforming of methane with dielectric barrier discharge and ferroelectric packed-bed reactors, Energy and Fuels. 28 (2014) 7621–7631. https://doi.org/10.1021/ef5020555.

[26] National Institute of Standards and Technology (NIST), Mass Spectrometer Data Center, (n.d.). https://chemdata.nist.gov/.

[27] C. de Bie, B. Verheyde, T. Martens, J. van Dijk, S. Paulussen, A. Bogaerts, Fluid Modeling of the Conversion of Methane into Higher Hydrocarbons in an Atmospheric Pressure Dielectric Barrier Discharge, Plasma Processes and Polymers. 8 (2011) 1033–1058. https://doi.org/10.1002/PPAP.201100027.

[28] R.W.B. Pearse and A.G. Gaydon (1965), The Identification of Molecular Spectra, 3rd ed., Chapman and Hall Ltd., England.

[29] C. de Bie, J. van Dijk, A. Bogaerts, The Dominant Pathways for the Conversion of Methane into Oxygenates and Syngas in an Atmospheric Pressure Dielectric Barrier Discharge, Journal of Physical Chemistry C. 119 (2015) 22331–22350. https://doi.org/10.1021/acs.jpcc.5b06515.

Chapter 10

General Conclusions

This conclusions chapter of the thesis work summarizes the main inferences of the study in relation to the proposed objectives (c.f., **Chapter 2**). The following general conclusions are proposed:

1. The use of ferroelectrics as discharge moderators in a packed-bed reactor (i.e., FBD packed-bed reactors) operated at atmospheric pressure promotes the formation of high-intensity plasma microdischarges.

This has been experimentally demonstrated in **Chapter 4**, where higher current intensities were obtained working with ferroelectrics ($BaTiO_3$, PZT) instead of dielectrics (Al_2O_3, Glass) at equivalent operating conditions. Specifically, PZT has resulted to be a good candidate as discharge moderator in FBD reactors for plasma-catalysis processes. This function relies on the high value of its dielectric constant at ambient temperature (1900), as well as its high Curie Temperature (332ºC). In **Chapter 4**, this positive effect regarding plasma intensity and formation of microdischarges has been demonstrated for the ammonia synthesis reaction, while in **Chapter 8** the same effect has resulted for the CO_2 splitting process, obtaining higher yields and efficiencies working with PZT than with $BaTiO_3$.

2. PZT-moderated packed-bed reactors are a suitable tool to carry out high-efficient plasma processes at atmospheric pressure and room temperature.

Reaction yields and energy efficiencies of 7% and 1 gNH_3/kWh, respectively, can be obtained for the ammonia synthesis reaction, while decomposition rates of 40% and efficiencies for hydrogen production of 30 LH_2/kWh have been obtained for the ammonia decomposition process. On the other hand, reaction yields around 9% and energy efficiencies around 8% have been obtained for the CO_2 splitting process in 15% air mixtures without producing N_XO_Y harmful compounds.

3. *Inefficient* plasma processes take place in the FBD packed-bed reactor, consume energy, and contribute to reducing the reaction yield and decreasing the energy efficiency of the process. Therefore, an efficient control of these *inefficient* processes through the adjustment of the working parameters is crucial to carry out more efficient plasma processes.

In **Chapter 5**, inefficient hydrogen exchange *reaction events* have been detected for the ammonia synthesis and decomposition reactions. On the other hand, in **Chapters 5**, **6,** and **8**, *back-reaction* processes have been highlighted for the ammonia synthesis and CO_2 splitting reactions. *Back-reaction* processes consist either in the decomposition of a product molecule as illustrated for the ammonia synthesis reaction in **Chapters 5** and **6,** or in the recombination of desired reaction products back to form reactants, as studied in **Chapter 8** for the CO_2 splitting reaction.

4. For the essayed operating conditions, the incorporation of a ruthenium metal catalyst into ferroelectric barriers does not substantially contribute to increasing the energy efficiency of the ammonia synthesis reaction. However, to a certain extent, it does enhance the reaction yield of the *ammonia to hydrogen* reaction process.

In **Chapters 5** and **6** it has been concluded that covering the PZT pellets with alumina-supported ruthenium catalyst particles significantly enhances the plasma intensity compared to a configuration with non-covered pellets and pellets cover only with an alumina coating. In **Chapter 6** it has been shown that this increase in plasma intensity does not result in a net improvement in the performance of the ammonia synthesis reaction. In **Chapter 7**, though, it is shown that this increase in plasma intensity is accompanied by a certain increase in the reaction yield of the ammonia decomposition reaction. However, whether these effects on reaction performance are the result of the observed increase of plasma intensity or stem from a catalytic effect associated with the ruthenium metal is still a matter of debate.

5. Optical Emission Spectroscopy (OES) has been demonstrated to be a powerful semi-qualitative tool to characterize excited species in the plasma and to figure out possible reaction mechanisms taking place in the gas phase.

OES evidence has been supporting the existence of high-energy electrons in the plasma when using PZT pellets in the FBD reactor. This is, for example, indicated by the detection of the first negative system of N_2^+, the emission bands of the CO_2^+ molecule, the Third Positive System of CO, or the C_2 Swan System. In addition, the detection of these and other species in the plasma has provided useful information related to the plasma mechanisms involved in each specific reaction.

6. The isotope labeling technique has been demonstrated to be a robust and useful methodology to unravel reaction mechanisms occurring in the plasma phase and on the surface of the barrier material.

The use of D_2 instead of H_2 in the study of *ammonia reactions* has revealed the existence of inefficient *reaction events*, which consist of the exchange of hydrogen atoms between NH_3 and H_2/D_2 molecules, as well as between reaction intermediates (NH_X/ND_X). Additionally, the involvement of PZT in promoting the activation of hydrogen species and their eventual interaction with nitrogen species has been demonstrated for the ammonia synthesis reaction. On the other hand, the use of $^{13}CO_2$ instead of $^{12}CO_2$ for the CH_4 & CO_2 valorization reaction has experimentally demonstrated that, in CH_4+CO_2 plasmas, CH_4 and CO_2 reactants follow independent plasma reaction pathways with practically no mixing steps.

Scientific Production

Related to the content of this thesis:

The following articles related with the thesis work have been published in peer review international journals:

- **Paula Navascués**, José Cotrino, Agustín R. González-Elipe, and Ana Gómez-Ramírez. *Plasma assisted CO_2 dissociation in pure and gas mixture streams with a ferroelectric packed-bed reactor in ambient conditions*, Chemical Engineering Journal, 430 (2022) 133066; https://doi.org/10.1016/j.cej.2021.133066
  (Chapter 10)

- **Paula Navascués**, Jose M. Obrero-Pérez, José Cotrino, Agustín R. González-Elipe and Ana Gómez-Ramírez. *Unraveling Discharge and Surface Mechanisms in Plasma-Assisted Ammonia Reactions*, ACS Sustainable Chemistry & Engineering, 8 (39) (2020) 14855–14866; https://doi.org/10.1021/acssuschemeng.0c04461
  (Chapter 5)

- **Paula Navascués**, Jose M. Obrero-Pérez, José Cotrino, Agustín R. González-Elipe, and Ana Gómez-Ramírez. *Isotope Labeling for Reaction Mechanism Analysis in DBD Plasma Processes*, Catalysts, 9 (1) 45 (2019); https://doi.org/10.3390/catal9010045
  (Chapter 5)

- Ana Gómez-Ramírez, Rafael Álvarez, **Paula Navascués**, Francisco J. García-García, Alberto Palmero, José Cotrino, Agustín R. González-Elipe. *Electrical and reaction performances of packed-bed plasma reactors moderated with ferroelectric or dielectric materials*, Plasma Processes and Polymers, 18 (3) (2021) 2000193; https://doi.org/10.1002/ppap.202000193
  (Chapter 4)

The following articles are in preparation and will be submitted for their publication in peer review international journals:

- **Paula Navascués**, Juan Garrido-García, José Cotrino, Agustín R. González-Elipe, and Ana Gómez-Ramírez. *Energy Efficiency and Reaction Mechanisms by the Ammonia Synthesis in a Ferroelectric Packed-bed Plasma Reactor Adding Ruthenium Catalyst*. Manuscript in preparations to be sent for publication as invited article in ACS Sustainable Chemistry & Engineering.
  (Chapter 6)

- **Paula Navascués**, José Cotrino, Agustín R. González-Elipe, and Ana Gómez-Ramírez. *Ammonia to Hydrogen by Plasma-Catalysis in a Ferroelectric Packed-Bed Reactor at Ambient Conditions*, Manuscript in writing process.
  (Chapter 7)

- **Paula Navascués**, José Cotrino, Agustín R. González-Elipe, and Ana Gómez-Ramírez. *Isotope Labeling for Reaction Mechanisms Analysis in CO_2+CH_4 Plasmas in a Ferroelectric Packed-Bed Reactor*, Manuscript in the writing process.
  (Chapter 9)

Other international scientific publications:

Other articles published in peer review international journals during the development of the Ph.D. thesis are:

- E Arroyo, **Paula Navascués**, Ana Gómez-Ramírez, Ricardo Molina, Álvaro Perea, José Luis García, José Cotrino, Manuel Cantos, Agustín R. González-Elipe, and Carmen López-Santos. *Triggering factors of germination in plasma activated cotton seeds: Water imbibition vs. Reactive Species Formation*, Journal of Physics D: Applied Physics, 54 325205 (2021); https://doi.org/10.1088/1361-6463/abfefc

- **P Navascués**, A R González-Elipe, J Cotrino, and A Gómez-Ramírez. *Large gap atmospheric pressure barrier discharges using ferroelectric materials*, Plasma Sources Science and Technology, 28 (7) (2019) 075002; https://doi.org/10.1088/1361-6595/ab28ce

Scientific publications in national journals:

The following article was published in the Journal of the Spanish Society of Materials regarding the SOCIEMAT Award "Best Master's Degree Thesis in Material Science" of 2019:

- **P Navascués**, A R González-Elipe y A Gómez-Ramírez. *Plasmas atmosféricos de barrera ferroeléctrica para la descomposición de CO_2*, MATERIAL-ES, Revista de la Sociedad Española de Materiales (SOCIEMAT), 3 (3) 2019.

Conference contributions:

The following contributions have been presented by the Ph.D. candidate as oral talks in international conferences, or have been submitted for upcoming international conferences:

- **Paula Navascués**, José Cotrino, Agustín R. González-Elipe, and Ana Gómez-Ramírez. *Plasma-assisted CO_2 splitting in a PZT-moderated packed-bed reactor*. Submitted. 18th International Conference on Plasma Surface Engineering (PSE 2022), 12th – 15th September 2022, Trade Fair Erfurt, Germany.

- **Paula Navascués**, Jose M. Obrero-Pérez, José Cotrino, Agustín R. González-Elipe, and Ana Gómez-Ramírez. *Unravelling the limitations of ammonia synthesis by non-thermal plasmas*, Plasma Tech 2021 On-line International Conference, 7th – 9th April 2021.

- **Paula Navascués**, Jose M. Obrero-Pérez, José Cotrino, Agustín R. González-Elipe, and Ana Gómez-Ramírez. *Ammonia synthesis and decomposition with a ferroelectric packed-bed plasma reactor*, RIVA On-line Conference 2021, 4th – 6th October 2021.

Additionally, the following contributions are accepted or submitted for upcoming international conferences:

- **Paula Navascués**, José Cotrino, Agustín R. González-Elipe, and Ana Gómez-Ramírez. *Plasma assisted CO_2 dissociation in pure and gas mixture streams a PZT-moderated packed-bed reactor*. Accepted. Plasma Tech 2022,27th – 29th April 2022, Barcelona, Spain.

- **Paula Navascués**, Jose M. Obrero-Pérez, José Cotrino, Agustín R. González-Elipe, and Ana Gómez-Ramírez. *Unravelling the limitations of ammonia synthesis by non-thermal plasma*. Accepted as invited talk. 18th International Conference on Plasma Surface Engineering (PSE 2022), 12th – 15th September 2022, Trade Fair Erfurt, Germany.

- **Paula Navascués**, Jose M. Obrero-Pérez, José Cotrino, Agustín R. González-Elipe, and Ana Gómez-Ramírez. *Discharge and surface mechanisms in plasma-assisted NH_3 synthesis.* Submitted. 5th International Symposium on Plasmas for Catalysis and Energy Materials (ISPCEM), 3rd – 7th July 2022, Liverpool, UK.

Agradecimientos

Me gustaría trasladar mi más sincero agradecimiento …

a mis directores, Ana Gómez Ramírez y Agustín Rodríguez González-Elipe, así como a Jose Cotrino, por haber confiado en mí para hacer este trabajo, por vuestro tiempo y enseñanzas, vuestra paciencia, comprensión, el haberme trasladado vocación y curiosidad científica. Pequeñas decisiones pueden influir una vida, así que, Pepe, menos mal que se me ocurrió ir a tu despacho a finales de 2016 para preguntarte por el Trabajo Fin de Grado. Muchas gracias a los tres por apostar por mí.

al Instituto de Ciencia de Materiales de Sevilla, a sus trabajadores y a las instituciones que lo componen, el Consejo Superior de Investigaciones Científicas (CSIC) y la Universidad de Sevilla (US). Con especial cariño al director de nuestro Instituto, Juan Pedro Espinós, que siempre se alegra por mí. A la Facultad de Física (US), en la que me he formado durante los últimos nueve años. Al Departamento de Física Atómica, Molecular y Nuclear y a todas las personas que hacen posible el Programa de Doctorado en Ciencias y Tecnologías Físicas por su ayuda y su amabilidad.

herzlichen Dank an den Deutscher Akademischer Austauschdienst (DAAD), das Leibniz Institut für Plasma Forschung und Technologie (INP), Prof. Dr. Jürgen Kolb, Dr. Volker Brüser und Prof. Dr. Ronny Brandenburg. Der Forschungsaufenthalt am INP war überlebenswichtig für meine Bildung als Forscherin. Danke auch für alle diese Leute, die in Greifswald mit mir waren und mir geholfen haben / thanks also to all the people that were with me in Greifswald and did help me.

Pensé que los párrafos anteriores serían suficientes. En realidad, todo lo que viene después ya se sabe, ya lo sabéis. Pero después pensé que una no agradece pensando en sí misma, sino en los demás, y que buscaréis vuestros nombres en estas páginas. Así que intentaré ser breve y dar lo mejor de mí. Objetivamente, estas palabras tienen como fin transmitir mi gratitud a aquellas personas que, de una forma u otra, han contribuido a que este trabajo salga adelante. En mi caso, eso son muchas personas, de distintos sitios. Así que, gracias de todo corazón …

a todas y cada una de las personas que componen el grupo de investigación de Nanotecnología en Superficies y Plasma. Permitidme un especial agradecimiento a Víctor Rico por su compañía y confianza. A Jose Obrero – todavía me acuerdo del día que me enseñaste a identificar picos en el masas – a Ester López – por enseñarme que la vida o es alegre, o no es vida – a Javier Castillo, una persona en la que sé que siempre podré confiar – a Xabier García, por mil motivos, como la fruta desecada – a Aurelio García, por dejarme ver las cosas antes de que me pasaran – a Nerea de Tena, por volver a estar juntas. A Ana Borrás y Carmen López, cómo decirlo, tendría que poneros un piso, pero bueno, podemos dejarlo en gracias por enseñarme que los sueños se cumplen y que los *ídolos* no están en la tele, están a mi lado … ¡y son mis amigas!

a todas las personas que han trabajado durante estos años en el Instituto de Ciencia de Materiales de Sevilla y han dedicado su tiempo a ayudarme. A Encarna Arroyo y Cristina López, por vuestro cariño y amistad. Al personal técnico, de limpieza, de seguridad y administración del Centro de Investigaciones Científicas Isla de la Cartuja, porque sin esas *personas que hacen las cosas* no podemos construir nada por encima. Con especial cariño a José Ignacio Ruiz y Juan Carlos Martín, por cuidarme y creer en mí.

a mis amigas y mi familia, términos que en mi caso se confunden. Sois muchas, muchísimas personas que habéis estado admirándome, animándome y compadeciéndome a la vez. Por ejemplo, *Pablo Collantes and Wiebke Mohr: you both have showed me that it is possible to build a family in months.* A Madeleine Brink, por hacerme comprensible. A mi familia paterna, por dejarme ocupar el lugar de mi padre para cerciorarnos de que sigue aquí. A mi tía Pepa, siempre a mi lado. A mi gente, mis hermanos y hermanas, de mi barrio, aunque el *buscarnos la vida* haga que ahora estemos lejos físicamente. A mis primas *políticas*. A muchísimas personas que sostienen mis ideas y gracias a ellas no me caigo. A mi médico de confianza, mi novio de mentira. A la que lleva conmigo un cuarto de siglo. A Pedro y a Isa, a mi hermano y a Marta, que sanamente alimentan mi ego. A Elena Cabello, por ser mi luz. A Conchi, el tritón, por su amor, paciencia y compañía en los momentos más duros de este trabajo.

a mis padres, por regalarme la vida, su inteligencia y su ideología. Todo lo que hago tiene perspectiva, nada está improvisado, tenemos un objetivo y voy a por ello. Todo por las desposeídas: esa motivación es nuestra mayor fortuna. Siempre, cogida de vuestra mano, estaré buscando la estrella.

Diseño de portada por Bruno Fito

Sevilla, marzo de 2022